Study and modelling of the thermohydraulic phenomena taking place during the quench of a superconducting magnet cooled with superfluid helium

Unai Duranona

université PARIS-SACLAY

Study and modelling of the thermohydraulic phenomena taking place during the quench of a superconducting magnet cooled with superfluid helium

Etude et modélisation de phénomènes thermohydrauliques résultant du quench d'un aimant supraconducteur refroidi en hélium superfluide

Thèse de doctorat de l'université Paris-Saclay

École doctorale n°576 : particules hadrons énergie et noyau : instrumentation, imagerie, cosmos et simulation (PHENIICS)
Spécialité de doctorat: physique
Graduate School : Physique, Référent : Faculté des sciences d'Orsay

Thèse préparée au Département des Accélérateurs, de la Cryogénie et du Magnétisme - DRF/IRFU (Université Paris-Saclay, CEA) sous la direction de Bertrand BAUDOUY et l'encadrement de Walid ABDEL-MAKSOUD

Thèse soutenue à Paris-Saclay, le 29 novembre 2022, par

Unai DURAÑONA

Composition du jury

Mme Monika Lewandowska Professeur, West Pomeranian University of Technology Szczecin (Institute of Physics)	Présidente
M. Luca Bottura Ingénieur de recherche, CERN (Magnet Group)	Rapporteur & Examinateur
M. Marco Breschi Professeur, University of Bologna (UNIBO)	Rapporteur & Examinateur
M. Bertrand Baudouy Ingénieur de recherche, CEA Saclay (IRFU/DACM)	Directeur de thèse

THESE DE DOCTORAT

NNT: 2022UPASP129

Amama eta Tatie Maite, Tatie Maite eta Amama
Lan hori eskaintzen dizuet.

Remerciements

Cette thèse est le résultat de 3 ans de dur labeur au Commissariat à l'Energie Atomique et aux Energies Alternatives (CEA) de Saclay, au sein du Laboratoire de Cryogénie et des Stations d'Essais (LCSE) du Département des Accélérateurs, de Cryogénie et de Magnétisme (DACM) de l'Institut de Recherche sur les Lois Fondamentales de l'Univers (IRFU).

Je souhaiterai donc commencer par remercier la direction du DACM et du LCSE, M. Pierre VEDRINE, M. Philippe BREDY, M. Christophe MAYRI ainsi que Mme. Roser VALLCORBA CARBONELL, qui m'ont accueilli au sein du CEA et de leur équipe. Je souhaite également les remercier d'avoir pu mettre à disposition les moyens techniques et financiers nécessaires à la réussite de ces travaux de thèse.

Je tiens également à remercier Mme. Moninka LEWANDOWSKA, M. Luca BOTTURA et M. Marco BRESCHI pour l'honneur qu'ils m'ont fait de faire partie de mon jury de thèse. Je les remercie pour le travail minutieux qu'ils ont fournis et pour les intéressantes discussions que leurs questions ont amenées. Grâce à eux, ce manuscrit de thèse n'en est que meilleur et le travail restant pour la suite est bien identifié.

De manière générale, je souhaite remercier toutes les personnes avec qui j'ai pu intéragir au DACM durant ces 3 dernières années. Remerciement spécial à François-Paul JUSTER pour les nombreuses discussions éclairantes sur la physique du quench, et sans qui je n'aurai probablement toujours rien compris à la détente isenthalpique. Gros big up aux autres doctorants du service, Clément GENOT, Mahmoud ABDEL-HAFIZ, Simon BAGNIS et Guillaume CAMPAGNA pour les bons moments de rigolade.

Comment ne pas avoir une pensée pour l'équipe MADMAX qui m'a accompagné ces 3 dernières années: mon duo d'italien préféré Francesco STACCHI et Valerio CALVELLI, Jean-Pierre LOTTIN le grand expert de THEA et de la cryo, El Professor Christophe BERRIAUD, Loris SCOLA Stéphane JURIE et François NUNIO même si j'ai tout donné j'ai toujours rien compris à la mécanique. Remerciement particulier à Clément LORIN pour ses conseils avisés, ses bonnes blagues et les nombreuses heures passées au chevet de notre MACQU bien aimé. Pour finir, comment ne pas remercier mon colloc de bureau, mon collègue et mon ami, Théophile PONTAROLLO pour les très nombreuses discussions intéressantes mais aussi celles un peu moins intéressantes, sur des sujets vastes et variés. Merci pour ton grand soutien et notre amitié qui perdurera même après le CEA !

Je souhaite aussi remercier spécialement toute la team du 198 pour m'avoir supporté pendant mes nombreuses heures de rédaction: Jean-Marc GHELLER, Nicolas COMMAUX, Thomas BARABE et Denis BOUZIAT. En plus de la rédaction, Romain GODON, Pascal GODON, Thomas DONGA, Ricardo CORREIA-MACHADO et Leo SEGRESTAN pour l'énorme travail fourni sur MACQU ainsi que les nombreux fous rires autour de café et autres viennoiseries en tout genre ! Dedicace aussi à Séverine CANDAU et Bénédicte PICCIRELLI pour les repas, les pauses et autres aides que vous avez pu m'apporter, sans parler des nombreuses rigolades !

Je voudrai aussi remercier Bertrand BAUDOUY, mon directeur de thèse, pour son encadrement tout au long de la thèse. Je voudrai insister sur sa disponibilité, son humour, ses nombreux conseils, la patience ainsi que toute la pédagogie dont il a pu faire preuve.

Ce travail de thèse n'a pu être aussi réussi que grâce à l'encadrement de Walid ABDEL-

MAKSOUD. Toujours le mot pour rire mais également le mot juste, une intelligence à toute épreuve ainsi qu'une gentillesse que j'ai rarement vu dans ma vie. Il a été un support constant durant ces 3 dernières années et je l'en remercie profondément pour cela. Sans ton aide Walid, je n'y serai pas arrivé alors merci encore énormement.

C'est l'heure d'être un peu plus sentimental. Toutes les personnes avec qui j'ai travaillé m'ont beaucoup aidé c'est vrai, mais la famille et les amis occupent aussi une place toute particulière dans la réussite de cette thèse. Tout d'abord, un merci tout particulier à Bixente et Oihan, mes deux meilleurs amis ainsi qu'à ma Mallaury pour votre soutien constant et les journées, après-midi ou soirées de décompression que vous avez pu me faire passer afin de juste penser à autre chose pendant quelques heures quand ça n'allait plus. Pour finir, les 3 derniers, ceux qui sont là depuis le début, et qui m'ont toujours encouragé et poussé vers le haut, qui n'ont pas besoin d'être cité mais qui le seront quand même: Aita, Ama et Jojo, milesker bihotzetik <3

Contents

List of Figures

List of Tables

General introduction

Since 2010, a new strategy for the detection of dark matter has emerged at the Max-Planck Institute (MPI) based on the research on hypothetical particles called axions [1,2]. The interest of the axion lies in its mass range which has not been explored with the previous experiments, and is assumed to be 40 - 400 µeV. To explore such a mass range, dielectric haloscopes, composed of dielectric disks placed in a magnetic field, are used [3]. At the interface of different dielectric media, the axion is expected to behave like a photon, generating electromagnetic radiation in a magnetic field [4]. Therefore, with the actual technologies, a figure of merit of 100 T^2m^2 (integrated square magnetic field along the direction of the warm bore on the cross-section of the bore) in a warm bore in which the different dielectric media would be inserted [5] is a challenging objective.

In the framework of an innovation partnership launched by the MPI in 2018, the role of the CEA is to design, develop and manufacture a dipole magnet with exceptional characteristics such as a 9 T magnetic field [6], with a large aperture of 1.35 m, on a length of 1.3 m, and a gigantic magnetic energy of 527 MJ [7]. It is the first time that a dipole allies all these characteristics compared to previous dipoles [8–11]. To generate such conditions, the best option is to use superconducting magnets. These magnets can transport large electrical currents in their conductor without generating losses, due to their null electrical resistance below a specific temperature. However, superconducting magnet can experience unexpected transitions from a superconducting state to a resistive state. When this transition occurs, the stored magnetic energy of the magnet is dissipated by Joule effect in the conductor and the cooling fluid. The fluid is heated and pressurized while the transited zone propagates along the magnet. Excessive pressure or temperature increases can lead to a local deterioration of the conductor or degradation of the superconducting properties of the magnet. However, detected soon enough, this transition, and the following propagation, can be stopped, preserving the magnet from any degradation. This multi-physical transition phenomenon is called a quench and must be analyzed when designing a superconducting magnet. The quench has been described by several predictive analytical [12–14] and numerical models [15–17]. Based on heat equations for the conductor and the fluid, these models describe the propagation of the quench in considering electric, thermal and hydraulic phenomena. Nevertheless, even if the quench phenomena has been studied a lot in the past, it remains an important risk for all magnet design especially when the magnet has a huge stored energy and a novel kind of conductor like MADMAX. Indeed, for the MADMAX conductor design, a novel concept of conductor has been developed. The conductor is based on a Cable-In-Conduit Conductor (CICC) technology [18]. This technology has been well-mastered on projects such as JT60-SA [19], W7X [20], ITER [21], DEMO [22], etc. Today, this technology is industrially manufacturable by several companies around the world while other concepts are no more existing in industry.

The novel conductor of MADMAX mixes the CICC technology with a bath cooling concept in superfluid helium. The idea is to fill the void fraction of the CICC with stagnant superfluid helium that will ensure the thermal stability of the conductor against heat perturbations and quench initiation. Using superfluid helium below 2 K allows getting higher current performances for the cable compared to the usual 5 K in forced-flow convection cooling for CICC. However, the unusual combination of superfluid helium with a CICC has been rarely used. As far as we know, the NHMFL 45-T Hybrid magnet is the only other project using stagnant superfluid to cool a classical CICC conductor [23]. However, a very important difference exists between

MADMAX and the 45-T magnet. In the 45-T magnet, the copper stabilizer are the copper strands twisted with the Nb-Ti strands which ensure a very good electrical contact between Nb-Ti and copper strands and protection against quench. In MADMAX, the cable is made of 100 % Nb-Ti strands and the stabilizer is an outer copper profile. This novel configuration is unique and thus no study is available in the litterature. Moreover, even with a classical CICC design, the NHMFL magnet must finally work at a downgraded current of 8 kA [24] instead of 10 kA due to an unprotected quench that damaged the coils. This shows once again how difficult the quench protection is in the MADMAX case and how important is our study without previous published studies.

The combination of filling a CICC with superfluid helium and ensuring thermal stability by a copper profile has never been done before. In fact, these two combined features are enough to justify that the quench behavior of MADMAX is unknown, and justifies our interest in studying and modeling the thermohydraulic phenomena taking place during the quench of a CICC-based superconducting magnet cooled down with superfluid helium.

When a quench occurs, the superconducting cable transits locally and a voltage is generated across the magnet. The quench starts propagating by heat conduction and then increases the voltage. This voltage must be measured to ensure the detection of the quench to protect the magnet. The driving parameter of the quench detection is the quench propagation speed. Indeed, if the quench propagation speed is high enough, the voltage increases rapidly and allows the quench detection. If the quench is too slow, the needed time to detect the quench becomes too important and risks damaging the magnet. Thereby, to study and understand the quench behavior of MADMAX, it has been decided to design, manufacture, and test a mock-up coil called MACQU (MAdmax Coil for Quench Understanding) reproducing the working conditions of MADMAX. The goal of MACQU is to reproduce and study a MADMAX-representative quench propagation and measure a MADMAX-representative quench propagation speed. The non-detection of a quench on MACQU would lead to an invalidation of the MADMAX CICC.

To achieve the goals of our study, the first step is to design and construct a coil reproducing the MADMAX quench behavior. Chapter 2 of this Ph.D. report is dedicated to the design of the superconducting mock-up coil MACQU, by presenting the design guidelines and the design method to reproduce the MADMAX quench behavior [25]. The driving parameters that must be reproduced are of course the conductor design and the dissipative heat losses by Joule effect, for a similar hydraulic diameter.

After the design presentation, the MACQU mock-up construction and the experimental environment are presented in chapter 3 where the integration and the instrumentation of the MACQU magnet inside the test facility are detailed. The different experimental measurement methods available for the studies, such as the Superconducting Quench Detectors, the voltage measurements or the temperature sensors are introduced.

The quench experimental results are presented and analyzed in chapter 4. These results demonstrated that the quench is detectable, validating the conductor concept for the MADMAX project. The experimental analysis of the quench dynamics showed that quench propagation can be divided into three main phases. Each phase is analyzed and the driving physical phenomena of each phase are identified.

Finally, in chapter 5, the THEA® software, for Thermal, Hydraulic and Electric Analysis, is used to simulate the quench propagation cases of MACQU and to complete the analysis of the experimental findings. By computing the pressure, velocity and temperature variation inside the coil, the numerical results allow us to deeply study each term of the heat, mass and

pressure equations and identify precisely the predominant physical phenomena that drive each single phase of the quench propagation.

1 - Quench in a superconducting magnet

Objectives

- Provide the context and the problem of this study
- Introduce the main issues related to the quench propagation in a superconducting magnet in order to carry out a detailed study of the quench tests of the MACQU coil
- Give a detailed description about the thermal and electric properties of a superconducting Cable-In-Conduit Conductor that will be applied to study the thermohydraulic phenomena during a quench

1.1. Context and problem

1.1.1. MADMAX project

MADMAX is a superconducting dipole magnet designed at CEA for the research of the axion particle [1]. The axion is a hypothetical particle that could solve the strong CP problem and is also a candidate for dark matter. The mass of the axion is expected to be around 100 µeV and the MADMAX project aims to explore the mass range of 40 - 400 µeV. To do so, one of the characteristics of the axion is used: as the photon, the axion seems to generate electromagnetic radiation between two non-conducting materials with a different refractive index, in a large magnetic field [4]. Therefore, the goal is to create a resonator by placing different dielectric surfaces in series [3] that would increase this photon effect. The generated electromagnetic radiation of the axion would then be boosted, and would be measurable. A simplified scheme of the phenomena can be seen in figure 1.1.

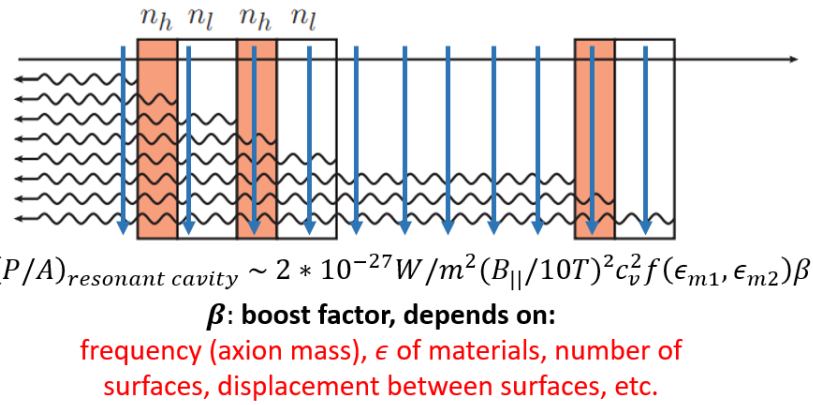

Figure 1.1: Simplified scheme for the photon wave created by the passing of a hidden photon through a dielectric mirror of low reflectivity surfaces. With the courtesy of J. Jaeckel and J. Redondo [4].

To observe such a phenomenon, a figure of merit of 100 T^2m^2 [5] must be generated. The figure of merit, defined in equation 1.1, is the square magnetic field along the direction of the warm bore integrated on a cross-section. To generate such conditions, CEA, in partnership with the Max Planck Institute (MPI), designed a large superconducting dipole magnet, that can generate a magnetic induction of 9 T in a 1.35 m diameter bore on a length of 1.3 m. The

magnetic stored energy of MADMAX is 527 MJ, which is one to two orders of magnitude higher than previous dipoles [8–11]. MADMAX allies great scientific challenges, such as large aperture dimensions, a large magnetic field and a gigantic stored energy. A scheme of the actual design of the MADMAX magnet can be seen in figure 1.2.

$$FoM = \iint B_y^2 dS \tag{1.1}$$

with FoM is the Figure of Merit and B_y the magnetic field in the direction of the bore.

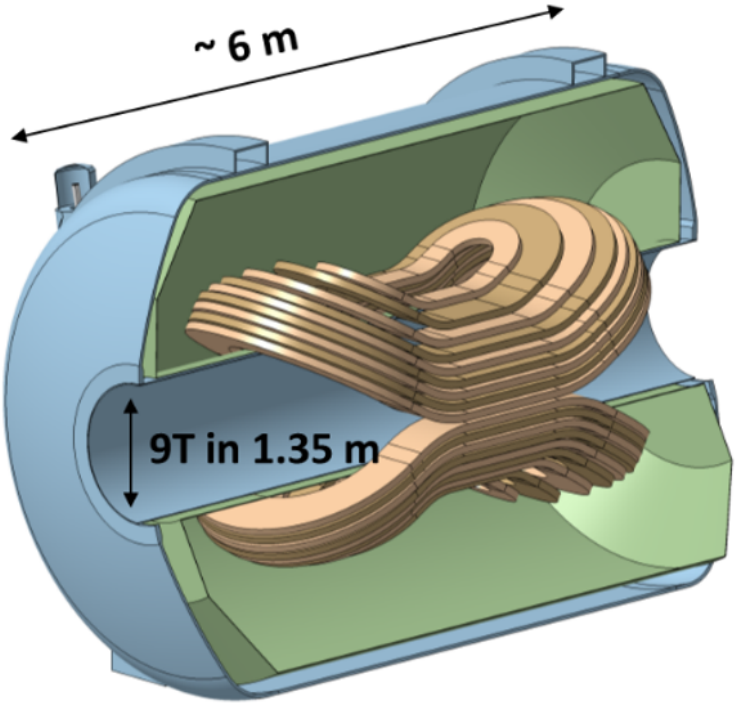

Figure 1.2: Scheme of the MADMAX entire dipole magnet. The skateboard shape CICC coils are stacked at the middle to maximize the magnetic field in the hot bore.

1.1.2. Technological characteristics of MADMAX

1.1.2.1. MADMAX magnet

The MADMAX magnet is composed of 18 skateboard shape coils, stacked in the middle of the warm bore in a dipole configuration. The dipole configuration leads to 9 different coil designs. The shortest one at the top is 158 m, compared to the 763 m of the longest coil at the bottom. Each coil is composed of one Double-Pancake with different turn counts, as can be seen in figure 1.3. Each rectangle thus represents the cross-section of one conductor. A varying thickness of insulation insulates each coil from the others. In addition, the coils lay on mechanical parts designed to support the important mechanical strains. The peak field in this configuration can reach 10.33 T, while each coil alone has its peak field, depending on the geometry [6].

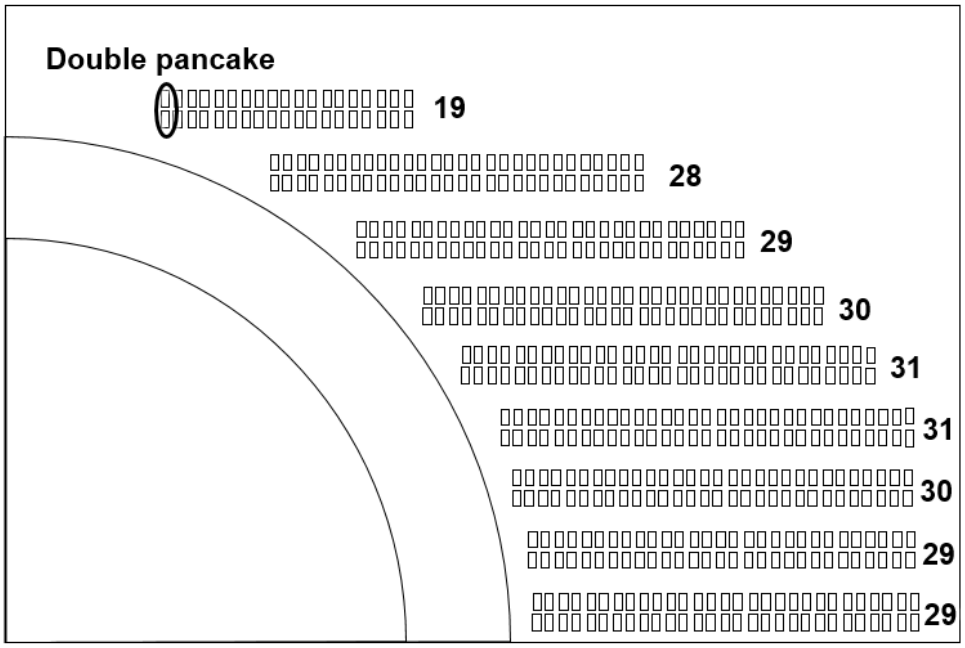

Figure 1.3: Detailed view of the MADMAX magnet, divided into 9 blocks, composed of one Double Pancake with different turn count.

1.1.2.2. Conductor design of MADMAX

The 18 skateboard-shaped coils are built with a Nb-Ti-based Cable-In-Conduit-Conductor (CICC) [7] as illustrated in figure 1.4. The CICC is composed of 108 Nb-Ti strands, with a Cu:Sc ratio of 1.15, twisted in several stages cable in a 3*3*3*4 configuration. The superconducting cable is wrapped in a 0.5 mm thick copper wrap and then inserted in a copper stabilizer. The void fraction of the cable inside the conduit is 30 % and is filled with stagnant superfluid helium to ensure the thermal stability of the coil. Each conductor can carry a nominal current of 23.5 kA. After the insertion, the CICC is wrapped in a 0.5 mm thick G10 epoxy insulation to avoid electrical shortcuts between the conductors.

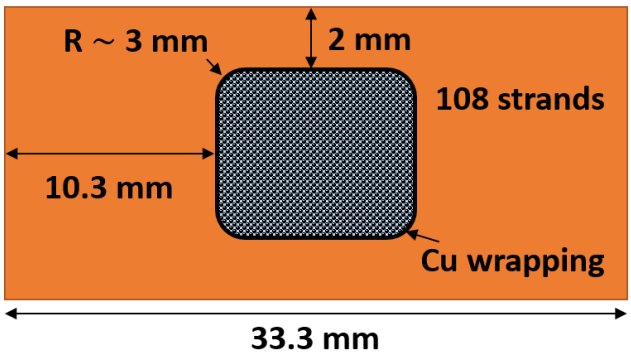

Figure 1.4: Cross-section of the CICC for MADMAX coils.

Table 1.1 summarizes the different cross-sectional areas of the CICC. These values are considered in the computations presented in section 1.2.3.

Table 1.1: MADMAX conductor cross-sectional areas.

Copper section (mm^2)	364
Helium section (mm^2)	28
Nb-Ti section (mm^2)	30.6
G10 section (mm^2)	48

1.1.3. Novelty of the MADMAX conductor

During the last decades [18], different CICC layouts [26] have been designed to manufacture high field superconducting magnets, such as ITER [21], Edipo [27], JT60-SA [28], etc. Nowadays, the CICC technology is a well-known technology and few variations remain between the different CICC configurations. The use of both Nb-Ti or Nb3Sn CICC is necessarily considered for the design of a high-field superconducting magnet, thanks to their ability to carry strong current (10-100 kA), coupled to high magnetic stored energy assembled in a mechanically strong structure.

However, even if the CICC technology is well-known, the conductor of MADMAX presents two novel features:

- The CICC of MADMAX is filled with stagnant superfluid helium. The cooling method of MADMAX is thus a hybrid solution between the bath, in which the coil is immersed, and the circulation of a supercritical flow inside the CICC. Superfluid helium allows increasing the performances of the coil, with an operating temperature below 2 K compared to the 5 K of supercritical helium. However, this method has been rarely used and never with Nb-Ti, only with Nb_3Sn [23]. For the LNCMI hybrid magnet [29], the cable is a Rutherford cable and so very different from our configuration.

- The superconducting cable is inserted in a mechanically strong structure, usually done in stainless steel. To ensure thermal protection and limit the temperature increase, copper wires are added to the superconducting cable. The mechanical strength and thermal protection are thus decoupled. However, on MADMAX, the wires are all superconducting wires, and there is not enough copper for thermal protection. Therefore, it has been decided to combine both thermal protection and mechanical strength by using a copper profile, that adds enough copper cross-section and is also a robust material.

The combination of both stagnant superfluid helium with a copper stabilizer has never been used before. The state of the art on this type of conductor does not exist. To combine the scientific challenges presented above with a novel conductor, different issues must be addressed and the "quench issue" is one them.

1.2. Quench of a superconducting magnet

The use of a superconductor can lead to unexpected transitions of the conductor, from the superconducting to the resistive state. This transition is called a "quench". When transiting, the electrical resistivity of the coil, initially very low due to the superconducting state of the conductor, increases greatly. The magnetic energy stored in the conductor is thus dissipated and large amounts of Joule effect energy are produced. The heat losses are evacuated in the helium contained in the CICC, generating its temperature and pressure increase. In parallel, the quench propagates along the coil. While the quench propagates, the temperature of the coil increases and can lead to irreversible damage to the superconducting properties of the coil

such as decrease of the critical current. In addition, the current, flowing before the quench in the superconducting cable, is redistributed in the stabilizer [30, 31]. With a novel copper conductor, the redistribution is not ensured: the current could slowly flow from the cable to the stabilizer, and generate excessive dissipative heat losses by Joule effect, leading to an unacceptable temperature increase of the coil. In addition, the pressure of the helium inside the CICC also increases due to the heat losses during a quench [32–34]. The pressure increase in the CICC is not estimable for such a novel conductor and the damages that it could generate can be important, as mechanical damages of the conductor or degradation of the electrical insulation around the conductor. Therefore, the quench of a superconducting magnet is a constant danger and must be predicted to avoid any risks.

The detection of a quench is the only way to protect a magnet of its stored energy and characteristics. When a quench is detected, the current inside the coil is discharged on a dump resistor. However, to detect a quench, the voltage the quench generates must reach a minimal voltage, usually 100 mV during 100 ms. Indeed, the faster the quench propagates, and the faster the voltage in the coil increases, and the earlier the quench can be detected. The driving parameter of the quench detection is thus the quench propagation speed. Several analytical [12–14] and numerical models [15–17] exist to estimate the quench propagation speed. Therefore, to give an overview of the state of the art models concerning the quench propagation, this section is dedicated to further explore the issue of the quench propagation. After presenting the critical surface of the Nb-Ti, which defines the performances of a superconducting magnet, the quench initiation, its propagation and the temperature increase it generates are studied. These models will be used to establish a strategy to benchmark the safety of the conductor of MADMAX in case of quench.

1.2.1. Performances of a superconducting magnet: the critical surface of Nb-Ti

The main characteristic of a superconducting material is that its electrical resistance is null below a temperature called the critical temperature T_c. Below this temperature, the superconducting material can transport any current density below a critical current density j_c. The critical current density is function of the temperature of the material and the magnetic field. Therefore, in addition to the critical current density, a critical temperature T_c and a critical magnetic field B_c can be defined to compose the critical surface of the Nb-Ti. This critical surface defines the performances of a superconducting magnet that depends of the cross-section of Nb-Ti in the conductor and of the performances of the superconducting cable itself. It is important to characterize the performances of the cable to determine, at working conditions, the current and temperature margins to reduce the risks to quench the magnet. The critical surface of the Nb-Ti can be seen in figure 1.5. For a null magnetic field, the critical temperature of the Nb-Ti is around 9.2 K, while for a temperature close to the absolute zero, the critical magnetic field is around 14.5 K. The critical current density is around 2×10^{10} A/m^2 for $T_c = 0$ K and $B_c = 0$ T. For the Nb-Ti, the Bottura fit [35] can be used to compute the critical current density, defined in equation 1.2.

$$j_c(B,T) = \frac{j_{c_{ref}} * C_0}{B} [\frac{B}{B_{c2}(T)}]^{\alpha} [1 - \frac{B}{B_{c2}}]^{\beta} [1 - (\frac{T}{T_{c0}})^{1.7}]^{\gamma} \tag{1.2}$$

B_{c2} is the upper critical field and T_c is the critical temperature. Both parameters, used in the Bottura fit 1.2, are coupled in a single equation written by Lubell [36,37], the equation 1.3. By rearranging equation 1.3, equation 1.4 can be obtained.

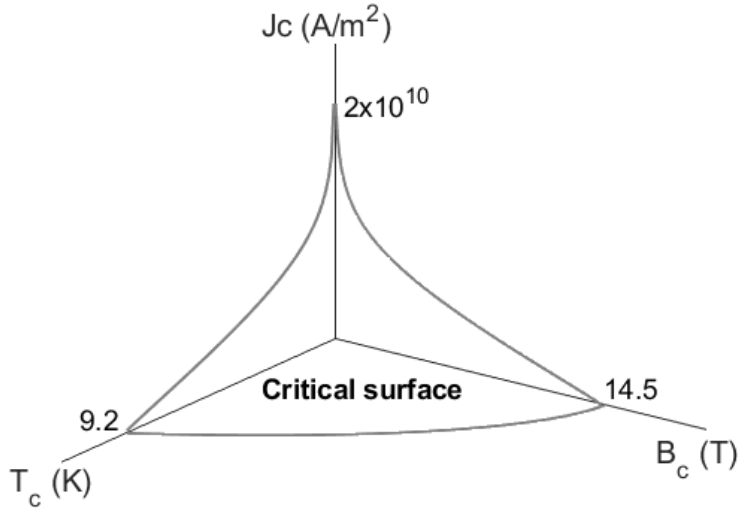

Figure 1.5: Scheme of the critical surface of the Nb-Ti.

$$B_{c2} = B_{c20}[1 - (\frac{T}{T_{c0}})^{1.7}] \tag{1.3}$$

$$T_c = T_{c0}(1 - \frac{B}{B_{c20}})^{1/1.7} \tag{1.4}$$

The values of the different parameters composing the equations can be found in table 1.2, associated with their physical meaning. These parameters can vary and depend on the superconducting strand.

Table 1.2: Critical parameters of the Nb-Ti strands used for MACQU.

Parameter	Value	Units	Physical meaning
$j_c(B,T)$		[A/m^2]	Critical current density
$j_{c_{ref}} * C_0$	1.04×10^{11}	[A.T/m^2]	Reference critical current density and field coefficient
T_{c0}	9.2	[K]	Maximum critical temperature for B=0 T
B_{c2}		[T]	Upper critical field
B_{c20}	14.5	[T]	Maximum upper critical field at T = 0 K
(α, β, γ)	$\alpha = 0.7946$, $\beta = 0.913$, $\gamma = 2.235$		Parameters

When reaching one of the critical parameters, the current of the superconducting cable is, after a diffusion time, fully redistributed in the copper cross-section. Before, the current is in a intermediate phase, shared between both the superconducting cable and the copper cross-section. Another parameter can then be introduced to define the beginning of this current redistribution, and is the current sharing temperature T_{cs}. T_{cs} is the temperature for which the critical current I_c is equal to the operating current. Therefore, when $T = T_{cs}$, the current

starts flowing in the copper cross-section, and while $T_{cs} < T < T_c$, the current remains in its intermediate phase. In figure 1.6, the evolution of T_{cs} and I_c in function of the magnetic field can be seen. T_{cs} is obtained by an iterative process in order to find the temperature for which the critical current I_c is equal to the operating current of MADMAX $I_{op} = 23500$ A. The product of j_c obtained with the Bottura fit 1.2 with a Nb-Ti cross-section of 30.6 mm^2 (table 1.1) gives I_c.

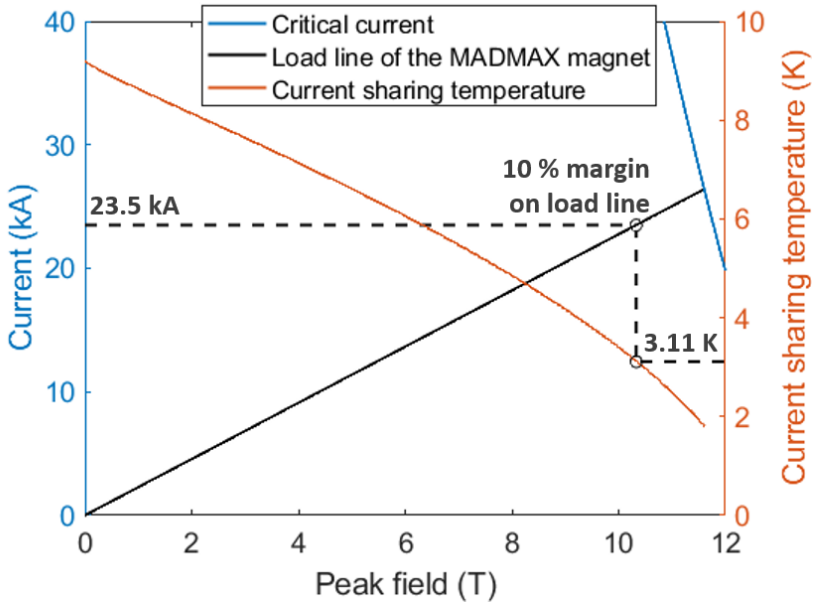

Figure 1.6: Evolution of the critical current I_c and the current sharing temperature T_{cs} in function of the magnetic field at 10 % margin on the load line. At 10.33 T, corresponding to the peak magnetic field, the current sharing temperature is $T_{cs} = 3.11$ K and the nominak current is the operating current $I_{op} = 23500$ A. The magnet has reached 90 % of its critical parameters, representing a margin of 10 % on the load line.

1.2.2. Quench initiation: the Minimum Propagating Zone and the Minimum Quench Energy

A quench can be initiated by reaching any of the three critical parameters: the critical magnetic field B_c, the critical current I_c or the critical temperature T_c. At nominal working conditions, these three parameters are fixed. However, by a local thermal perturbation, that can have multiple origins, the temperature of the conductor may increase until reaching the current sharing temperature T_{cs} and initiate a quench propagation. To have an estimation of the needed power to make the magnet quench, two notions must be introduced: the Minimum Propagating Zone (MPZ) and the Minimum Quench Energy (MQE) [38]. The MPZ is the assumed minimum length of the magnet that should totally transit to make the quench propagate. If a shorter length than the MPZ quenches, the magnet would recover to its initial steady-state working conditions: the quench is absorbed. The MQE is the minimum energy that makes the magnet to make quench. In the following, the MQE is assimilated to the homogeneous energy margin of the conductor and not the exact computation described by Wilson in [38]. In our case, the homogeneous energy margin formula gives coherent results.

These notions are important to understand the local energy margins of a superconducting magnet. These notions allow to verify if a thermal disturbance can initiate a quench or not. The MPZ length and the MQE (computed by unit length) are defined as:

$$L_{MPZ} = \sqrt{\frac{2\bar{k}(T_c - T_{op})}{\eta_{st} J_{op}^2}}, \tag{1.5}$$

where $\bar{k}$ is the homogeneous thermal conductivity including the different materials of the conductor, T_c the critical temperature, T_{op} the operating temperature, η_{st} the electrical resistivity of the copper, and J_{op} the current density in the conductor. The material properties are considered at $\frac{T_{cs} + T_0}{2}$. This equation compares the conduction in the solid and the dissipative heat losses by Joule effect.

$$MQE = \sum_{i=Cu,Nb-Ti,G10,SS} \rho_i S_i \int_{T_0}^{T_{cs}} Cp_i dT + \rho_{He} S_{He} \Delta h_{He}, \tag{1.6}$$

where ρ is the density at T_0, S the cross-sections, C_p the specific heat capacity and Δh_{He} the variation of mass enthalpy between T_{cs} and T_0. Note that the enthalpy variation of the helium has been estimated at constant pressure, as the pressure variation is low until reaching T_{cs}. This equation shows that the minimal energy to make the magnet quench is the enthalpy storage of the different materials (solid and fluid) of the conductor in a cross-section.

For MADMAX, the MPZ is 14.8 mm and the MQE is 23.8 J/m. For the MPZ length, the MQE represents 0.35 J which is small compared to usual losses in superconducting magnets, such as training phenomena (mostly 1 -10 J) [39]. Thermal disturbances can be of several nature, going from a "crack" of the insulation on a few millimeters to the displacement of a whole coil on several centimeters, with losses due to the current variation.

Therefore, with an energy deposition higher than 0.35 J on 14.8 mm, the quench should be initiated and start propagating. The following section is thus dedicated to estimate the quench propagation speed, by using the different state of the art models.

1.2.3. Propagation of the quench: the quench propagation speed

This section is dedicated to detail the different state of the art models to compute the quench propagation speed.

1.2.3.1. Adiabatic case: the "analytic" formula

The first model introduced is for the adiabatic case, where no helium is considered and where it is assumed that the quench propagates by heat conduction only along the CICC. The goal is to obtain an analytic formula (later called the "analytic quench speed" formula) for the quench propagation speed computation. To do so, the demonstration of such formula is done below where it is assumed that the conductor is an equivalent homogeneous material, composed of the superconducting cable and the copper stabilizer.

If the conductor of a superconducting magnet quenches locally, the magnet can be divided in two distinct parts: a first normal zone where dissipative heat losses by Joule effect will heat the conductor and make its temperature increase, and a superconducting zone where there are no Joule losses. In these conditions, the heat balance equations of both parts can be written as equation 1.7.

$$\begin{cases} C_{cond} \dfrac{\partial T(x,t)}{\partial t} = \lambda_{cond} \dfrac{\partial^2 T(x,t)}{\partial x^2} + \eta_{Cu} \dfrac{I^2}{S_{Cu} S} \text{ in the normal zone} \\ C_{cond} \dfrac{\partial T(x,t)}{\partial t} = \lambda_{cond} \dfrac{\partial^2 T(x,t)}{\partial x^2} \text{ in the superconducting zone} \end{cases} \tag{1.7}$$

with C_{cond} the mean volumetric heat capacity of the conductor, T the temperature, λ_{cond} the mean thermal conductivity of the conductor, η_{Cu} the electrical resistivity of the copper, I the current, S_{Cu} the cross-section of the copper and S the cross-section of the conductor, with x and t respectively the space and time coordinate.

As is, the equation set considers that the current diffusion between the superconducting cable and the copper profile is instantaneous at T_t, the transition temperature defined as $T_t = \frac{T_{cs} + T_c}{2}$. It is considered then that below T_t, the current flows only in the superconducting cable, while above T_t the current flows fully in the copper profile. Moreover, the equation set is written by considering that all the material properties of the conductor are temperature independent because the propagation of the normal length is mostly due to the propagation front dynamics at T_t. In these conditions, it has been shown that the equation set has a solution under the "progressive wave" type [40]. Therefore, by using the variable change $T(x,t) = T(\xi)$, $T(x,t)$ becomes $T(\xi)$ with $\xi = x - v_q t$, and equation 1.7 is transformed into equation 1.8.

$$\begin{cases} -v_q C_{cond} \dfrac{\partial T(\xi)}{\partial \xi} = \lambda_{cond} \dfrac{\partial^2 T(\xi)}{\partial \xi^2} + \eta_{Cu} \dfrac{I^2}{S_{Cu} S} \text{ in the normal zone} \\ -v_q C_{cond} \dfrac{\partial T(\xi)}{\partial \xi} = \lambda_{cond} \dfrac{\partial^2 T(\xi)}{\partial \xi^2} \text{ in the superconducting zone} \end{cases} \tag{1.8}$$

with v_q is the longitudinal quench propagation speed.

This equation set can be resolved by considering the initial temperature $T_0 = 1.8$ K and the following boundary conditions:

$$\begin{cases} T(\xi) = T_0 \textbf{ when } \xi \to +\infty \\ T(\xi) = T_t \textbf{ when } \xi = 0 \\ \dfrac{\partial^2 T(\xi)}{\partial \xi^2} = 0 \textbf{ when } \xi \to -\infty \end{cases} \tag{1.9}$$

where $\xi \to +\infty$ corresponds to the right extremity of the superconducting magnet, where the temperature is considered at the boundary condition T_0. The $\xi = 0$ condition is the interface between the normal and the superconducting zone, where the temperature is the transition temperature T_t. Finally, the $\xi \to -\infty$ condition corresponds to left extremity of the conductor, where the quench started and so where the temperature will tend to a hot-spot, leading to $\frac{\partial^2 T}{\partial \xi^2} = 0$.

The quench propagation speed solution is presented in equation 1.10. This formula is called the "analytic quench speed" formula in the following.

$$v_q = \frac{j}{C_{cond}} \sqrt{\frac{\eta_{eq} \lambda_{cond}}{\Delta T}} \quad \textbf{with} \begin{cases} j = \dfrac{I}{S} \\ \Delta T = T_t - T_0 = \dfrac{T_{cs} + T_c}{2} - T_0 \\ \eta_{eq} = \eta_{Cu} \dfrac{S}{S_{Cu}} \end{cases} \tag{1.10}$$

where the material properties are computed at the transition temperature of MADMAX $T_t = 3.73$ K.

Finally, to consider the important variation of the physical properties of the material between 1.8 K and 5 K, it is more accurate to consider the enthalpy variation term ΔH [41] instead of

$C_{cond}\ \Delta T$. To do so, it is assumed that the pressure is constant. It is equivalent to consider a mean value of C_{cond} between T_t and T_0 by:

$$\hat{C}_{cond} = \frac{1}{T_t - T_0}\int_{T_0}^{T_t} C dT \Longleftrightarrow \hat{C}_{cond}(T_t - T_0) = \int_{T_0}^{T_t} C dT = \Delta H \tag{1.11}$$

The equation 1.10 can then be written as in equation 1.12.

$$v_q = \frac{j}{\Delta H}\sqrt{\eta_{eq}\lambda_{cond}\Delta T} \quad \text{with} \begin{cases} j = \dfrac{I}{S} \\ \Delta T = T_t - T_0 = \dfrac{T_{cs} + T_c}{2} - T_0 \\ \eta_{eq} = \eta_{Cu}\dfrac{S}{S_{Cu}} \end{cases} \tag{1.12}$$

with $\Delta H = \frac{S_{Cu}}{S_{Cond}}\Delta H_{Cu} + \frac{S_{Nb-Ti}}{S_{Cond}}\Delta H_{Nb-Ti} + \frac{S_{G10}}{S_{Cond}}\Delta H_{G10}$ and S_{Cond} the total cross-section of the conductor.

With this computation, the quench propagation speed is computed to 23.3 m/s. However, this formula does not consider the contribution of the helium that would decrease v_q. To correct this value, the helium should be considered in the consideration of the conductor as an equivalent homogeneous material. The cross-section and enthalpy variation of the helium would then be added to the conductor one. Adding the contribution of the helium leads to the "infinite exchange quench speed" formula developed in section 1.2.3.3.

3-D phenomena are not considered in this description of the quench. In fact, a transversal propagation should also be considered and is presented below.

1.2.3.2. Transversal quench propagation formula

In parallel of the longitudinal quench propagation, transversal propagation of the quench is a phenomenon that must be considered. Indeed, the conductors are insulated from each other by thermal insulation composed of G10 epoxy glass. In these conditions, the quench can also thermally diffuse through the insulation. This phenomena participates to increase the temperature of the neighbor conductors, and can even lead to quench the neighbor conductor. This other phenomena can contribute to increase the quench propagation speed, and even be dominant in certain configuration of the quench propagation. In case of a slow quench propagation, the diffusion through the insulation could make the neighbor conductor quench earlier than by longitudinal conduction. To compare with the longitudinal quench propagation, the heat diffusion velocity can be estimated by [42]:

$$v_t = \sqrt{\frac{\lambda_t}{\lambda_{Cond}}}\, v_q \ \textbf{with}\ \ \lambda_t = \frac{e_{insulation} + e_{conductor}}{e_{insulation}}\lambda_{insulation} \tag{1.13}$$

v_t is the transversal quench propagation speed.

At 1.8 K, the $\sqrt{\frac{\lambda_t}{\lambda_{Cond}}}$ term is equal to 7.5×10^{-3}. The transversal heat diffusion seems then negligible compared to longitudinal quench propagation for the case of MADMAX.

1.2.3.3. "Infinite exchange quench speed" formula

The helium is now considered as a part of the conductor in this section. It is thus considered that the conductor is composed of an equivalent homogeneous material composed of the superconducting cable and the copper stabilizer (as in the previous "analytic quench speed" formula)

and also the helium. The cross-section of the helium is thus added to the conductor one. The enthalpy variation is added to the conductor one multiplied by the cross-section ratio $\frac{S_{He}}{S_{Cond}}$. Here, the helium is considered stagnant in the cross-section. This assumption is not verifiable yet because the pressure increase in the conductor during a quench can not be estimated.

$$v_q = \frac{j}{\Delta H}\sqrt{\eta_{eq}\lambda_{cond}\Delta T} \quad \text{with} \begin{cases} j = \dfrac{I}{S} \\ \Delta T = T_t - T_0 = \dfrac{T_{cs}+T_c}{2} - T_0 \\ \eta_{eq} = \eta_{Cu}\dfrac{S}{S_{Cu}} \end{cases} \tag{1.14}$$

$$\text{with } \Delta H = \frac{S_{Cu}}{S_{Cond}}\Delta H_{Cu} + \frac{S_{Nb-Ti}}{S_{Cond}}\Delta H_{Nb-Ti} + \frac{S_{G10}}{S_{Cond}}\Delta H_{G10} + \frac{S_{He}}{S_{Cond}}\Delta H_{He}$$

By considering the characteristics of MADMAX, the quench propagation speed given by equation 1.14 is 0.42 m/s, which is lower than the one given by the equation 1.12. The difference between both formulas is important, there is a factor of 55 between the quench propagation speed. The following section proposes a last method to compute the quench propagation speed.

1.2.3.4. Universal scaling laws for quench

In 1994, Shajii and Freidberg proposed a quench model [14] for the numerical tool Quencher [15]. They proposed a set of universal scaling relations, describing the quench propagation in a CICC [43]. According to the models, depending on the initial quenched length L_q, the coil length L and the current density inside the stabilizer J, each coil can have different quench regimes. Four quench regimes are introduced: the "short coil - low pressure rise" regime, the "short coil - high pressure" rise regime, the "long coil - low pressure rise" regime and the "long coil - high pressure rise" regime. In addition, in function of the quench regime, they also proposed correlations for the computation of the quench propagation speed. The classification into four regimes in function of the parameters with the associated quench propagation speed are presented in figure 1.7. The parameters x and y are defined in equation 1.15.

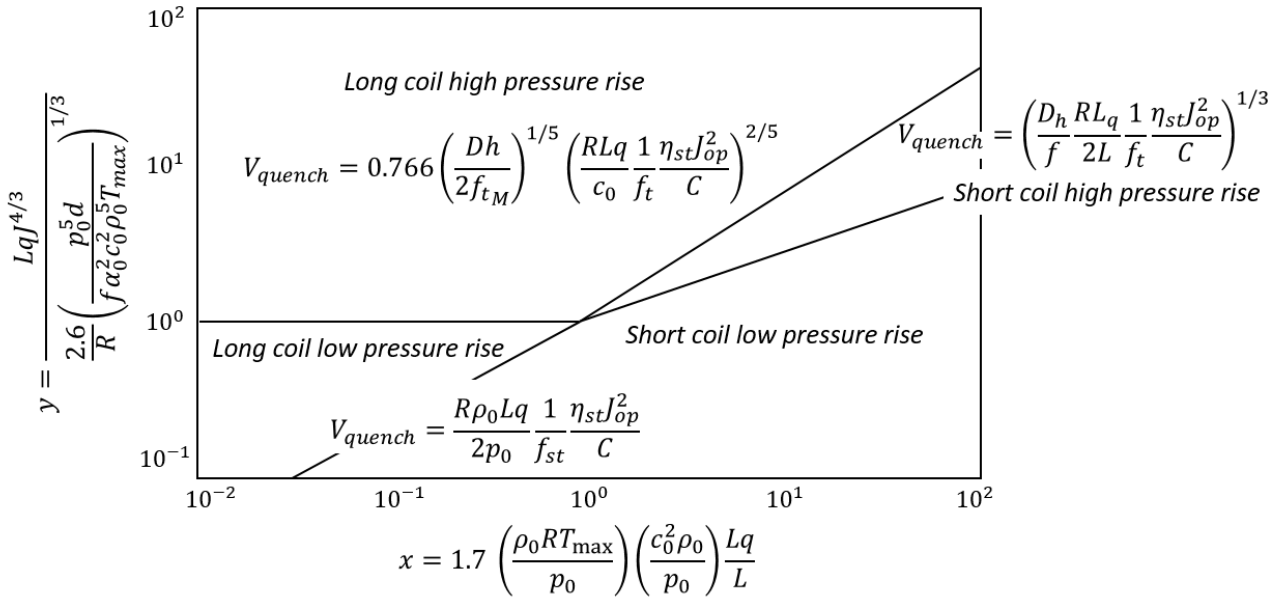

Figure 1.7: Universal scaling laws for quench propagation taken from [43], depending on the coil's length and the pressure rise.

$$\begin{cases} x &= 1.7\left(\dfrac{\rho_0 RT_{max}}{p_0}\right)\left(\dfrac{c_0^2\rho_0}{p_0}\right)\dfrac{L_q}{L} \\ y &= \dfrac{L_q J^{4/3}}{\dfrac{2.6}{R}\left(\dfrac{p_0^5 D_h}{f\alpha_0^2 c_0^2 \rho_0^5 T_{max}}\right)^{1/3}} \\ \alpha_0 &= \dfrac{S_{Cu}\eta_{Cu}(T)}{S_{Cond}\rho_{Cond}C_{Cond}} \end{cases} \tag{1.15}$$

R is the gas constant, p the pressure, c the sound speed, L the length of the coil, D_h the hydraulic diameter, f the friction factor, and the index 0 standing for "initial".

The model has been applied for the case of the MADMAX coils. The unknown parameter to quantify is the initial quenched length L_q. Indeed, it corresponds to the quenched length that makes the quench propagate and could be assimilated to the MPZ. In reality, this value can not be predicted as it depends of the quench initiation. Therefore, the quench regime is computed for a large L_q range, going from 1 mm to 0.5 m. This range has been selected to correspond to different quench initiation scenarios: a short initial quenched length could be due to an insulation "crack", where the insulation of the coil moves slightly (few mms), often due to the vacuum conditions around the coils. A longer length could be due to the movement of an entire coil due to magnetic forces ($\approx$ m). Therefore, the quenched length can take several values and can not be predicted. The obtained regimes have been plotted in figure 1.8. The quench propagation has been estimated to increase with L_q starting at 2.5 mm/s to 0.61 m/s. The quench propagation speed range is again very wide, with a gap of two orders of magnitude.

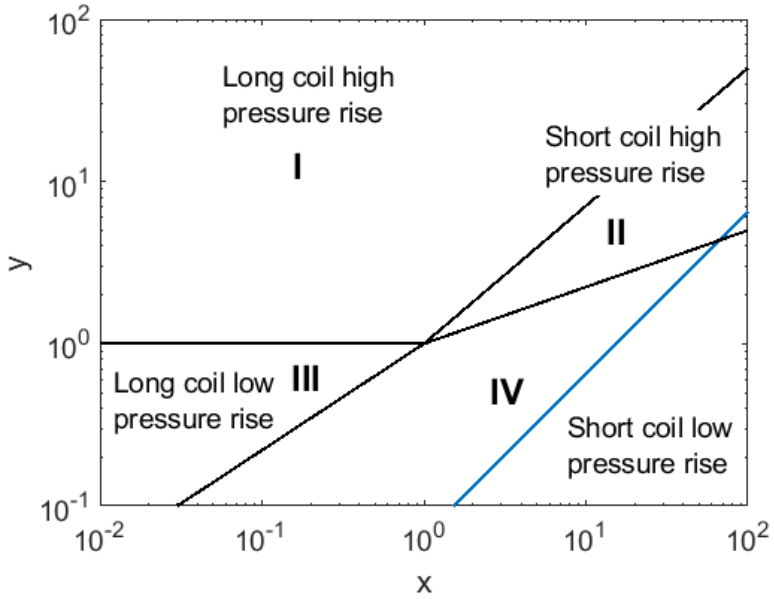

Figure 1.8: Evolution (in blue) of the MADMAX possible regimes, depending on the initial quenched length L_q. The MADMAX coils are in a "short coil low pressure rise" regime while L_q is shorter than 0.16 m, and in "short coil high pressure rise" regime if L_q is longer.

These different models lead to a difference of several orders of magnitude between the computed quench propagation speeds. The last step is to determine the detection time of a quench on MADMAX, in order to estimate the temperature increase a quench generates, with the "hot-spot temperature" model.

1.2.4. Quench detection: the quench detection time and the hot-spot temperature

The detection time usually corresponds to the time that the voltage stays at 100 mV for 100 ms. When this criteria is fulfilled, it is considered that the quench is detected and the discharge of the current starts. The hot-spot temperature is the maximum temperature that the coil can reach at the initiation point of the quench. Both are estimated in the following section, in function of the above-detailed quench propagation speed estimation.

1.2.4.1. The quench detection time

The estimation of the quench propagation speed allows us to estimate a quench detection time. To estimate the detection time, the equation 1.16 is used, based on the Ohm's law and written in function of the quench speed. The material properties are estimated at the peak field of 10.33 T, corresponding to the peak field of MADMAX. This point is chosen because with the highest field, at 1.8 K and 23500 A everywhere in the coils, this point is the less stable of the magnet and then the most likely to quench first. The temperature increase is maximum at this location as the Joule dissipation is the most important.

$$U = RI \Longleftrightarrow U = \frac{\eta_{Cu} v_q \Delta t}{S_{Cu}} I \Longleftrightarrow \Delta t = \frac{U S_{Cu}}{\eta_{Cu} v_q I} \tag{1.16}$$

U is the 100 mV voltage threshold.

According to the previous computations, the quench propagation speed is included between 2.5 mm/s and 0.61 m/s. The adiabatic case has been voluntarily excluded as it is unrealistic to neglect the effect of the helium in the quench propagation. With this quench propagation

speed range, the quench detection time can thus be estimated between 3.3 s and 800 s. The range of detection time is very wide and affects largely the hot-spot computations presented below.

1.2.4.2. The "hot-spot" temperature model

While the quench propagates, large amounts of Joule energy are dissipated and the temperature of the conductor increases. The maximum temperature increase can be estimated with a hot-spot computation, which is detailed in this section. The hot-spot computation assumes that the conductor that has quenched does not exchange any heat with the conductors nearby. It is then a conservative computation as it maximizes the temperature. It is used for the design of a superconducting magnet, in order to limit the risks of burning the magnet in case of a quench. The usual criteria to ensure the safety of the magnet is a hot-spot temperature of 100 K after the quench because there is no risk to damage the properties of the superconductor. In addition, the themal expansion is low below 100 K and the thermal strains generated would remain low. This value is considered for MADMAX.

The hot-spot computation is based on the equation 1.17, where it is assumed that the temperature increases by Joule effect only in the cross-section where the quench is initiated. It is assumed that the temperature is homogeneous in the cross-section of the conductor. Indeed, the high convective heat exchange coefficient allows to consider that the helium and the copper stabilizer are at the same temperature. In addition, the high thermal conductivity of the copper allows to assume an homogeneous temperature in the copper stabilizer.

$$\frac{d(C_{Cond}(T)T(x,t))}{dt} = \frac{\eta_{Cu}(T,B)}{S_{Cond}S_{Cu}}I^2(t) \tag{1.17}$$

C_{Cond} is the volumetric heat capacity of the conductor (including the helium), defined the same way than the specific heat at constant pressure in equation 1.21.

The current is constant during the MADMAX experiment until the detection of a quench. After the quench detection, the current is discharged exponentially on a dump resistor with a time constant τ. The current in function of the time $I(t)$ can then be written as in equation 1.18.

$$\begin{cases} I(t) = I_0 & \textbf{when } \ t < \tau_d \\ I(t) = I_0\, e^{\dfrac{-(t-\tau_d)}{\tau}} & \textbf{when } \ t \geq \tau_d \\ \textbf{with } \tau = \dfrac{L}{R} \end{cases} \tag{1.18}$$

L the self-inductance of the coil and τ the discharge time constant estimated to 24.6 s.

The maximum temperature reached at the end of the discharge T_{hs}, the hot-spot temperature, can be computed with equation 1.19, after discretization and resolution of equation 1.17.

$$T_{hs} = T_0 + \int_{t=0}^{t=\tau_d} \frac{\eta_{Cu}(T,B)I_0^2}{C_{cond}(T)S_{Cu}S}dt + \int_{t=\tau_d}^{t=\infty} \frac{\eta_{Cu}(T,B)I(t)^2}{C_{cond}(T)S_{Cu}S}dt \tag{1.19}$$

T_0 is the initial temperature (1.8 K).

The results of the hot-spot computation can be seen in figure 1.9. To compare the hot-spot on all the quench detection time range, the computation has been done for a detection time between 3.3 s and 10 s. The detection time of 800 s leads to a unrealistic temperature increase,

largely above 1000 K. However, even at 3.3 s, the hot spot is higher than the safety criteria of 100 K and keeps increasing with the detection time.

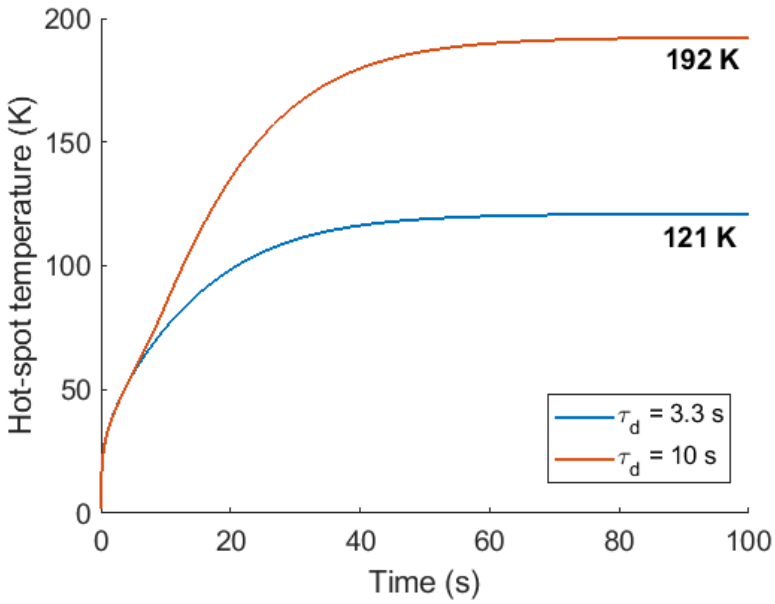

Figure 1.9: Hot-spot computation of the MADMAX conductor. The cross-sections of each materials are considered from table 1.1.

Therefore, it is clear that the quench detection is a big issue that must be addressed in the framework of the MADMAX project. With the computed hot-spots, the magnet is not safe in case of quench. The different models introduced above give results varying from the mm/s to m/s. The following section will be dedicated to introduce the heat balance equations of the coil, the conductor one and the helium one. The goal is to present the different phenomena driving the heat transfers in the conductor and settle on the strategy for the quench protection of the conductor.

1.2.5. Heat balance equations in the conductor

The design of MADMAX is greatly influenced by the thermal stability of the magnet, including the conductor but also the fluid. The time evolution of the temperature of the conductor can be described by the heat equation of the conductor 1.20. The time evolution of the temperature of the helium is described by the energy conservation equation 1.22 written in a non conservative form to express it with the temperature variable (see Appendix A) [16], in 1-D for simplification purpose. It is assumed that the conductor is an homogenized material, composed of both the superconducting cable and the copper stabilizer, with the material properties defined in equation 1.21.

$$\rho_{Cond} C_{p_{Cond}} S_{Cond} \frac{\partial T_{Cond}}{\partial t} - \frac{\partial}{\partial x}(S_{Cond} \lambda_{Cond} \frac{\partial T_{Cond}}{\partial x}) = \dot{q} + \dot{q}_{Joule} + \dot{q}_h, \tag{1.20}$$

where ρ is the density defined in equation 1.21, C_p the volumetric heat capacity defined in equation 1.21, S the cross-section defined as the sum of the composing cross-section of the conductor, T the temperature, λ the thermal conductivity defined in equation 1.21, $\dot{q}$ is an external heat flux, $\dot{q}_{Joule}$ the dissipative heat losses by Joule effect per unit length, $\dot{q}_h$ the convective heat flux per unit length and t and x for the time and spatial coordinates. The index "Cond" stands for conductor.

$$\begin{cases} \rho_{Cond} = \dfrac{S_{Cu}}{S_{Cond}}\,\rho_{Cu} + \dfrac{S_{Nb-Ti}}{S_{Cond}}\,\rho_{Nb-Ti} \\ C_{p_{Cond}} = \dfrac{\rho_{Cu}}{\rho_{Cond}}\,C_{p_{Cu}} + \dfrac{\rho_{Nb-Ti}}{\rho_{Cond}}\,C_{p_{Nb-Ti}} \\ \lambda_{Cond} = \dfrac{S_{Cu}}{S_{Cond}}\,\lambda_{Cu} + \dfrac{S_{Nb-Ti}}{S_{Cond}}\,\lambda_{Nb-Ti} \end{cases} \tag{1.21}$$

$$\frac{\partial T_h}{\partial t} + \varphi_h T_h \frac{\partial v_h}{\partial x} + v_h \frac{\partial T_h}{\partial x} = \frac{2f}{C_{v,h}} \frac{v_h^2 |v_h|}{D_h} + \frac{\dddot{q}_h}{\rho_h C_{v,h}} - \frac{1}{\rho C_{v,h}} \frac{\partial \dot{q}''_{cf}}{\partial x}, \tag{1.22}$$

where C_v is the specific heat at constant volume, φ the Grüneisen parameter defined in section 1.3.2.3, v is the velocity, f is the friction factor, D_h is the hydraulic diameter, $\frac{\dddot{q}_h}{\rho C_v}$ is the volumetric convective heat flux term and $\dot{q}''_{cf}$ is the areal superfluid counterflow heat flux, given by the Gorter-Mellink law detailed in [44]. The "h" index stands for helium.

Several phenomena are taken into consideration as the heat conduction, the dissipative heat losses by Joule effect, the convective heat exchange between the fluid and the solid, the compression forces, the heat transport of helium (advection), the friction forces and the Gorter-Mellink counterflow mechanism. These phenomena will be further studied later in this Ph.D. thesis report. In addition, there is no certitude of the relevance of the above-developed models on our case, due to the novel conductor type used on MADMAX. Without certainty on our ability to detect the quench, the success of the project is compromised. However, to settle on the quench propagation speed, the most dominant phenomena in the quench propagation must be identified. Therefore, it has been decided to design, manufacture and test a mock-up coil, called MACQU (MAdmax Coil for Quench Understanding), to study the thermohydraulic phenomena happening during the quench of such a CICC, cooled down with superfluid helium. The design of MACQU is presented in chapter 2.

Before presenting the design of the mock-up coil MACQU, the heat balances introduce the properties of the materials, as the copper, the Nb-Ti and the superfluid helium. The material properties are used for the identification of the dominating phenomena. The electric and thermal properties of the conductor materials are presented below, being the materials composing the conductor (copper and Nb-Ti) and the cooling fluid.

1.3. Properties of materials and fluid in the conductor

1.3.1. Materials in the conductor: the copper and the Nb-Ti

Note that the databases used for the computations of the thermophysical properties of the materials of the CICC are from the THEA® [45] code for the materials of the conductor and HEPAK [46] for the helium. THEA® obtains the thermophysical properties of the copper and the G10 from Cryocomp [47]. For the Nb-Ti, the reference is indicated for each property. THEA® is a program dedicated to the Thermal, Hydraulic and Electrical Analysis of superconducting cables and will be used in chapter 5 to compute and analyze the quench behavior of the mock-up coil MACQU. Therefore, for reasons of consistency, the databases of THEA® and HEPAK will be applied in the following studies.

1.3.1.1. Electrical resistivity of the copper

When a quench is triggered, the current flows from the superconducting cable to the copper stabilizer because the electrical resistivity of the Nb-Ti (η_{Nb-Ti}) becomes several order of

magnitude higher that the copper one (η_{Cu}). The current in the copper stabilizer produces heat losses by Joule effect, defined as $\eta_{Cu}(\frac{I}{S_{Cu}})^2$, where I is the current and S_{Cu} the copper cross-section in which the current is redistributed. The dissipative heat losses by Joule effect depend on the electrical resistivity, which is function of three main parameters: the magnetic field, the temperature and the Residual Resistivity Ratio (RRR). The RRR is a parameter that allows characterizing the quality of a copper sample. It is defined as the ratio of the resistivity at 300 K (room temperature) and the resistivity at 0 K, leading to RRR $= \frac{\eta_{Cu}(300\ K)}{\eta_{Cu}(0\ K)}$. For a superconducting material for which the resistivity is close to 0 below T_c, the RRR is estimated just before the transition of the superconducting cable, as defined in equation 1.23.

$$RRR = \frac{\eta(300\ K)}{\eta(9\ K)} \tag{1.23}$$

with $\eta(300\ K)$ and $\eta(9\ K)$ being respectively the electrical resistivity at 300 K and 9 K.

In addition, the electrical resistivity tends to a constant value at low temperature, called the residual resistivity η_0. This residual resistivity is function of the purity and different imperfections in the metal [48].The total resistivity can then be expressed as in equation 1.24 according to Matthiessen's rule [49].

$$\eta = \eta_0 + \eta(T, B) \tag{1.24}$$

Figure 1.10 shows the evolution of the electrical resistivity as a function of the temperature at 0 T, 5 T and 10 T, for RRR = 60 and RRR = 125. These two RRR values have been chosen as both will be used in further studies. It can be seen that the electrical resistivity increases with the temperature and the magnetic field, while it decreases with the RRR.

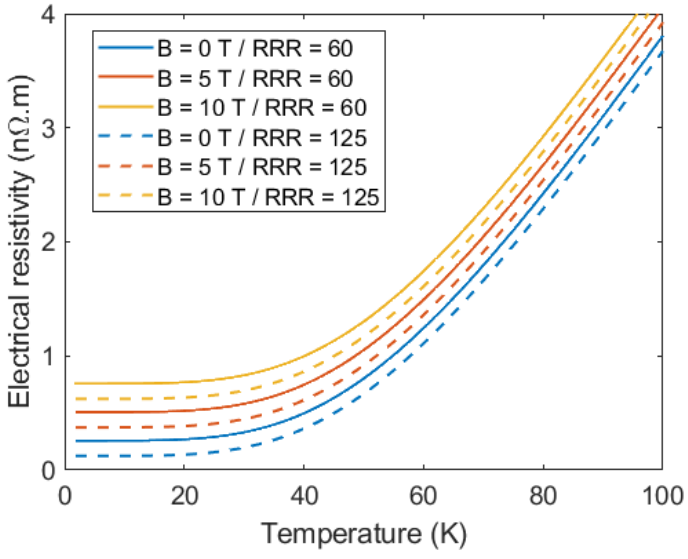

Figure 1.10: Temperature evolution of the electrical resistivity for the magnetic field varying from 0 T to 10 T and for RRR = 60 and RRR = 125.

1.3.1.2. Thermal conductivity of the conductor

The thermal conductivity of the Nb-Ti [50], the copper and the G10 have been plotted in figure 1.11. It shows that the thermal conductivity of the copper is 7 - 8 times higher than the

Nb-Ti one. On the opposite, the thermal conductivity of the G10 is several order of magnitude lower than both copper and Nb-Ti. Around 20 K, the thermal conductivity of the copper reaches its maximal value, between 650 W/m.K and 2850 W/m.K, depending on the magnetic field and the RRR. After 20 K, the thermal conductivity of the copper and Nb-Ti decreases with temperature, while the G10 one increases monotonously. Compared to the electrical resistivity, the thermal conductivity increases with the RRR and decreases with the magnetic field. The thermal conductivity increases with the quality and the purity of the copper.

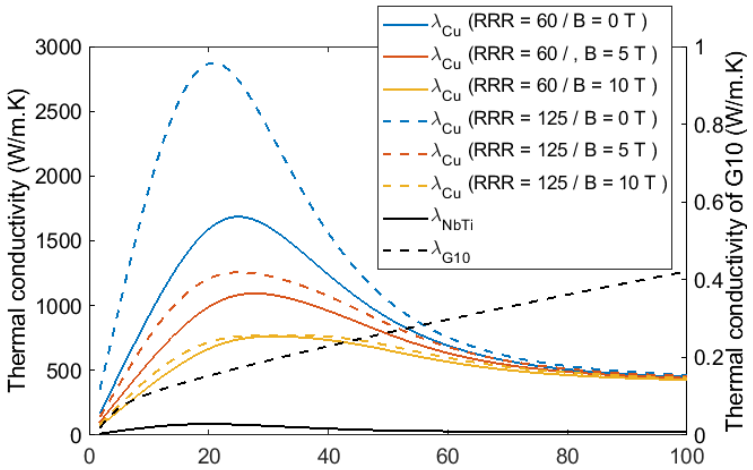

Figure 1.11: Temperature evolution of the thermal conductivity (on the left: copper and Nb-Ti, on the right: G10) for the magnetic field varying from 0 T to 10 T and for RRR = 60 and RRR = 125.

Nonetheless, at low temperature, the thermal resistivity can vary by a factor 2 - 3 depending of the RRR. To quantify the impact of the conduction on the quench propagation, the RRR appears then as a parameter that must be well-characterized.

1.3.1.3. Heat capacity of the conductor

The volumetric heat capacity is the product of the mass density by the specific heat of a material. It is an important parameter for the computation of the hot-spot temperature as it represents the ability of the material to store energy before its temperature increase of one kelvin. The mass density of the different materials can be found in table 1.3.

Table 1.3: Mass density of the different materials of the CICC.

Material	Mass density (kg/m^3)
Copper	8960
Nb-Ti	6550
G10	1948

Figure 1.12 shows the volumetric heat capacity of the copper, the Nb-Ti [51] and the G10, as a function of the temperature. The plotted values are under 0 T. As it can be seen, the volumetric heat capacity increases with the temperature. Under 10 K, the Nb-Ti has the highest volumetric heat capacity, between 2 and 7 times higher than the copper and the G10. However, with the biggest cross-section in the cross-section of the conductor, the copper will be the predominant material to store the energy dissipated during the quench.

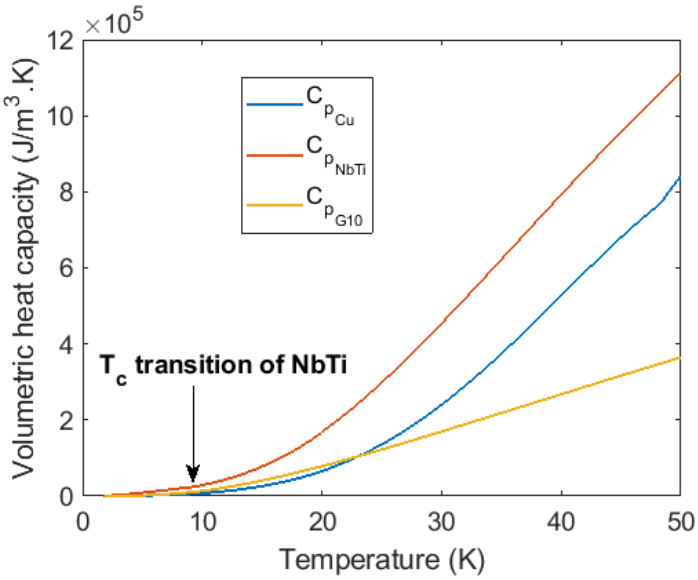

Figure 1.12: Temperature evolution of the thermal conductivity for the magnetic field varying from 0 T to 10 T and for RRR = 60 and RRR = 125.

1.3.2. Cooling fluid: the helium

The MADMAX coils are filled with stagnant superfluid helium. The phase diagram of the helium depicted in figure 1.13 shows that the transition between liquid helium (He I) and superfluid helium (He II) occurs at 2.163 K and 1 bar. For the same pressure, the liquid/gas transition occurs at 4.22 K. Finally, from 2.17 K and 0.05 bar (where superfluid, liquid and vapor states coexist) to 1.76 K and 29.7 bar, the λ line separates the two liquid phases of helium.

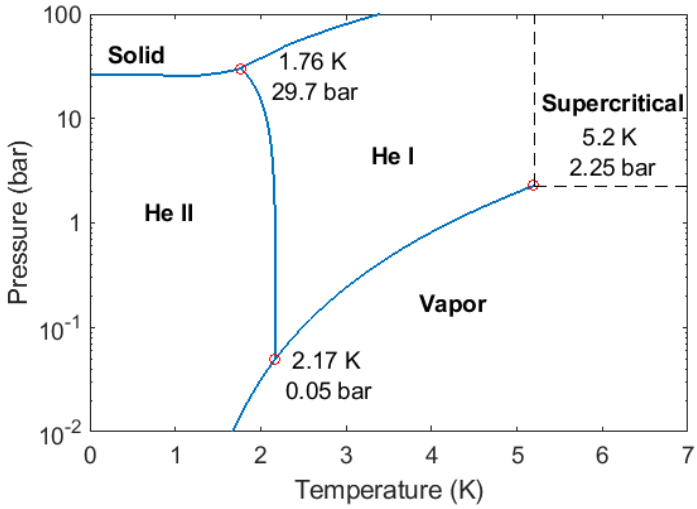

Figure 1.13: Phase diagram of the helium in pressure and temperature.

Another "phase" of the helium appears at higher pressure (above 5.2 K and 2.25 bar) : the supercritical helium. This phase is largely used for forced-flow cooling of CICC. The pressure increase during a quench can not be predicted. Therefore, to have a large spectrum of the thermophysical properties of the helium, the properties are considered below between 1.8 K and 10 K. The pressure is adapted in function of the property. The properties are coming from the HEPAK database [46].

1.3.2.1. Mass density

The mass density is presented in figure 1.14 at 1 bar, 5 bar and 10 bar. The density of the helium increases between 1.8 K and 2.17 K.

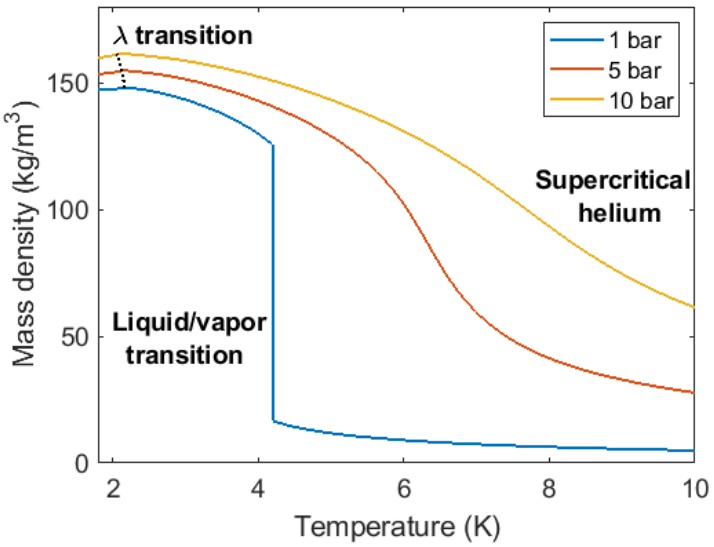

Figure 1.14: Temperature evolution of the mass density of the helium at 1 bar, 5 bar and 10 bar.

Indeed, contrarily to classic fluids, the density of the superfluid helium increases with the temperature. However, it can also be seen that the density decreases with the temperature above 2.17 K, the helium recovering the behavior of a classic fluid. At the transition between liquid and gas, the mass density greatly decreases from 125 kg/m^3 to 17 kg/m^3. It can also be seen that there is no clear transition between liquid/vapor at higher pressure because the fluid is supercritical above 2.25 bar and 5 K.

1.3.2.2. Heat capacity

Another characteristic of the superfluid helium is the peak of its heat capacity around 2.17 K, as it can be seen in figure 1.15. The pressure is 1 bar as the evolution is similar at higher pressure. The volumetric heat at constant volume C_v increases from 4.3×10^5 J/m^3.K at 1.8 K to 1.1×10^6 J/m^3.K at 2.17 K. The volumetric heat capacity strongly decreases to 3.2×10^5 J/m^3.K at 4.2 K in liquid state and to 5.3×10^4 J/m^3.K in vapor. In case of quench, this important heat capacity can be very useful. Indeed, the superfluid helium is able of storing a large energy without significant temperature increase. Therefore, the superfluid helium acts as an important enthalpy storage in case of a quench. In liquid state and vapor states, the enthalpy storage is thus less important because the volumetric heat capacity decreases.

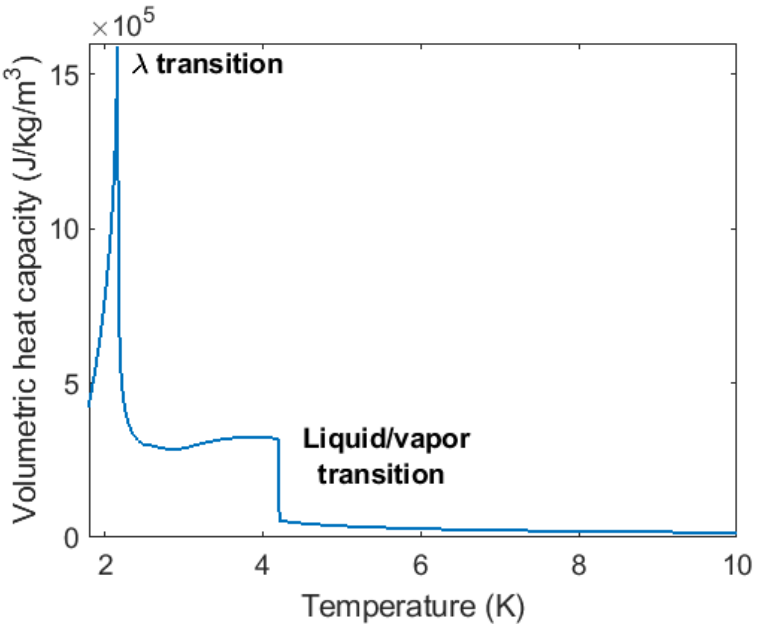

Figure 1.15: Temperature evolution of the heat capacity of the helium.

1.3.2.3. Isochoric heating of helium

The Grüneisen parameter, defined as $\varphi = \frac{1}{\rho}(\frac{\partial p}{\partial u})_V$, is a dimensionless number that characterizes the pressure evolution in case of an isochoric heating, so at constant mass density. As it can be seen in figure 1.16, the Grüneisen parameter of the helium is negative between 1.8 K and 2.18 K, meaning that contrarily to classis fluids, in case of an isochoric heating the pressure of the helium will decrease. However, above 2.18 K, the Grüneisen parameter becomes positive. The pressure of the helium evolves similarly to a classic fluid, and increases with heat. This characteristic of the helium can be very useful in case of a quench, as it can slow down the pressure increase.

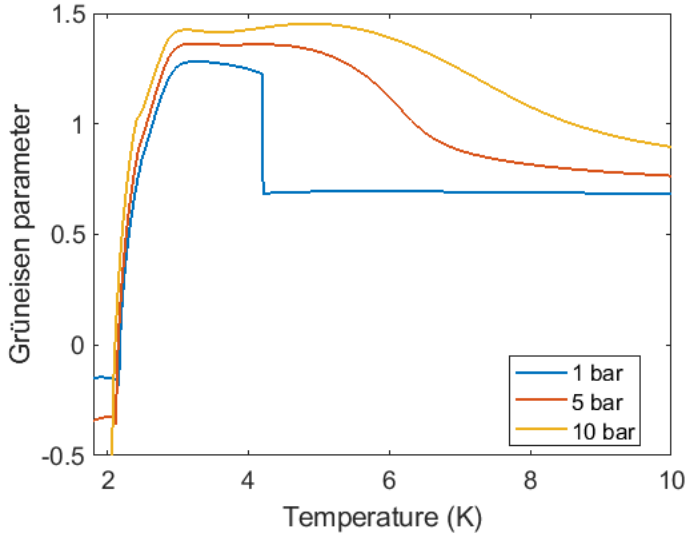

Figure 1.16: Temperature evolution of the Grüneisen parameter of the helium.

1.3.2.4. Heat transfer inside superfluid helium

The superfluid helium is a very efficient heat conductor. Again, this characteristic is very useful in case of quench, as the superfluid helium is able to evacuate a large amount of heat to the cold source, usually placed several meters away from the local heat source. This phenomenon is known as the Gorter-Mellink effect [44]. The evacuated heat flux by the Gorter-Mellink mechanism can be written as in equation 1.25 in function of the temperature gradient.

$$q^3 = -F(T,P)\frac{\partial T}{\partial x} \tag{1.25}$$

where q is the extracted flux by the Gorter-Mellink mechanism and $F(T,P)$ the characteristic heat conductivity function of the superfluid helium, function of the temperature and the pressure and expressed in $\mathrm{W^3m^{-5}K^{-1}}$. Figure 1.17 shows the temperature evolution of the $F(T,P)$ function.

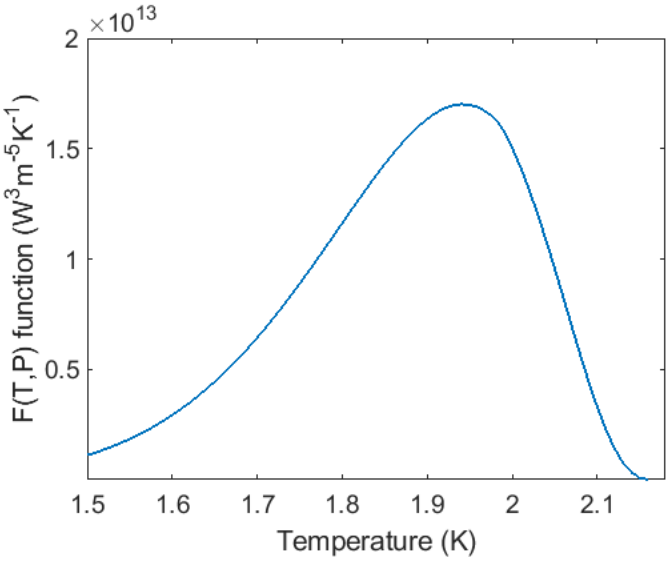

Figure 1.17: Temperature evolution of the heat conductivity function of the superfluid helium.

To estimate the large Gorter-Mellink heat transfer, by analogy with Fourier's law, an equivalent thermal conductivity of the superfluid helium λ_{eq}^{He} can be estimated with equation 1.26.

$$\lambda_{eq}^{He} = \frac{F(T,P)}{q^2} \tag{1.26}$$

where q the dissipated heat losses density by Joule effect is 4.1×10^4 W/m^2 and gives $\lambda_{eq}^{He} = 7 \times 10^3$ W/m/K. The superfluid helium has an equivalent thermal conductivity 104 times more important than the copper one (for an RRR of 60 at 10.33 T).

Finally, the maximum extracted flux q_{max} by the superfluid helium can be estimated by equation 1.27. By assuming a temperature gradient in the coil, with the center at 2.17 K and the extremities at 1.8 K, the extracted heat flux is included between 2.2×10^3 W/m^2 and 3.7×10^3 W/m^2, depending on the length of the coil. The considered length are 79 m and 381.5 m, respectively the half of the shortest (158 m) and the longest coil (763 m) of MADMAX. Figure 1.18 shows the temperature evolution of the $f_{int}(T_0)$ function of the superfluid helium. The function decreases with the increase of the initial temperature T_0.

$$q_{max} = \frac{1}{L^{1/3}} f_{int}(T_0) \textbf{ with } f_{int}(T_0) = (\int_{T_0}^{2.17} f(T)dT)^{1/3} \tag{1.27}$$

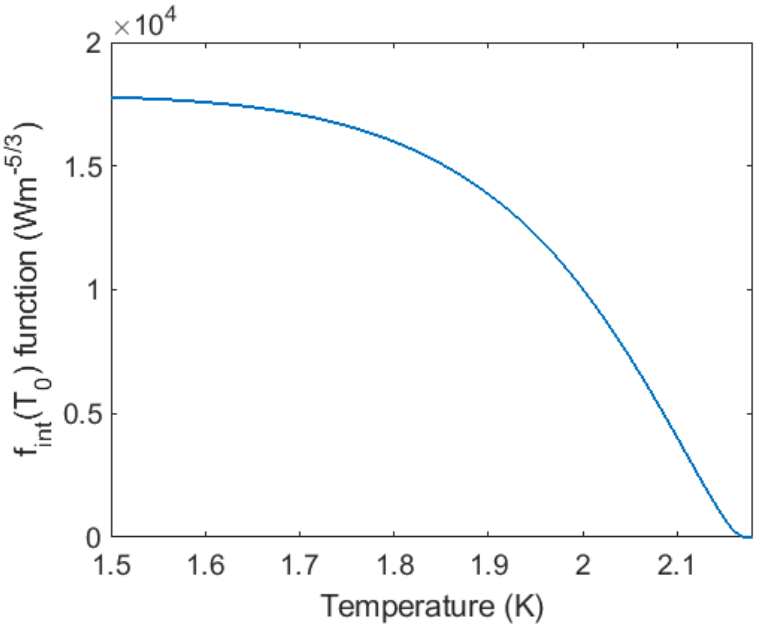

Figure 1.18: Temperature evolution of the $f_{int}(T_0)$ function of the superfluid helium.

1.3.2.5. Heat transfer between superfluid helium and a wall

The last characteristic to present is the heat exchange at the interface between superfluid helium and a wall, controled by the Kapitza resistance [52] and defined in equation 1.28.

$$q = \alpha(T_s^n - T_f^n) \tag{1.28}$$

T_s and T_f are the temperature of the solid and the fluid respectively, and α and n are characteristic coefficients of the Kapitza heat transfer, estimated at $\alpha = 200$ Wm^{-2}K^{-3} and $n = 3.8$ for copper [53]. These coefficients depend on several parameters as the surface condition, the geometry and the material itself. From equation 1.28, an equivalent convective heat exchange coefficient h_K can be deducted and is linearized as in equation 1.29. By assuming that initially the solid and the fluid are at 1.8 K, the coefficient can be estimated to be $h_K = 4.6 \times 10^3$ W/m^{-2}K^{-1}. Compared to usual convective heat exchange, as natural convection with an order of magnitude of $h = 10$ W/m^{-2}K^{-1} or forced convection with an order of magnitude of $h = 100 - 1000$ W/m^{-2}K^{-1}, the heat transfer of the superfluid helium is much more efficient.

$$h_K = \alpha(T_s + T_f) * (T_s^2 + T_f^2) \tag{1.29}$$

Conclusions

This first chapter introduces all the notions allowing us to analyze the quenching problems in a Cable-In-Conduit-Conductor (CICC) magnet. We started by presenting the background of the MADMAX project, highlighting its interest in the field of fundamental physics research.

The novelty of the MADMAX project was presented, based on the use of a new type of CICC. The specificities of the CICC were described, such as the use of a copper stabilizer, and the cable is inserted in a wrap and filled with stagnant superfluid helium. The characteristics of the superconducting Nb-Ti have been detailed. Simple models such as quench propagation speed and hot spot temperature calculations were detailed. These calculations revealed a difference of several orders of magnitude in the quench propagation speed, from mm/s to tens of m/s. Therefore, quench propagation speed is an obvious issue for MADMAX magnet design. In order to address the issue of quench propagation speed and to understand the quench behavior of a new CICC, it was decided to design, fabricate and test a mock-up coil called MACQU. The objective is to measure the propagation speed of an experimental quench in order to verify the detection capability, in order to verify the detection capability of this new type of CICC. In the remainder of this thesis report, we will build on the concepts presented to design a superconducting magnet that reproduces the quenching behavior of MACQU and perform a detailed quench analysis of this superconducting magnet filled with stagnant superfluid helium.

2 - Design of a superconducting magnet for quench propagation studies

Objectives

- Describe and justify the guidelines of the MACQU coil design strategy
- Perform the design of a superconducting magnet that reproduces the MADMAX quench behavior
- Illustrate the relevance of MACQU to study the MADMAX quench behavior

2.1. Guidelines for the design of the MACQU coil

The quench behavior of the MADMAX magnet is unpredictable due to both the use of a novel type of CICC and stagnant superfluid helium for cooling. To study experimentally the quench behavior of the MADMAX magnet, and understand better how such a CICC behaves in case of quench, a prototype coil called MACQU (MAdmax Coil for Quench Understanding) has been designed, manufactured and tested during this Ph.D. thesis. This chapter is dedicated to the design phase of the MACQU coil. First of all, the guidelines of the design are presented. The main goal of MACQU is to reproduce the MADMAX quench behavior. To do so, MACQU is designed by reproducing specific driving parameters of the quench propagation, as the conductor concept, the heat dissipation by Joule effect, the current sharing temperature T_{cs} or the hydraulic diameter and void fraction. By reproducing or approaching as much as possible these parameters, the quench behavior of MADMAX should be reproduced. The design method of MACQU will then be detailed by presenting each driving parameter and demonstrating its impact in the quench behavior. Manufacturing constraints, cost or time schedule, will also impact the technical solutions chosen in the design that are presented in details in a second phase. The conductor and the magnetic design are detailed and the different technological choices are justified. Finally, the relevance of studying the MACQU quench behavior in comparison with the MADMAX one is discussed. By studying the current range and quench propagation time spectrum, the quench studies range is detailed. These studies will allow us to justify the relevance of MACQU by introducing first quench speed estimations and comparing them to the results obtained and presented earlier for MADMAX.

2.1.1. Similar conductor concept

The study of the quench propagation originates in the use of a novel CICC type coupled with a rare cooling concept. The actual design of the conductor is represented in figure 2.1 [7]. The conductor of MADMAX is composed of a rectangular shape copper profile, with a conduit inside. A 108-strands Nb-Ti superconducting cable is inserted inside the conduit, with a copper wrap that maintains the strands during the insertion process. The remaining void is filled with stagnant superfluid helium, to ensure the cooling and thermal stability of the magnet. The magnet is cooled at 1.8 K thanks to superfluid helium. This cryogenic temperature allows getting higher current density performances for the Nb-Ti cable and thus higher field, compared to a classical forced-flow convection cooling at around 5 K.

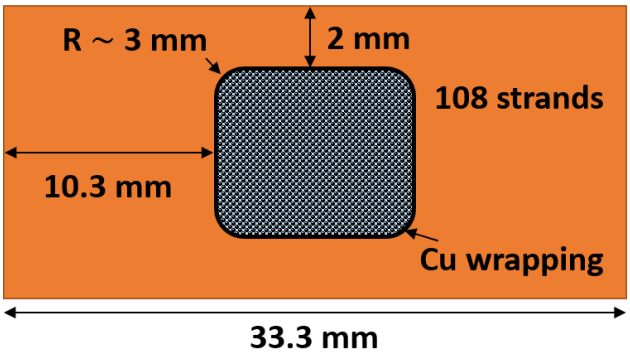

Figure 2.1: Schematic of the actual MADMAX conductor design, with a copper profile. The cable is composed of 108 Nb-Ti strands, maintained by a copper wrap and immersed in superfluid helium [7].

The nominal conditions of the MADMAX experiment are summarized in the table 2.1 with the main characteristics of the conductor.

Table 2.1: Main MADMAX magnet and experiment characteristics.

Nominal current (A)	23500
Maximum magnetic field (T)	10.33
Working temperature (K)	1.8
Hot-spot temperature (K)	100
Current sharing temperature (K)	3.11
Load line margin (%)	10
RRR	60
Copper section (mm^2)	364
Helium section (mm^2)	28
Void fraction (%)	30
Hydraulic diameter (mm)	0.33
Wet perimeter (mm)	340
Nb-Ti section (mm^2)	30.6
Glass epoxy section (mm^2)	48

To reproduce the MADMAX quench behavior, it is important to use a conductor built on the same general concept. The features that will be reproduced for MACQU are the use of Nb-Ti cable with a copper wrap inserted in a copper stabilizer, filled with superfluid helium with its cooling temperature set at 1.8 K. We list below the main characteristics or parameters used to design MACQU.

2.1.2. Similar heat dissipation by Joule effect

The use of very high current creates another unusual feature for MADMAX. In fact, when a quench occurs, the current is redistributed from the superconducting cable to the copper stabilizer, dissipating heat by Joule effect. The dissipated heat by Joule effect appears clearly as a term source in equation 1.20 and is defined as $\dot{q}_{Joule} = \frac{\eta_{Cu} I^2}{S_{Cu}}$. In MADMAX case, the dissipated heat by Joule effect can be estimated at $\dot{q}_{Joule} = 1.17$ kW/m in nominal conditions (see table 2.1). This value is very high compared to recent similar size magnets where the

dissipated heat by Joule effect is the order of 100 W/m, with 45 W/m for ISEULT the MRI magnet [54] for example. In recent magnet history, only JT60-SA has been close to this value with 972 W/m, but with a different cryostable forced flow CICC technology working at 4.5 K with more than 2 K of temperature margin [55], while MADMAX is much challenging as having no forced flow, a small superfluid helium cross-section and only 1 K of temperature margin. To study a representative quench, our first design guideline will thus be to have close heat dissipation by Joule effect between MACQU and MADMAX. Moreover, the impacting parameters, as the electrical resistivity (depending on the temperature, magnetic field and RRR), the operation current and the cross-section of the copper stabilizer are carefully designed.

2.1.3. Similar current sharing temperature T_{cs}

The heat dissipation by Joule effect appears when the temperature of the superconducting cable reaches the current sharing temperature T_{cs}. The temperature margin, defined as $\Delta T = T_{cs} - T_0$, represents the maximum temperature increase of the conductor that can be allowed before initiating the quench. For MADMAX, the magnet is cooled at 1.8 K and the current sharing temperature is 3.11 K, the temperature margin is $\Delta T_{MADMAX} = 1.31$ K. However, a temperature increase of the conductor will also induce a temperature increase of the coolant helium inside the conduit. This energy deposition can lead to change the helium's phase from superfluid to liquid, that happens at 2.17 K for 1 bar. In liquid state, the specific heat of the helium strongly decreases, and the enthalpy margin is much smaller than in superfluid state. The change in enthalpy margin impacts then the quench behavior, as the temperature of the conductor will increase more for the same heat load.

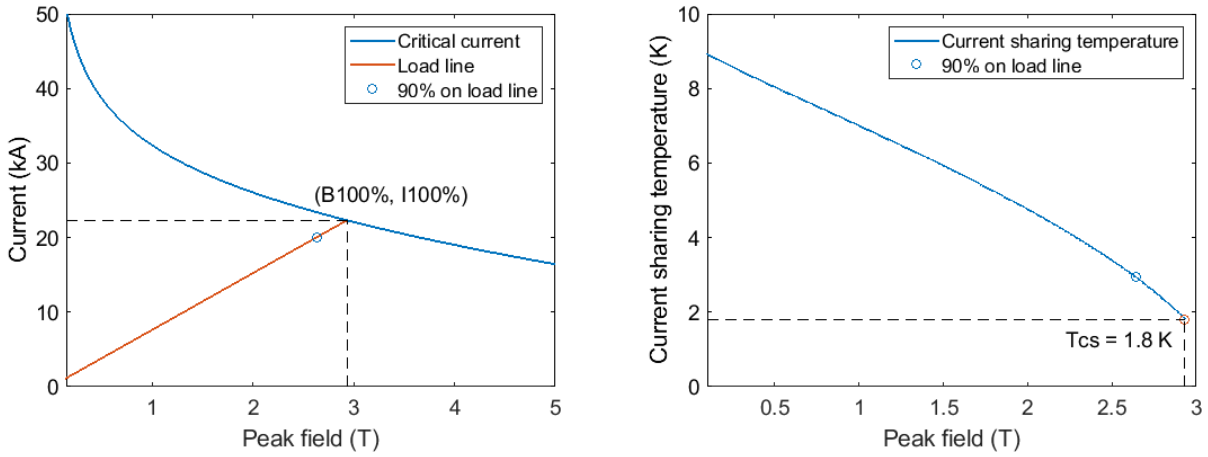

(a) Load line and critical current evolution.

(b) Current sharing temperature evolution.

Figure 2.2: Comparison of the load line and the current sharing temperature to the critical current on the left. The intersection of both curves corresponds to the critical conditions. The current sharing temperature in function of the field is plotted on the right with the associated critical conditions, estimated with the Bottura fit [35].

Moreover, as shown in equation 1.14, the quench propagation speed is directly dependent on the current sharing temperature of the conductor as the speed increases like the inverse of the enthalpy margin. Therefore, a second important design guideline is to have an equivalent current sharing temperature i.e. equivalent temperature margin, with the helium in similar physical states, to reproduce an equivalent temperature increase and quench behavior. In terms of magnetic design, having a close current sharing temperature can be obtained by imposing

the same load line margin to the MACQU conductor, as shows figure 2.2. The margin on the load line is calculated by $LL_{margin} = 1 - \frac{I}{I_{100\ \%}}$ with I being the considered current and $I_{100\ \%}$ the current at the intersection of the load line and the critical current, being the current at 100 % on the load line.

2.1.4. Similar hydraulic diameter and void fraction

As presented in section 1.2.5 and in both equations 1.20 and 1.22, the cryostability is ensured by stagnant He II and therefore the temperature variation of the small helium quantity inside the conduit is an essential parameter. The thermal coupling is done by the wetted perimeter in the heat flux term $\dot{q}_h = P_w h(T_h - T_{Cond})$, written as a convective heat flux but with h being the parietal heat transfer coefficient. In MADMAX case, the wetted perimeter is only the perimeter of the wetted wires summed to the perimeter of the conduit, defined as $P_w = \pi(D_{conduit} + \frac{5}{6} N_{strands} \times D_{strands})$, where P_w is the wetted perimeter, $D_{conduit}$ is the diameter of the conduit, $N_{strands}$ is the number of wires, $D_{strands}$ is the diameter of the strands and the factor $\frac{5}{6}$ is used to consider the covering of the strands in the cable [56]. In usual bath concepts, the magnet is immersed in the bath so the external faces of the conductor are in contact with the superfluid helium. For MADMAX, adding such a contact length would increase the wetted perimeter of around 30 %, and would then increase the cryostability of the magnet.

However, another thermal coupling between solid and fluid can be seen in the friction term, driven by the hydraulic diameter defined as $D_h = \frac{4S_h}{P_w}$, with S_h is the helium cross-section and P_w is the wet perimeter. The friction term derives from the conservative form of the energy equation as explained in section 1.2.5 and links the helium cross-section to the wetted perimeter by the hydraulic diameter.The friction term represents the variation of the temperature due to the pressure losses generated by the porous structure of the CICC. On one side, an important wetted perimeter allows a good thermal exchange between both components, ensuring an efficient cooling of the conductor by the helium. On the other side, the helium cross-section represents the enthalpy storage inside the CICC to absorb heat depositions and is defined by the void fraction of the conduit. With some trivial algebra, it is possible to write equation 2.1 to link the void fraction of the conduit to the hydraulic diameter and the diameter of the strand:

$$
\begin{aligned}
S_{strands} = (1 - v_f) S_{conduit} &= N_{strands} \frac{\pi D_{strands}^2}{4} \\
S_h = v_f S_{conduit} &= \frac{v_f}{1 - v_f} S_{strands} \\
P_w = \pi(D_{conduit} + \frac{5}{6} N_{strands} \times D_{strands}) &\approx N_{strands} \times \pi D_{strands} \\
D_h = \frac{4S_h}{P_w} &\approx \frac{v_f}{1 - v_f} D_{strands}
\end{aligned}
\tag{2.1}
$$

with S being the cross-section, v_f the void fraction of the conduit and the indices corresponding respectively to the strands ("strands"), the helium ("h") or the conduit ("conduit").

Reproducing an equivalent hydraulic diameter on MACQU ensures geometrically an equivalent ratio between the helium cross-section and the wetted perimeter. The hydraulic diameter

can be scaled thanks to equation 2.1 by reproducing an equivalent void fraction and by considering a superconducting strand of similar dimension of the MADMAX one. Therefore, the third guideline of the design is to reproduce an equivalent hydraulic diameter by a similar void fraction and close strand dimension. To fit the design of the conductor, but also to have a similar thermal stability, the void fraction is set to 30 %, to be equivalent to the MADMAX one. In that way, the MACQU conductor is geometrically similar and also with a similar thermal solid-fluid coupling, leading to an equivalent thermal behavior and quench behavior. It is shown in chapter 5 that the hydraulic diameter has an important role in the quench propagation.

2.1.5. Simple magnet configuration for physics analysis

The goal of the MACQU coil is to reproduce and study experimentally the quench behavior of the MADMAX magnet. However, even by considering the above-described parameters in the design phase, the quench behavior of the MADMAX magnet is a complex and multi-physical phenomenon. Figure 2.3 compares the magnetic field map of the B1 and B9 coils, respectively the biggest and the smallest coils of MADMAX. It can clearly be seen that the magnetic field can take almost every value between 0.4 T and 9.5 T for B1, whereas for B9 the magnetic field varies only between 6 T and 10 T. With the dipole configuration, each coil impacts the field map of the other coils, hence with different field maps, each coil has its own quench behavior.

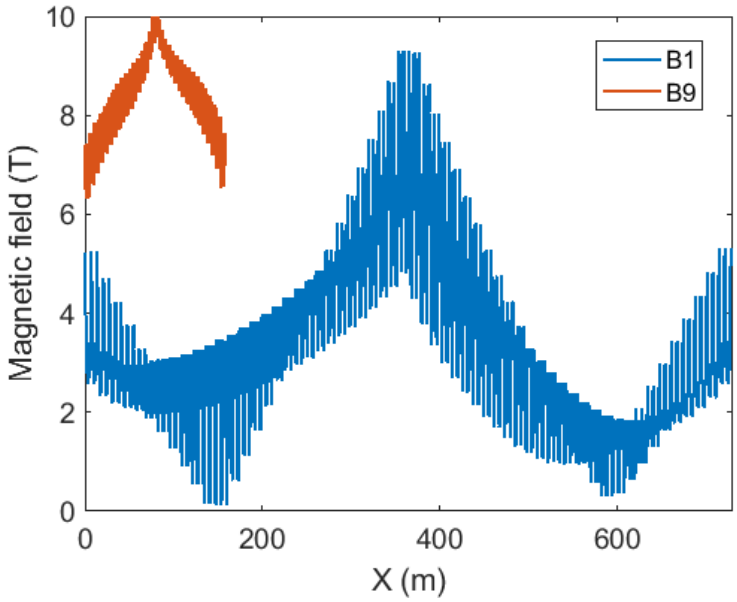

Figure 2.3: Comparison of the magnetic field map of the B1 and B9 coils in MADMAX. B1 is the biggest and the closest one to the warm hole, when B9 is the smallest and farthest one.

Moreover, as explained in section 1.2.3, the quench can propagate in 3-D: the longitudinal direction along the conductor, the neighbor conductor through the insulation direction, or even to the neighbor pancake through the insulation direction, as shows figure 2.4.

The quench propagation appears as a 3-D phenomenon, difficult to analyze experimentally and to reproduce numerically. From a numerical point of view, each direction of quench propagation can be studied (almost) independently in 1-D models, but reproducing an entire 3-D design is an important work, without ensuring accurate results. Moreover, THEA® is still being tested for the particular conductor design of MADMAX, and testing the MACQU case can benchmark the results obtained numerically. Then, to understand clearly the physical phenomenon driving the quench but also validate the numerical results, MACQU should allow us

to study the quench phenomenon in simple configurations and a few design choices should be done to do so. First of all, the quench will be studied at constant current. A constant current quench scenario simulates a non detected quench that propagates without intervention, and is typically the kind of phenomenon that can damage a superconducting magnet. Moreover, the geometry of the magnet is designed to make the magnetic field vary less along the magnet length. For that, the magnet geometry adopted is a solenoid. That way, the impact of the magnetic field variation on the quench propagation, as for B1 for example, is greatly decreased. Finally, the winding of the solenoid is designed to study only longitudinal quench propagation along the conductor, meaning that the design will consider the transversal diffusion as negligible. To avoid a 3-D diffusion in the insulation and to facilitate the winding of the magnet, the solenoid is single-layered. To avoid heat diffusion between two neighbor conductors, a specific thermal design had to be done to consider longitudinal quench propagation only.

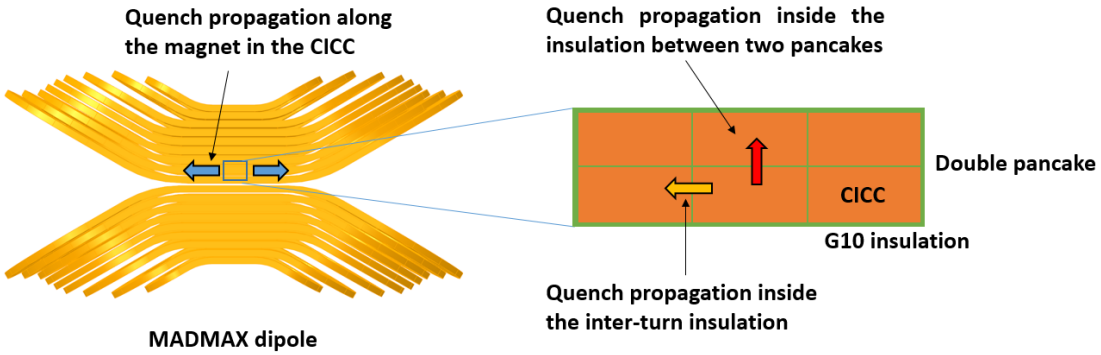

Figure 2.4: Scheme of the three quench propagation modes: along the CICC (longitudinal) or inside the insulation, through the inter-turn or the casing (transversal).

2.1.6. Cost and schedule

The quench behavior of MADMAX is a clear issue in the design of the magnet. If the quench is undetectable, the entire conductor and quench protection design have to be changed. Changing the conductor design would imply important delays and would represent a high cost increase for the project. So, it is mandatory to settle on the ability to detect the quench, as fast and cost efficient as possible. An important design guideline will then be to choose already existing products on catalog, as the superconducting wires or the copper profile, to be able to manufacture the magnet as soon as possible and avoid dedicated tooling and qualifications for particular products. Already bought products can also be reused. The products are chosen to be as close as possible to the design objectives.

2.2. Description of the MACQU magnet design

This section presents the design of the MACQU magnet. In a first step, the design of the conductor is done, by reproducing a MADMAX-like conductor concept. The goal is to reproduce the linear heat dissipation by Joule effect and the current sharing temperature of MADMAX, by carefully designing the copper stabilizer and the superconducting cable. In a second step, the geometry of the magnet will lead to the magnetic design. The inner radius, the inter-turn distance and the length of the magnet is studied to optimize the magnetic field for the linear heat dissipation. The field map of the solenoid is computed in a last step.

Note that the design method presented in this section aims to reproduce best the design parameters driving the quench behavior of MADMAX. Due to several reasons as strong hy-

pothesis, manufacturing constraints or time span of the project, some of the presented values will be updated in chapter 3 with the final configuration of the magnet.

2.2.1. Description of the conductor design

The design of the MACQU magnet is mostly driven by the linear heat dissipation by Joule effect. By using the same conductor concept, the linear heat dissipation of MADMAX, which is worth 1.17 kW/m, should be reproduced. Defined as $\dot{q} = \frac{\eta_{Cu} I^2}{S_{Cu}}$, several parameters as the magnetic field, the copper cross-section or the current should be taken into account to reproduce the linear heat dissipation. The first component of the conductor to design is the copper stabilizer, to set the copper cross-section. In a second step, the superconducting cable is designed. The manufacturing constraints are taken into account to define a cable pattern that can fit into the chosen copper stabilizer. The cable pattern will also allow us to set the performances of the superconducting cable. Depending on the performances of the superconducting cable, the current sharing temperature will then be calculated. This step by step method will lead to a conductor design, inspired in its concept by the existing design of MADMAX, always having in mind that the quench behavior must be reproduced.

2.2.1.1. Copper profile for the CICC conductor

MACQU is designed to have the linear heat dissipation by Joule effect equivalent to the MADMAX one. However, some assumptions have to be done to determine the copper profile cross-section. A 10.33 T peak magnetic field is too high and would be too expensive to be reproduced with a simple one-layer solenoid geometry. A scaling strategy is used for the design of MACQU. The magnetic field decrease can be compensated by a copper cross-section decrease. By assuming that the current, the Residual Resistivity Ratio and the temperature are the same than for MADMAX, the following equation can be written:

$$\begin{aligned} \dot{q}_{MADMAX} \approx \dot{q}_{MACQU} &\iff \frac{\eta_{Cu}(T,B,RRR)I^2}{S_{Cu}}|_{MADMAX} \approx \frac{\eta_{Cu}(T,B,RRR)I^2}{S_{Cu}}|_{MACQU} \\ &\iff \frac{\eta_{Cu}(B_{MADMAX})}{S_{Cu,MADMAX}} \approx \frac{\eta_{Cu}(B_{MACQU})}{S_{Cu,MACQU}} \\ &\iff \frac{\eta_{Cu}(B_{MADMAX})}{\eta_{Cu}(B_{MACQU})} \approx \frac{S_{Cu,MADMAX}}{S_{Cu,MACQU}} \end{aligned} \tag{2.2}$$

where $\dot{q}$ is the linear heat dissipation for each magnet, η_{Cu} is the electrical resistivity, S_{Cu} is the copper cross-section, I is the current set at 23500 A, T the initial temperature set at 1.8 K, B the magnetic peak field and RRR set at 60.

The copper cross-section can be defined by comparing the electrical resistivity ratio depending only on the magnetic field. An acceptable assumption done for the MACQU design is that a magnetic field range of 2-2.5 T should be obtained thanks to the high working current. The electrical resistivity can be estimated at $\eta_{Cu}(10.33\text{ T}) = 7.74 \times 10^{-10}$ Ω.m and $\eta_{Cu}(2\text{-}2.5\text{ T}) = 3.58\text{-}3.83 \times 10^{-10}$ Ω.m. The equation 2.2 becomes:

$$\begin{aligned} S_{Cu,MACQU} \approx \frac{\eta_{Cu}(B_{MACQU})}{\eta_{Cu}(B_{MADMAX})} S_{Cu,MADMAX} &\iff S_{Cu,MACQU} \approx \frac{\eta_{Cu}(2-2.5T)}{\eta_{Cu}(10.33T)} S_{Cu,MADMAX} \\ &\iff S_{Cu,MACQU} \approx 168 - 180\ mm^2 \end{aligned} \tag{2.3}$$

The equation 2.3 allows us to define the cross-section range of the copper profile to reproduce the heat dissipation by Joule effect, with equivalent nominal current (23500 A) and RRR (60) than MADMAX.

To reduce the cost, the copper profile has been chosen on catalogue. It was important to choose the section range to chose a copper profile that was close to our specifications. The M3HE0014 copper profile, fitting with our needs, has been finally chosen and bought to the *Aurubis* company [57]. The dimensions of the profile are summarized in figure 2.5. With such dimensions, the copper cross-section can be estimated to 215 mm^2. The cross-section is voluntarily larger than needed, as the cross-section is reduced during the compaction process. Finally, the RRR of the profile has a lower value than 60.

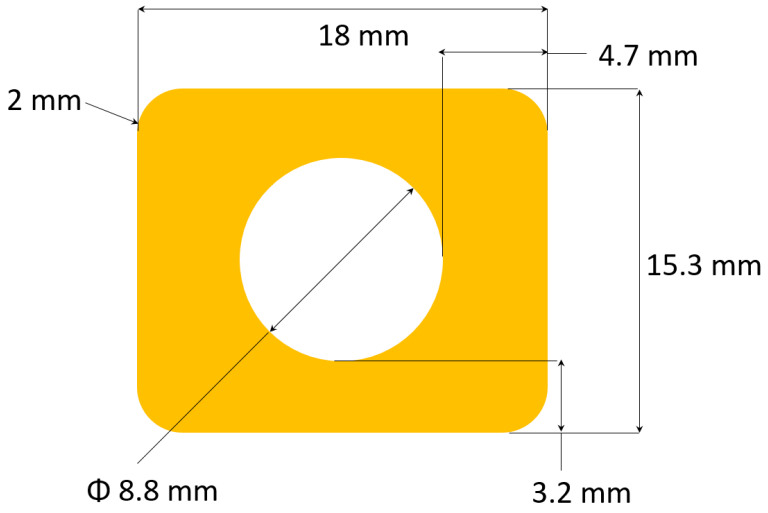

Figure 2.5: Aurubis M3HE0014 copper profile.

2.2.1.2. Superconducting strand design

The MADMAX cable is composed of 108 Nb-Ti strands, divided into a 3*3*3*4 cable pattern. The superconducting strand of MADMAX has a diameter of 0.88 mm, with a cross-section of $S_{cable} = 66$ mm^2. With the copper profile presented in section 2.2.1.1, the section of the conduit would be 60.8 mm^2, so the MACQU copper profile is not large enough to fit such a number of strands. It has been decided to remove one stage, reducing by the way the number of strands. Margins and tolerances should be taken for the insertion of the cable inside the conduit and patterns with higher number of strands would barely fit in the conduit, so only three are studied here: the 3*3*3 pattern, the 3*3*4 pattern and the 3*4*4 pattern.

To follow the "on-catalog" strategy, the superconducting strands were chosen depending on their industrial availability, by considering a size close to the strands of MADMAX. The most fitting strands have been bought to the *Western Superconducting Technologies* (WST) [58] company. The characteristics of the strands are resumed in table 2.2:

Table 2.2: Characteristics of the WST strands used for MACQU superconducting cable.

Strand diameter (mm)	0.825
Cu/Sc ratio	1.105
Number of filament	630
Critical current at 4.2 K @4T (A)	850
Critical current at 4.2 K @5T (A)	750

2.2.1.3. Cable pattern, compaction level and void fraction

The superconducting cable of MACQU is inserted in the CICC conduit and surrounded by superfluid helium. To insert the cable in the CICC conduit, the cable pattern has to be set first. The cable is composed of a multi-stage stranding as for a classic CICC. However, the number of stages and of strands is still to be determined. The entire cabling, insertion and compaction process is detailed in figure 2.6. The example presented is a 3*3*4 multi-stage cable. Initially, the strands are gathered and stranded in a triplet, which form the 1^{st} stage bundle. The formed triplets are again stranded with 2 other triplets forming the second stage of the cable called 2^{nd} stage bundle (or 3x3 bundle). Finally, the other four 2^{nd} stage bundles are stranded together to form a 3^{rd} stage bundle, until forming the final cable. This process can continue to higher number of stages if needed. In a second step, the cable is wrapped in a 0.2 mm thick copper tape, before being inserted in the CICC conduit. A minimal gap of 2 mm is needed between the cable and the conduit dimensions, to ensure not deteriorating the cable during the insertion process. Finally, the copper profile is compacted by rollers/turk heads up to the nominal conductor external dimensions which will reduce its cross-section. The maximum compaction level in one pass is around 20%-25% of section reduction. For a higher section reduction, several passes are needed and the possible section reduction decreases with the number of passes. The compaction process ensures a good electrical contact between the cable and the copper profile, in order to diffuse the current in the copper stabilizer in case of a quench and then slow down the temperature increase.

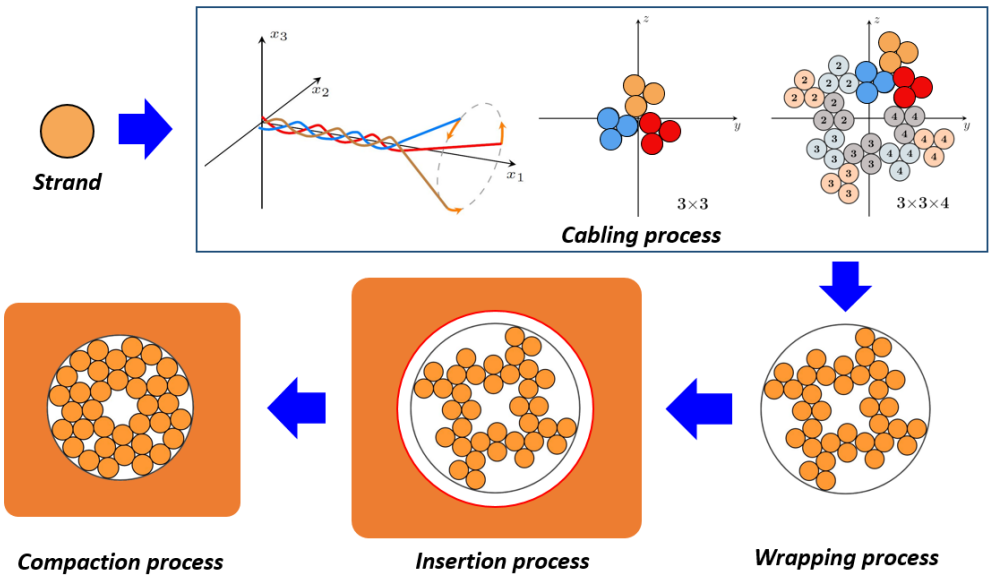

Figure 2.6: Scheme of the cabling, insertion and compaction process for a 3*3*4 cable pattern (with the courtesy of Francesco Stacchi).

For manufacturing constraints, it has been chosen to perform the compaction process in one pass. The maximum section reduction will then be around 25 %. To simplify the compaction computations, it is assumed that the compaction process reduces the total cross-section of the profile homothetically. This assumption will allow to calculate the minimum needed diameter to be able to insert the cable in the conduit. Moreover, as explained in section 2.1.4, the aimed void fraction and hydraulic diameter for MACQU are respectively 30 % and around 0.3 mm, in order to reproduce the thermal behavior of the conductor, i.e. the cooling efficiency and cryostability. The cross-section of the strands is assumed to remain constant during the

compaction process. Then, the cable and the conduit cross-section are driven by the equations defined below:

$$v_f = 1 - \frac{S_{cable}}{S_{conduit,minimum}} \approx 0.3 \tag{2.4}$$

$$D_{conduit,minimum} = \sqrt{\frac{4S_{conduit,minimum}}{\pi}} \tag{2.5}$$

$$D_{conduit,f} = D_{conduit,minimum} + 2 * 0.2mm \leq D_{conduit,i} - 2mm \tag{2.6}$$

$$e_{conductor,f} = e_{conductor,i} - (D_{conduit,i} - D_{conduit,f}) \tag{2.7}$$

$$h_{conductor,f} = h_{conductor,i} - (D_{conduit,i} - D_{conduit,f}) \tag{2.8}$$

$$S_{stabilizer,f} = e_{conductor,f} \times h_{conductor,f} - \frac{\pi D^2_{conduit,f}}{4} \tag{2.9}$$

$$C_l = 1 - \frac{S_{stabilizer,f}}{S_{stabilizer,i}} \leq 0.25 \tag{2.10}$$

where v_f is the void fraction, S_{cable} is the cross-section of the superconducting cable, $S_{conduit}$ is the cross-section of the conduit, $D_{conduit}$ is the diameter of the conduit, D_{cable} is the diameter of the cable, $e_{conductor}$ and $h_{conductor}$ are respectively the thickness and height of the conductor, $S_{stabilizer}$ is the cross-section of the stabilizer, C_l is the compaction level, and the indices f, i and $minimum$ are respectively the final (after compaction), initial (before compaction) and minimal (to respect the gap) dimension.

The equations 2.4 and 2.5 allow to calculate the minimum needed cross-section and the equivalent diameter of conduit. Equation 2.6 allows to verify if the gap between the initial conduit and the wrapped cable criterion is sufficient. Equation 2.7, 2.8 and 2.9 are used to calculate the dimensions of the stabilizer after compaction. Equation 2.10 is a design criterion that has to be verified, to ensure a doable compaction level in one pass (lower than 25 %). The results are summarized in table 2.3 in function of the different cable patterns. The first analysis that can be done is that equation 2.1 scales well the hydraulic diameter of MACQU in function of the void fraction and the diameter of the strand as the hydraulic diameter is almost equal to the MADMAX one (0.33 mm). However, as it can be seen, the 27-strands configuration does not respect the compaction level criterion defined in equation 2.10, as the compaction level is almost 29 %. On the other side, the 48-strands configuration has a too small insertion gap, as it is 1.57 mm, below the minimum insertion gap of 2 mm, as defined in equation 2.6. Clearly, the only configuration that respects the both criteria is the 3*3*4 = 36 strands cable pattern which is then chosen for MACQU. It represents then a copper cross-section of 167.5 mm^2 for the stabilizer, with 15.5×12.8 mm^2 final external dimensions.

Table 2.3: Different scaling parameters of MACQU as function of the initial triplets configuration.

	27 strands (3×3×3)	36 strands (3×3×4)	48 strands (3×4×4)
Strand section (mm^2)	14.43	19.24	25.66
Helium section (mm^2)	6.19	8.25	11.0
Wet perimeter (mm)	76	98	126
Hydraulic diameter (mm)	0.33	0.34	0.35
Insertion gap (mm)	3.28	2.48	1.57
Compaction level (%)	28.7	21.9	14.0
Stabilizer section (mm^2)	153.1	167.5	184.6

2.2.1.4. Superconducting cross-section and current sharing temperature

The last parameter to freeze on the conductor design is the superconducting cross-section i.e. the number of Nb-Ti strands in the cable. It depends on the needed performances of the superconducting cable. As explained in section 2.1.3, the current sharing temperature should be around 3 K, with a load line margin around 10 %. Obviously, the higher the number of superconducting strands, the higher the current sharing temperature and the load line margin are. Only 3 combination of superconducting strands exist for a 3*3*4 cable pattern: 12, 24 or 36 Nb-Ti strands, out of the 36 of the cable.

The total number of superconducting strands depends then on the number of strands defined in the initial triplet. The three options are:

- Have three Nb-Ti strands out of three of the initial triplet. This configuration corresponds to a full Nb-Ti cable.
- Have two Nb-Ti strands out of three of the initial triplet, and have a copper strand to complete the triplet. This configuration corresponds to a 24 Nb-Ti - 12 copper strands cable.
- Have one Nb-Ti strand out of three of the initial triplet, and have two copper strands to complete the triplet. This configuration corresponds to a 12 Nb-Ti - 24 copper strands cable.

To choose the configuration the most adapted for MACQU, the table 2.4 shows the margin on the load line and the current sharing temperature at 23500 A being the same current as MADMAX. The calculation is made by considering the peak field of the magnet being arbitrarily set at 2 T for 23500 A. This calculation is recomputed with the real field map presented in the next chapter. The copper-cross section of the conductor considered in the computation is estimated by taking into account the cross-section of the stabilizer after the estimated compaction (167.5 mm^2) and the copper cross-section of the strands.

Table 2.4: Margin on the load line and current sharing temperature of MACQU depending on the number of superconducting strands compared to the MADMAX configuration.

	12 Nb-Ti	24 Nb-Ti	36 Nb-Ti	MADMAX
Number of superconducting strand	12	24	36	108
Superconducting section (mm^2)	3.047	6.094	9.141	30.50
Copper section in the strands (mm^2)	16.20	13.15	10.10	35.14
Total copper section (mm^2)	183.7	180.7	177.6	367.7
Margin on the load line (%)	7.2	42.7	55.6	10
Current sharing temperature (K)	2.66	5.53	6.4	3.11

As shown in table 2.4, no configuration can reach the specifications with the same current of MADMAX. For the 12 Nb-Ti strands configuration, 7.2 % margin on the load line is reached while for the 24 and 36 Nb-Ti strands one, respectively only 42.7 % and 55.6 % margin on the load line are reached. The options are, on one side, to increase the current for the 24 and 36 Nb-Ti strands configuration to reach the 10 % margin on the load line. The criterion is reached for respectively 36.9 kA and 3.14 T and 47.7 A and 4.06 T, with a linear heat dissipation by Joule effect of 3.1 kW/m and 5.9 kW/m and a current sharing temperature of 2.95 K and 2.96 K. On the other side, the current can be decreased for the 12 Nb-Ti configuration, to reach the 10 % on the load line at 22.8 kA and 1.94 T, with a heat dissipation by Joule effect of 1.0 kW/m and a current sharing temperature of 2.94 K.

Even if it allows reaching "only" 85.5 % of the linear heat dissipation of MADMAX, the 12 Nb-Ti strands configuration has been chosen for MACQU as it is the closest one to reproduce both MADMAX working conditions of heat dissipation and load line margin. The 2 other configurations, on the opposite, would create a dissipation higher than the MADMAX one, altering, that way, the quench behavior. Moreover, the 2 other configurations would ask for important technical modifications, such as having a power supply feeding more than 30 kA while the maximal available current in the testing facility is 25.7 kA. Figure 2.7 represents the view of the MACQU cable in a cross-section, with the chosen 3*3*4 pattern and the 12 Nb-Ti strands configuration.

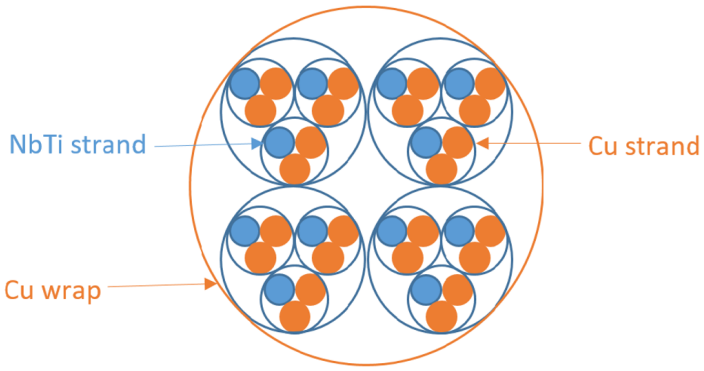

Figure 2.7: The MACQU cable 3×3×4 pattern with 12 superconducting strands and 24 copper strands.

Note that strong hypotheses have been taken concerning the compaction process and the magnetic field. These hypotheses are updated in the next chapters once the overall design is

Table 2.5: Summary of the characteristics of the MACQU conductor.

Number of superconducting strands	12
Number of copper strands	24
Nominal current (A)	22809
Linear heat dissipation by Joule effect (W/m)	1004
Margin on the load line (%)	10
Current sharing temperature (K)	2.94

achieved and the manufacturing of the magnet finished.

2.2.2. Description of the winding design

The conductor of the MACQU magnet has been designed in the previous section. The next step towards the magnet design is then to define the detailed coil winding geometry. As explained in section 2.1.5, the winding general concept is already chosen as a single-layered solenoid. Therefore, the geometrical parameters of the magnet have to be designed in a first step. Defining the geometrical parameters of the solenoid allows us to compute the magnetic field map distribution. Finally, all these parameters will allow us to compute the first preliminary quench studies in section 2.3.

2.2.2.1. Design of the magnet length

Three geometrical parameters have still to be designed: the length of the magnet, the internal radius of the solenoid and the inter-turn distance. Here, an arbitrary length of 50 m was chosen for MACQU. The length is chosen as a compromise between the fabrication and integration constraints, the cost of the magnet and the needed length to study the quench behavior without being impacted by the boundary conditions at the center and the extremities. During the 50 m of propagation, it is estimated to be independent of the boundary conditions on around 40 m. Indeed, with 200 mm long heaters glued in the mid of the coil (see section 2.3.1), it is considered to be fully independent from quench initiation conditions after roughly 10 times this dimension. On the other side, the coil ends are supposed to have a constant temperature of 1.8 K, it is considered to be independent from this boundary conditions after 4 m of diffusion, estimated with the following equation 2.11, derived from the 1-D heat equation in the copper:

$$\frac{\rho C_p}{\Delta t} = \frac{\lambda}{\Delta x^2} \Longleftrightarrow \Delta x = \sqrt{\frac{\rho C_p \Delta t}{\lambda}} \tag{2.11}$$

with ρ being the density of the material, C_p the specific heat, λ the thermal conductivity and Δt and Δx being respectively the characteristic time and characteristic length. The copper properties have been estimated at 1.8 K, 2 T and for a RRR of 60, with a characteristic time of 1 s.

Taking off these two boundary conditions "impact zone" from the coil length, we still have twice 20 m available for quench propagation studies, without having any impact from the boundary conditions. This value seems to us largely enough for both detecting and studying the quench. Indeed, by assuming the pessimistic case where only the half of the length quenches, by using equation 1.16, the voltage variation would be still be of 700 mV, largely detectable compared to the 100 mV Magnet Safety System threshold.

2.2.2.2. Design of the internal radius

The design of the geometrical parameters of the solenoid are lead by the linear heat dissipation by Joule effect. As seen in section 2.2.1.4, at 10 % margin on the load line, 85.5 % of the linear heat dissipation of MADMAX can be reached in the present MACQU design, with a current of 22809 A. One way to make this value closer to MADMAX is to increase the magnetic field and thus the copper resistivity and Joule effect. To reach the 1174 W/m of MADMAX at 10 % margin on the load line, an electrical resistivity of 4.15 $\times$ $10^{-}10$ Ω.m is needed, corresponding to a magnetic field of 3.15 T. However, the critical magnetic field at similar working conditions is 2.794 T. Reaching the MADMAX nominal value of linear heat dissipation is thus impossible. Even if the gap can not be compensated, it is still possible to decrease the coil inner radius to reduce the gap between MACQU and MADMAX. To estimate the magnetic field in function of the internal radius, a model has been developed based on C. Lesmond's work [59]. In the cited document, Lesmond presents several analytical models for the calculation of a magnetic field for different type of superconducting magnet. The case of a thick solenoid, the case of MACQU, is presented in figure 2.8 with the associated analytical formula, on which the self field of the cable has been added.

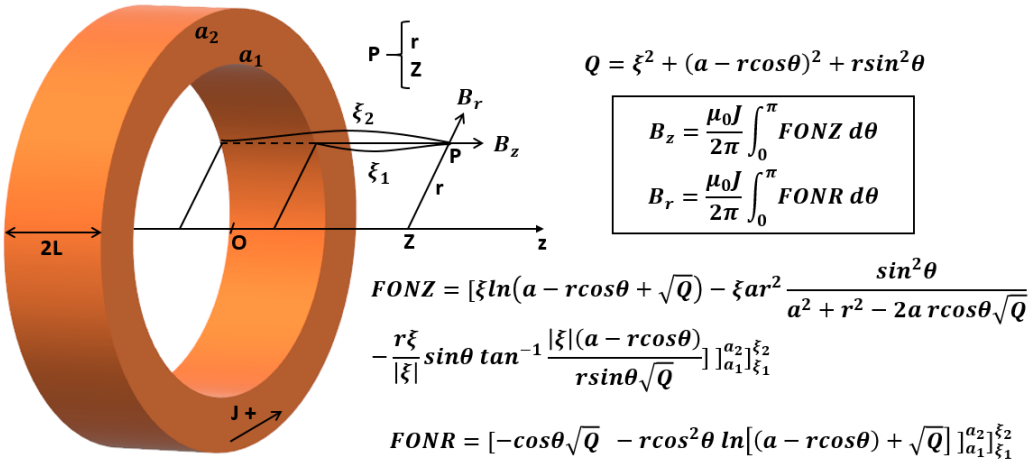

Figure 2.8: Scheme of the thick solenoid model used for magnetic field computation. The field is calculated at r = a_1 and Z = 0.

Figure 2.9 shows the variation of the magnetic field of a 1 m long full solenoid, in function of the internal radius. The current density is $J = \frac{22809}{183.7 \times 10^{-6}} = 1.24 \times 10^8$ A/m^2. To have a representative magnetic field, the total magnetic field corresponds to the contribution of the magnetic field of the solenoid and the contribution of the self field of the cable. The self-field of the cable is obtained by comparing a 2-D and a 3-D OPERA model (see section 2.2.3). In the 2-D model, all the superconducting strands are modeled, while in the 3-D model, a full profile, at the dimension of the MACQU profile, is considered. The difference obtained between both models leads to a self-field of the cable of 0.658 T for 22809 A. For the developed model, the current is supposed to be uniformly distributed in a rectangular shape profile, with the dimensions estimated in section 2.2.1.3.

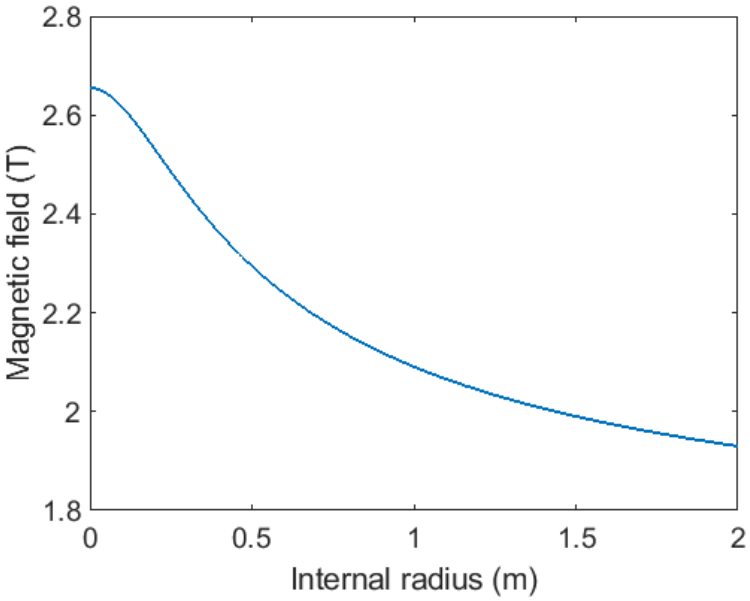

Figure 2.9: Variation of the magnetic field in function of the internal radius of a solenoid, calculated at the internal radius and at the longitudinal center of the magnet.

The calculation, thanks to the model of Lesmond, is not as precise as a 3-D calculation, as it is presented in section 2.2.3 but gives a trend of the needed internal radius. As it can be seen in figure 2.9, the magnetic field decreases with the increase of the internal radius but reaching the value of 2.794 T seems not possible even with the smallest radius. Then, to maximize the magnetic field, the minimal doable internal radius is considered for the solenoid. In fact, to avoid damaging the conductor during the winding process, a safety factor of 10 between the conductor width and the winding radius is taken. The factor 10 comes from destructive tests done on previous internal projects with short conductor samples. In fact, with a factor 7-8 and lower, conductor deteriorations were observed. By considering the estimated final dimensions of the conductor after compaction, estimated at 15.5×12.8 mm^2, the internal radius is set at $12.8 \times 10 \approx 130$ mm.

2.2.2.3. Solenoid inter-turn thickness design

As MACQU is designed to study longitudinal quench propagation only, the magnetic field increase is not the only consideration that has to be taken into account in the inter-turn distance design. Indeed, the inter-turn distance should act as a thermal insulator, to neglect the transversal heat diffusion and favor longitudinal quench propagation. However, the magnetic field increases with the decrease of the inter-turn thickness. Then, a compromise has to be found between the magnetic field optimization and the impact of the transversal heat diffusion. Therefore, the winding supporting mandrel of MACQU will have a double function: support the magnet and help for the winding process but also thermally insulate two consecutive turns of the solenoid.

For this, two types of materials are used, with different functions: the G10 epoxy and the stainless steel. Both materials are good thermal insulators, for different temperature ranges. The stainless steel has a low thermal diffusivity below 10 K, lower than 2×10^{-5} m^2/s. But the G10 epoxy, in addition to being a good thermal insulator above 10 K, with a thermal diffusivity lower than 7×10^{-6} m^2/s, is also used as electrical insulation. The idea is to use a stainless steel cylinder, with a helicoidal groove machined around it, and wind MACQU inside the helicoidal path. Before the winding process, the conductor is wrapped in a G10 epoxy

tape for electrical insulation. The cylinder is used to insert MACQU in the JT60-SA cryostat and an adapted handling frame is designed and fabricated. Figure 2.10 shows the cross-section view of the mandrel, with the 3 main characteristics of the solenoid: the internal radius r, the inter-turn distance i_d and the longitudinal distance between the center of two consecutive conductors h_{turn}. The internal radius has been set to 130 mm in the previous section, but the two others are still to determine. h_{turn} is used to determine the length of a turn l_{turn} and are defined as:

$$i_d = e_{G10} + e_{SS} + e_{G10} = e_{SS} + 2e_{G10} \tag{2.12}$$

$$h_{turn} = i_d + h_{conductor} \tag{2.13}$$

$$l_{turn} = \sqrt{h_{turn}^2 + 4\pi^2(r + \frac{e_{conductor}}{2})^2} \tag{2.14}$$

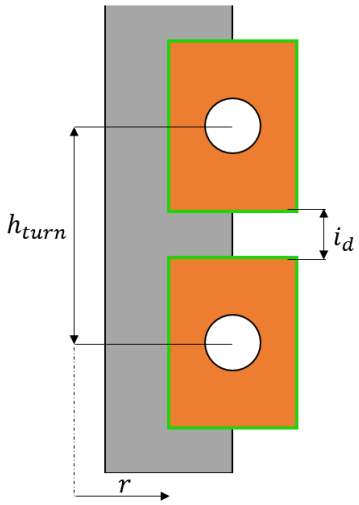

Figure 2.10: Scheme of the stainless steel mandrel, with the G10 epoxy insulation. h_{turn} is the longitudinal distance between the center of two consecutive conductors, being also called the helix step. i_d is the inter-turn distance between two consecutive conductors, from stabilizer to stabilizer.

As explained in section 1.2.3.2, by comparing the thermal conductivities of the longitudinal quench propagation and the transerval heat path, it is possible to estimate which phenomenon is the fastest to travel across one turn. As defined in equation 1.13, the thermal conductivity of the conductor and of the insulation should be compared. The thermal conductivity of the conductor and the insulation are defined as follows:

$$\lambda_{Cond} = \frac{S_{He}}{S_{Cond}}\lambda_{He} + \frac{S_{Cu}}{S_{Cond}}\lambda_{Cu} + \frac{S_{Nb-Ti}}{S_{Cond}}\lambda_{Nb-Ti} \tag{2.15}$$

$$\lambda_{Insulation} = \frac{e_{SS}}{e_{SS} + e_{G10}}\lambda_{SS} + \frac{e_{G10}}{e_{SS} + e_{G10}}\lambda_{G10} \tag{2.16}$$

The G10 epoxy is usually a thin epoxy tape and a few tenth of mm are enough to ensure the electrical insulation (30 kV/mm at high temperature). A 0.5 mm thick G10 epoxy tape was available and has been chosen. It is shown in chapter 3 that this thickness is extremely over-estimated as the maximum voltage is during the fast discharge and should be around 120 V.

However, the most important role of the G10 epoxy is the thermal insulation above 10 K. The most important thermal insulation should be under 10 K, as it is the quench initiation temperature range, and the stainless steel has a better behavior in this temperature range. Therefore, at fixed thickness, the stainless steel thickness should be maximized compared to the G10 epoxy thickness. Figure 2.11 shows the ratio of the longitudinal propagation speed and the transversal diffusion speed, estimated with equation 1.13, by comparing the square root ratio of the tranversal to longitudinal heat conductivity as a function of the temperature. The goal of this comparison is to find a compromise between the thickness increase of the inter-turn for thermal performances and the thickness reduction of the inter-turn for magnetic performances.

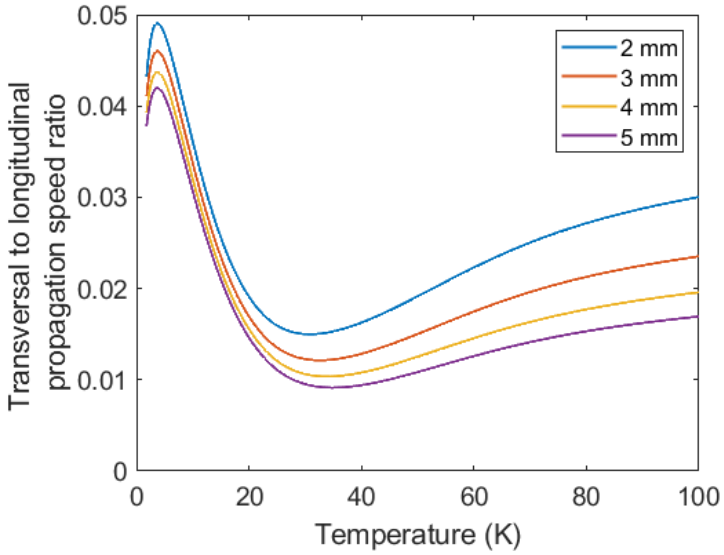

Figure 2.11: Temperature evolution of the transversal heat diffusion speed and longitudinal quench propagation speed ratio, as a function of the stainless steel mandrel thickness. The material properties have been considered at each temperature step with Cryocomp [47].

As it can be seen in figure 2.11, the ratio of the transversal heat diffusion speed and longitudinal quench propagation speed is the order of 0.01 to 0.05, meaning that the quench propagation phenomenon is 20 to 100 times faster than the transversal diffusion. In agreement with the manufacturer, a 4 mm thick stainless steel inter-turn distance has been chosen. This way, the total inter-turn distance is 5 mm. A short summary of the dimensions is presented in table 2.6.

Table 2.6: Geometrical parameters of the MACQU solenoid. All the length are written in mm.

e_{G10}	0.5
e_{SS}	4
i_d	5
r	130
$h_{conductor}$	15.5
$e_{conductor}$	12.8
h_{turn}	20.5
l_{turn}	857

2.2.3. Magnetic field map computation

With the geometry entirely set, the magnetic field map can be computed. The geometry of MACQU has been reproduced with the numerical code OPERA [60]. A 3-D model has been generated by the MADMAX team, resolving the Biot-Savart law in the defined geometry. The mesh is composed of approximately one million nodes. Figure 2.12 shows the magnetic field map of MACQU, as a function of the curvilinear abscissa along with the magnet. This calculation considers also the impact of the self-field of the cable, added to the field produced by the solenoid. The self field represents between 22 % and 32 % of the total magnetic field, depending on the location on the magnet. The impact is more important near the ends where the magnetic field decreases.

The 3-D model gives a higher magnetic field than the one expected with the 1-D model. It is particularly impacted by the discrete turns of the solenoid, compared to a full cylinder. In order to work at 10 % margin on the load line, our nominal current design value, estimated with the 3-D model, has then been updated here to 20086 A. The critical current for this nominal current is 23374 A.

The result of the magnetic field map computation is presented in figure 2.12. The calculation is done at 20086 A, corresponding to the nominal current at 10 % margin on the load line. As expected for a solenoid, the field is maximum at the center and is 2.640 T. The magnetic field then decreases along the magnet until reaching 2.524 T, before having an increase near the ends of the magnet reaching 2.634 T. The magnetic field decreases strongly to 1.838 T at the very ends. The magnetic field outside of the solenoid, so just after the very ends, is nearly zero and not plotted here. The magnetic field map is symmetrical along the magnet.

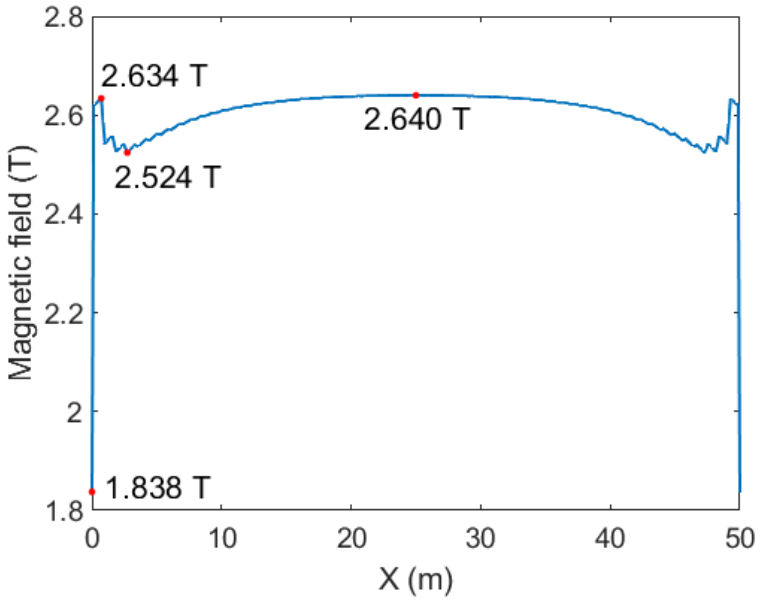

Figure 2.12: Magnetic field profile of MACQU along the magnet, depending on the curvilinear abscissa.

2.2.4. Summary of the MACQU magnet design

The design of the MACQU magnet has been described above. The last parameter of the coil to compute is the inductance of the coil. The inductance is needed in section 2.3.2 to estimate the fast discharge time. Indeed, the length of one turn l_{turn} has been estimated to be 0.857 m, and the length of the magnet fixed at 50 m, the solenoid can be composed of $\frac{50}{0.857} \approx 58$ turns.

The inductance of the solenoid is then estimated to be 0.2 mH with the following equation:

$$L_{MACQU} = \frac{\mu_0 N^2 A}{L} \tag{2.17}$$

with L_{MACQU} is the inductance of the magnet, μ_0 the vacuum permeability, N the number of turns, A the cross-sectional area of the solenoid and L the length of the solenoid.

Figure 2.13 shows a CAD draft of the solenoid wound on the stainless steel mandrel. This CAD draft is used to design the handling frame for the insertion of the coil in the test facility, described in the next chapter.

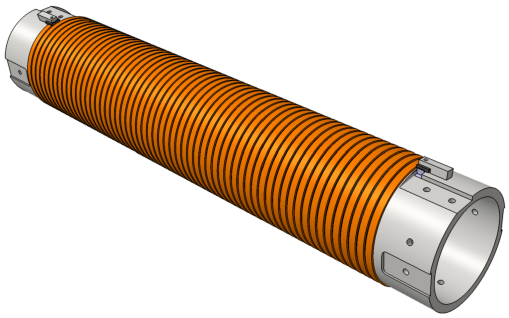

Figure 2.13: Scheme of the 58-turns MACQU solenoid wound on its supporting mandrel.

Finally, table 2.7, in the following page, summarizes the designed characteristics of the MACQU coil. With the current and magnetic field at the center of the magnet of 20086 A and 2.640 T, the linear heat dissipation by Joule effect is 855 W/m, reaching finally 72.8 % of the MADMAX one.

2.3. Preliminary quench studies

Every parameter of the design phase being set, first preliminary quench studies can be computed. The goal is to use the tools presented in section 1.2.3 to estimate the quench behavior of MACQU. To do so, hot-spot computations and quench propagation speed estimations are presented. The thermal stability of the magnet must also be studied.

2.3.1. Heaters design

When reaching the nominal conditions, the magnet stays in thermal steady state conditions. However, a quench can be initiated by a local perturbation. As presented in section 1.2.1, three parameters can lead to a quench: reaching the critical current, the critical magnetic field or the critical temperature. The magnetic field depends linearly of the current, and reaching the critical magnetic field or the critical current asks necessarily to increase the current. MACQU is designed to be studied at constant current to simulate a non-detected quench, so the only degree of freedom is to modify the temperature. By increasing the temperature locally, a small part of the magnet could reach the critical temperature and then initiate and propagate a quench. To increase the temperature, flexible heaters can be fixed on the magnet to bring an external heat load to the system. These heaters are small electrical resistances usually wrapped in a Kapton foil to ensure the electrical insulation. With a small current going through, a small heat dissipation by Joule effect is generated by the resistance and then heat the magnet locally. The available heat dissipation can reach hundreds of W/m and they can be used on a large temperature range.

Table 2.7: Principal characterictics of the designed MACQU coil, considered at 10 % margin on the load line.

Characteristic	Symbol	Value & Unit
Peak field	B_{max}	2.640 T
Nominal current	I_{nom}	20086 A
Nominal temperature	T_{nom}	1.8 K
RRR	RRR_{MACQU}	60
Linear heat dissipation	$\dot{q}$	855 W/m
Coil self inductance	L_{MACQU}	0.2 mH
Current sharing temperature	T_{cs}	2.94 K
Critical current density	J_c	7671 A/mm^2
Operating current density	J_{op}	6592 A/mm^2
Stored energy	E_{MACQU}	40 kJ
Conductor external dimension	$h_{conductor} \times e_{conductor}$	15.5 mm × 12.8 mm
Coil external dimension	$L \times w$	1.19 m × 0.29 m
Void fraction	v_f	30 %
Hydraulic diameter	D_h	0.34 mm
Insulation thickness	e_{G10}	0.5 mm
Nb-Ti section	S_{Nb-Ti}	3.047 mm^2
Cu section	S_{Cu}	183.7 mm^2
He section	S_{He}	8.28 mm^2
Wrapping section	S_{G10}	29.1 mm^2
Strand diameter	$D_{strands}$	0.825 mm
Nb-Ti strand number	N_{Nb-Ti}	12
Cu strand number	N_{Cu}	24
Length of the magnet	L	50 m

The only fluid used for MACQU is superfluid helium inside the conduit as the coil is not immersed in a bath. The helium is inserted from the extremities and fills the rest of the magnet. Therefore, a cold source placed close to the magnet extremities supplies the magnet with superfluid helium. This cold source as an important enthalpy storage compared to the enthalpy storage of the small helium quantity in the CICC and this important difference can impact the quench behavior, particularly slow it down. To neglect as much as possible these side effects, the quench should be initiated as far as possible from the cold sources. In that respect, the heaters are placed in the middle of MACQU, allowing having nearly 25 m of propagation length on each side of the magnet. Moreover, as the quench should propagate symmetrically along each direction, the measured experimental quench propagation speed are doubled, reducing the detection time. Then, the MQE and MPZ computations are done by considering the magnetic field at the middle of the magnet, at X = 25 m. The computations are done between 0 and 22 kA, to verify our ability to study the quench behavior for low and high magnetic field zones of MADMAX (corresponding respectively to low and high current quench behaviors).

As it can be seen in figure 2.14, the maximum MQE (70 J/m) is obtained where the current tends to zero. With several hundreds of W/m, a large range of heaters can be used to initiate a quench in less than a second. However, it is interesting to notice that the MPZ length varies much more and can reach the order of magnitude of the meter at low current. It is clear that having such long heater would ask for several technical adaptations. As the magnetic field

on MADMAX varies between 0.4 T and 10.33 T, the linear heat dissipation can be estimated between 421 W/m and 1174 W/m. To reproduce this linear heat dissipation range, MACQU should be tested at current values between 14800 A with a magnetic field of 1.942 T and the nominal one of 20086 A and 2.64 T. The linear heat dissipation that is produced for such values varies between 412 W/m and 855 W/m. The heaters dimensions should then be higher than the MPZ at 14.8 kA which is 40.3 mm. We will thus use in our application four on catalog heaters (see section 3.2.1) of 50.8 mm each. The length of the heaters is voluntarily over-estimated to have margin on the quench initiation, but also to be able to study the quench behavior on a larger current range.

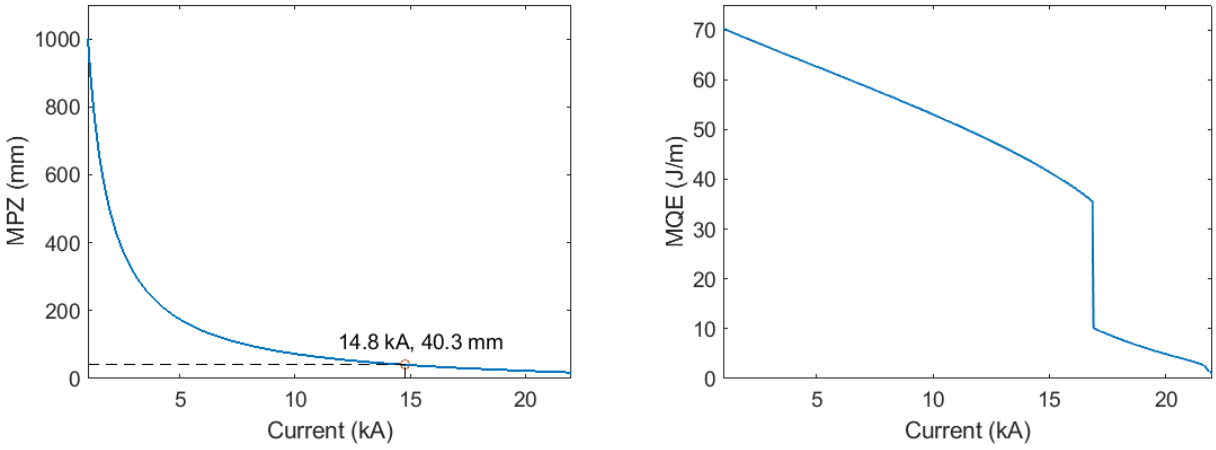

(a) MPZ evolution.

(b) MQE evolution.

Figure 2.14: Evolution of the MPZ and MQE as a function of the current in the conductor. The results are obtained with equation 1.6 and 1.5.

2.3.2. Protection design

Once the quench is initiated, it is possible to compute the temperature increase, thanks to equation 1.19 presented in section 1.2.4. The goal of this computation is to estimate the time during which the quench can propagate at nominal conditions (20086 A and 2.64 T), with no need of fast discharge, while the hot-spot temperature stays below 100 K. In this calculation, as estimated further in section 3.4.3 and explained in equation 1.19, we consider a time constant of the fast discharge being $\tau = \frac{L_{MACQU}}{R_{discharge}} = 0.031$ s, the ratio of the inductance of the coil L_{MACQU} and the discharge resistance $R_{discharge}$.

In nominal conditions, the center of the magnet needs approximately 5.0 s to reach the 100 K hot-spot criterion, as it can be seen in figure 2.15 in the following page. Compared to the 1 s usual detection criterion, having the possibility to let the quench propagate during 5 s leaves a lot of margin on quench detection. The different phenomenon happening during the propagation can also be analyzed during this delay. However, the detection can only be ensured with a fast enough quench propagation speed.

2.3.3. Relevance to MADMAX quench behavior

The quench propagation speed is the last parameter to verify the relevance to study MACQU quench behavior for the MADMAX magnet. As presented in section 1.2.3, two analytical methods are used to estimate the quench propagation speed: Shajii and Freidberg's universal scaling laws and the introduced quench speed formulas, the "analytic" one and the "infinite exchange"

one. These two methods predicted an order of magnitude of difference for MADMAX.

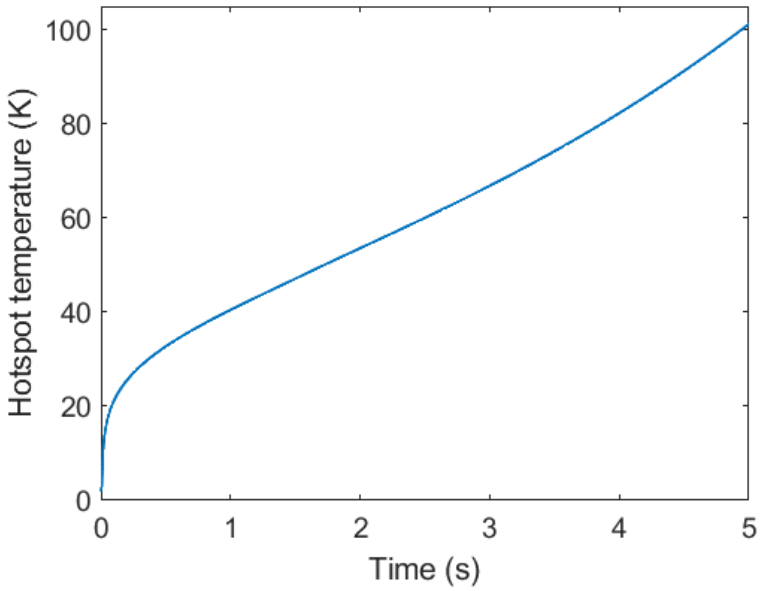

Figure 2.15: Hot-spot computation result, representing the time evolution of the temperature at the center of the magnet at constant current.

2.3.3.1. Shajii and Freidberg's universal scaling laws

Based on Shajii and Freidberg's universal scaling laws [43], defined in section 1.2.3.4, MADMAX was estimated to be in two possible quench regimes, depending on the initial quenched length L_q. With an initial quenched length shorter than 0.3 m, MADMAX should be in the "short coil - low pressure rise" regime. Higher than 0.3 m, the regime should be "short coil - high pressure rise" regime.

Now that MACQU is fully designed, the same computations can be done to estimate and compare its quench behavior with MADMAX. By considering the same initial quenched length variation, from 1 mm to 0.5 m, the different possible regimes for MACQU have been added to figure 1.8, and presented in figure 2.16.

MACQU follows the same evolution than MADMAX, going from "short coil low pressure rise" regime to "short coil high pressure rise" regime, with the increase of the initial quenched length. The initial temperature is 1.8 K and the initial pressure is 1 bar. The unknown friction coefficient, depending on the coil and its manufacturing process, is considered at 0.03, corresponding to the order of magnitude of the measurements done on MACQU and detailed in [61]. Between the different regimes, the quench propagation speed varies from 6.3 mm/s to 1.18 m/s. Even if the values are doubled compared to MADMAX, the order of magnitude is equivalent and the regimes variations are well reproduced.

The initial quenched length could be compared to the length of the heaters that would initiate the quench. By assuming that L_q is equal to 40 mm as presented in section 2.3.1, the quench propagation speed could reach 0.25 m/s.

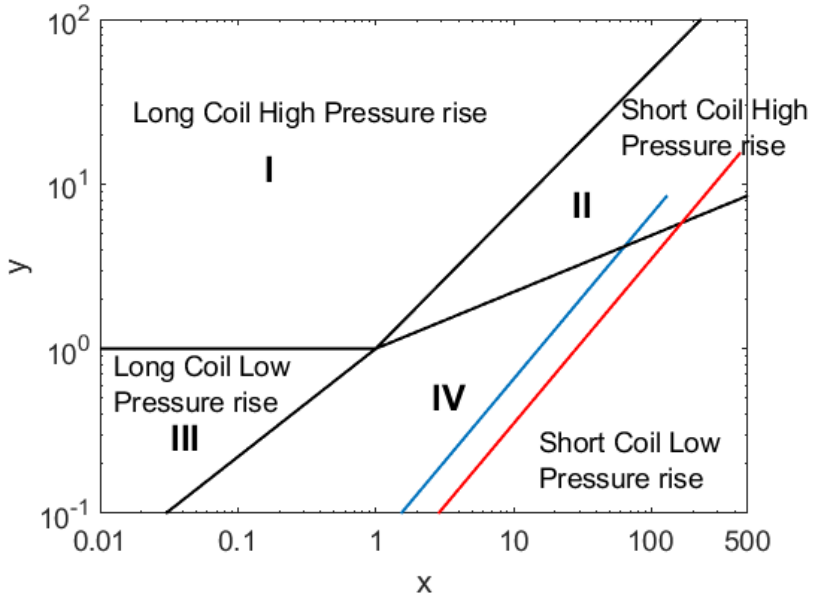

Figure 2.16: Evolution of the MADMAX (in blue) and MACQU (in red) possible regimes, depending on the initial quenched length L_q.

The x and y parameters are the same as detailed in section 1.2.3.4, $x = 1.7(\frac{\rho_0 R T_{max}}{p_0})(\frac{c_0^2 \rho_0}{p_0})\frac{L_q}{L}$ and $y = \frac{L_q J^{4/3}}{L_0 J_0^{4/3}}$ with $L_0 J_0^{4/3} = \frac{2.6}{R}(\frac{p_0^5 d}{f \alpha_0^2 c_0^2 \rho_0^5 T_{max}})^{1/3}$, defined in equation 1.15.

2.3.3.2. "Infinite exchange quench speed" method

With the "analytic" formula 1.12, the quench propagation speed is estimated to be 25.1 m/s at nominal conditions. By considering the "infinite exchange quench speed" formula 1.14, the quench propagation speed falls to 0.47 m/s. This big decrease is due to the large enthalpy of the helium in the superfluid and liquid state. The values obtained for MADMAX were respectively 23.3 m/s and 0.42 m/s, by considering the parameters of table 2.1. As it can be noticed, the order of magnitude of quench propagation speed is well reproduced.

Conclusions

This chapter presented the design of a superconducting coil aimed to reproduce MADMAX quench behavior. Several influent parameters have been presented and the most important ones have been chosen following the design guidelines. The most relevant parameter to compare between both magnets is the linear heat dissipation $\dot{q} = \frac{\eta I^2}{S_{Cu}}$ reaching 1.17 kW/m on MADMAX. In the MACQU case, the linear heat dissipation by Joule effect reaches 855 W/m in nominal conditions, at 20086 A and 2.64 T. It represents 72.8 % of the MADMAX linear heat dissipation and is representative of the high dissipation of the magnet. Moreover, the hydraulic diameter has been well reproduced (0.34 mm for MACQU and 0.33 mm for MADMAX) thanks to the established scaling equation 2.1. Finally, the supporting mandrel has been designed for the study of longitudinal quench propagation only. The G10 epoxy and the stainless steel mandrel, of a total thickness of 5 mm, allows to neglect the transversal quench diffusion. Preliminary quench studies have also been detailed and it has been shown that the quench behavior of

the MACQU coil is representative of MADMAX's one in terms of quench propagation speed. The goal of MACQU is to measure experimentally the quench propagation speed and assess its value. Before going into the analysis of the experimental results, the following chapter describes the MACQU coil quench experimental layout in the JT60-SA Cold Test Facility (CTF).

3 - Description of MACQU coil quench experiment in the JT60-SA Cold Test Facility

Objectives

- Detail the characteristics of the manufactured MACQU coil
- Describe the instrumentation available for studying the normal zone propagation and the physical phenomena during the MACQU coil quench experiments
- Describe the functioning scheme of the MACQU coil in the Cold Test Facility

3.1. Overview of the MACQU coil final manufactured characteristics

The MACQU coil design used for the quench experiments has been presented in the previous chapter. As a reminder, the MACQU coil has a CICC conductor made of a copper profile and filled with superfluid helium. Mostly driven by the dissipative heat losses by Joule effect and the conductor concept, the goal of the design was to specify the desired characteristics of the MACQU coil to reproduce the quench behavior of MADMAX.

In this section, an overview of the manufactured MACQU coil characteristics is given. Some of the driving design parameters have been modified due to the manufacturing process [62]. During this process, the final dimensions of the conductor, the RRR or the magnetic peak field have been slightly modified. By presenting the manufactured conductor and the winding of the solenoid, the modifications from the design are detailed. In a second step, the new performances of the manufactured magnet are presented. It is shown that the modifications from the design will decrease the dissipative heat losses by Joule effect by around 40 % at nominal conditions.

3.1.1. Description of the manufactured conductor

The manufacturing process of the coil has been carried out by two main manufacturers. The conductor manufacturing process has been done in China by *Chang Tong Inc* [63]. The conductor manufacturing process is composed of the insertion and the compaction process. The superconducting cable is inserted in the profile and then compacted to ensure good electrical contact between the cable and the copper profile. The superconducting cable, composed of a multi-stage 3*3*4 cable pattern, is stranded with a twist pitch of 45 mm/85 mm/145 mm. As the impact of the twist pitch is negligible in DC mode, its definition has been left to the manufacturer, in accordance with its extensive experience on the ITER project [64]. The superconducting cable is wrapped in copper tape before insertion, to maintain the cable in its position during the process. After the manufacturing, it has been measured that the copper wrap has a cross-section of 4.1 mm^2. The copper wrap has not been considered in the previous chapter since the deformation and cross-section reduction of the wrap was not estimable.

During the compaction process, the cross-section of the copper profile is reduced. In a first approximation, it was assumed that the copper cross-section of the stabilizer was reduced homothetically. The compaction level was estimated to be around 22 %. However, it has been observed that the compaction level was lower than expected, with C_l = 16.9 %. This lower compaction level makes that the copper cross-section of the stabilizer is higher than the designed one. Figure 3.1 shows a picture of the profile after insertion and compaction and shows that the final external dimensions are 16.0 mm x 13.1 mm, with a conduit diameter of 6.3 mm.

The void fraction has also been measured to 29.8 % by the manufacturer, in good agreement with the designed value. The total copper cross-section is thus estimated to 198.7 mm^2, by considering the copper inside the superconducting and copper strands (16.2 mm^2), the copper stabilizer (178.4 mm^2) and the copper wrap (4.1 mm^2). The copper cross-section was then estimated 8 % smaller than it was manufactured.

In addition, the RRR of the copper profile bought on catalog has been measured to 125 after compaction. The RRR was designed to be around 60. The increase of the RRR from 60 to 125, decreases the copper resistivity by a factor 1.5 from 3.9 $\times$ 10^{-10} Ω m to 2.6 $\times$ 10^{-10} Ω m. The cross-section and the RRR increase will thus decrease the linear heat dissipation by Joule effect $\dot{q} = \dfrac{\eta I^2}{S_{Cu}}$ by 38 %.

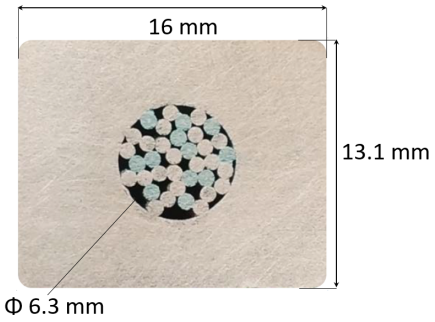

Figure 3.1: Profile of the MACQU coil, after insertion and compaction process. The Nb-Ti strands are in blue, where the copper strands appears in grey. The void is filled with superfluid helium. The copper wrap can not be differentiated from the stabilizer in this picture.

3.1.2. Description of the manufactured solenoid

Once the conductor is manufactured, the coil has to be wound on the supporting mandrel and assembled on its supporting structure. This second manufacturing phase was done in Germany by *Noell Bilfinger* [65] that worked on various recent project as Edipo [66] and W7X [67].

The geometrical parameters of the solenoid are reminded in table 3.1, with the parameters of the manufactured solenoid. The internal radius of the coil was set at 130 mm. The inter-turn distance was designed at 5 mm, composed of two times 0.5 mm thick epoxy tape and 4 mm thick stainless steel mandrel. However, tolerances had to be considered to ease the manufacturing process, making the longitudinal distance between two consecutive conductor increased to 21.8 mm. This helix step increase reduces the peak field of the coil by 3 mT.

Table 3.1: Geometrical parameters of the designed MACQU solenoid, with the accepted dimension range. All lengths are written in mm.

e_{G10}	0.5	0.45 - 0.5
e_{SS}	4	4.0 - 4.15
i_d	5	5.05 - 5.55
r	130	130 - 130.1
$h_{conductor}$	15.5	16.0 - 16.1
$e_{conductor}$	12.8	13.1 - 13.2
h_{turn}	20.5	21.5 - 22.1

To connect the coil to the CTF, the extremities of the conductor have been lengthened, as it can be seen in figure 3.2. The added lengths are called arms and are respectively 1.89 m long for the longest side and 0.62 m for the shortest. The arms add approximately 2.5 m to the total length of the magnet. The coil was finally measured to be 52.9 m long. However, the addition of the arms also slightly modifies the magnetic field map and the inductance of the coil and thus the performances of the magnet.

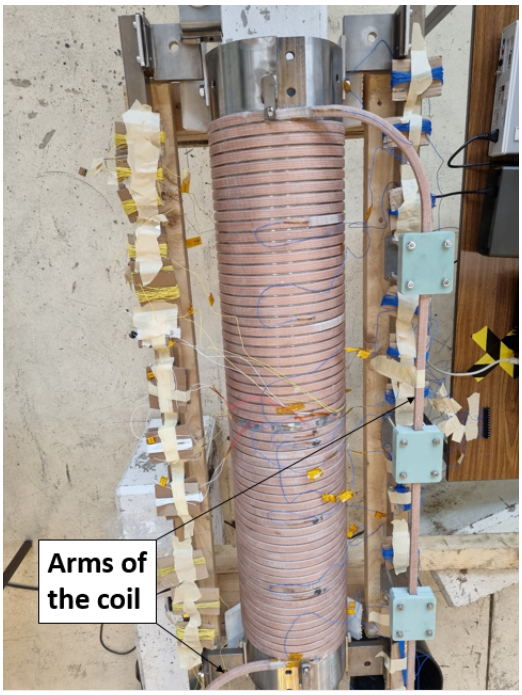

Figure 3.2: Picture of the manufactured MACQU coil, wound on a stainless steel mandrel. The arms can be seen as well as the instrumentation cables.

3.1.3. Performances of the MACQU coil

Inductance measurements have been carried out after the coil manufacturing and indicated that the inductance of the coil was 0.193 mH. The measured value was in good agreement with the estimated value considered without the arms. It allowed us to obtain a more precise value of the stored energy being 38.6 kJ.

In addition, the extension of the solenoid by the arms modifies the magnetic field map which is detailed in chapter 5. Indeed, the addition of the curvature at the exits of the solenoid adds a small local self-field. This region was already close to the peak field at the center of the coil. Therefore, the contribution of the added self-field is enough to move the peak field at the extremities. The magnetic field is increased to 2.674 T and 2.643 T respectively to the left side and right side of the magnet. The 10 % margin on the load line criterion must be estimated at the peak field position and thus has to be recalculated with the new peak field. The new magnetic peak field of 2.674 T leads to a new nominal current estimated at 20005 A, compared to the previous 20086 A. With this new current value, at the middle of the magnet where the quench is initiated, the load line margin becomes 11.1 %.

By combining the decrease of the nominal current and magnetic field to the increase of the copper cross-section and RRR, all of this provides the final value of the MACQU Joule heat dissipation of $\dot{q}_{MACQU} = 517$ W/m. This value must be compared to the minimal linear heat dissipation on MADMAX which is worth 421 W/m. Then, to study MADMAX-representative quenches, the minimal value of linear heat dissipation must be reproduced on MACQU and

it is reached for operating conditions at 18.5 kA for 2.432 T, representing a 17 % margin on the load line. However, the maximum linear heat dissipation of 1.17 kW/m is not possible to reproduce. The linear heat dissipation of MACQU represents thus 44.6 % of the MADMAX one at nominal conditions. For more details, the main characteristics of the MACQU coil have been summarized in table 3.2 and compared to the designed ones. These final values are the reference ones used for the study of the quench behavior in chapter 4 and chapter 5.

Table 3.2: Principal characterictics of the MACQU coil, considered at 10 % margin on the load line.

Characteristic	Symbol	Manufactured value	Designed value
Nominal current	I_{nom}	20005 A	20086 A
Peak field	B_{max}	2.674 T	2.640 T
Nominal temperature	T_{nom}	1.8 K	1.8 K
RRR	RRR_{MACQU}	125	60
Linear heat dissipation	$\dot{q}$	517 W/m	855 W/m
Measured coil self inductance	L_{MACQU}	0.193 mH	0.2 mH
Current sharing temperature	T_{cs}	2.94 K	2.94 K
Critical current density	J_c	7642 A/mm^2	7671 A/mm^2
Operating current density	J_{op}	6565 A/mm^2	6592 A/mm^2
Stored energy	E_{MACQU}	38.6 kJ	40 kJ
Conductor external dimension	$h_{conductor} \times e_{conductor}$	15.5 mm × 12.8 mm	16.0 mm × 13.1 mm
Coil external dimension	$L \times w$	1.22 m × 0.29 m	1.19 m × 0.29 m
Void fraction	v_f	29.8 %	30 %
Hydraulic diameter	D_h	0.34 mm	0.34 mm
Insulation thickness	e_{G10}	0.5 mm	0.5 mm
Nb-Ti section	S_{Nb-Ti}	3.047 mm^2	3.047 mm^2
Cu section	S_{Cu}	198.7 mm^2	183.7 mm^2
He section	S_{He}	8.28 mm^2	8.28 mm^2
Wrapping section	S_{G10}	29.1 mm^2	29.1 mm^2
Strand diameter	$D_{strands}$	0.825 mm	0.825 mm
Nb-Ti strand number	N_{Nb-Ti}	12	12
Cu strand number	N_{Cu}	24	24
Length of the magnet	L	52.9 m	50 m

3.2. Instrumentation of the MACQU coil

In order to carry out the quench behavior studies, the magnet has been equipped with a set of electric and cryogenic measuring instrumentation. MACQU is equipped with heaters, voltage taps, Superconducting Quench Detectors (SQD) and temperature sensors. This instrumentation allows having a large range of physical measurements for the quench analysis. The following section is dedicated to the presentation of the whole instrumentation, starting from the quench heaters.

3.2.1. Heaters for quench initiation

As detailed in section 2.3.1, heaters are used to initiate the quench, by increasing locally the temperature up to the quench temperature. Several heaters from previous projects were already available at CEA. The heaters chosen and used on MACQU are four HAP6945 heaters,

from *MINCO* [68]. These heaters are 50.8 mm long and 12.7 mm width. In terms of width, the heaters fit perfectly on the conductor and aligning four of them represents a 203.2 mm long deposition length. The heaters are installed at the center of the magnet as presented in figure 3.3.

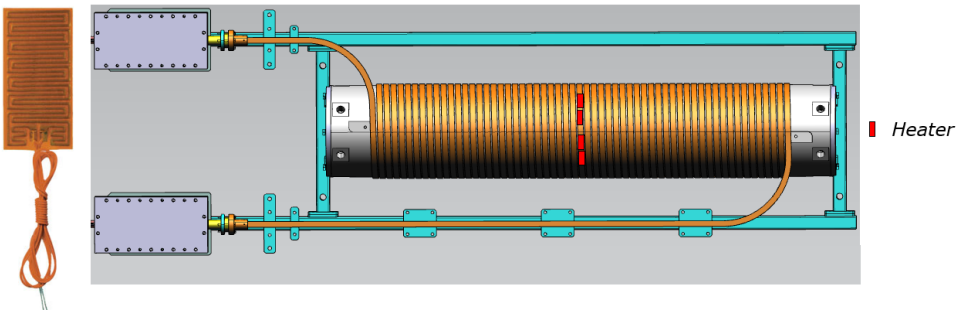

Figure 3.3: Picture of the heaters on the left and position of the heaters at the center of the MACQU magnet on the right.

The heaters are glued directly on the bare copper of the stabilizer with Black Stycast conducting glue [69] and below the insulation of the magnet, in order to have an efficient heat deposition. It will be considered that the Stycast does not affect the heat deposition on the coil. These heaters are designed by the manufacturer to handle 28 V maximum, with a resistance of around 40 Ω each. In terms of control, the heaters are managed by a power supply of maximum 150 A and 40 V. The heaters are connected in parallel to not be limited in terms of voltage. By connecting them in series, and the maximum voltage being 28 V, the maximum current that could be used would be 0.17 A. It would represent a maximum deposition power of only 50 W/m. In parallel, with a resistance measured to 9.7 Ω, the maximum deposition power is around 400 W/m. The characteristics of the heaters can be found in table 3.3.

Table 3.3: Characteristics of the heaters.

	HAP6945 heaters
Length (mm)	50.8
Width (mm)	12.7
Measured resistance (Ω)	9.7
Maximum voltage (V)	28
Maximum power deposition (W/m)	398

Due to the increase of the copper cross-section, the MPZ has been slightly increased, as it is mostly a heat conduction phenomenon. At the opposite, the MQE is driven by the heat capacity of the superfluid helium at cryogenic temperature. The copper cross-section variation is negligible in increasing the total heat capacity of the conductor and the RRR has no impact on the heat capacity. Therefore, the MQE computation is not impacted by the modifications of the coil during the manufacturing process. Figure 3.4 shows the actualized result of the MPZ computation for the heater design.

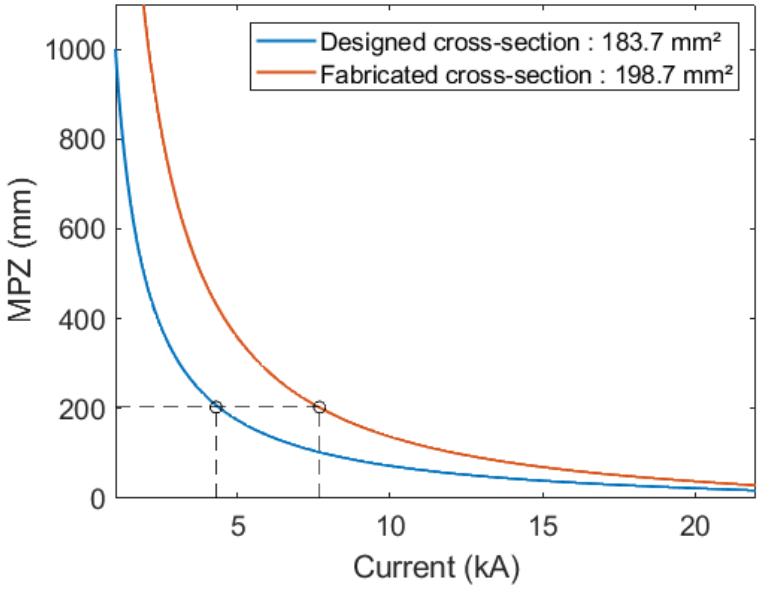

Figure 3.4: Comparison between the designed and the actualized evolution of the MPZ in function of the current.

By considering the MQE computations, the deposition power of the heaters is largely sufficient to initiate the quench at any current compared to the needed maximum 70 W/m. However, at constant MPZ, due to the cross-section increase, the minimum current for which it is possible to quench is increased from 4.3 kA to 7.7 kA. As the current range study of MACQU is above 15 kA, using four HAP6945 heaters, with a length of 203 mm, is over-estimated. However, the margin taken on the heaters length is used to study quenches with lower Joule heat dissipation than on MADMAX, to understand the quench behavior of such a copper CICC on a large Joule heat dissipation range.

3.2.2. Voltage measurement

3.2.2.1. Voltage measurement on the MACQU coil

The goal of MACQU is to study a MADMAX-representative quench behavior at constant current. During the quench propagation, a resistive voltage appears and grows in the transited zone. The voltage variation must be measured to study the normal length propagation. The resistive voltage can be related to the electrical resistance thanks to the Ohm's law:

$$U(t)_{MACQU} = U_{quench} = R(t)_{quench} I = \frac{\eta(t) L_q}{S_{Cond}} I \tag{3.1}$$

with U_{MACQU} being the measured voltage, equal to the voltage of the quenched part of the magnet U_{quench}, R the normal resistance, I the current, η the electrical resistivity, L_q the quenched length, S_{Cond} the cross-section of the conductor and the time t.

This voltage variation is detected and followed thanks to voltage taps put all along the coil. The voltage taps are made of a silver wire spot and a tungstene electrode spot welded with electrical impulse welding on the bare conductor. They are finally maintained with some Stycast [70]. 11 voltage taps are dispatched in total along the solenoid, evenly distributed. Two of the 11 voltage taps are placed on each side of the heaters after one solenoid turn, to refine the center zone in order to have a better measurement precision near the quench initiation location. Moreover, 6 voltage taps are added for the busbars, making the connection between

the magnet and the CTF (see section 3.4.1). The position of the voltage taps and the heaters is given in figure 3.5.

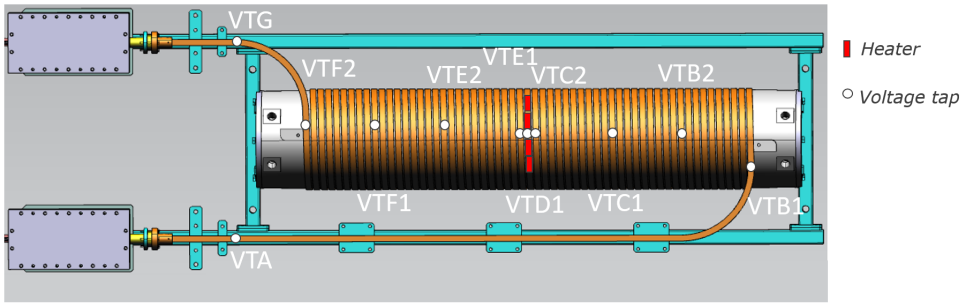

Figure 3.5: Position of the voltage taps and the heaters dispatched all along the MACQU magnet.

MACQU has two different types of voltage measurements, one for data acquisition and physical analysis and the other for quench protection. Both schemes are presented in the following.

3.2.2.2. MSS and protection scheme

If a quench occurs, the magnet is protected thanks to the protection scheme integrated in the Magnet Safety System (MSS) which can be seen in figure 3.6. The MSS allows protecting the coil by opening the circuit and discharging the magnetic stored energy on a dump resistor during a quench. The MSS ensures the detection by comparing the measured voltage differential to the time and voltage threshold. The principle of the quench detection can be written as in equation 3.2.

$$\begin{aligned} U_1 &= R_1 I + L_1 \frac{dI}{dt} \\ U_2 &= R_2 I + L_2 \frac{dI}{dt} \\ DUP1 &= U_1 - \alpha U_2 = (R_1 - \alpha R_2) I \end{aligned} \tag{3.2}$$

where U_1 and U_2 are the resistive voltage measurements on the coil, corresponding respectively to the right arm and L1 and L2 and to L3 and L4 .

Even if MACQU is studied at a constant current, and that inductive voltages are negligible compared to resistive voltages, the coefficient α is applied so that only the resistive voltage part $(R_1 - \alpha R_2)I$ can be detected by DUP1. For instance, when any of the two length is quenched, DUP1 measures the resistive voltage increase and triggers the Fast Discharge if the resistive voltage is higher than the detection threshold. This detection method is used for the other DUPs to protect the magnet against a quench. Each electrical section of the coil is thus protected, including the different parts of the magnet, the terminals and the busbars.

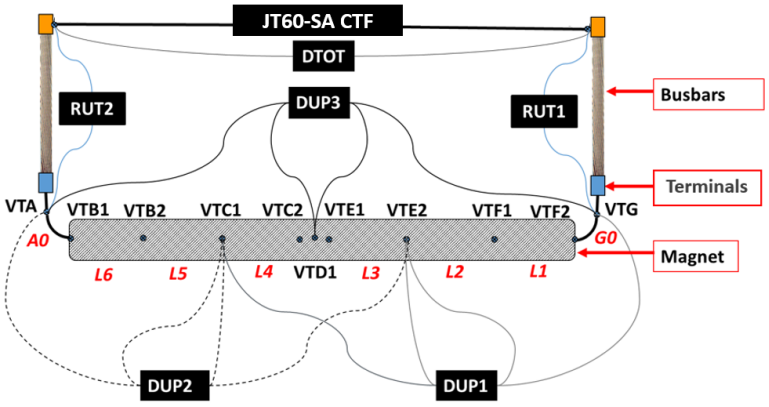

Figure 3.6: Protection scheme of the coil. The different signals, by reaching the 100 mV threshold during at least 100 ms, can trigger the opening of the breakers to discharge the current.

Finally, table 3.4 details the voltage range measurement of the different signals, with the minimum voltage threshold, associated respectively to the time detection threshold. Note that the detection time threshold for the DUP and DTOT is easily editable, to let the quench propagate in the magnet during an editable time.

Table 3.4: Characteristics of the protection scheme.

	Measurement range (+/- V)	Voltage threshold (mV)	Detection treshold range (ms)
DUP1	10	50 to 100	100 to 4000
DUP2	10	50 to 100	100 to 4000
DUP3	10	50 to 100	100 to 4000
DTOT	1	50 to 100	100 to 7000
RUTH	0.1	5	10

3.2.2.3. Acquisition scheme

The acquisition scheme is used for data analysis and allows measurement with a frequency of 10 kHz. The acquisition scheme can be seen in figure 3.7. The magnet is subdivided in different lengths (named as L1 to L6 in the scheme). The multi-channel acquisition scheme takes thus into account every part of the magnet and allows to precisely follow the quench propagation.

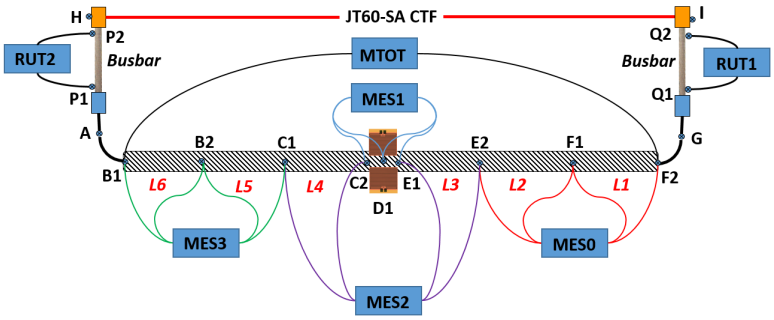

Figure 3.7: Acquisition scheme of the MACQU coil. The different measuring lengths are identified, with the associated signal name.

All the lengths and measurement ranges are summarized in table 3.5. To have a symmetrical distribution of the voltage taps, the L3 and L4 lengths corresponds to 10 turns of the solenoid while the rest are for 9 turns. The missing two turns to complete the 58 turns of the coil are measured with the MES1 signal to have a high precision measurement near the quench initiation location.

Table 3.5: Characteristics of the acquisition lengths.

	Measurement range (+/- V)	Length (m)
L1	5	7.80
L2	5	7.82
L3	5	8.70
L4	5	8.73
L5	5	7.86
L6	5	7.87
MES1	1	2×0.87
MTOT	160	50.5
RUT1, RUT2	5	0.38, 1.64

Equation 3.1 presented earlier correlates directly the measured voltage to the quenched length. By knowing the electrical resistivity and the conductor section, the quenched length can be directly computed. Then, the quench propagation can be followed and the quench propagation speed deduced from the calculation. However, as the electrical resistivity strongly increases with the temperature of the conductor, the temperature variation of the quenched zone must be known accurately. Another method to measure the quench propagation speed could be to observe the consecutive transition of two following zones of the magnet. By identifying the initiation of the quench in each region, it is possible to precisely estimate the mean quench propagation speed in each zone. This method allows to not consider the temperature evolution of the zone, as the length of the different zones is well-known and the initiation time can be precisely measured.

The following section will introduce the SQDs that will provide a third method for the quench propagation following.

3.2.3. Superconducting Quench Detectors (SQD)

The SQD are thin superconducting wires co-wound with the solenoid. The role of the SQD is to accurately measure the transited length of the coil. When the coil transits, the dissipative heat losses by Joule effect will heat the magnet up. When the coil will reach 9 K, being the critical temperature of the SQD, the SQD will also transit. Thanks to a very small RRR measured to 1.12, the high electrical resistance of the SQD can be precisely measured as it is weakly impacted by the temperature or the magnetic field. The quenched length can be calculated with the following equation 3.3:

$$L_q = u_{SQD} \frac{L_{SQD}}{R_{SQD,9K} I_{SQD}} \tag{3.3}$$

with L_q being the normal length, u_{SQD} the measured voltage of the SQD, $R_{SQD,9\ K}$ the electrical resistance of the SQD before the transition at around 9 K and being respectively 212.6 Ω±0.5Ω and 209.0 Ω±0.5Ω for the right and left side and I_{SQD} the current used for the SQD measurement.

The combination of the high resistance with the critical temperature higher than the MACQU one makes the SQD a precise indicator of the transition of a zone of the magnet. The SQD technology have already been proven on other projects such as Atlas [71] or R3B [72].

Figure 3.8 shows the SQD wound around MACQU. The SQD have a bifilar lay-out to minimize any inductive voltage perturbation on the measurement. For redundancy, 3 SQDs have been placed on each side of the magnet.

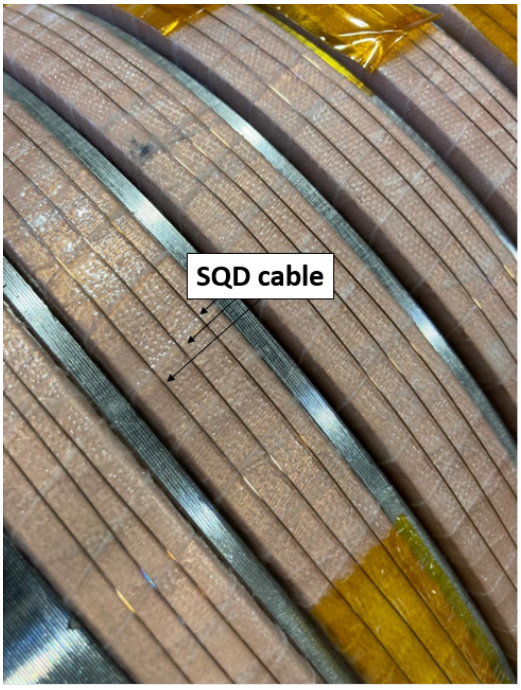

Figure 3.8: Picture of the SQDs wound around MACQU, placed between 2 insulations layers.

To follow the quench propagation along all the magnet, the SQD are not perfectly symmetric compared to the heaters placed at the middle of the magnet. As it can be seen in figure 3.9, one SQD goes under the heaters while the other stops just before the heaters. In that way it is possible to follow the quench propagation since the very beginning, by detecting the voltage variation due to the energy deposition of the heaters on the magnet and on the SQD.

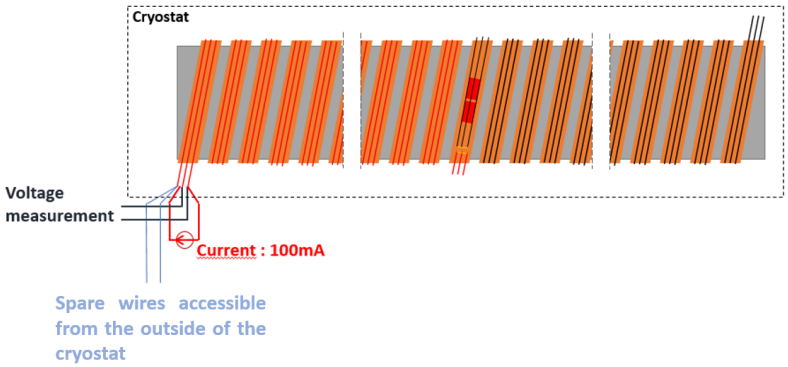

Figure 3.9: Scheme of the SQD on the solenoid, in the cryostat. The SQD are not symmetrical to detect more precisely the quench initiation during the energy deposition of the heaters.

To measure the voltage variation, the SQD must be electrically supplied but also insulated from the coil. Therefore, the SQD is wound around the magnet between 2 insulation layers and

supplied with a small current of 100 mA. The linear resistivity of the SQD is 4.44 Ω/m and thus represents a voltage of around 22.2 V for 50 m long. Due to its low RRR, the temperature increase of the coil increases the measured voltage by around 0.1 V every 10 K. If the whole magnet is at 100 K, which is a very pessimistic hypothesis, the voltage variation due to the temperature increase will then generate an increase of around 4.5 % on the measured voltage. In this conditions, the direct correlation between the normal length of the magnet and the measured voltage seems very accurate with a sensitivity of 5 %.

Finally, it is important to notice that the SQDs has no impact on the quench propagation. Indeed, when transiting due to a quench, the SQD will dissipate heat due to Joule effect. Nevertheless, due to its very low current compared to the one inside the magnet, the dissipated heat by Joule effect is only of $\dot{q}_{SQD} = \frac{\eta_{SQD}}{RRR_{SQD}} I_{SQD}^2 = 40$ mW/m, with η_{SQD} being the SQD resistance at 20 °C. As a reminder, the dissipated loss by Joule effect is 517 W/m on MACQU, making the SQD one totally negligible. Therefore, in the following, it will be considered that the quench propagation speed is only driven by the quench of the coil and not by the SQD one. All the SQDs characteristics are summarized in table 3.6.

Table 3.6: Characteristics of the SQD.

Diameter (mm)	0.3
Resistance @ 20°C (Ω/m)	4.44
Measured RRR	1.12
Material	Nb-Ti with Cu-Ni matrix

The quench following, thanks to the SQD, allows then having a third method for a precise measurement of the quench propagation speed.

3.2.4. Temperature measurement

The temperature measurements are carried out by Cernox® 1050 temperature sensors, of CX-SD [73] type. Figure 3.10 shows the rectangular temperature sensor, being 2 mm large and 1 mm thick. The CX-SD have a wide operating temperature range, from 1.4 K to 500 K. This sensor have a high resolution below 30 K, with an accuracy of ± 5 mK at 5 K, thanks to its high resistance variation at low temperature. Particularly used for flat surfaces, their adherence make them very simple to install on any surface and totally appropriate for our cryogenic environment.

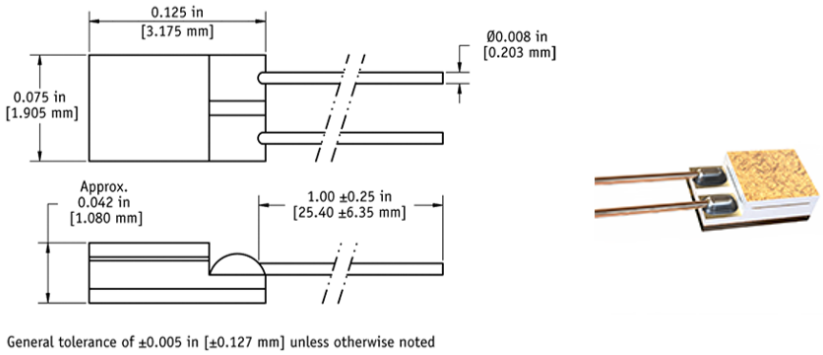

Figure 3.10: Position of the voltage taps, heaters and temperature sensors dispatched all along the MACQU magnet.

The temperature sensors are dispatched all along MACQU and also placed on the arms, as it can be seen in figure 3.11. The arms are thermally decoupled from the mandrel (see section 3.3), compared to the solenoid. It is then interesting to compare the thermal behavior of the arms to the magnet itself and six temperature sensors are used for that. In addition, the sensor TE9810 has been placed at the center of the magnet to measure the hot-spot during a quench. The sensors TE9844 and TE9841, placed respectively after 10 turns and 29 turns on the right side of the magnet, will allow to study the thermal profile of the magnet.

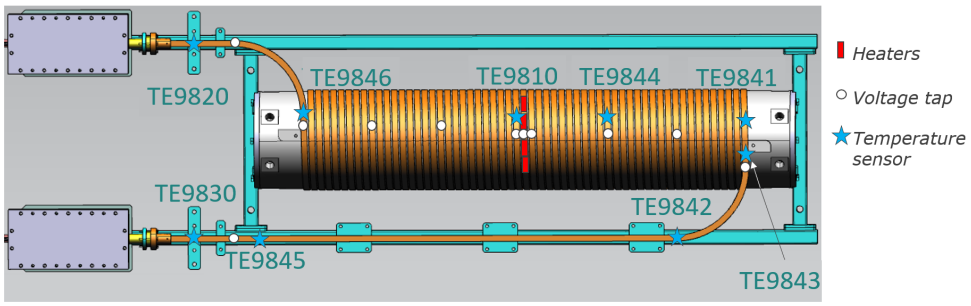

Figure 3.11: Position of the voltage taps, heaters and temperature sensors dispatched all along the MACQU magnet.

To have an accurate measurement, a good thermal contact between the sensor and the magnet is necessary, as well as a minimization of the heat loads arriving on the sensor. The combination of both ensures that the temperature of the sensor and of the magnet are locally the same and allow measuring an accurate temperature. To ensure the accuracy of the measurement, the thermal heat loads arriving on the sensors should be reduced. To do so, Multi Layer Insulation (MLI) foil is used to cover the sensors to act as a radiation shield. In addition, the wires are thermalized at the fluid temperature directly on the magnet and on the helium tubes reducing the conductive heat loads. Figure 3.12 shows two temperature sensors (TE9844 and TE9810) protected by the MLI and an aluminum tape, with the wires thermalized first on the magnet at 1.8 K, and then joined in a bundle on the top of the magnet to ensure a good thermalization. The wires were also thermalized at 5 K and 80 K to reduce the heat loads coming on the 1.8 K bath (not visible in the figure).

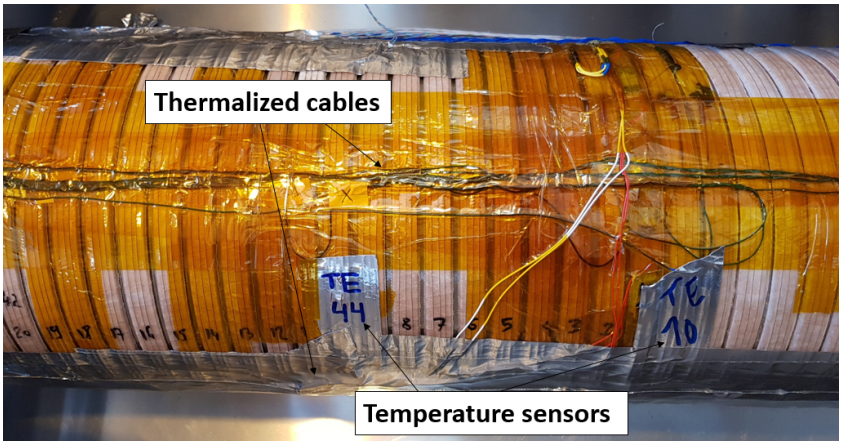

Figure 3.12: Picture of the thermalization of the TE9810 and TE9844 temperature sensors. Most of the cables and the sensors are hidden under the MLI and the aluminum tape.

In addition, to improve the thermal contact between the sensors and the conductor, an

Apiezon grease mixed with copper powder has been used to stick the sensors. However, these CX-SD sensors were installed directly on the insulation of the magnet. Having a thin G10 epoxy tape between the sensor and the conductor induces a diffusion time between the conductor and the sensor, due to the induced thermal gradient inside the insulation. This thermal gradient can then reduce the accuracy of the measurement. To estimate the thermal gradient, a simple model can be developed based on following equation 3.4.

$$\begin{cases} \dfrac{d(C_{cond}(T)T_{cond}(t))}{dt} = -\dfrac{\lambda_{ins}(T)}{e_{cond}}\dfrac{T_{cond}(t) - T_{G10}(t)}{e_{ins}} + \dfrac{\eta_{Cu}(T,B)I^2}{S_{Cu}S_{cond}} \\ \dfrac{d(C_{G10}(T)T_{G10}(t))}{dt} = -\dfrac{\lambda_{ins}(T)}{e_{cond}}\dfrac{T_{G10}(t) - T_{cond}(t)}{e_{ins}} \end{cases} \tag{3.4}$$

with C being the volumetric heat capacity, T the temperature, λ the heat conductivity, e the thickness, η the electrical resistivity, I the current, S the cross-section, and t the time index. The *cond*, *G*10 and *ins* indices stand respectively for conductor, G10 epoxy and insulation.

A pessimistic scenario is considered, where the conductor is at $T_{cs} = 2.98$ K, with nominal conditions of 20005 A and 2.63 T, while the insulation is at 1.8 K. The comparison between the temperature evolution of each component, with the delay that it generates, can be seen in figure 3.13.

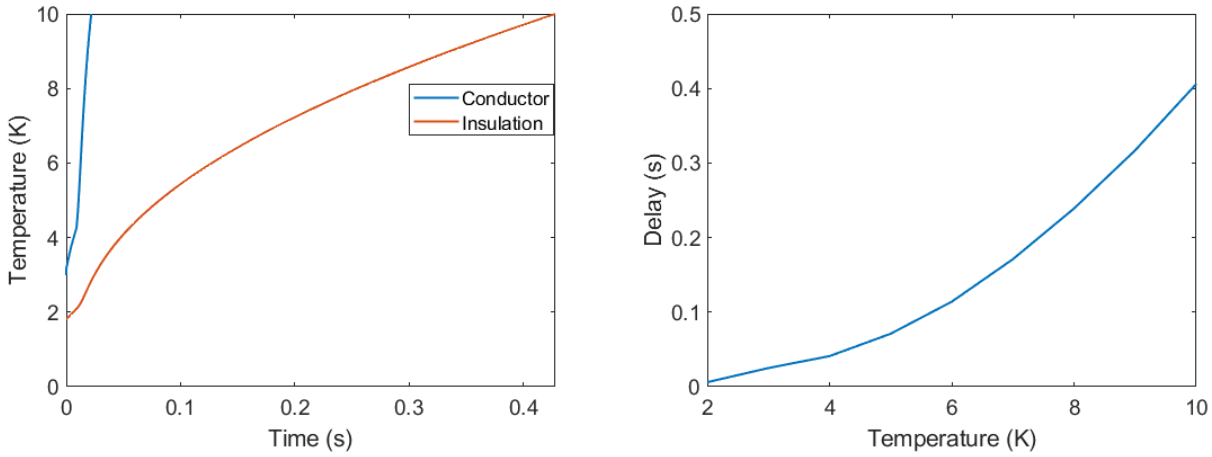

Figure 3.13: Temperature evolution of the conductor and the insulation, and temperature evolution of the delay between the conductor and the insulation.

Note that in the previous computation, the gradient induced by the grease is not considered, as filled with copper powder and being a very thin layer. As it can be seen, the diffusion time is around 25 ms at 3 K but quickly increases to 0.4 s at 10 K, and higher for higher temperature. However, this delay is obtained for a conservative case, and the delay is considered as acceptable. To fit with the voltage measurements in further chapters, the temperature measurements will probably have to be replaced by considering this delay.

3.3. Cooling concept of the MACQU experiment

After having presented the instrumentation of the coil itself, the cooling concept of the MACQU experiment is detailed in this section. In fact, contrary to usual cooling concepts with superfluid helium, MACQU is tested in a vacuum environment and there is no bath directly around the magnet. The only fluid is the helium inside the CICC conduit. Such a small

helium cross-section has a very low thermal extraction power, estimated at 45 mW, according to equation 1.27. The least heat load arriving on the magnet can thus make its temperature increase in an important way. Then, each heat load must be carefully studied and reduced as much as possible. As the magnet is tested in a vacuum environment, the heat loads arriving on the magnet can be radiative from the cryostat or conductive from the supporting structure of the coil. To reduce the radiative heat loads, MLI and a 4 K thermal shield is installed, and its design is detailed in the following section. Moreover, the conductive heat loads is reduced by carefully designing the supporting structure of the experiment. Therefore, a specifically designed cooling concept is used and its design is presented in this section.

3.3.1. Cooling of the MACQU coil

MACQU is cooled down thanks to the superfluid helium inside the CICC conduit. Historically, the JT60-SA CTF had been used for the study of the quench propagation of the 18 JT60-SA superconducting coils [74]. It was designed to supply the coils with supercritical helium for which nominal conditions are 5 K and 15 bar. Therefore, the JT60-SA CTF was upgraded in order to supply MACQU in superfluid helium. The superfluid helium for our application would be at 1.8 K and 1 bar. The existing cryogenic systems was transformed and adapted to produce it.

The method to produce superfluid helium is to use a Claudet bath and a detailed explanation of the functioning has been given in Appendix B. An existing Claudet bath called TH0, used for the ISEULT experiment [32], has been retrieved and adapted for MACQU. However, in usual superfluid helium bath concepts, the Claudet bath can be found in the valve box of the test facility, and supplies directly the magnet. In the JT60-SA case, the valve box is full and TH0 can not be integrated in. It has thus been decided to place TH0 directly inside the cryostat. The helium tank inside the valve box (see section 3.4.2) supplies TH0 with 4.2 K and 1 bar liquid helium. However, placing TH0 inside the cryostat asks for a special sealed valve to control the opening of the lambda plate, as TH0 is in vacuum environment at cryogenic temperature. Therefore, an immersed on-off valve has been added on TH0 to control it even from inside the vacuum of the cryostat, as it can be seen in figure 3.14.

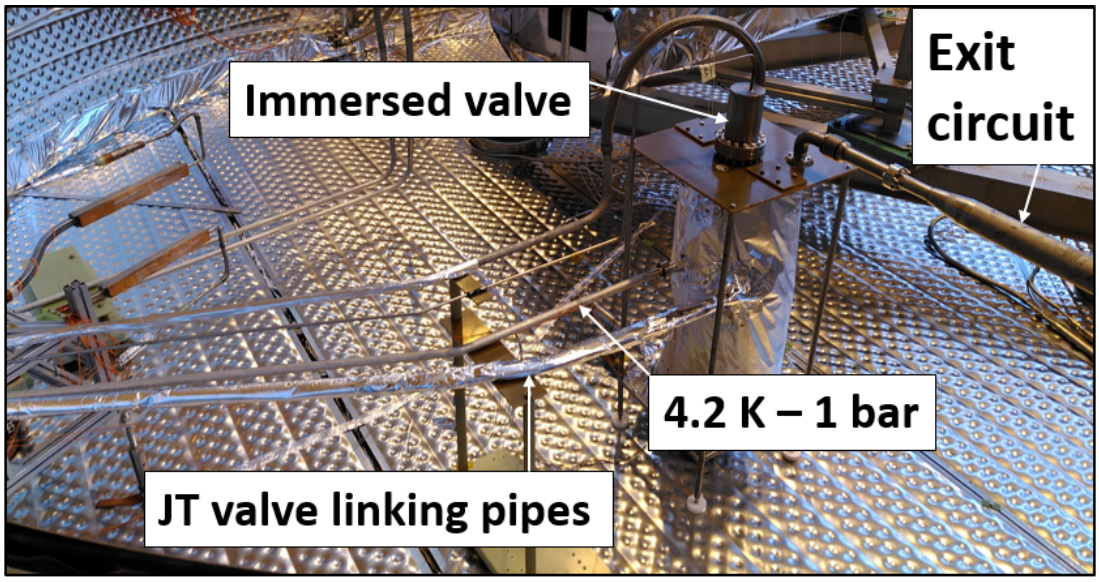

Figure 3.14: Picture of TH0 in the cryostat. All the different circuits are detailed, as the valve controlling circuit, the pipe between the helium tank and TH0, the link with the JT valve and the exit. With the courtesy of Théophile Pontarollo for the picture.

The on-off valve is controlled with a pair of pressurized and vacuum tanks outside of the cryostat, to open and close the tap of the lambda plate. In addition, a pumping group was added to pump the saturated superfluid bath of TH0. The pumping group controls both the helium gas flow and the pressure of the saturated superfluid bath. With a gauge going from 0 to 100 %, it is possible to control the speed of the group, that controls both the pressure and temperature of the saturated bath, and so the temperature of the pressurized superfluid bath.

The Claudet-bath TH0, the saturated superfluid helium pumping group with the associated tubes and the immersed valve with the controlling tanks have been retrieved from previous projects done at CEA, particularly ISEULT [75]. Figure 3.15 shows the immersed valve controlling tanks and the pumping group of the saturated superfluid helium. The tube going from the pumping group to inside the cryostat can also be seen on the top of it.

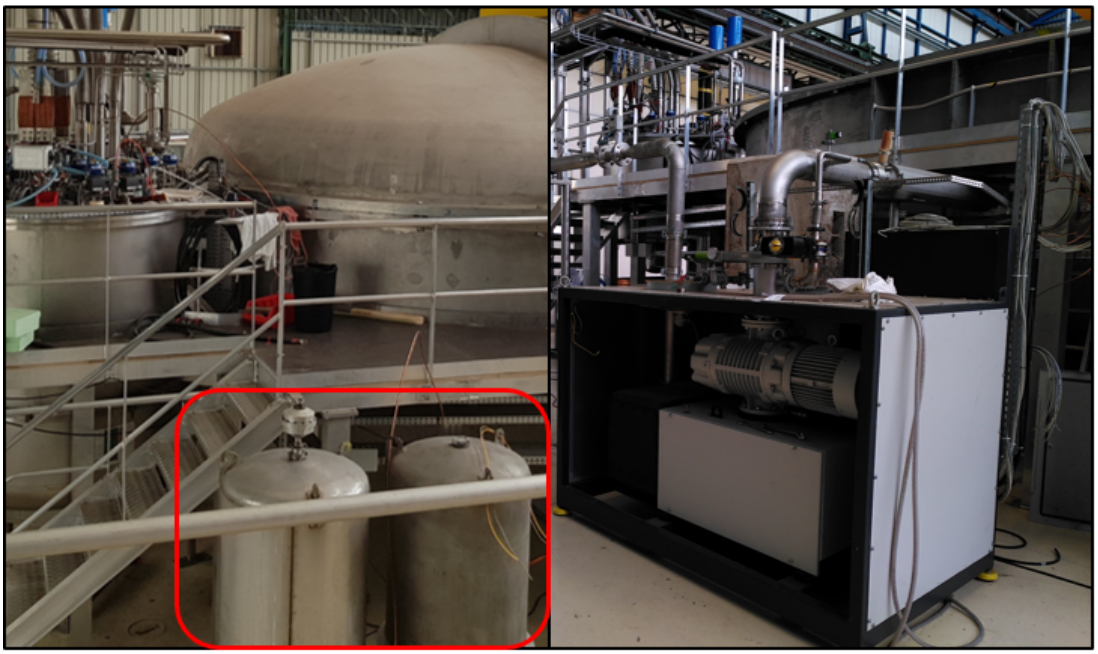

Figure 3.15: Picture of the pressurized and vacuum tank on the left and picture of the pumping group on the right.

3.3.2. Cooling of the supporting mandrel

As explained, the thermal extracting power from the center of the magnet to the exits is only of 45 mW. With such a small extraction power, reaching 1.8 K at the center of the magnet would need around 25 days. To help on the cooling down process, two tubes, welded with the mandrel and also filled with superfluid helium have been added. The internal diameter of the tubes is 38.4 mm, representing a possible extraction power of 10 W for each tube. Figure 3.16 shows the mandrel tubes on the left and right sides which are in dead end. The tubes at the middle were supposed to be filled with supercritical helium to accelerate the cooling down process. It was noticed that below 2 K, the heat load brought by these tubes was too important and counter-productive for the cooling of the coil, as the circulating helium was around 5 K. These tubes were thus finally not used.

Figure 3.16: Picture of the mandrel tubes filled with the superfluid helium, on the left and right sides. The tubes are installed to help the center of the magnet to cool down. With the courtesy of Théophile Pontarollo for the picture.

The superfluid tubes of the mandrel act as thermal exchangers on each side of the magnet. The thermal diffusion time can be estimated to 66 s in the 30 mm thick mandrel, thanks to equation 3.5, obtained from the 1-D heat equation.

$$\frac{\rho C_p}{\Delta t} = \frac{\lambda}{\Delta x^2} \Longleftrightarrow \Delta t = \frac{\rho C_p \Delta x^2}{\lambda} \tag{3.5}$$

with ρ being the density of the material, C_p the specific heat, λ the thermal conductivity and Δt and Δx being respectively the characteristic time and characteristic length.

For slow phenomenon like the cooling-down of the magnet, that takes a few days, the diffusion time is low enough to allow these tubes highly contribute to the cooling down. At the opposite, the diffusion time is important enough to not affect the quench behavior, that should last around 5 s.

In theory, the tubes were supposed to be welded all along the mandrel length. For manufacturing constraints, the welding on such length was not possible. Therefore, to improve the quality of the heat exchange between the tubes and the mandrel, thin aluminum foils were glued with copper powder charged DP 190 epoxy. The RRR of the aluminum foils is around 20000, and more information on the process can be found in [70]. A picture of the thin foils glued on the mandrel can be found in figure 3.17.

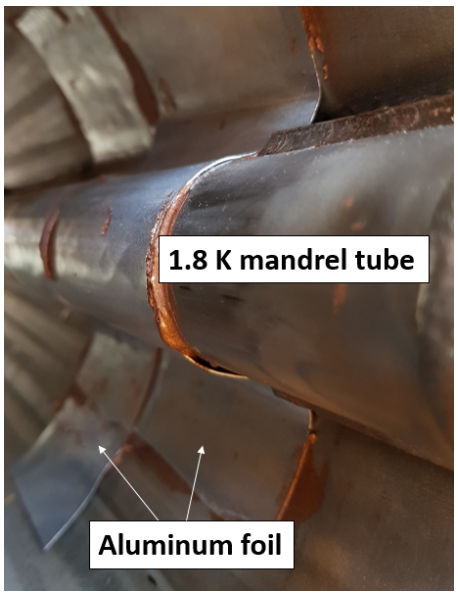

Figure 3.17: Picture of the thin aluminum foils glued inside the mandrel to improve the thermal contact between the tubes and the magnet. With the courtesy of Théophile Pontarollo for the picture.

3.3.3. Cooling of the thermal shield

To follow the strategy of reducing as much as possible the thermal loads, a 5 K thermal shield surrounds MACQU. The shield is a rectangular cuboid, made of 3 mm thick Al-1050 aluminum plates, that allies mechanical properties and a good thermal conductivity. The goal of the thermal shield is to reduce the radiative heat flux arriving on the magnet from the 80 K. By considering the Stefan-Boltzmann law with a form factor of 1, the maximum radiative heat flux φ_R is estimated at $\varphi_R = \epsilon\sigma(T^4_{cryostat} - T^4_{magnet}) \times A_{external} = 2.6$ W, with σ being the Stefan-Boltzman constant, $T_{cryostat}$ is the temperature of the cryostat (80 K), T_{magnet} is the temperature of the magnet (1.8 K) and $A_{external}$ is the external area of the solenoid, being $\pi w \times L = 1.12$ m^2. The radiative heat flux can be decreased by anchoring the thermal shield to a lower temperature than 80 K. The thermal shield has thus been thermalized with the already existing supercritical helium circuit, at around 5 K, with a back and forth circuit. To improve the homogeneity of the temperature of the shield, the thermal contact between the shield and the pipes has been improved with aluminum loaded resin, as shows figure 3.18.

Figure 3.18: Picture of improved thermal contact between the tubes and the shield, all along the shield length.

Moreover, 10 MLI layers have been used to reduce the emissivity of the shield, estimated at 0.1 after the process. Thanks to all the adaptations, the radiative heat flux is estimated to be reduced to around 0.13 mW [61]. Figure 3.19 shows the thermal shield, with the MLI starting to be laid on it.

Figure 3.19: Picture of the thermal shield, at the beginning of the MLI laying. The front face of the shield allows to hydraulically and electrically supply the magnet. At the back, the back and forth cooling tubes can be seen.

3.3.4. Cooling of the supporting structure

Finally, still by having in mind the low thermal budget of the magnet, the supporting structure for the experiment had to be designed. One goal of the structure is to reduce the conductive heat flux reaching the magnet, defined in its most simple form as $\phi_{cond} = -\lambda_{structure} S_{exchange} \frac{\partial T}{\partial x}$, where $\lambda_{structure}$ is the thermal conductivity of the structure and $S_{exchange}$ is the conductive exchange surface. To do so, the thermal length between 300 K and 1.8 K must be maximized. Therefore, three different supporting structures, thermalized at three different temperatures and thermally insulated from each other with 20 mm thick G10 pads, have been designed. The supporting structure is composed of 80x80 mm^2 stainless steel hollow rectangular shape cylinders, with 3 mm thickness, to minimize the heat exchange section. Figure 3.20 shows a CAD draft of the three different structures: the pink one, the dark blue one and the light blue one.

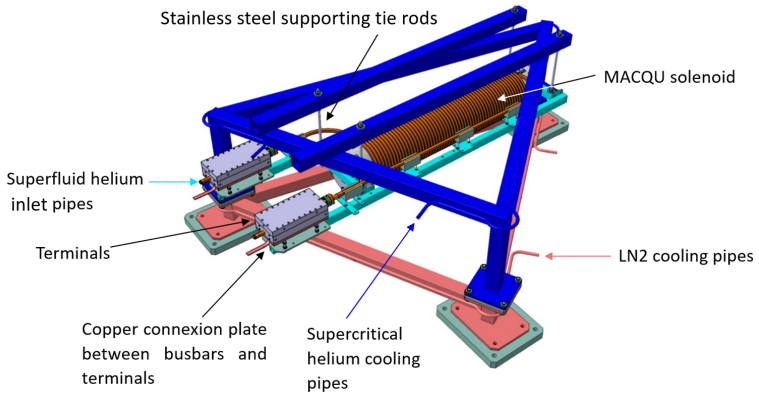

Figure 3.20: CAD draft of MACQU inside its supporting structure, under vacuum. The thermal shield, surrounding the solenoid, is not represented in the figure.

The pink structure lies on the testing frame of the cryostat, insulated from the 300 K vacuum vessel with G10 pads. To reduce the heat loads arriving from the 300 K, the pink structure is thermalized at 80 K thanks to LN2 circulation pipes that are welded on the first stage. The LN2 circuit is also used to cool-down the thermal shield of the cryostat. The distance between the testing frame and the thermalization is 230 mm. The second structure is the dark blue structure, placed on the pink one and insulated from it with G10 pads. This dark blue structure is thermalized at 5 K with forced-flow supercritical helium. The dark blue structure is 600 mm high. From the dark blue structure, four M8 and 50 cm long tie rods, made of stainless steel, hang on MACQU with the light blue structure. Small holes are drilled in the thermal shield as the rods go through it. Finally, the light blue structure supports MACQU by the mandrel, thermalized at 1.8 K. With these different structures, it is estimated that the thermal heat loads arriving on MACQU by heat conduction are around 0.2 mW [61].

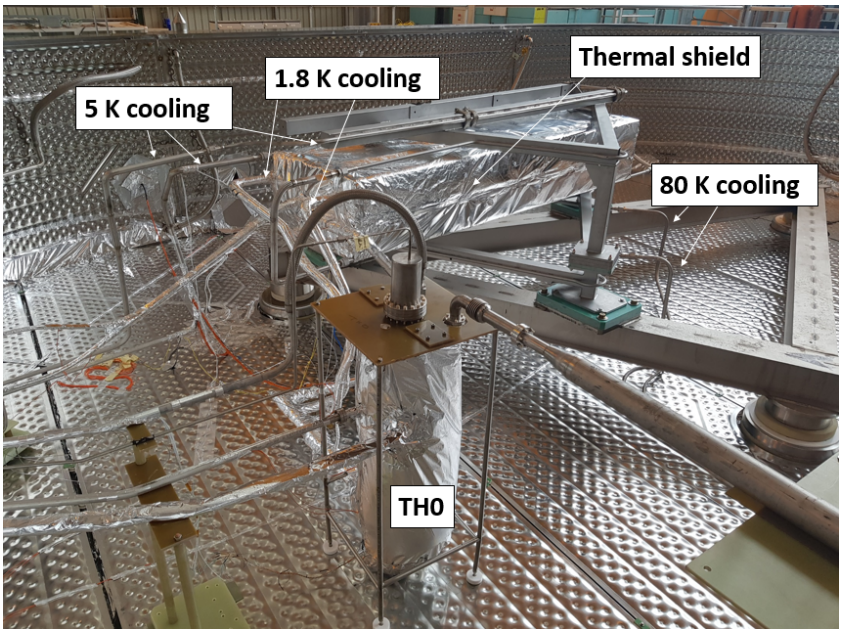

Figure 3.21: Picture of the supporting structure and the thermal shield on the testing frame inside the cryostat. TH0 can be seen in the forefront.

All the cooling circuits are punctually welded on the structure. A highly conductive copper braid or a copper charged glue have been added in the gaps to improve the thermalization. Thanks to all the presented improvement and thermalizations, the temperature on the magnet could have been reduced from 1.95 K to 1.70 K in the best cases between the first commissioning phase and the nominal quench campaign.

3.4. The MACQU coil quench experiment in the JT60-SA Cold Test Facility

After describing the cooling concept of the structure, a more global view of the test facility is presented. To reach the working nominal conditions, the coil must be hydraulically and electrically supplied. The valve box is the key component of the facility that supplies the coil both electrically and hydraulically inside the cryostat. In a first step, the connections between the cryostat and the coil, and the technical solutions to do so are presented. Two main components allow connecting electrically the coil to the facility: the W7X connection boxes and the busbars. Their functioning and design are detailed in this section. In order to

give a more global view of the functioning of the facility, the hydraulic scheme of the facility is also presented. Finally, by detailing the functioning of the 25.7 kA power supply and the fast discharge, handled by the MSS already described higher, a brief description of the electric scheme of the facility will also be done.

3.4.1. Electric supply of the MACQU coil

The MACQU coil has to be electrically connected to the CTF. To do so, two main components have been designed and added to the cryostat, i.e. the W7X connection boxes and the busbars. The W7X boxes are placed at the end of the arms of the coil and allow to decouple the hydraulic and electric circuit of the CICC conductor. Clamped to the boxes on one side, the busbars are clamped on the other side to the current feeders of the CTF. That way, the electrical continuity is ensured and the coil is electrically supplied. The design of both is shown in this section, starting with the W7X boxes.

3.4.1.1. W7X connection boxes

The W7X boxes, also called terminals, are used to decouple the hydraulic and electrical circuits of the coil. Their design is described in [76]. However, their design has been adapted for the MADMAX project. In fact, at the end of the arms, the CICC is inserted in the W7X box. A connector is brazed to ensure the sealing at the interface of the CICC and the box. The boxes are filled with superfluid helium arriving from TH0 and will fill MACQU too. The cable from the CICC is untwisted in 1^{st} stage bundles and indium-brazed in small grooves to the copper sole of the boxes. The current comes through the copper sole into the untwisted cable, as the outer face of the boxes is clamped with the busbars. The decoupling of the electrical and hydraulic circuits is thus done.

To maintain the bundles in their position, a small copper cover has been added to the bundles and welded, as can be seen in figure 3.22. Instead of the added copper cover, with the first design of the boxes, the top of the box was used to press the bundles to maintain them in their position. The pressing piece has been removed to fill the boxes with superfluid helium, in order to increase the performance in terms of critical temperature and the stability of the boxes.

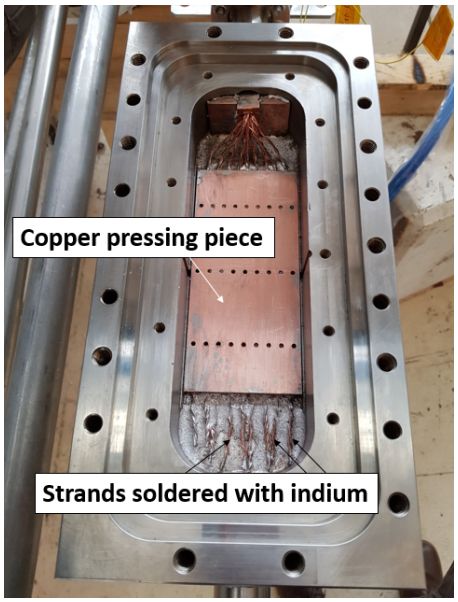

Figure 3.22: Picture of the cable soldered at the bottom of the W7X box and maintained in its position thanks to the small copper piece.

Figure 3.23 shows the location of the boxes. The busbars and the tubes containing the superfluid helium can be clearly seen arriving from different paths to the boxes. Note that the G10 plate that can be seen was removed in the final configuration.

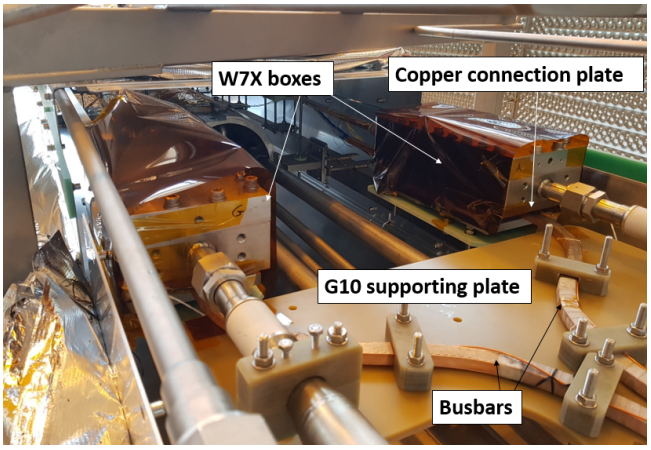

Figure 3.23: Picture of the W7X boxes, covered with a Kapton foil in case of electrical shortcut. The pictures shows the decoupling of the hydraulic and electric circuits.

3.4.1.2. LNCMI busbars

The electrical connection between the boxes and the CTF is ensured by superconducting busbars manufactured with the LNCMI project conductor [29]. This conductor is a Rutherford cable brazed in a copper profile having in the MACQU experiment no active cooling. These busbars are clamped on the coil side to the W7X boxes by a copper plate. On the other side, the busbars are clamped with the terminals of the CTF superconducting feeders, which are CICC cables actively cooled with a supercritical helium 2 g/s forced flow. The busbars are then in a vacuum environment and mechanically maintained by the clamps on each side.

When crossing the copper plate that connects the busbars and the box, as the copper is resistive, a small loss by Joule effect happens locally. The resistance of the boxes has been measured to 6.3 nΩ. At 20000 A, 2.5 W are dissipated per connection box. To ensure good electrical contact on the different clamps, indium filaments have been used. By improving the electrical contact, the local electrical resistivity can be reduced, and then the heat losses generated by Joule effect. Figure 3.24 shows the connection done between the terminals of the feeders and the busbars.

However, several parameters should be taken into account concerning the choice of the busbars. On the CTF side, the busbar is clamped to the terminal of the feeders and thermalized at 5 K. On the coil side, the busbars are connected to the connection boxes that are filled with superfluid helium, thus thermalizing the busbars at the superfluid helium bath temperature. The LNCMI busbars are in a vacuum environment and there is no active cooling. Therefore, to not exceed the thermal budget of the magnet at 1.8 K, the radiative and conductive heat fluxes must be carefully studied and can be found in [61]. There is a competition between the length of the busbars, which would reduce the conductive heat loads arriving on the magnet with the length increase, and the heat exchange surface increase due to the lengthening of the busbars, making the radiative heat loads larger. The thermal budget is calculated at 0.5 W per busbar to stay at 1.8 K in the helium of the connection boxes. A compromise has been found with a length of 2.5 m, limiting the thermal loads to 0.26 W per busbar and matching with our requirements. To reach this value, MLI has been added around the busbars to reduce the radiative heat loads from the 80 K thermal shield of the cryostat.

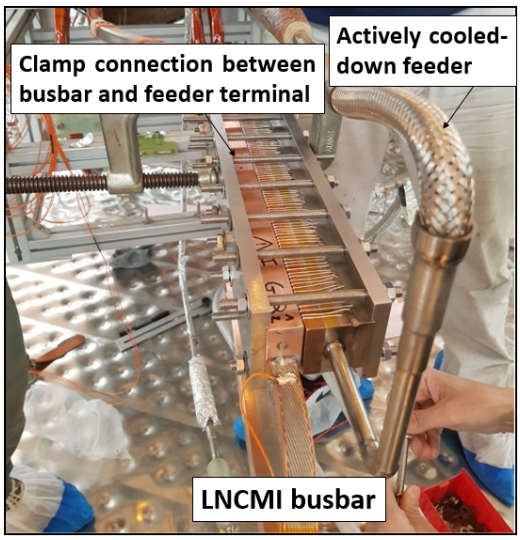

Figure 3.24: Picture of the connection between one busbar to a feeder terminal. The connection is done by clamping and indium filaments are added to improve the electrical contact.

However, the electromagnetic load line margin of the busbars must also be taken into account. Indeed, the electrical margin of the busbar has to be at least as high as the MACQU one, and the copper cross-section important enough to maintain the hot-spot temperature in the case of a quench of the busbars below 100 K. In working conditions, the busbars are estimated to be at around 6 K. The hot-spot temperature is computed at 41 K at 2 T. The hot-spot temperature value is estimated for a detection time of 1 s. Such a detection time is a quite pessimistic case, as the usual detection criterion for the busbars is 100 ms. Figure 3.25 shows the integration of the busbars in the cryostat with the electrical link between the CTF and the coil.

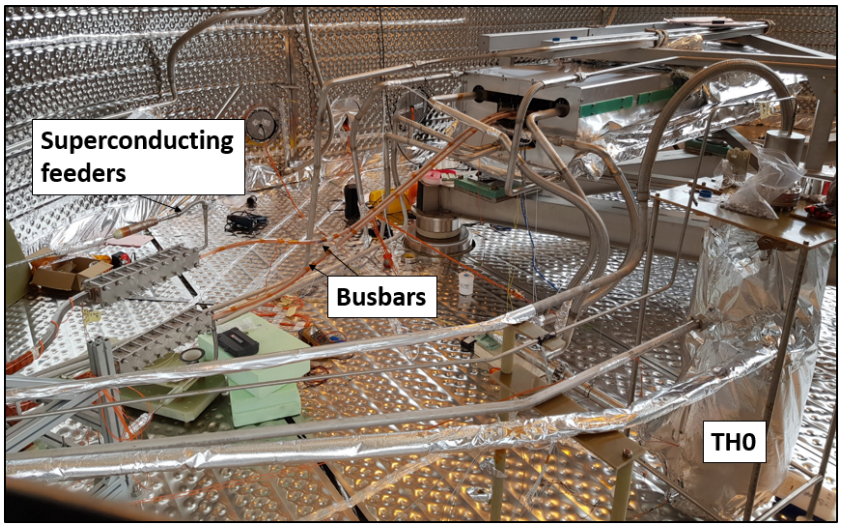

Figure 3.25: Picture of the busbars in the cryostat, connecting MACQU to the CTF. The superconducting feeders can be seen on the left, with the clamping system to attach them to the busbars.

3.4.2. Hydraulic functioning of the CTF

The JT60-SA CTF is equipped with several cryogenic circuits to supply all the components and reach the nominal temperature conditions. The goal of this section is to present simply

the existing different circuits that allow to supply, thermalize and cool down the components inside the cryostat during the experiment. Three main circuits can be identified on the CTF side, the 80 K LN2 circuit, the 5 K supercritical helium forced-flow circuit and the 4.2 K liquid helium circuit coming from the helium tank inside the valve box.

As explained earlier, the cryostat has thermal shields cooled at 80 K by the LN2 circuit and surrounded by MLI. The coil is tested in vacuum conditions to avoid convective exchanges with the 80 K thermal shields. The vacuum system allows to reach 10^{-5} mbar inside the cryostat [77]. In such conditions, the coil can be considered thermally insulated from the thermal shield of the CTF.

During the cooling down process of the coil, the helium refrigerator composed of a compressor, an oil removal system and a cold box, starts cooling the helium from 300 K to around 4.5 K. The refrigerator has a maximal refrigerating power of 500 W at 5 K. The refrigerator is linked to the valve box thanks to a cryoline and supplies the whole system inside the cryostat. From there, the helium can be pressurized at 15 bar in supercritical state at around 5 K or at 1 bar and in liquid state at 4.2 K. Figure 3.26 shows the hydraulic but also the electrical circuits to supply the experiment. In general, the blue lines are for hydraulic circuits only, the orange for electrical circuits only and green for both in a CICC. Finally, the hatched lines are for forced-flow convection (supercritical helium) while the regular ones are for static or laminar flows (superfluid or liquid helium). The 4.2 K and 1 bar circuit, that comes directly from the helium tank inside the valve box, supplies TH0 that creates superfluid helium. The superfluid helium will then fill the mandrel and the magnet through the connection boxes. The supercritical circuit cools the supporting structure and the thermal shield of the coil, but also the superconducting feeders.

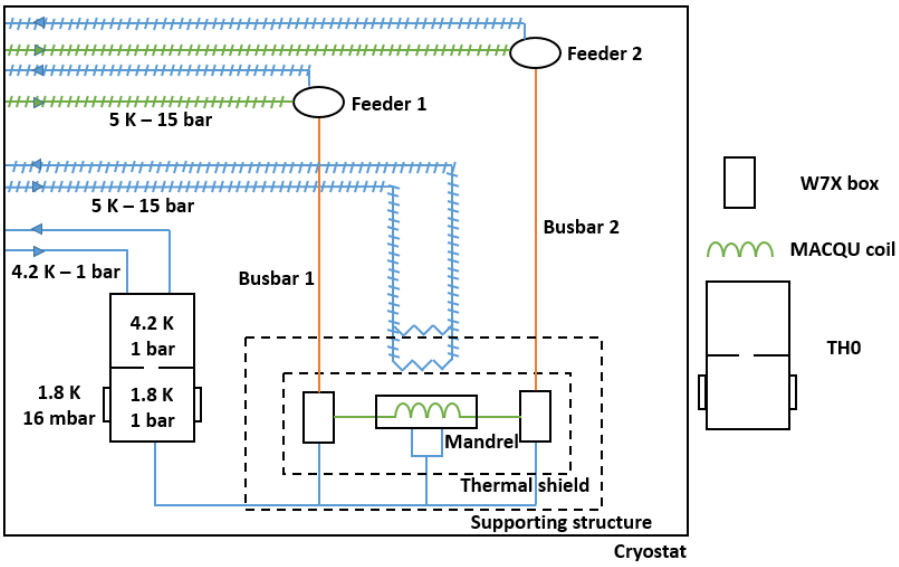

Figure 3.26: Hydraulic and electrical circuit of the experiment, inside the cryostat. The orange lines are only electrical circuits, where blue lines are only hydraulic circuits. The green lines are both, being a CICC. The hatched lines represent a forced-flow convection circuit where the full lines are represented for static or laminar helium flows.

3.4.3. Electric scheme of the CTF

Finally, the electric scheme is briefly presented in this section. The goal of this section is to introduce the functioning of the power supply and the fast discharge. As can be seen in figure 3.27, the power supply feeds the coil through copper busbars and water-cooled cables,

before reaching the cryostat. The DCCT measures accurately the current going through the coil. While the coil is electrically supplied, the MSS measures the resistive voltage of the superconducting coil and compares it to the discharge threshold of 100 mV during at least 100 ms. If the measured resistive voltage reaches the discharge threshold, the MSS opens the main breaker (CP) and cuts the connection to the power supply. The magnetic stored energy is then discharged in the dump resistance of the power supply (RD) which resistance is 6.2 mΩ. The discharge time can be estimated by $\tau_{discharge} = \frac{L_{MACQU}}{RD} = 31$ ms. Compared to several seconds of propagation, a characteristic time discharge of 31 ms is totally negligible. Then, for all the following calculations and analysis of the measurements, the discharge phase will not be studied and is considered instantaneous.

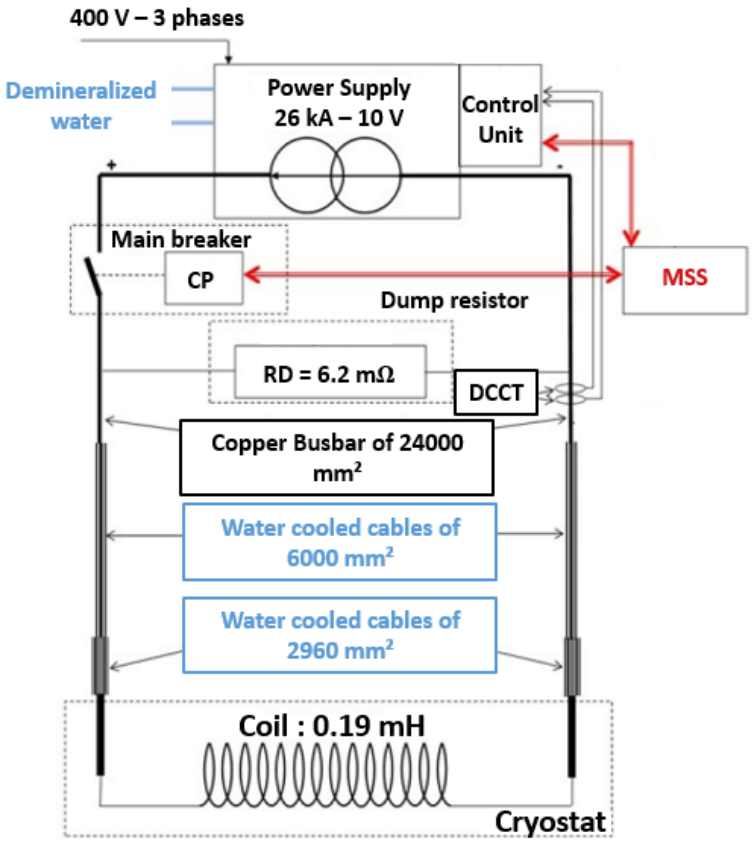

Figure 3.27: Protection scheme of the coil. The different signals, by reaching the 100 mV threshold during at least 100 ms, can open the breakers to discharge the current.

Conclusions

This chapter presented an overview of the MACQU magnet. Due to manufacturing or integration constraints, some changes have been done on MACQU from the initial design. Between the main differences, we can find the final dimensions of the coil or the RRR. The new characteristics of the coil have been summarized in table 3.2. Due to the modifications, the new nominal linear heat dissipation of MACQU is 517 W/m for a nominal current of 20005 A and a 2.674 T peak field. It represents 44.6 % of the MADMAX linear heat dissipation. The instrumentation used on the magnet has also been detailed, by presenting the voltage measurements, the protection and acquisition scheme handled by the MSS, the SQD and the temperature measurements. The instrumentation has been installed and designed to perform an

accurate measurement. All these instruments will allow to investigate the quench propagation, in order to analyze the experimental data in the next chapter. In a second phase, the cooling concept of the coil and of its supporting frame has been presented. To be able to cool-down MACQU to the nominal conditions, the thermal heat loads arriving on the magnet have been carefully studied and the design of the supporting frame derives directly from it. Finally, a more global view of the CTF has been given. The design of the connection boxes and of the busbars has been presented to ensure the electrical connection between the coil and the CTF. The hydraulic diagram was detailed to present the hydraulic circuits and supplying of the coil but also the mandrel, the thermal shield, TH0 and the feeders. The electric scheme finally allowed to detail the functioning of the power supply and the fast discharge controlled by the MSS. The functioning of the power supply showed that the fast discharge time was negligible and that should not be considered for the next studies. The next chapter is dedicated to the experimental analysis of the quench tests of the MACQU coil. The experimental quench protocol is detailed in a first part and the instrumentation presented in this section is used to analyze the quench propagation and determine the different quench dynamics.

4 - Analysis of the experimental results of the MACQU coil quench tests

Objectives

- Explain the experimental protocol of performing a quench test
- Highlight the different dynamics during the quench propagation in the MACQU coil
- Study the impact of different experimental parameters on the quench behavior

4.1. Experimental protocol of the quench study for the MACQU coil

After going through the description of the characteristics of the coil, the description of the instrumentation and the electrical and cryogenic functioning of the whole MACQU experiment, this chapter is dedicated to the analysis of the experimental results obtained during the quench tests of the MACQU coil. The main steps of the quench protocol are presented in this section. An example of a typical quench is studied, detailing step-by-step each phase of the quench protocol. For this example, the quench study is carried out at 15 kA. The first phase is the current ramp-up, that can be divided into two slopes depending on the desired current for the quench study. Once the current has reached the desired nominal value, thermal steady-state must be obtained before performing heat depositions to initiate the quench. These heat depositions are performed thanks to the heaters and the goal is to progressively increase the deposited energy until initiating the quench. Once the quench is initiated, the first objective is to benchmark the safety of the detection system design, by verifying the system ability to detect the quench. The other objective is to study the quench behavior, by letting the quench propagate during a fixed time. Finally, the fast discharge is triggered and will decrease the current with a time constant of 31 ms. More details are explained step by step in the following sections.

4.1.1. Current ramp-up and thermal steady-state

The first step of the experimental protocol is to reach the nominal current. As it can be seen in figure 4.1, the current ramp-up has been divided into two different phases: a first phase at 20 A/s until 14 kA, and a second phase at 6 A/s until 15 kA. The goal of limiting the current ramp-up is to limit the losses generated by the current variation, proportional to $\propto B\frac{dB}{dt}$. Despite this, the temperature increases by 0.1 K on the Claudet bath and on the magnet.

After the current ramp-up, one has to wait for the thermal steady-state, with the current at constant value. The heat dissipated during the ramp-up must be thus extracted and the temperature sensors thermally stabilize after a small increase. The center of the magnet lasts the longest to recover, as it is the furthest from the cold source, with the lowest extracting capacity. When a quench is initiated, the TE9810 temperature sensor is the reference temperature to estimate the time to reach the steady-state after the heat dissipation.

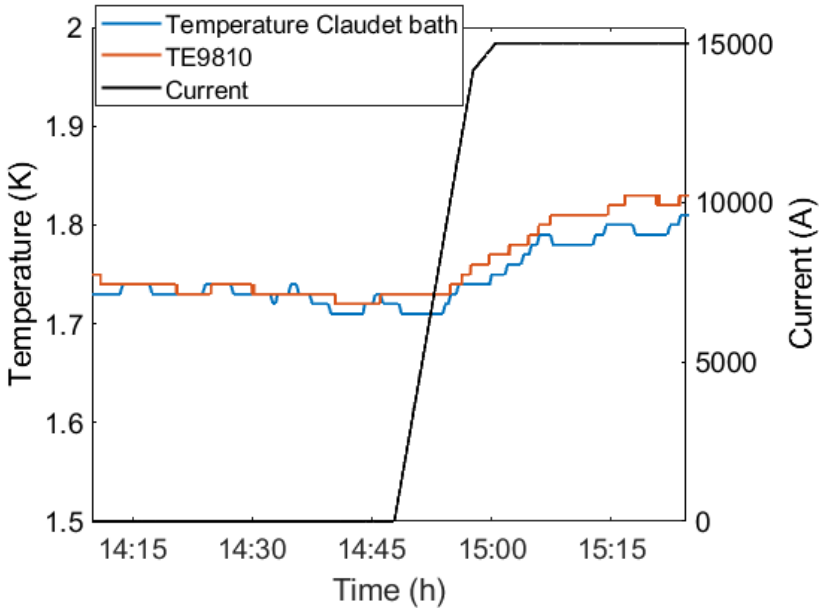

Figure 4.1: Current ramp-up in function of the time inside the MACQU magnet. The temperature evolution of the Claudet Bath, in blue, is plotted, in comparison with the temperature at the middle of the magnet, in orange. The temperature TE9810 is chosen because it is the furthest temperature sensor from the cold source and close to where the quench is initiated.

The temperature increase can be explained by two hypothesis, without being able to discriminate which one is the preponderant one. On one side, even with a reduced current slope, the losses generated by the variable current are not null and can create enough energy deposition to increase the temperature. On the other side, the resistive copper plate connecting the W7X boxes to the busbars, which has been measured to 6.3 nΩ [61], generates dissipative heat losses by Joule effect. However, trying to maintain constant thermal conditions before the ramp-up, and then maintain a constant extraction capacity of the Claudet bath, it has been decided to regulate the helium pumping group on a 80 % filling level of the saturated superfluid bath. Therefore, with increasing losses but with a constant extraction power, the temperature of the Claudet bath and of the magnet must increase since the beginning of the ramp-up. Finally, it can also be seen that the temperature difference between the bath and the magnet is also increased. Indeed, due to the very small superfluid helium cross-section ($S_{He} = 8.28$ mm^2) inside the conduit, the extraction power of the helium in the coil is limited. At the opposite, the extraction power of the Claudet bath is more important and a thermal gradient exists between the magnet and the Claudet bath.

4.1.2. Quench initiation

After the thermal recovery of the steady-state, the heat pulses can be performed to quench MACQU. We start the heat pulses with a lower value than the computed MQE, and increase them step-by-step until the quench initiation, in order to measure the MQE. Moreover, with more energy deposition than necessary, the quench would be accelerated and the measured quench propagation speed over-estimated. The goal is also to measure a representative quench propagation speed. In addition, the safety of the quench detection system would be ensured, as an over-estimated quench propagation speed could distort the detection ability.

Therefore, for the same energy deposition, a compromise must be found between the deposition time and the deposition power. With a deposition time too long, the initial quenched length would increase by heat diffusion, and would over-estimate the initial quench propaga-

tion speed. The quench propagation speed would also be over-estimated with too much power deposition, as the temperature would increase much higher than only T_{cs}. It has been thus decided that the heaters' power supply should deliver 0.7 A (4.75 W) or 1 A (9.7 W), during a time included between 1 s and 3 s. The deposited energy is comprised between 5 J and 30 J. In order to have a precise measurement, the deposition time is increased with a time step of 0.1 s until the magnet quench. For this quench, the first deposition time was of 2.40 s with a 0.7 A current, corresponding to a deposition of 11.4 J.

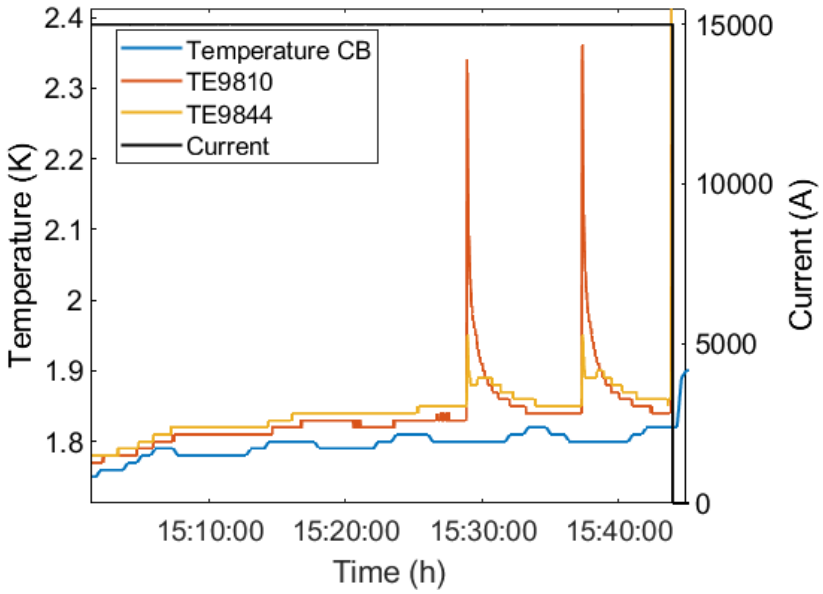

Figure 4.2: After a thermal recovery time, heat pulses are done and the third pulse (4.75 W during 2.6 s) makes MACQU quench.

As it can be seen in figure 4.2, the temperature measured by the TE9810 temperature sensor increases by 0.51 K with the first pulse and by 0.53 K with the second one. The TE9844 temperature sensor, placed at 9 m from the TE9810, measures a temperature increase of respectively 90 mK and 100 mK, when all other temperature sensors show no temperature increase.

During the two first heat pulses, the magnet does not quench and no variation of the measured voltage can be seen. However, the heat pulses are high enough to increase the temperature of the SQD until its critical temperature, since the left SQD is placed just below the heaters. The voltage increase that can be seen in figure 4.3, on the next page, corresponds to the voltage variation of the left SQD.

The third pulse quenched the magnet. The deposited power of the heaters was manually handled and the deposition time was recalculated thanks to the acquisition system. For the presented case of quench initiation, the quench has been initiated with a deposition time estimated between 2.46 s (2^{nd} pulse) and 2.52 s (3^{rd} pulse). With a current of 0.7 A, the MQE of MACQU for 15 kA and 1.97 T at the heaters position is measured between 11.69 J and 11.96 J.

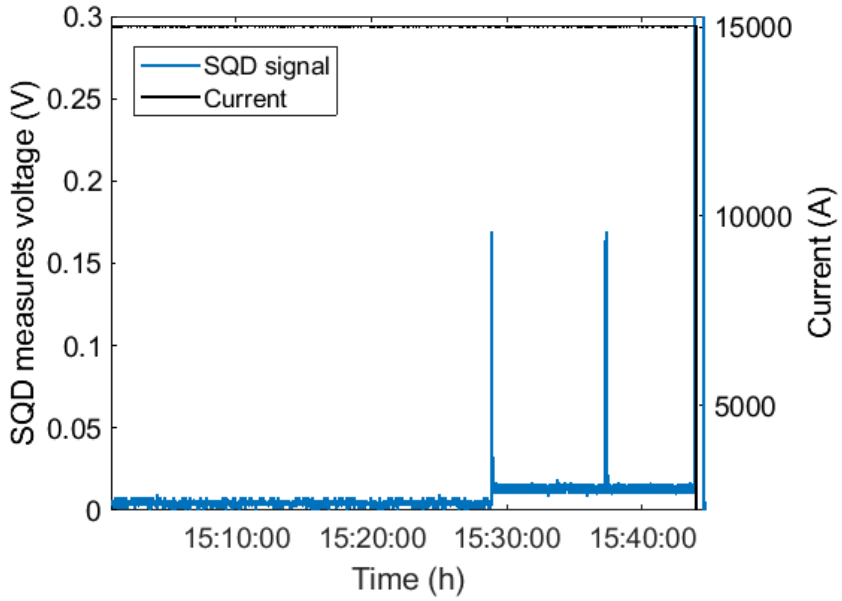

Figure 4.3: The heat pulses generate a voltage increase on the SQD placed under the heaters.

4.1.3. Quench detection

One of the main objectives of MACQU is to benchmark the detection system that will be used for MADMAX in the future. When the quench starts propagating, a voltage variation is seen on the DTOT signal, as it can be seen in figure 4.4. The time scale has been zoomed to the quench initiation time, with 0 indicating the beginning of the voltage variation on the SQD, i.e the beginning of the pulse.

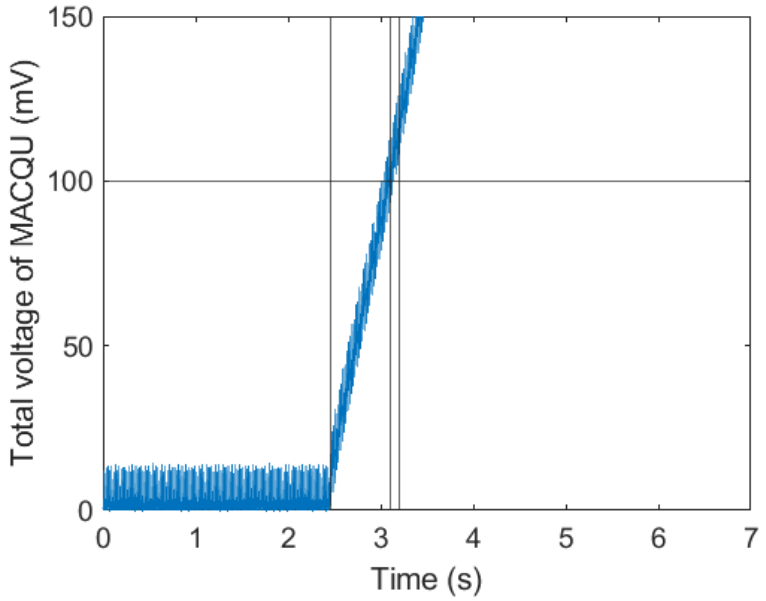

Figure 4.4: Beginning of the quench propagation measured by the DTOT signal. The DTOT signal measures the voltage variation of the entire coil, including the terminals and the busbars. The detection treshold is fixed at 100 mV during 100 ms. The horizontal black line is the 100 mV detection threshold and the two vertical black lines represent the reaching of the threshold and the 100 ms above this value.

The time observed between the quench initiation and the reaching of the threshold of 100 mV is 701 ms. This detection time is totally reasonable for the temperature increase and especially the hot-spot, as it is estimated at 30 K for such a detection time. Such a short detection time is a reassuring information on the quench detection system safety, and similar results have been observed several times for other quench tests. Thanks to the provoked quench tests, but also to the several detected quenches during the ramp-up of the current, the goal of MACQU to verify the quench detection ability has been validated soon.

4.1.4. Fast discharge

As presented in section 3.2.2, the detection time can be increased from 100 ms up to 7 s to study the quench propagation. Therefore, in the previous quench detection test, the fast discharge was launched after 4.2 s of propagation. Figure 4.5 shows the evolution of the signal DTOT during the quench propagation, measured by the MSS.

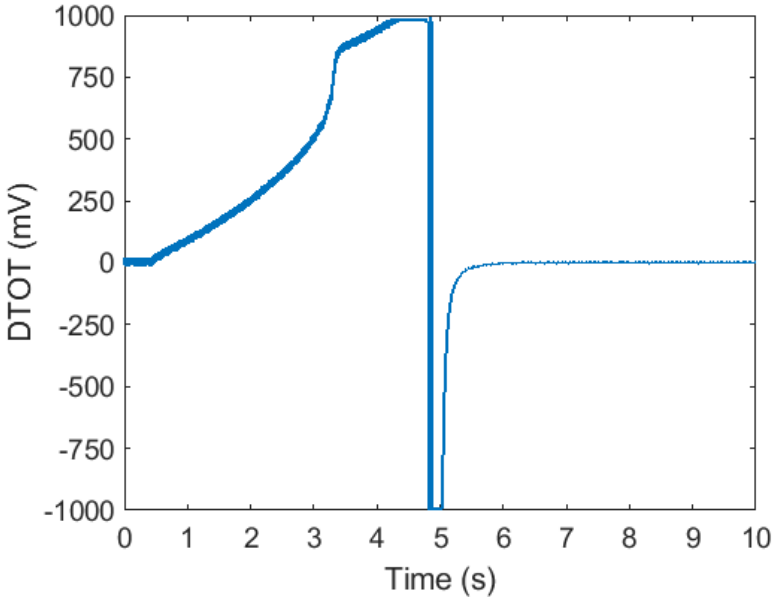

Figure 4.5: Quench propagation and fast discharge measured by the DTOT signal.

After 4.2 s of propagation, the fast discharge is triggered and the voltage decreases strongly and instantaneously, until being negative. During the discharge, the voltage taps measure a contribution of the quench resistive voltage, as presented in section 3.2.2, but also a contribution of the inductive voltage due to the current variation that was null before:

$$\begin{aligned} U_{MACQU} &= U_{quench} + U_{ind} \\ &= R_{quench} I + L_{MACQU} \frac{dI}{dt} \end{aligned} \tag{4.1}$$

with U_{MACQU} being the measured resistive voltage, U_{quench} being the voltage contribution of the quenched part of the magnet, U_{ind} being the contribution of the inductive voltage, R_{quench} the resistance of the quenched part of the magnet, I the current, L_{MACQU} the inductance of the magnet and the time coordinate t.

The DTOT signal is calibrated on a ± 1 V range. Even if the signal overloads between 4.3 s and 4.8 s, the effect of the quench to the voltage variation can be roughly estimated

around U_{quench} = 1 V. By considering the characteristic time of the discharge, the inductive contribution can be estimated to $U_{ind} = L_{MACQU} \frac{dI}{dt} = 0.193 \times 10^{-3} \frac{0 - 15000}{0.031}$ = - 93.4 V. The contribution of the inductive voltage term is largely higher than the quench contribution voltage and explains the negative values of the measured voltage. However, in one second, the voltage comes back to 0.

4.1.5. Nominal conditions range of the MACQU coil quench tests

Twenty initiated quenches have been carried out on a large current and initial temperature range, that are summarized in table 4.1. As it can be seen, the minimal load line margin reached for the MACQU experiment is around 24 % and the target of 10 % margin on the load line has not been reached. Indeed, during the current ramp-up, several unexpected quenches happened, limiting the maximum reached current to 17530 A. The main hypothesis explaining these unexpected quenches is a current redistribution issue in the terminals, and further studies are necessary to comprehend this phenomenon. However, these quenches did not compromise the main objective of MACQU of benchmarking the detection ability of the quench. In total, including provoked and unexpected quenches, 60 quenches happened on MACQU and all of them have been detected in less than a second. It allowed us to validate both the quench detection sensitivity and the conductor design for MADMAX. Moreover, as the Joule heat losses are lower than for MADMAX, it can be expected that the quench should propagate faster for MADMAX, and would then be easier to detect.

Table 4.1: Temperature, current and magnetic field range of the test campaing of the MACQU magnet.

	Minimum testing value	Maximum testing value
Temperature (K)	1.75	2.01
Current (kA)	10	17
Peak field at heaters position (T)	1.31	2.23
Load line margin (%)	55.2	23.8
Joule heat loss (W/m)	95	342

Also, the second interest of MACQU is to study the quench behavior of the conductor, over a large nominal conditions range summarized in table 4.2. For all these quench tests, the detection time has been increased in order to let the quench propagate as much as possible. The first parametrical study has been carried out on the current, with a step of around 1000 A (gathering the first six quenches of the table 4.2). The initial temperature of the quench test was not kept constant between two consecutive tests, as the different losses increase with the current. Therefore, the last three quenches have been performed to study the impact of the initial temperature on the quench behavior, for a similar current. The temperature of the Claudet bath has been increased of 150-200 mK by reducing the flow of the saturated bath.

As a reminder, the goal of MACQU is to simulate a non-detected quench that could propagate at constant current. After a certain propagation time, the current is discharged in around a second. Therefore, to not consider the effects of the current variation on the quench behavior, the study of the quench propagation is limited to the propagation time and the fast discharge will not be further studied. The further sections are dedicated to the study of the quench propagation and quench behavior. The goal is to study the propagation of the quench presented

in this section, by showing the different methods to compute the normal length but also to identify and analyze the different dynamics of the propagation.

Table 4.2: Summary of the nominal conditions of the MACQU coil quench tests.

Current (A)	Magnetic field (T)	Initial temperature (K)	Linear heat dissipation (W/m)
17018	2.209	1.865	341
16002	2.077	1.84	293
15003	1.948	1.82	250
13993	1.816	1.805	211
12999	1.687	1.785	177
10009	1.299	1.75	95
16012	2.079	2.00	294
15002	1.947	1.99	250
13005	1.688	1.975	177

4.2. Study of a typical quench propagation pattern

After presenting the experimental protocol, the experimental results can be detailed and analyzed. The goal of this section is to study a typical quench propagation pattern, by analyzing the normal length propagation. In a first step, due to the symmetry of the quench behavior, it is shown that the study of the quench propagation can be reduced to the right side of the magnet only. This will allow to develop different methods to compute the normal length, depending on the different available instrumentation, and the most appropriate ones are considered for the rest of the study. In a second step, the study of the typical quench propagation pattern is carried out. It is shown that a repetitive quench behavior can be observed for most of the quench tests, divided in three propagation phases that are analyzed further.

4.2.1. Symmetry of the quench behavior

Different methods can be used to compute the normal length during a quench test, by using the different acquisition measurements but also the SQD measurements. However, to identify the most relevant measurements for the quench propagation study, the first step is to compare the different signals, in function of the different sides of the magnet. The goal is to demonstrate a symmetric, or almost symmetric behavior of the quench dynamics, to reduce the study to one side only. In a first step, the voltage variation of the half of the coil can be seen in figure 4.6. The initial phase, between 0 and 2.5 s, corresponds to the pulse time.

The quench initiation is captured at 2.5 s for both sides. Until 4 s, the increase of the voltage is quasi-linear. At 4 s, the slope starts increasing progressively until an important increase at 5.2 s. Finally, at 5.4 s, the slope strongly decreases and keeps increasing quasi-linearly until 6.8 s where the discharge is triggered (not plotted here). During the first quasi-linear phase, the signals are well superposed, but the difference increases after the first acceleration at 4 s. The maximum difference is 43 mV, at the end of the acceleration at 5.4 s. However, both signals reproduce the different phases at the same time.

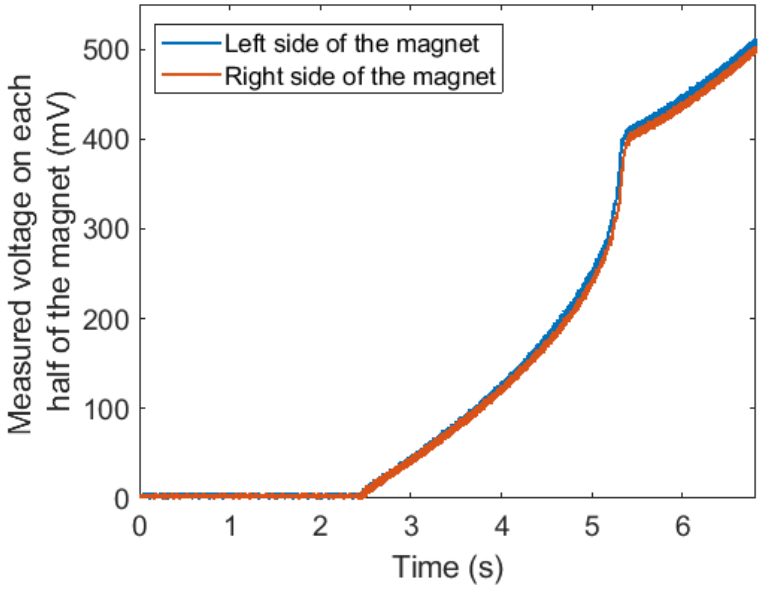

Figure 4.6: Voltage variation of each side of the magnet (without the arms).

The quench behavior is also similar on both sides with the SQD measurements. However, the difference is slightly more important for the SQDs, as it can be seen in figure 4.7.

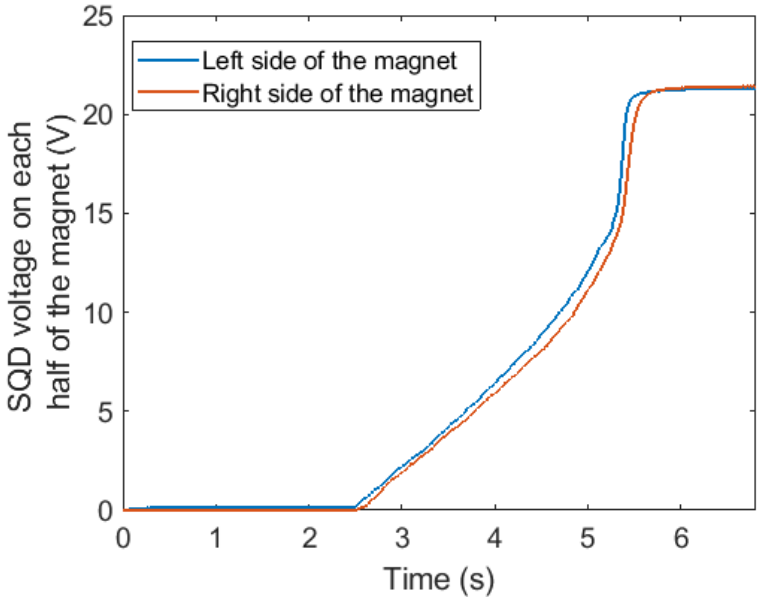

Figure 4.7: Comparison of the measured SQD voltage on each half of the magnet.

The SQD signal starts with a first quasi-linear phase from 2.5 s to 4 s and is followed by a progressive acceleration from 4 s to 5.2 s. Again, an important acceleration appears until 5.4 s. Finally, an important decrease and a plateau can be observed until the discharge, where in figure 4.6 the signal was still increasing.

The slight difference between the signals can be explained by simple means. Due to the positioning of the voltage taps, the length of the measured zones is not exactly the same, as the right side of the magnet is 25.3 m and the left side is 25.6 m. As the length is more

important, the total voltage variation of the left side is coherently more important than for the right side. Concerning the SQD measurements, the explanation is not only on the length difference. Indeed, the right side is longer than the left side, with respectively 27.7 m and 27.1 m, and is coherent with figure 4.7 where the right signal is higher than the left signal before the discharge. However, the left side starts clearly earlier than the right side. As it has been explained earlier, the SQD are not perfectly symmetric, as it can be seen in figure 4.8. The left SQD is directly under the heaters while the right one is after the heaters zone. Then, the quench being initiated in the heaters zone, the right SQD cannot see the initiation of the quench, while the left measures the initiation of the quench in the heaters region.

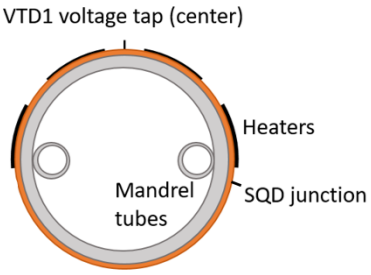

Figure 4.8: Cut view of the solenoid. The junction of the SQD can be seen after the heaters, explaining the time delay between both signals.

However, even if a small delay exists between both sides of the SQD measurements, the dynamics seems to be equivalent. The same conclusion can also be done for the voltage measurement signals of the coil. Therefore, the quench behavior is considered symmetrical and the propagation is studied only on the right side of the magnet during the further studies. The right side has been kept for two main reasons. Indeed, most of the temperature sensors are positioned on the right side of the magnet. Moreover, as said, one SQD (left) goes below the heaters while the other one (right) stops slightly before. Then, at the quench initiation, the left SQD would see a double contribution of the quench propagation: as the quench propagates into two directions, the SQD will measure the transition of the left side of course, but also the transition of the distance between the heaters and the right SQD. The measured initial quench propagation speed would then be over-estimated. For all these reasons, only the measurements of the right side are studied for the computation of the experimental quenched length.

4.2.2. Computation method of the experimental quenched length

The three different methods to compute the quenched length are presented in this section. The goal is to determine which method is the most accurate to follow the quench propagation front and properly estimate the normal length of the coil. The first method is based on the SQD measurements. The SQD have been installed particularly to follow the quench propagation. The RRR of the SQD is 1.12 so the measured voltage can be linearly correlated to the quenched length. The second method uses the global voltage measurement of the right side of the magnet presented earlier. By using the temperature measurements, the resistivity of the copper is estimated and the normal length computed. The third method is based on the L1 to L6 and RUT measurements, that divide MACQU into several consecutive lengths. By detecting the quench initiation at each region interface, it is possible to know precisely the position of the quench propagation front, and then reconstruct a normal length propagation map depending on the time. The study case is a quench at 15003 A, with an initial temperature of 1.82 K.

4.2.2.1. Method 1: Computation with the SQD measurements

The SQD voltage measurement has been presented in the previous section. The interest of the SQD is to linearly compute the quenched length from the measured voltage, by using equation 4.2.

$$L_q = u_{SQD} \frac{L_{SQD}}{R_{SQD,10K} I_{SQD}} \tag{4.2}$$

with L_q being the normal length, u_{SQD} the measured voltage of the SQD, L_{SQD} the length of the SQD, $R_{SQD,10\ K}$ the electrical resistance of the SQD before the transition at around 10 K and being respectively 212.6 Ω ± 0.5 Ω and 209.0 Ω ± 0.5 Ω for the right and left side and I_{SQD} the current used for the SQD measurement. The factor $\frac{L_{SQD}}{R_{SQD,10K} I_{SQD}}$ varies between 1.24 and 1.28 depending on the current of the SQD that is 101 mA ± 2 mA.

However, to compare the quenched length with the position of the quench propagation front, it is necessary to take into account that the SQD is placed on the external radius of the solenoid. It adds thus a small extra length compared to the real length of the solenoid, measured on the length of the conductor. The length of the SQD must thus be readjusted to fit with the length of the conductor. Moreover, as explained earlier, the SQD is not symmetric and does not follow the exact same path than the conductor. To illustrate the difference between both, figure 4.9 shows the superposition of the SQD with the length of the conductor.

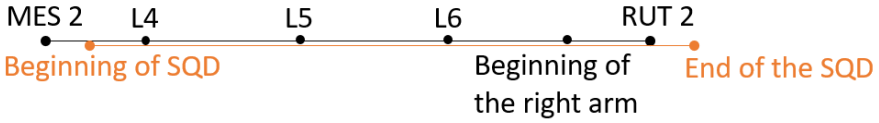

Figure 4.9: Superposition of the SQD length with the length of the conductor.

To be comparable with the normal length of the magnet, it is then necessary to readjust the SQD length on the conductor length. Table 4.3 compares the crossed-length between the acquisition measurements and the SQD, for the same regions. As it can be seen, due to the non-symmetry of the SQDs, the right SQD will not measure the quench on the first 33 cm of the coil. On the other side, the SQD is 18 cm longer than the acquisition system, and can then follow the quench propagation further. However, the 18 cm long last portion of the SQD is placed on the arms and stop just before the connection, so the length of the SQD is the same than the length of the conductor during this portion. Therefore, to readjust the normal length of the SQD on the normal length of the magnet, the length of the SQD is considered as 0.55 + 8.73 + 7.86 + 7.87 + 1.64 + 0.18 = 26.83 m.

Table 4.3: Characteristics of the acquisition lengths compared with the SQD length.

	Conductor length (m)	SQD length (m)
MES2 - Beginning of the SQD	0.33	0
Beginning of the SQD - L4	0.55	0.57
L4 - L5	8.73	9.04
L5 - L6	7.86	8.14
L6 - Beginning of the arm	7.87	8.14
Beginning of the arm - RUT2	1.64	1.64
RUT2 - end of SQD	0	0.18
Total length	26.98	27.71

Finally, by knowing the length of the SQD, equation 4.2 can be used for the quenched length computation, and the result can be seen in figure 4.10.

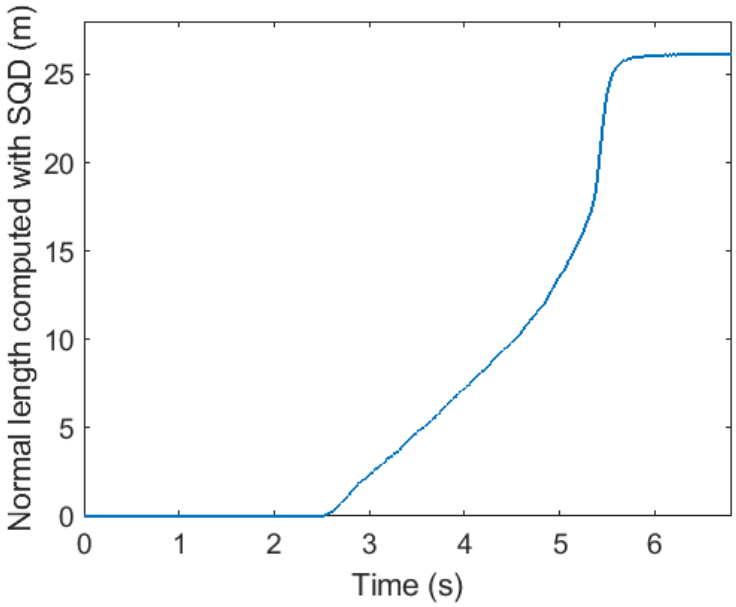

Figure 4.10: Normal length of the coil computed with the SQD method, for the quenc case at 15 kA and 1.82 K.

The quenched length is measured with a precision of around ± 2.2 %, estimated with equation 4.3. The length of the SQD is 26.83 m ± 0.01 m, the resistance of the right SQD is 212.6 Ω ± 0.5 Ω and the current of the SQD 101 mA ± 2 mA. The main uncertainty comes from the measured voltage. Due to its low RRR of 1.12, the measured voltage of the SQD increases of 0.1 V for every 10 K increase. In the following section, it is shown that the hot-spot temperature is estimated to 30 K. By considering the conservative case where the whole coil would be at 30 K, the voltage measurement error is 0.2 V. This conservative value of ± 0.2 V has been considered for the precision calculation presented in the equation 4.3.

$$\frac{\Delta Lq}{Lq} = \sqrt{(\frac{\Delta u_{SQD}}{u_{SQD}})^2 + (\frac{\Delta L_{SQD}}{L_{SQD}})^2 + (\frac{\Delta R_{SQD,10K}}{R_{SQD,10K}})^2 + (\frac{\Delta I_{SQD}}{I_{SQD}})^2} \tag{4.3}$$

In conclusion, the SQD method appears as a precise and representative method to compute the quenched length of the coil. However, the right SQD has a defect: it is not possible to capture the quench initiation with it, as it is not under the heaters. Then, the first 33 cm of the quench propagation are not measured. To verify the quench dynamics from the beginning, the right SQD is not enough and acquisition measurements must be used. The following section presents the second method for normal length computation, based on the DUP3 half coil voltage measurement, able of following the quench propagation since the beginning.

4.2.2.2. Method 2: Computation with the DUP3 voltage measurement

The DUP3 signal presented earlier measures the voltage variation of the half of the coil. The DUP3 signals covers the half of the coil and has the big advantage of being able to detect the quench anywhere on that part of the coil. The goal in this section is to use the equation 3.1 to compute the quenched length. However, the quenched length computation is function of more

parameters than for the previous method such as the RRR, the temperature, the magnetic field, the measured voltage, the current and the copper cross-section.

$$U(t)_{MACQU} = U_{quench} = R(t)_{quench} I = \frac{\eta(t) L_q}{S_{Cond}} I \tag{3.1}$$
$$\iff L_q = \frac{U_{quench} S_{Cond}}{\eta(t) I}$$

with U_{MACQU} being the measured voltage, equal to the voltage of the quenched part of the magnet U_{quench}, R the normal resistance, I the current, η the electrical resistivity, L_q the quenched length, S_{Cond} the cross-section of the conductor and the time t.

With DUP3, the voltage variation of the conductor is measured. The DUP3 measured voltage depends of the magnetic field, the RRR of the conductor and the temperature of the conductor. The magnetic field map presented earlier has shown that the magnetic field does not vary more than 0.1 T depending on the position, so the resistivity function is weakly dependent of the magnetic field in our case. On the opposite, as the RRR of the conductor is 125 ± 1, the electrical resistivity is a strong function of the temperature, compared to the SQD. Therefore, the temperature of the conductor must be well-known along the magnet to estimate the electrical resistivity of the conductor and then compute the quenched length.

The time evolution of the temperature at the center of the coil has been plotted in figure 4.11. Even if the end is not plotted here, the temperature finally reaches 30 K after the discharge. The discharge happens at 6.8 s, and the temperature keeps increasing but with a lower slope.

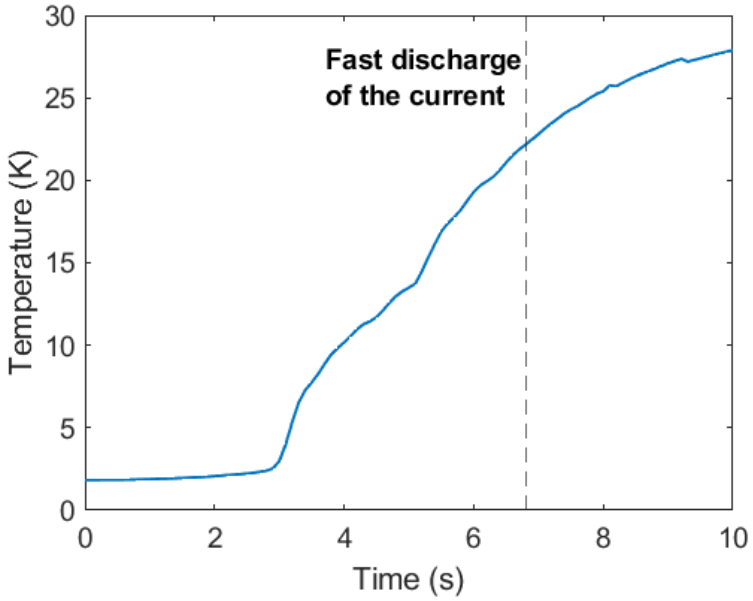

Figure 4.11: Temperature evolution during the quench measured by TE9810 temperature sensor. The black line represents the fast discharge, and the temperature slowly keeps increasing after.

For the normal length computation, the temperature that is considered is the temperature of the TE9810 sensor, at the center of the magnet, and the result is shown in figure 4.12. The assumption done is that the whole quenched length is at the temperature measured by the TE9810 sensor. However, by considering the other sensors, a part of the propagation would have been neglected, generating an error in the estimation of the resistivity. The made assumption is then conservative.

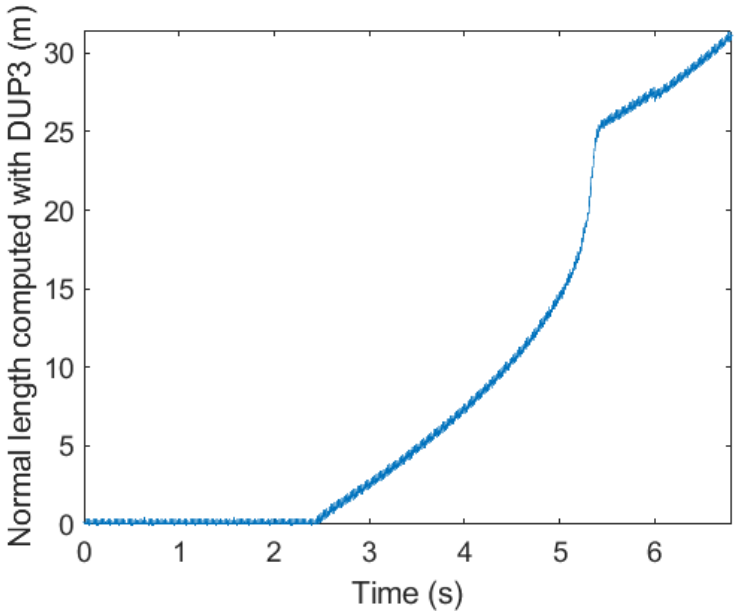

Figure 4.12: Normal length of the coil computed with the DUP method.

For the normal length computation, the evolution until 5.2 s should only be considered, as the final slope corresponds to the voltage increase due to the temperature increase in the whole magnet, and not linked with a lengthen of the quenched length. However, as it can be seen, before the final phase, the quenched length is under-estimated, being around 25 m. The DUP3 measures the entire half coil, including the arms, and the length is 27.7 m. This method presents then a gap compared to the SQD one. This gap is due to the temperature measurements that present two main defects:

- The first one is the important delay between the temperature increase and the arrival of the quench to the measurement point. For example, the temperature at the TE9810 sensor position, placed at 0.88 m from the heater zone, goes from 3 K to 10 K between 3 s and 4 s, meaning that the quench arrived to this position. However, the previous method shows that the quench should have arrived before 3 s. The delay between the temperature measurement and the real position of the quench is slightly under the second and the considered temperature for the computation is under-estimated. However, this delay could not be corrected, as the delay seems to vary with the temperature but also between the sensors.

- The second issue is the value of the measured hot-spot. After the discharge, the temperature of the coil keeps increasing and stabilizes between 25 K and 30 K. The hot-spot is computed at 59 K at the center from equation 1.19. Between the measured hot-spot at 25-30 K and the computed one at 59 K, the electrical resistivity varies a factor 4 from 2.95×10^{-10} Ω m to 1.16×10^{-9} Ω m. The uncertainty on the resistivity is then very important.

For these two reasons, the accuracy of the temperature measurements is questionable, and so the computation of the resistivity. It creates then a not estimable and important uncertainty on the normal length computation and the obtained result is not accurate. Fortunately, the last method to be presented does not need an accurate measurement of the temperature, but uses the different signals composing the DUP3 signal that are MES2, L4, L5, L6 and RUT2 signals.

4.2.2.3. Method 3: Computation with the method of the top

The last method presented in this section uses the MES2, L4, L5, L6 and RUT2 signals. The interest of this method relies on the fact that the quenched length can be computed without the temperature measurements, but only with precise voltage measurements. It is based on the fact that the distance between each voltage tap is well known and the quench initiation clearly visible. For example, when the voltage starts increasing at L5, it means that the quench has totally crossed the L4 region. Therefore, by identifying the initiation of the quench in each region, it is possible to evaluate the precise location of the quench propagation front. Even if it not possible to properly reconstruct a refined total normal length propagation map depending on the time, the signals help identifying the quench at six locations and can also be used to estimate the mean quench propagation speed.

Figure 4.13 shows the different signals MES2, L4, L5, L6 and RUT2 signals measured by the MSS. The initiation of each signal is identified by a black line and obtained by the local tangent method. The arm signal has been deducted from the difference between the DUP3 signal and the sum of the other signal.

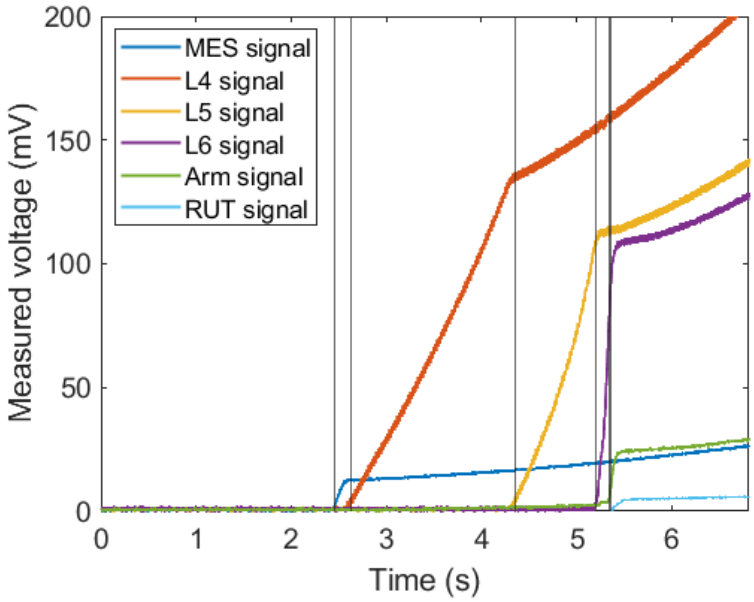

Figure 4.13: Superposition of the different signals (MES, L4, L5, L6, the deducted Arm signal and RUT) on the right side of the magnet. The black lines represent the initiation time of the different signals.

By plotting the crossed-length between two consecutive measurements in function of the initiation time, the position of the quench propagation can be found, and the result is depicted in figure 4.14.

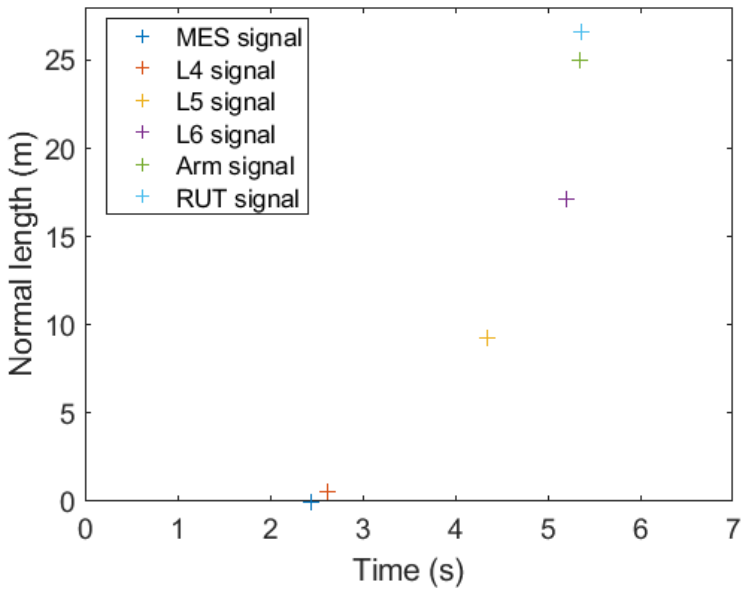

Figure 4.14: Normal length of the coil computed with the method of the tops.

As it has been shown above, the SQD can not measure the first 33 cm of the quench propagation. Therefore, to compare the results between both methods, instead of considering that MES and L4 are respectively at X =0 m and X =0.88 cm, the whole distances are 33 cm down-shifted in order to have the points at X =- 0.33 m and X =0.55 m. That way, except the non-measurable first point, the other points are comparable between the method of the top and the SQD method.

The measurements precision is ± 1 mV. Due to the frequency of the signal, the error on the time is estimated to be ± 0.05 s and the length are known to be ± 0.01 m. Finally, this method appears as even more precise than the SQD method with a global error on the measurement of around 1 % and is also the most accurate one. Despite its high precision, this method presents a small defect though: the distance between consecutive zones can be important, up to 9 m. With such a length, if a change on the quench dynamics happens, a precise location would not be possible to identify. This method can however be used to precisely estimate the mean propagation speed between two consecutive zones, and particularly initial quench propagation speed.

4.2.2.4. Conclusion on the different methods

Three method to compute the normal length have been presented, and this section is dedicated to choosing which one is the most appropriate for the study of the quench behavior. Figure 4.15 shows the superposed results obtained with the three methods.

As it can be seen, the three methods seem to represent a similar quench behavior. Small differences can be seen though, particularly in time, because the SQD seems to have a small delay compared to the other two methods. This delay can simply be explained by the fact that the SQD follows the propagation front at 9 K, while the two other methods follow the quench propagation front at $T_{cs} = 4.83$ K for this example. However, the biggest difference is for the DUP method, on the final quenched length: when the magnet has totally transited, the quenched length is only 25 m, compared to the 26.8 m for the other two methods. As explained earlier, this difference is due to the temperature measurements that are measured with a delay, and probably not in an accurate way. For this main reason, the method of the DUP will not be further considered, being the less accurate of the three methods.

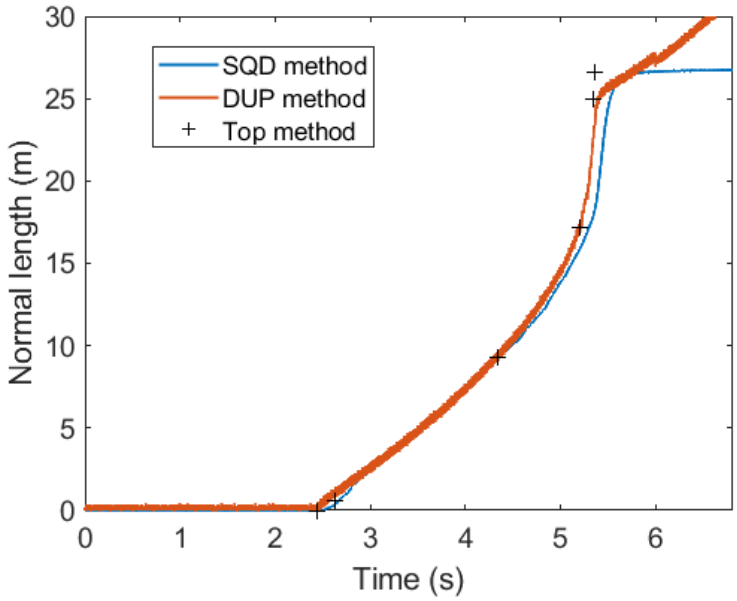

Figure 4.15: Normal length of the quench at 15 kA and 1.82 K, computed with the three methods: the method of the SQD, the method of the DUP and the method of the top.

In conclusion, the SQD method and the top method seem to be the two best options for the study of the quench behavior. By using the top method, it is possible to punctually know the position of the quench propagation front in a very accurate way. This method can be used for determinations of quench propagation speeds, particularly for the initial and final one, where the distance between two consecutive voltage tap is short. At the opposite, due to the important length between the regions between the initial and final one, the top method will not be as accurate and the SQD method is preferred. Moreover, thanks to the SQD, the quench behavior changes can be studied and more precisely identified. The two method will then be complementary for the quench behavior study that is carried out in the following sections.

4.2.3. Identification of the different quench dynamics

The previous computations allowed to choose two complementary methods to calculate the experimental quenched length. Both methods are used to estimate the quenched length that can be seen in figure 4.16. The study case is still the case at 15 kA and 1.82 K. The computations are done and plotted until the fast discharge time.

The quench propagation can be divided into three clear phases:

- The first phase is called the *quasi-linear phase*. It corresponds to the propagation between 2.50 s and 3.30 s and between 0 and 3.3 m. The *quasi-linear phase* corresponds to the establishment of the initial quench regime, with a quench propagation speed measured of 4.9 m/s.

- The second phase is the acceleration phase. This phase happens between 3.30 s and 5.36 s and between 3.3 m and 18.4 m. The quench follows a progressive acceleration, increasing the quench propagation speed with the time and disconnecting slowly the normal length from the initial tangent. The quench propagation speed is then obviously higher than initially, and the mean quench propagation speed during the whole phase is estimated to around 7.3 m/s.

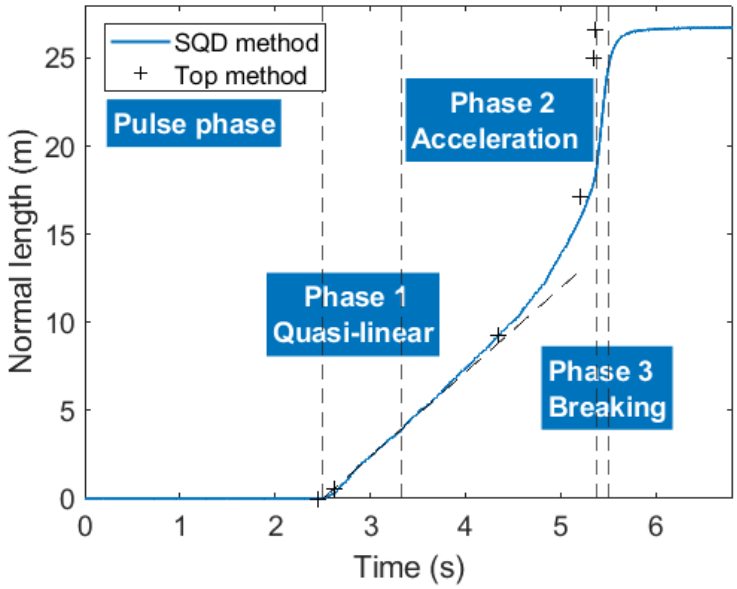

Figure 4.16: Different regimes of quench propagation, divided in three phases: the *quasi-linear phase*, the *acceleration phase* and the *breaking phase*. The study case is the case at 15 kA and 1.82 K.

- The third phase is the breaking phase, characterized by a clear break, corresponding to an important acceleration. This phase starts at 5.36 s but is really short and finishes around 5.47 s and lasts between 18.4 m and 23.3 m. The quench propagation speed is strongly accelerated and measured to around 126 m/s.

A last flat phase can be seen only with the SQD method and corresponds to the final part of the curve that lasts until the fast discharge. It starts with an important slow down of the quench propagation speed, until quenching the whole magnet, with the quenched length going from 23.3 m to the full 26.83 m. This phase is discussed later, in the lights of the voltage measurements.

Each phase will thus have a dedicated section for a further analysis. The goal is to study the quench behavior during each phase and try to explain the quench dynamics changes along the propagation.

4.2.4. Analysis of the normal length propagation

This section is dedicated to the analysis of the different quench propagation phases. As shown earlier, the quench dynamics can be divided into four phases. First, the *quasi-linear phase* is studied. It is shown that small oscillations are visible initially and the main hypothesis to explain these oscillations are presented. In a second step, the *acceleration phase* is studied. Not quasi-linear anymore and characterized by a progressive acceleration of the quench propagation, this phase is compared to a well-known phenomenon of the literature: the Thermal-Hydraulic-Quench-Back (THQB). Finally, the *breaking phase* is analyzed, for which the quench propagation greatly increases after a characteristic break. The *breaking phase* reaches a quench propagation speed an order of magnitude higher than during the *quasi-linear phase*, and some hypothesis are presented to explain such a spectacular acceleration.

4.2.4.1. Study of the *quasi-linear phase*

The *quasi-linear phase* is the establishment phase of the quench. This first phase can be seen in figure 4.17. The SQD voltage measurement shows a slight increase between 2.5 s and

2.8 s of the propagation, before the normal length stabilizes on a quasi-linear regime, with a quench propagation speed of 4.9 m/s.

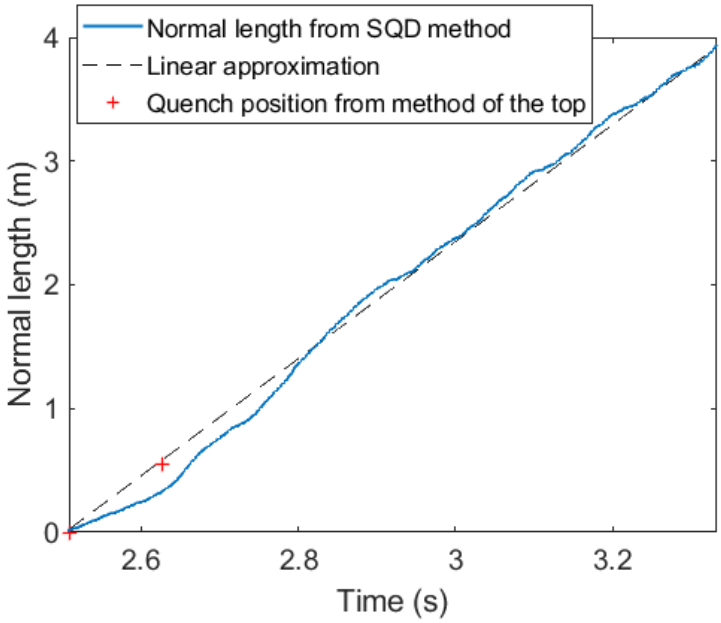

Figure 4.17: First quench propagation phase, in comparison with a linear approximation. The SQD shows oscillations on the quench propagation speed before stabilizing in a quasi-linear regime after 2.8 s.

During the first 0.3 s, oscillations of the SQD voltage can be seen, which are not visible for the voltage measurements. Three main hypotheses can be made to explain such oscillations. The first one is due to the specific heat of the mandrel which is not negligible compared to the specific heat of the coil. It creates an enthalpy storage that decreases the initial quench propagation speed. At 1.8 K, the specific heat of the stainless steel is 1.6×10^4 J/m^3/K. In comparison, the copper one is 217 J/m^3/K, 75 times smaller. Moreover, by considering the whole volume of stainless steel in the mandrel, and by dividing by the length of the coil (50.5 m), the equivalent cross-section is $S_{SS} = 274$ mm^2, which is a higher cross-section than the conductor one. Due to this important enthalpy storage, the quench propagation speed could be initially reduced, before reaching the nominal quasi-linear regime. The second assumption is the extraction power of the superfluid helium tubes of the mandrel. Even if the diffusion time was computed to be important enough not to impact the quench propagation, it can be assumed that the continuous extraction slightly reduces the quench propagation speed. The tubes are placed on every half turn which is approximately every 0.45 m. The first minima can be seen for 0.4 m and 0.9 m, corresponding closely to a minimum for each half turn, where the tubes are placed. The last hypothesis is the movement of the helium itself in the CICC. Pressurized by the quench, it can be assumed that the movement of the helium strongly modifies the heat exchange between the conductor and the helium. This modifications can lead to changes of the quench dynamics.

The quench propagation, on a quasi-linear regime, will start progressively accelerating at the end of the first phase. In comparison with the initial quench propagation speed, the normal length will start coming off the curve. It is then the beginning of the second phase: the *acceleration phase*.

4.2.4.2. Study of the *acceleration phase*

This second phase of propagation is characterized by a progressive acceleration of the quench propagation. The goal of this section is to analyze this *acceleration phase* and to give the main assumptions to explain why this progressive acceleration happens. Figure 4.18 shows the first *quasi-linear phase* and the second *acceleration phase*. As it can be seen, the SQD and the voltage measurement that were in good agreement until here starts having a time gap, particularly at 17.2 m where the delay is 0.1 s.

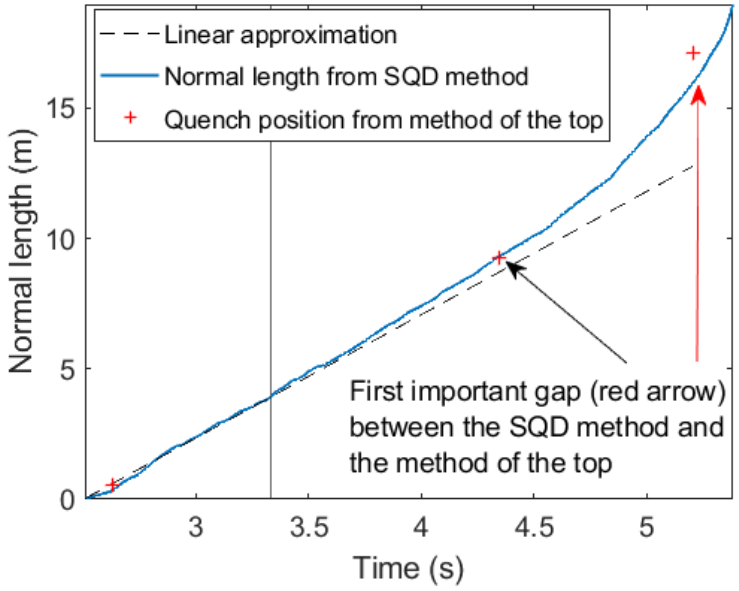

Figure 4.18: Second quench propagation phase called competition phase, characterized by a first small acceleration phenomenon.

The time delay can be explained in a simple way. As explained earlier, the top method follows the T_{cs} front while the SQD follows the 9 K front. Then, there must be a delay between both, due to the heating of the SQD between T_{cs} and 9 K. The time to heat from 4.83 K to 9 K is constant with similar initial conditions. However, when the *acceleration phase* starts, due to the already existing delay, the voltage measurements shows an earlier acceleration than the SQD. Therefore, the acceleration seen by the SQD is delayed, and the time delay between both methods keeps increasing with the quench propagation speed increase.

To explain the acceleration of the quench, the main hypothesis is the Thermal Hydraulic Quench Back (THQB) phenomenon, described largely in the literature [78–80] . This phenomenon is characterized by a pre-heating of the coil, upfront from the quenched length. The pre-heating is caused by the helium itself, generating this progressive acceleration. Indeed, due to the dissipative heat losses by Joule effect during the quench, a large amount of energy (around 250 J/m for this example) is deposited in the helium. The energy deposition in the helium generates a temperature increase. Therefore, as the Grüneisen parameter of helium is positive above the T_λ temperature, the pressure of the helium also increases. As it can be seen in figure 4.19, the expulsion helium flow creates a global movement of the helium inside the CICC. Above the T_λ temperature, the helium flow warms up the helium in the non-quenched zone (cold zone), due to the compression forces, the transport of warm helium and the work performed by the flow against the friction drag. This warmed helium progressively pre-heats the non-quenched zone, and particularly the superconducting cable, creating a progressive ac-

celeration of the quench because the temperature margin $\Delta T = T_{cs} - T_0$ is decreasing. This THQB phenomenon is a runaway phenomenon, where the pressure increase generates a flow, that warms the non-quenched zone, that contributes to increase the pressure, so the flow etc.

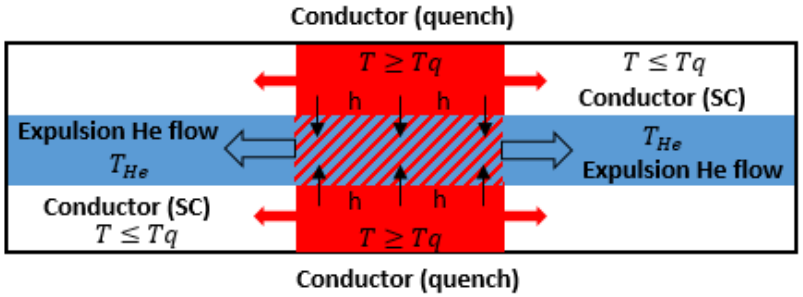

Figure 4.19: Simple scheme of the generated expulsion flow inside the CICC, showing that the expulsed flow warms the coil away from the quenched zone.

With small pressure increase, no pre-heating should be visible. This is the condition that explains a first *quasi-linear phase*, only driven by the heat conduction along the conductor. For larger quench propagation time, the pressure increases and reinforces the pre-heating effect. This pressure increase can be estimated in a first approximation with the analytical equation 4.4 from [33, 34]. The obtained value is 21 bar, by considering that 5 m of the coil have quenched. The goal is not to discuss of the obtained value, but to support the THQB hypothesis, as the pressure increase seems important in the conductor, strongly driving the THQB runaway phenomenon.

$$P_{max} = 0.65 \left[\dot{q}^2 \frac{f}{D_h} \left(\frac{L}{2} \right)^3 \right]^{0.36} \tag{4.4}$$

with P_{max} is the maximum reached pressure, $\dot{q}$ is the volumetric Joule power in the conductor, f is the friction coefficient, D_h is the hydraulic diameter and L is the length of the quenched conductor.

The next phase, called the *breaking phase*, presents a clear break and a strong acceleration, that is analyzed under the prism of the THQB phenomenon.

4.2.4.3. Study of the *breaking phase*

The goal of this section is to study the *breaking phase* and to highlight the role of the THQB in the characteristic clear break. Figure 4.20 shows the acceleration and *breaking phase*, and as can be seen, after a clear break, the quench strongly accelerates with a propagation speed of 126 m/s. Due to the propagation speed increases, the delay between the SQD and the voltage increases to 0.2 s.

This clear break has been rarely observed experimentally [81]. During the THQB, the temperature margin along the coil is constantly reducing because of the pre-heating. Therefore, one can assume that the temperature margin could be reduced to zero, or close to it, after some time of propagation. Moreover, in the MACQU case, the temperature margin is almost constant and included between 3.01 K and 3.07 K. The collapse of the temperature margin in the non-quenched zone would then generate an instantaneous (or at least very rapid) quench. The quench would then be driven by the thermal hydraulic heating, and not by the heat conduction in the conductor.

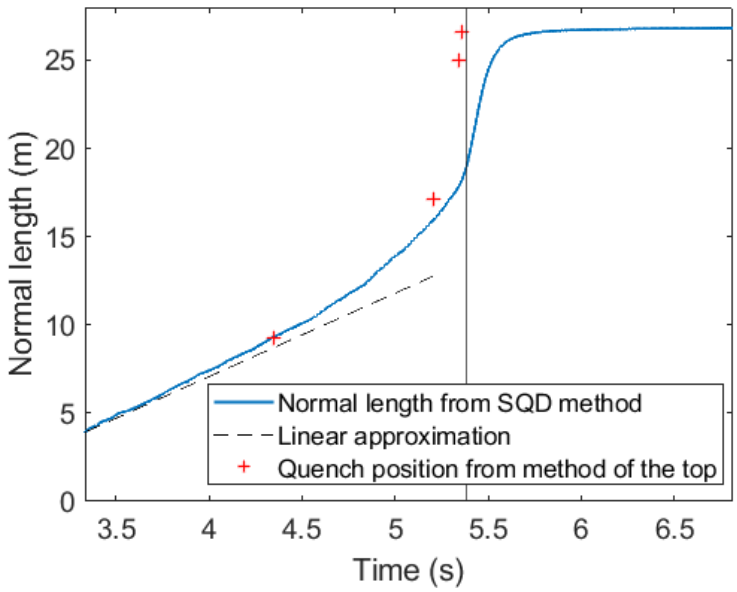

Figure 4.20: *Breaking phase* with an important second acceleration phenomenon.

To summarize, this section was dedicated to the study of a typical quench propagation pattern. It has been shown that the quench propagates with three different phases. The first phase, the *quasi-linear phase*, seems driven by the heat conduction along the magnet. The quench seems to propagate at a constant speed of 4.9 m/s. The *acceleration phase* is assumed to be due to a Thermal Hydraulic Quench Back phenomenon: with the important dissipative heat losses by Joule effect deposited on the helium, the temperature and pressure of it strongly increases. The pressure increase, by pressure difference, generates a flow along the conductor, that pre-warms the helium by compression, advection and friction. The non-quenched zone is the pre-warmed and the quench accelerates while the temperature margin reduces. The *breaking phase*, accelerates the quench even more after a clear break in the normal length propagation. The warm helium makes the cable reach its current sharing temperature T_{cs} in the non-quenched zone, creating the observed spectacular and almost instantaneous quench of the rest of the coil.

Therefore, as explained, the temperature margin is a key of the triggering of the acceleration of the quench propagation speed. As the temperature margin is also a function of the current, the following section is dedicated to the different parametric study of the quench behavior.

4.3. Parametric study of the normal length propagation

The goal of this section is to compare the quench behavior between the different quench tests. It is shown that the three propagation phases studied earlier appear on most of the quenches. A parametric study of the initial quench propagation speeds is proposed. By comparing the experimental quench propagation speeds to the one computed with the "infinite exchange quench speed" formula 1.14, the goal is to verify the dependence of the quench propagation speed on the current and the temperature margin. It is shown that the quench propagation speed is much faster than the one expected and the main hypothesis to explain this gap is given. Moreover, an "improved" equation is proposed to obtain more realistic results. Finally, a parametric study of the *breaking phase* is given, and particularly on the triggering of the break.

4.3.1. Parametric study of the global quench behavior

The above detailed quench propagation pattern, in three phases, with the first linear phase, the *acceleration phase* and then the *breaking phase*, can be found on almost all the quench propagation tests. Figure 4.21 shows the normal length variation of all the quench propagation tests. As it can be seen, the three phases pattern can be seen for most of the tests, except the 10 kA and the first 13 kA case where only the first two phases can be seen. These two quench cases are particular because the quench did not propagate enough time to entirely transit the magnet before the fast discharge, indicated by the vertical green and blue lines. The effect is clearer for the 10 kA case as the discharge is launched when 21.9 m of the magnet has quenched. Even with the heat generated by the fast discharge, only 24 m of the coil transit. Then, even if an acceleration can be seen, it is due to the general temperature increase generated by the fast discharge of the magnet. Therefore, to avoid the consideration of both phenomenon at the same time, these tests are considered only for the initial propagation speed estimation, but not for the third *acceleration phase*.

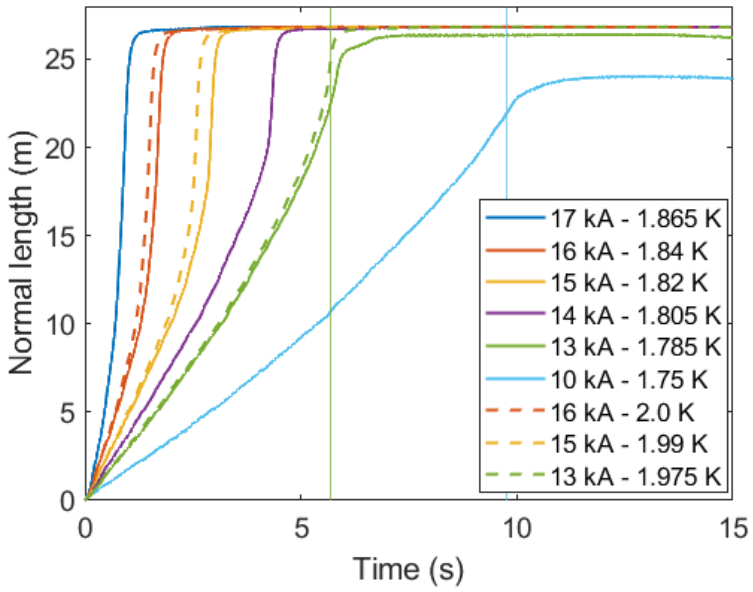

Figure 4.21: Summary of the entire quench propagation patterns, in function of the current and the initial temperature.

Even if the *breaking phase* is not seen, it does not mean that this phase does not exist for these two cases, only that a longer propagation time or a longer length would have been needed to see it. However, the quench propagation speed clearly increases with the current and the initial temperature for all the cases. The *breaking phase* also appears earlier with the current increase. Moreover, at equivalent current, the increase of the initial temperature, corresponding to a decrease of the temperature margin, makes the *breaking phase* also appear sooner. This behavior is completely consistent with the THQB hypothesis. Indeed, with the increase of the current, all the runaway phenomenon is more important: the dissipative heat losses by Joule effect are higher, making the pressure increase more important and therefore the expulsion flow. In these conditions, the pre-heating effect is also more important. Both the reduction of the temperature margin, due to an increase of the current or the increase of the initial temperature, and the increase of the dissipative heat losses by Joule effect can reduce the time and the distance to trigger the *breaking phase*.

After this first phenomenological analysis, a parametric study of the initial quench propagation and of the triggering of the *breaking phase* is done. The objective is to further analyze the impact of the current (and implicitly the dissipative heat losses by Joule effect) and the temperature margin on the quench propagation.

4.3.2. Parametric study of the initial quench propagation speed

The goal of this section is to compare the measured initial quench propagation speeds. As explained earlier, the quench propagation speed has been estimated with the method of the top (and not the SQD, see section 4.2.2.4) and the result of the computation can be seen in figure 4.22.

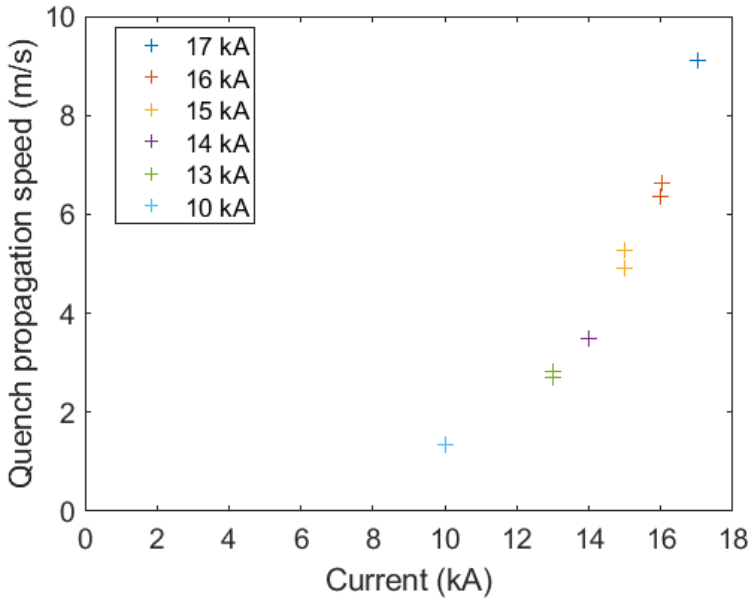

Figure 4.22: Parametric study of the initial quench propagation speed, in function of the current.

As expected, the quench propagation speed strongly increases with the current, going from 1.3 m/s to 9.1 m/s, with the current varying from 10 kA to 17 kA. Moreover, for a similar current, the quench with the lowest temperature margin has the highest propagation speed. For example, at 15 kA ($T_{cs} = 4.83\ K$), the quench propagation speed increases from 4.9 m/s to 5.3 m/s, with the temperature margin decreasing from 3.01 K ($T_0 = 1.82\ K$) to 2.84 K ($T_0 = 1.99\ K$).

To compare with the "infinite exchange quench speed" formula 1.14, that is reminded below, figure 4.23 shows the measured quench propagation speed and the computed one. The goal of this comparison is to verify the dependence of the quench propagation speed on different parameters, as the current and the temperature. Therefore, the comparison of the speeds is done in function of $\frac{I\sqrt{T_t - T_0}}{\Delta H}$, as considering only I or ΔT could skew their mutual dependence.

$$v_l = \frac{j}{\Delta H}\sqrt{\eta_{eq}\lambda_{cond}(T_t - T_0)} \quad \text{with} \begin{cases} j = \dfrac{I}{S} \\ T_t = \dfrac{T_{cs} + T_c}{2} \\ \eta_{eq} = \eta_{Cu}\dfrac{S}{S_{Cu}} \end{cases} \tag{1.14}$$

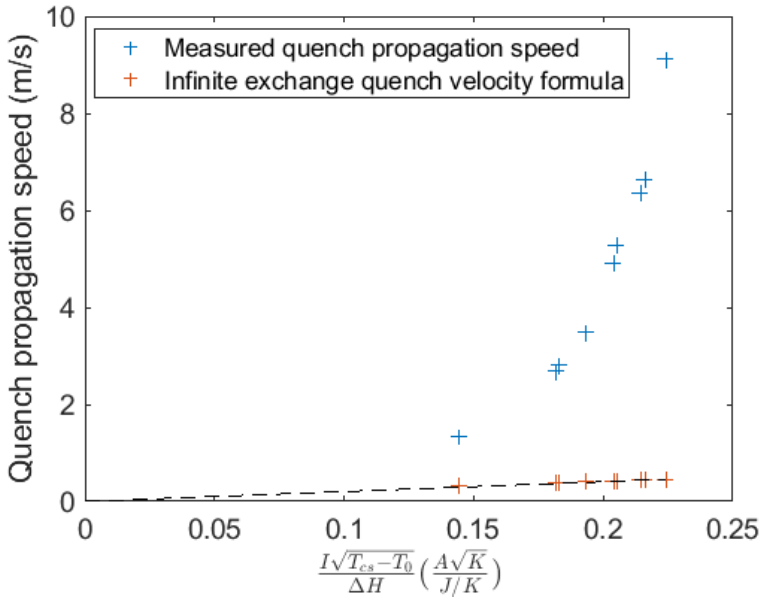

Figure 4.23: Comparison of the measured experimental quench propagation speed with the 1-D longitudinal quench propagation equation, applied with the contribution of helium.

The computed quench propagation speed is linear with the $\frac{I\sqrt{T_t - T_0}}{\Delta H}$ parameter, while the measured quench propagation is not linear, only monotonous. Moreover, the difference between the computed and measured values is important, the measured values being between 4 and 20 times more important. Therefore, a phenomena must explain the gap between both.

As it has been explained earlier, the THQB phenomena is due to the flow and the friction forces inside the CICC that make increase the quench propagation speed. However, it is clear that in the "infinite exchange quench speed" formula, these two phenomena are not taken into account, as the main driving parameter are the heat conduction of the dissipative heat losses by Joule effect. Indeed, the "infinite exchange quench speed" formula seems limited for our particular case. Therefore, the next section is dedicated to the demonstration of an "improved" formula, called the "helium flow quench velocity" formula, in order to take into account the transport of the warm helium and the friction forces in the computation of the quench propagation speed.

4.3.3. "Helium flow quench velocity" formula

It has been shown that the "infinite exchange quench speed" formula was giving slower results than the one measured during the quench experiments. Therefore, this section is dedicated to the development of an "improved" formula, the "helium flow quench velocity" formula, that takes into account the friction forces and the transport of warm helium, to retrieve the speeds measured during the quench experiments. In addition to the infinite exchange assumption, the velocity of the helium is taken into account to consider the phenomena observed during a THQB. To do so, a similar method as the one presented in section 1.2.3.1 is used. In this section, the heat equation of the conductor was used to demonstrate the "infinite exchange quench speed" formula. It was considered that the exchange between the conductor and the helium was infinite. A homogenized material, composed of the copper, the Nb-Ti and helium was then considered. However, the friction forces and the advection of the warm helium appear only in the heat equation of the helium and not in the temperature balance of the conductor. Therefore, the idea is to obtain a homogenized equation built from the sum of the conductor

heat equation, composed of the copper and the Nb-Ti, and of the helium heat equation. To do so, the two equations are presented in equation 1.7. The heat equation of the conductor is the same that the one presented in chapter 1 and the helium equation is the energy conservation equation [82], that is deeper presented in chapter 5.

$$\begin{cases} \rho_s C_{p_s} \dfrac{\partial T_s}{\partial t} & = \lambda_s \dfrac{\partial^2 T_s}{\partial x^2} + \eta_{eq} J^2 - \dfrac{P_{wet}}{S_s} h(T_s - T_h) \\ \rho_h C_{v_h} \dfrac{\partial T_h}{\partial t} + \rho_h C_{v_h} \varphi_h T_h \dfrac{\partial v_h}{\partial x} + \rho_h C_{v_h} v_h \dfrac{\partial T_h}{\partial x} & = \dfrac{2 f \rho_h v_h^2 |v_h|}{D_h} + \dfrac{P_{wet}}{S_h} h(T_s - T_h) - \dfrac{\partial \dot{q}''_{cf}}{\partial x} \end{cases} \tag{1.7}$$

with ρ being the density, C_p and C_v respectively the specific heat capacity at constant pressure and constant volume, T the temperature, λ the heat conductivity, η_{eq} the electrical resistivity of the conductor defined as $\rho_{eq} = \rho_s \dfrac{S_s}{S_{Cu}}$, J the current density in the conductor, P_{wet} the wet perimeter, h the convective heat transfer coefficient, v the velocity, φ the Grüneisen parameter, f the friction factor, D_h the hydraulic diameter, $\dot{q}''_{cf}$ the counter-flow mechanism heat flux. The indexes s and h stand respectively for solid and helium.

In order to conserve only the heat transport and the friction forces, it is considered that all other terms, being the compression and Goerter-Mellink terms, are negligible. These assumptions are verified in the next chapter, but are necessary to obtain the "improved" equation of the quench propagation speed. Moreover, to obtain a homogenized material, it must be considered that the temperature is equal between them. Therefore, it is considered that $T_s = T_h$. This way, the convective heat term is null, and the two equations can be gathered in one, by multiplying each equation by the associated cross-section. The result of the gathered equation can be seen in equation 4.5.

$$(\rho_h C_h S_h + \rho_s C_s S_s) \frac{\partial T}{\partial t} + \rho_h C_h v_h S_h \frac{\partial T}{\partial x} = \lambda_s S_s \frac{\partial^2 T}{\partial x^2} + \rho_{eq} J^2 S_s + \frac{2 f \rho_h v_h^2 |v_h|}{D_h} S_h \tag{4.5}$$

By dividing by S_s, we set $\hat{C}_h = C_h \dfrac{S_h}{S_s}$. From there, is it possible to write $(\rho_h \hat{C}_h + \rho_s C_s) = \rho_h (\hat{C}_h + \dfrac{\rho_s}{\rho_h} C_s) = \rho_h \hat{C}_t$, with $\hat{C}_t = \hat{C}_h + \dfrac{\rho_s}{\rho_h} C_s$. The equation can then be reduced at equation 4.6.

$$\rho_h \hat{C}_t \frac{\partial T}{\partial t} + \rho_h \hat{C}_h v_h \frac{\partial T}{\partial x} = \lambda_s \frac{\partial^2 T}{\partial x^2} + \rho_{eq} J^2 + \frac{2 f \rho_h v_h^2 |v_h|}{D_h} \frac{S_h}{S_s} \tag{4.6}$$

Finally, by using the $T(x,t) = T(\xi)$ substitution, with $\xi = x - v_q t$, as in the chapter 1, the equation is written as equation 4.7.

$$\frac{\partial^2 T}{\partial \xi^2} + [\hat{C}_t v_q - v_h \hat{C}_h] \frac{\rho_h}{\lambda_s} \frac{\partial T}{\partial \xi} = -(\frac{\eta_{eq} J^2}{\lambda_s} + \frac{2 f \rho_h v_h^2 |v_h|}{\lambda_c D_h} \frac{S_h}{S_s}) \tag{4.7}$$

The same resolution method is used, by considering a normal zone where the dissipative heat losses by Joule effect contribute to heat the conductor, and a superconducting zone where there is not heating by Joule effect. Therefore, the quench propagation speed can be written as equation 4.8.

$$v_q = \frac{\hat{C}_h}{\hat{C}_t} v_h + \frac{1}{\rho_h \hat{C}_t} \sqrt{(\frac{\lambda_s}{\Delta T})[\frac{2 f \rho_h v_h^2 |v_h|}{D_h} \frac{S_h}{S_c} + \eta_{eq} J^2]} \tag{4.8}$$

Finally, to take into account the phase change of the helium on the temperature range, the specific heat terms are approximated by an enthalpy variation, as it can be seen in equation 4.9.

$$v_q = \frac{\Delta\hat{h}_h}{\Delta\hat{h}_h + \Delta h_s} v_h + \frac{1}{\Delta\hat{h}_h + \Delta h_s} \sqrt{(\lambda_s \Delta T)[\frac{2 f \rho_h v_h^2 |v_h|}{D_h} \frac{S_h}{S_c} + \eta_{eq} J^2]} \tag{4.9}$$

This equation written as is takes into account the impact of three phenomena. The first one, already present in the classic "infinite exchange quench speed" formula 1.14, is the term linked to the dissipative heat losses by Joule effect, proportional to $\eta_{eq} J^2$. The second term inside the square root is linked to the friction forces. It appears that the friction forces act as a second heat source, that contribute to increase the quench propagation speed. The last term is linked to the warm helium transport, and is proportional to the velocity of the flow. At 1.8 K, the term $\frac{\Delta\hat{h}_h}{\Delta\hat{h}_h + \Delta h_s}$ is 0.97, meaning that slightly less than helium's velocity should be added to the "infinite exchange quench speed" of the dissipative heat losses to obtain a more realistic value of the quench propagation speed. Moreover, as it can be seen, by considering a null flow, the classic "infinite exchange speed" formula is retrieved. Therefore, by adding the different contributions considered in this "improved" equation to the already existing one of the dissipative heat losses by Joule effect, one can think that the experimental quench propagation speed could be retrieved.

This formula clearly shows that the helium transport velocity and friction can contribute to increase the value obtained with the "infinite exchange quench speed" formula and maybe explain the gap between these values and the experimental one. This depends on the contribution of each term of the formula to the overall speed that will be studied in chapter 5.

4.3.4. Parametric study of the *breaking phase*

The goal of this section is to study the triggering of the *breaking phase*. As before, the 10 kA case and the 13 kA case at 1.785 K are excluded. Figure 4.24 shows the normal length of all the quench tests in consideration.

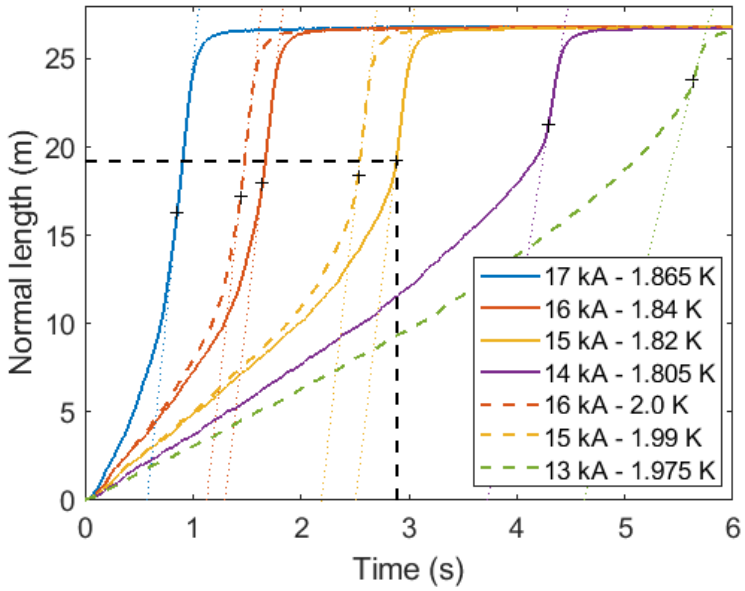

Figure 4.24: Normal length in function of the time of the quench cases presenting a *breaking phase*.

The *breaking phase* initiation points have also been plotted. They have been determined by assuming that the strong acceleration of the *breaking phase* was quasi-linear, and the goal is to find the point where the normal length curve and the linear curve meet. It corresponds then to the second derivative discontinuity point, corresponding to the important change of dynamics. The *breaking phase* initiation depends of both the crossed-length by the quench but also of the time that the quench propagated. As it can be seen in figure 4.24, the quenched-length and the propagation time before the break increase with the temperature margin increase. On the opposite, both the quenched-length and the propagation time decrease with the current increase. Therefore, to understand the impact of each parameter, the dependence of the space and time coordinates of the *breaking phase* in function of the current and the temperature margin can be looked at in detail. Figure 4.25 shows the quenched-length and the propagation time before the *breaking phase* in function of the current.

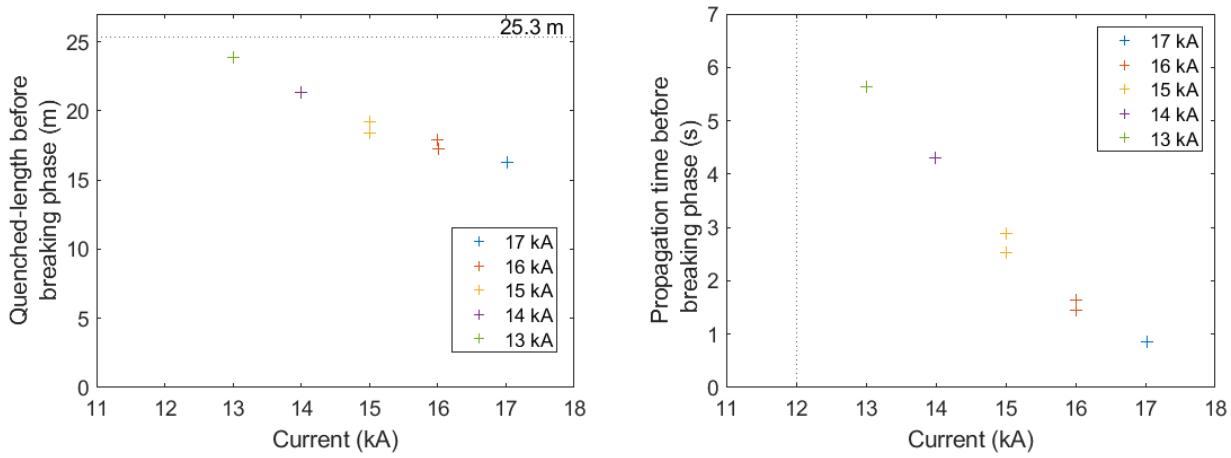

Figure 4.25: Quenched-length and propagation time before the *breaking phase* in function of the current.

The quenched-length and the propagation time before the *breaking phase* decrease quasi-linearly with the current. With a simple linear function, it can be extrapolated from figure 4.25 that with an available length of 25.3 m, the minimum current for triggering the *breaking phase* is around 12 kA. And with such a current, the minimal propagation time for triggering the *breaking phase* should be around 7 s. These simple analysis shows that there must be a current offset, depending on the available length and the propagation time, to allow seeing the *breaking phase* or not. Under this value, it should not be possible to identify the *breaking phase*. This theory is supported by the experiment: no *breaking phase* has been seen for the 10 kA (< 12 kA) case ; the 13 kA case is more difficult to comprehend, but the *breaking phase* would probably have started with a little longer propagation. The 13 kA case is then at the limit of the explained simple physics.

However, it is clear that the temperature margin decrease also decreases the time and distance before the *breaking phase*. Therefore, the same exercise than for the current can be done by considering the parameter $\frac{I\sqrt{T_t - T_0}}{\Delta H}$. This parameter is an arbitrary parameter, that has been chosen from the "infinite exchange quench speed" formula. It has been preferred to the temperature margin, influenced by both the initial temperature and the current. It allows to compare all the quenches, even the one done at the same current but at different initial temperature. The results are presented in figure 4.26.

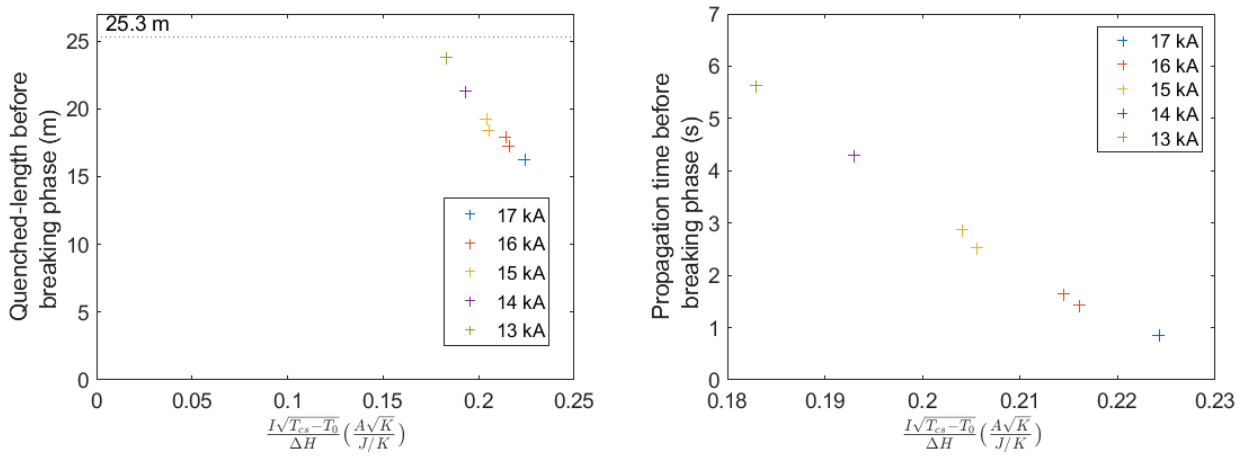

Figure 4.26: Quenched-length and propagation time before the *breaking phase* in function of the $\frac{I\sqrt{T_t - T_0}}{\Delta H}$ parameter.

For a higher temperature margin, corresponding to a low $\frac{I\sqrt{T_t - T_0}}{\Delta H}$ parameter, it is clear that the quenched-length and the propagation before initiating the *breaking phase* are more important. Moreover, both seem to also vary quasi-linearly with $\frac{I\sqrt{T_t - T_0}}{\Delta H}$. Indeed, the temperature margin can be reduced, either by decreasing the current sharing temperature T_{cs} or by increasing the initial temperature. For the first case, it can be done by increasing the current in MACQU and both lead to an earlier *breaking phase*. It is coherent that with equivalent Joule losses, the propagation time before the *breaking phase* decreases with the increase of the initial temperature.

Moreover, by extrapolating with an available length of 25.3 m, the minimum value of $\frac{I\sqrt{T_t - T_0}}{\Delta H}$ is around 0.17 SI, higher than the 0.14 SI obtained for the 10 kA case. The same conclusion as for the current can be done here; there must be an offset that allows seeing the *breaking phase*.

In conclusion, the *breaking phase* initiation time and location appears as both function of the current and of the temperature margin. Moreover, to see the appearance of the *breaking phase*, four coupled parameters seem to exist: a minimal current, a maximum temperature margin, a minimal propagation time and a minimal quenched-length.

Conclusions

This chapter allowed us to analyze the experimental results of the MACQU coil quench tests. By presenting the experimental protocol first, it has been shown that the goal of MACQU to verify the sensitivity of the quench detection system has been totally validated. With a quench propagation speed measured between 1 m/s and almost 10 m/s, the quench is largely fast enough to ensure the quench detection in any case. Moreover, it appeared that the quench propagation was divided in three phases: a first *quasi-linear phase*, an *acceleration phase* where the quench starts accelerating and a *breaking phase* where the quench greatly accelerates after a characteristic break. The assumption to explain such an acceleration is the Thermal Hydraulic Quench Back phenomenon: due to the important Joule losses generated during the quench, the pressure of the helium inside the CICC drastically increases and generates a flow towards

the magnet. The highly pressurized flow, compressed adiabatically and above the T_λ temperature, transporting warm helium and performing work against the friction drag, pre-warms the magnet far away from the quenched length. After some establishment time, corresponding to the *quasi-linear phase*, the quench starts accelerating due to the temperature increase far away from the quenched zone, corresponding to the *acceleration phase*. If the length is enough, the pre-warming can even make the magnet reach its critical temperature outside of the quenched length. At this moment, an important part of the coil will almost instantaneously quench, generating the *breaking phase*. However, it also appeared that the experimental quench propagation speed, estimated during the quasi- linear phase, was largely higher than the results obtained with the "infinite exchange quench speed" formula 1.14. To take into account the friction forces and the transport of warm helium, an "improved" quench propagation speed formula has been proposed, called the "helium flow quench velocity" formula. This equation needs the velocity of the helium to be used and is computed in the following chapter. Finally, it has been shown that the triggering of the *breaking phase* was strongly impacted by the current and the temperature margin. An increase of the current or a decrease of the temperature margin generates a sooner and closer *breaking phase* from the initiation point. The quenched-length and propagation time also appeared as offset parameters of the triggering of the *breaking phase*. Below the offsets, the break would arrive later and could not be seen in our boundary conditions.

The next chapter is the conclusion of this Ph.D. report. In order to further study the impact of each parameter on the different quench dynamics phases, the numerical tool THEA® is used to obtain some missing physical parameters as the pressure or the velocity. The goal is to present and compute a quench propagation model, based on the studied case of 15 kA at 1.82 K. Therefore, the different parameters as the flow, the pressure increase or the temperature profile, computed by THEA®, will allow us to analyze further the particular quench behavior of the MACQU coil.

5 - Numerical modeling and analysis of the quench behavior of the MACQU magnet

- Model the MACQU coil quench tests with the numerical code
- Analyze in details the mechanisms of the different quench dynamics phases
- Compare qualitatively and quantitatively the results obtained with the numerical code
- Verify the relevance of the "helium flow quench velocity" formula

5.1. Numerical implementation of the physical model in THEA®

After focusing on the different phenomena taking place during the quench propagation, the goal of this section is to analyze further the quench behavior of MACQU by a numerical approach. The well-developed THEA® code was chosen for its robustness and its open source files, allowing to modify several parameters to reproduce the experimental study conditions. In a first step, the physical model of the CICC is presented, divided in two distinct parts: the solid parts model, corresponding to the superconducting cable and the copper profile, and the fluid model, corresponding to the helium inside the CICC. In a second step, the boundary conditions of the model are presented, introducing the boundary conditions that THEA® can manage but also the "input" data such as the field map or the friction factor correlation, inherent to the characteristics of the MACQU coil.

5.1.1. Physical model for the quench propagation in a CICC

This section is dedicated to presenting the numerical quench model of the CICC, divided into the solid parts model and the fluid model. Both models are defined by two distinct equation sets. Concerning the solid parts model, the heat transfers are the heat conduction, dissipative heat losses by Joule effect, external heat loads and convective heat exchange with the fluid. For the fluid model, the heat transfers are the compression forces, the heat transport, the friction forces, the convective heat exchange with the solid and the Gorter-Mellink heat exchange mechanism. Indeed, to obtain comparable results between numerical and experimental approaches, it has been decided to model only the right side of the MACQU coil. As it has been shown in the previous chapter, the quench propagation is not perfectly symmetric, and only the quench propagation of the right side has been studied. Note that the arms, with their important decrease of the magnetic field, are not modeled. The model and the boundary conditions will then be adjusted to fit with this assumption and both are described in the following sections.

5.1.1.1. Thermal conduction model

The CICC is composed of different solid components. For the MACQU case, the different components are the superconducting cable and the copper profile. The components are assembled in one homogeneous "thermal" component and the material properties are assumed to be homogeneous in the cross-section. Each component can transport heat by conduction. The dissipative heat losses by Joule effect are generated in the copper cross-section, for which the RRR is 125. Moreover, the different thermal components can exchange heat by convection with the fluid component. By taking into account these parameters, a 1-D thermal conduction model of the CICC described by equation 5.1 is used for two main reasons. The first one is that

MACQU has been designed to neglect transversal heat diffusion (cf. chapter 2), so the thermal transverse heat conduction is not modeled which reduces the 3-D model to a 2-D model for the conductor. Moreover, it is also assumed that the temperature gradients in the conductor cross-section and the helium cross-section are small. This is not a strong hypothesis because the highest thermal diffusion time in the conductor between 1.8 K and 10 K is 5 ms, estimated with equation 3.5. The temperature is assumed to be constant in the cross-section. In these conditions, the quench propagates only longitudinally, and the 2-D model can be reduced to a 1-D model. It will then be considered that the thermal components exchange heat only longitudinally. The heat transfer equation reads,

$$\rho_s C_{p_s} \frac{\partial T_s}{\partial t} = \frac{\partial}{\partial x}(\lambda_s \frac{\partial T_s}{\partial x}) + \dot{q}'''_{Joule} + \dot{q}'''_{ext} + \frac{P_{wet}}{S_s} h (T_h - T_s), \tag{5.1}$$

where ρ is the density of the thermal component, C_p the specific heat capacity at constant pressure, T the temperature, λ the thermal conductivity, P_{wet} the wet perimeter, S_s the cross-section of the solid, h the convective heat transfer coefficient and x and t for the spatial and time coordinate. The temperature is considered constant in the cross-section of the thermal component, composed of two materials being the Nb-Ti and the copper, respectively 1.5 % and 98.5 % of the component's cross-section. The thermal properties are assumed to be homogeneous in the cross-section, and estimated by area weighting (for ρ and λ) or mass weighting (for the volumetric heat capacity).

Three heat sources appear in the model. The first one is $\dot{q}'''_{Joule}$, representing the volumetric dissipative heat losses by Joule effect if the component carries a current, and defined in equation 5.2,

$$\dot{q}'''_{Joule} = \frac{IE}{S_s} \tag{5.2}$$

with I the current, E the electric field and S_s the cross-section of the thermal component. For a purely resistive material, the electric field is defined in equation 5.3, with a linear relation between the field and the current density.

$$E = \eta_s J_s \tag{5.3}$$

with η_s the electrical resistivity of the solid and J_s the current density going through the solid, defined as $J_s = \frac{I_s}{A_s}$.

For a component containing a superconductor, a more general equation is obtained by distinguishing the superconducting cross section A_{sc} from the other materials A_{st} [16]. The total current in the thermal component is divided in part in the superconductor and part in the stabilizer, to follow the current conservation $I = I_{st} + I_{sc}$. Hence, the longitudinal electric field is the same in both components. Therefore, the electric field inside the superconductor verifies the equation 5.4 [16].

$$E = E_0 (\frac{I_{sc}}{I_c})^n \tag{5.4}$$

where E_0 is the electric field criterion to define the critical current I_c. In the case of MACQU, E_0 is set at 10^{-5} V/m, corresponding to the usual criteria of 0.1 µV/cm. The n parameter characterizes the dependence of the electric field to the critical current transition. The high value of 50 is used in the model [62].

The voltage equality between the superconductor and the stabilizer can be written as in equation 5.5. I_{sc} is solved by an iterative technique and the electric field E is deduced from equation 5.4.

$$\eta_{st}\frac{I - I_{sc}}{A_{st}} = E_0(\frac{I_{sc}}{I_c})^n \tag{5.5}$$

The second heat $\dot{q}'''_{ext}$ is an external heat flux. The power deposition of the heaters, used to initiate the quench, is modeled as external heat source. The last heat source is the convective heat flux term, representing the heat exchange between the thermal component and the fluid component. This term will be more detailed in the following section, concerning the fluid model.

5.1.1.2. Fluid model

The fluid model is written in three conservation equations: the mass, the momentum and the energy [82]. The three equations are written in the non-conservative form and present the 3 independent variables to be solved: the pressure P in equation 5.6, the velocity v in equation 5.7 and the temperature T in equation 5.8 [16]. Hence, the compression and friction forces terms, the advection term and the convection term are then explicitly appearing. Terms like the friction forces term comes from the conservation of the momentum equation, intervening in the derivation of both conservation of mass and energy equations, as it is demonstrated in Appendix A. Moreover, written as are, the equations present several advantages: the pressure term appears explicitly and then is easier to treat as it is directly computed ; the numerical simulations are more stable with the equations written in this way as just simple linearizations are needed and no iterative techniques ; as the model can be used for any fluid, the model is also more accurate ; finally, the Gorter-Mellink term, highly non-linear, can be linearized in function of the temperature, which could not be done with the energy equation written with the internal energy variable. Moreover, MACQU is composed of a unique channel, the hydraulic coupling terms will therefore not be considered and presented here.

$$\frac{\partial P_h}{\partial t} + \rho_h c_h^2 \frac{\partial v_h}{\partial x} + v_h \frac{\partial P_h}{\partial x} = 2f\rho_h\varphi\frac{v_h^2|v_h|}{D_h} + \varphi\dot{q}'''_{conv} - \varphi\frac{\partial \dot{q}''_{cf}}{\partial x} \tag{5.6}$$

$$\frac{\partial v_h}{\partial t} + v_h\frac{\partial v_h}{\partial x} + \frac{1}{\rho_h}\frac{\partial P_h}{\partial x} = -2f\frac{v_h|v_h|}{D_h} \tag{5.7}$$

$$\frac{\partial T_h}{\partial t} + \varphi_h T_h\frac{\partial v_h}{\partial x} + v_h\frac{\partial T_h}{\partial x} = \frac{2f}{C_{v_h}}\frac{v_h^2|v_h|}{D_h} + \frac{\dot{q}'''_{conv}}{\rho C_{v_h}} - \frac{1}{\rho C_{v_h}}\frac{\partial \dot{q}''_{cf}}{\partial x} \tag{5.8}$$

where P is the pressure, ρ the density, c the isentropic sound speed, v the velocity of the flow, f the friction coefficient, φ_h the Grüneisen parameter, D_h the hydraulic diameter, T the temperature, C_v the specific heat capacity at constant volume, the index h for helium and the time and space coordinate t and x. The terms $\dot{q}'''_{conv}$ and $\dot{q}''_{cf}$ are heat sources that are defined below.

The $\dot{q}''_{cf}$ term is defined by the equation 5.9. It represents the heat flux due to the counter-flow mechanism present in the superfluid helium, and also identified as the Gorter-Mellink mechanism. As explained in chapter 1, this mechanism is responsible of the important heat transport capability of the superfluid helium. This term will influence the heat balance while the temperature of the helium is below T_λ.

$$\dot{q}''_{cf} = -[F(P,T)\ \frac{\partial T}{\partial x}]^{1/\eta} \tag{5.9}$$

where $\dot{q}''_{cf}$ is the counter-flow heat flux in the x-direction, $F(P,T)$ the characteristic thermal conductivity of the superfluid helium defined in function of the temperature and the pressure, and $1/\eta$ an empirical parameter in the range of 1/3.

The second heat source $\dot{q}'''_{conv}$ (Eq. 5.10) represents the volumetric heat flux exchanged between the solid and the helium by the wetted perimeter, and couples then the solid parts and fluid model and reads as.

$$\dot{q}'''_{conv} = \frac{P_{wet}}{S_h} h(T_s - T_h) \tag{5.10}$$

where P_{wet} is the wet perimeter, S_h the helium cross-section, h the convective heat transfer coefficient, T_s the temperature of the solid and T_h the temperature of the helium.

5.1.2. Boundary conditions for the quench propagation in a CICC

5.1.2.1. Boundary conditions of the solid part

Two types of boundary conditions can be defined for the solid components:

- Dirichlet boundary conditions that allow to impose the temperature.
- Neumann boundary conditions that allow to impose the heat flux.

As explained in chapter 3, the CICC is connected to the W7X boxes, filled with superfluid helium. Therefore, it is considered that no heat flux arrives on the CICC from the boxes. The Neumann boundary conditions defined in equation 5.11 are used at the extremities of the coil and a null heat flux is imposed because the extremities are thus assumed to be adiabatic. Only half of the coil is modeled, so on the other side, corresponding to the center of the coil, the heat flux is also considered null, by symmetry.

$$-S_s \lambda_s \frac{\partial T_s}{\partial x} = q_{boundary} = 0 \tag{5.11}$$

The initial temperature of the solid is 1.82 K. To initiate the quench, the heaters, represented by an external heat flux, are defined on half their length, corresponding to 0.102 m. The deposited power is 48 W/m during 0.5 s, in a square window-type deposition. Once the quench is initiated, the quench can be accelerated in function of the magnetic field map. As the right side of the magnet only has been studied in the previous chapter, the field map of the right side of the coil only has been integrated to THEA®, represented in figure 5.1. The magnetic field varies from 1.97 T to 1.88 T, and increases to 1.99 T before the extremity, and corresponds to the field map at 15 kA. As it can be noticed, the right side is 25.34 m long. As the *breaking phase* of the quench propagation has been seen below 25 m, which means that the quench propagation front is still inside the solenoid, the arms of the coil have not been modeled. Moreover, the magnetic field is much slower in the arms and can strongly slow down the quench propagation. Then, there will be a slight difference in length between numerical and experimental results, but that will not affect the analysis of the quench behavior.

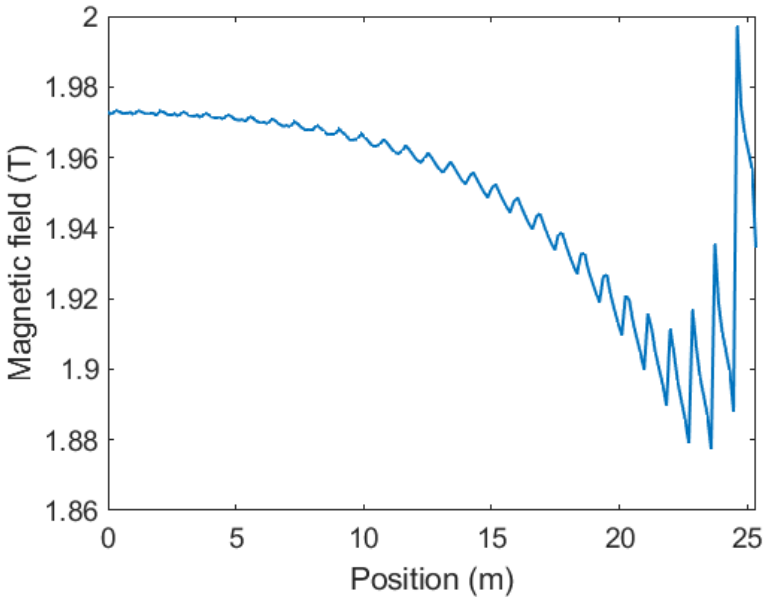

Figure 5.1: Field map implemented in the THEA® model, at 15 kA. The field map is adjusted in function of the current.

Finally, concerning the meshing, the coil is divided in 20000 elements, being the maximum possible element number with THEA® [25]. On the 102 mm of heaters, the number of THEA® 1-D elements (1200) is higher than anywhere else in the coil, to have a high precision in the zone of the quench initiation. The mesh is uniform outside of this zone. Having 1200 elements in the refined zone and 18800 in the rest of the magnet is the mathematical optimum in terms of mesh dimensions, as it minimizes the sum of the element dimension in each region.

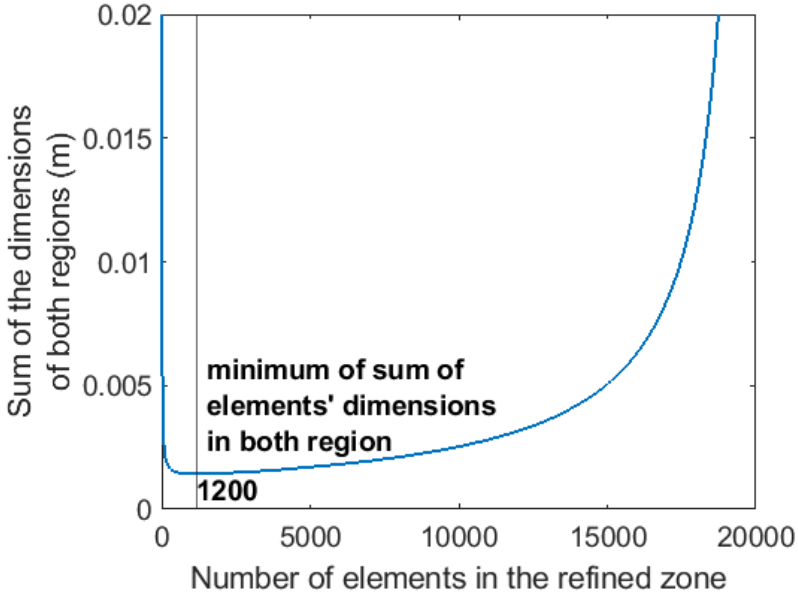

Figure 5.2: Sum of the dimensions of the elements in both regions in function of the number of element in the refined zone which is the heaters region. The equation $nb_{refined\ zone} + nb_{rest\ of\ coil} = 20000$ must be constantly verified, with nb being the number of element in the region.

THEA® also allows an adaptive mesh to follow the quench propagation front [45]. However, with the maximum number of points, the mesh is anyway very thin, so refining it even more near the quench propagation front has a negligible effect on the final results. A parametrical study has been carried out and for an equivalent number of elements, the results are different by less than 2 %. In addition, the adaptive-grid calculation leads to several hours of computation compared to less than two hours for a non-adaptive grid. Therefore, a non-adaptive grid is used with an adaptive time scheme. The time step varies from 10^{-5} s to 1 s.

5.1.2.2. Boundary conditions of the fluid domain

There are two possible boundary conditions for the fluid model:

- A closed pipe condition, with an imposed null flow, corresponding to a null velocity $v_h = 0$.
- A reservoir condition, with a large volume of helium at imposed pressure and temperature.

Both boundary conditions are used in the model. The closed pipe condition is used at X = 0 m, corresponding to the center of the coil, so by symmetry the velocity is imposed at 0. The reservoir condition is used at the extremity of the coil, with a helium bath considered at the initial conditions, which are 1.82 K and 1 bar.

The friction factor and the convective heat transfer coefficient must be fixed before the computation. The friction factor depends of the regime of the flow, laminar or turbulent. Therefore, two correlations are used, depending on the Reynolds number, as defined in equation 5.12. The first one is based on a correlation already defined in THEA® for a laminar flow [83]. The second one is for a turbulent flow, with the transition laminar-turbulent fixed at 3500, and empirically built based on measurements done on MACQU CICC [61].

$$\begin{cases} f = \dfrac{16}{Re} \textbf{ if } Re \leq 3500 \\ f = 0.25(\alpha + \beta Re^{\gamma}) \textbf{ if } Re > 3500 \end{cases} \tag{5.12}$$

with $\alpha = 0.031$, $\beta = 7691$ and γ = -1.537. The 0.25 factor is used to link Darcy's and Fanning's friction factors, as THEA® uses the Darcy's definition of the friction factor in the code.

Several correlations are also defined in THEA® for the computation of the heat transfer coefficient [84]. As the helium is initially superfluid, the correlation must reproduce the important heat transfer due to the low Kapitza thermal resistance [52]. Based on equation 1.28 reminded below, the heat transfer coefficient is defined as $h_K = \alpha(T_s + T_f) * (T_s^2 + T_f^2)$, T_s and T_f stand for the temperature of the solid and the fluid respectively. α and n are characteristic coefficients of the Kapitza heat transfer, estimated at $\alpha = 200$ $\mathrm{Wm^{-2}K^{-3}}$ for the copper [53] and $n = 3.8$.

$$q = \alpha(T_s^n - T_f^n) \tag{1.28}$$

As the helium changes of phase during the quench propagation, the correlation should not be relevant above T_{lambda}. However, for simplicity, it has been decided to keep the Kapitza correlation for the entire calculation. Indeed, at initial conditions, the heat exchange coefficient can be estimated to 4.6 $\times$ 10^3 $\mathrm{Wm^{-2}K^{-1}}$. During the quench propagation, the helium is set in turbulent motion. At the quench propagation front, the temperature of the helium is around 5 K (close to T_{cs} and the pressure varies on a range between 5 bars to 15 bars, with a Reynolds number of 3500 (transition value of Reynolds). With conservative values then, it is possible to estimate the heat exchange coefficient with the Dittus-Boelter correlation [84] to be 1.1-1.2 $\times$ 10^3 $\mathrm{Wm^{-2}K^{-1}}$. The heat exchange coefficient is then anyway very high. A

sensitivity study has been carried out and a variation of a factor 10 of the convective heat exchange coefficient shown that the overall results was maintained. It is shown in the following section that the temperature difference between the conductor and the helium is very small anyway. This assumption, as anyway the real physics of the turbulent heat exchange is not well-mastered, ensures giving conservative results of the quench propagation speed.

In conclusion, the coupled solid and fluid models have been presented. Assumptions were presented, such the modeling of only half of the coil, or the non-modeling of the inter-turn thermal diffusion. It has been also shown that different key parameters were needed to represent as well as possible the experimental quench conditions, in terms of initial temperature or for the friction factor coefficient, for which the correlation has been presented. As a reminder, the table 5.1 gathers the implemented characteristics of the model. The following section is dedicated to the analysis of a typical quench propagation pattern, as it was done in the previous chapter. The goal is to verify the quench dynamics predicted by THEA® but also to analyze each phase of the quench dynamics with all the physical variables that were not measured during the experiment.

Table 5.1: MACQU characteristics used in the computations.

Copper section (mm^2)	198.7
Helium section (mm^2)	8.28
Current (A)	15003
Initial temperature (K)	1.82
Initial pressure (Pa)	10^5
Copper RRR	125
n factor	50
Hydraulic diameter (mm)	0.34
Wet perimeter (mm)	96
HTC correlation	Kapitza
Total conductor length (m)	25.34
Number of elements	20000
Dimension of elements (mm)	1.3
Number of refined elements	1200
Dimension of refined region (mm)	102
Dimension of refined elements (μm)	85

5.2. Analysis of a typical quench propagation pattern with THEA®

The goal of this section is to qualitatively analyze the quench phenomena, with the numerical tool THEA®, in order to identify, analyze and explain the different quench dynamics but also verify its behavior at different current. To do so, a numerical computation on the already studied quench propagation case at 15 kA at 1.82 K is performed. On purpose, this section will focus on the physics behind the quench produced by THEA® with no comparison yet with experimental results. In a first step, it is shown that THEA® qualitatively reproduces well the three phases observed experimentally. The goal will then be to verify the assumptions done on the previous chapter concerning the different phenomena occurring during the propagation. To do so, each phase is further analyzed thanks to the three independent variables of the helium. A phenomenological study is done by focusing on the different profiles of the parameters, and

presenting their variation. To go further in the analysis, the different terms of the model equations and their time integrals are computed, to see which phenomenon dominates during each phase. To do so, four study points are considered to compare the evolution of the different phenomena in function of the position in the coil: X = 0.5 m close to the initiation point for the *quasi-linear phase*, X = 7.5 m and X = 15 m where the quench has already started to accelerate and X = 22.5 m where the *breaking phase* is already triggered. The "helium flow quench velocity" formula is also punctually used to support the physical analysis. Finally, as for the previous chapter, a parametric study of the current is done to verify more globally the quench behavior.

5.2.1. Identification of the different quench dynamics

This section is dedicated to the study of the normal length evolution, in order to identify the different quench dynamics. The goal is to qualitatively verify the quench behavior that our code predicts for the studied quench case in chapter 4 (15 kA case at 1.82 K). The normal length evolution is depicted in the figure 5.3.

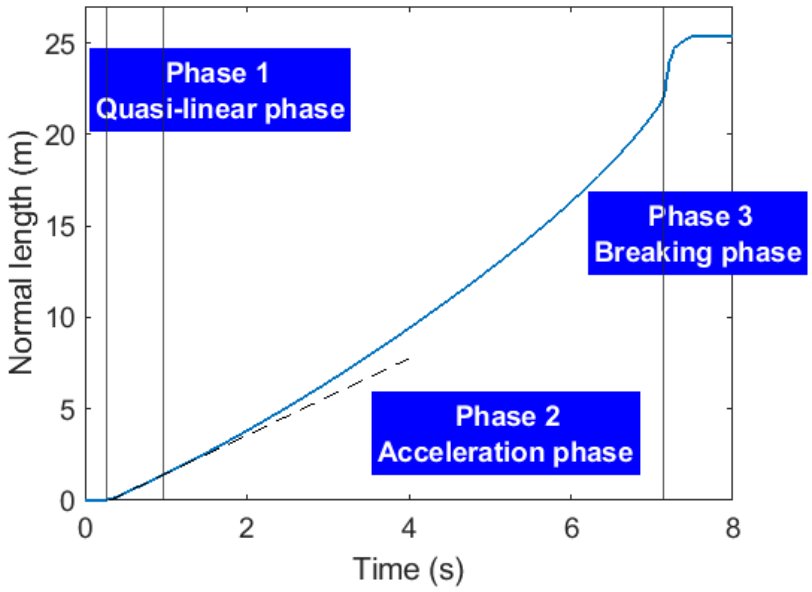

Figure 5.3: Time evolution of the normal length, obtained with our code. The experimental behavior is well captured with three distinct phases: the *quasi-linear phase*, the *acceleration phase* and the *breaking phase*. The plateau means that the whole coil has quenched and there is no evolution of the normal length anymore.

As it can be seen, the three main phases observed experimentally can also be seen in the results of the numerical simulations. Indeed, the propagation starts after a short pulse phase, with the *quasi-linear phase* where the quench seems to propagate at constant speed. The progressive acceleration of the quench propagation characterizes the second phase, the *acceleration phase*. Finally, after a clear break, the quench propagation speed greatly increases during the *breaking phase* before reaching the plateau where the whole coil has quenched.

The first conclusion is that our code reproduces well the quench dynamics. During the following sections, the goal is then to analyze each phase, by studying the computed variables such as the pressure or the velocity, variables not measured during the experimental studies.d

5.2.2. Analysis of the *quasi-linear phase*

This section is dedicated to the analysis of the *quasi-linear phase*. The goal of this section is to analyze the cause of this propagation at constant speed, by presenting a phenomenological analysis of the *quasi-linear phase* and by highlighting the variations of the different physical variables. In a second step, the different phenomena dominating the *quasi-linear phase* are identified.

5.2.2.1. Phenomenological analysis of the normal length evolution during the *quasi-linear phase*

A focus has been done on the *quasi-linear phase* in figure 5.4, where the pulse phase is not shown. Two phases can be seen: a first erratic phase, where the quench propagation speed is initially high, and a second phase where the quench propagation speed decreases quickly towards the quasi-linear regime. During the quasi-linear regime, the quench propagation speed is computed to 2.10 m/s.

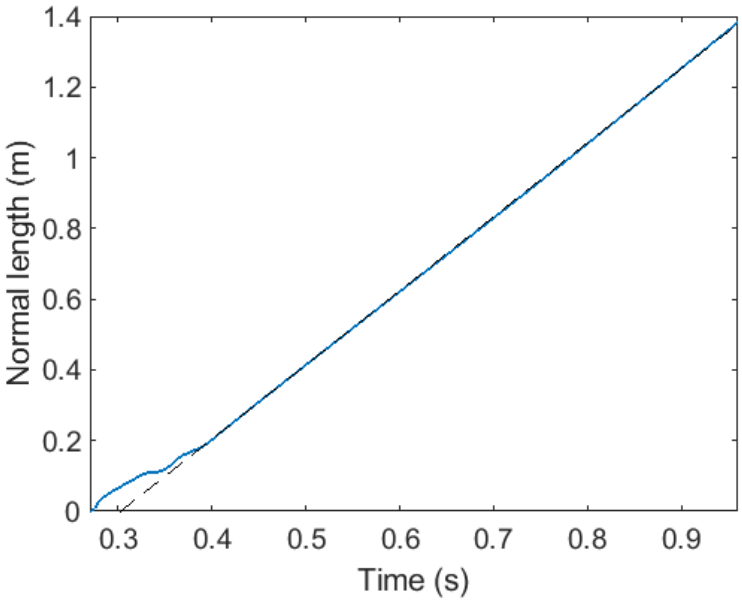

Figure 5.4: Time evolution of the normal length in the *quasi-linear phase* of the quench propagation, obtained with THEA®.

The initial erratic evolution can be seen on several other cases, particularly for lower current cases, and seem to be due to the power deposition of the heaters that slightly accelerates the quench initially. Indeed, the power deposition of 48 W/m is not negligible compared to the dissipative heat losses by Joule effect, that are between 95 and 342 W/m for a current between 10 kA and 17 kA. Therefore, the external power of the heaters contributes to accelerate the quench initially. Moreover, the oscillations seem to stop, or at least strongly decrease, at around 0.1 m, corresponding to the end of the heaters zone. It corresponds to the interface between the zone where the coil is heated due to the heaters and the rest of the CICC. The effect of the heaters seems thus only local and does not affect the rest of the propagation. As it can be seen, just after 0.2 m, the quasi-linear regime is reached. In addition, this erratic evolution also evokes the initial oscillations observed in chapter 4.

The temperature profile of the solid part, the pressure profile and the helium velocity profile are presented in figure 5.5. The temperature of the solid part increases in the quenched zone,

and a bit further, but the temperature is unchanged in the rest of the coil. Therefore, it could be assumed that the quench propagates in a similar way as in the "infinite exchange quench propagation" formula as presented in chapter 1, with the stagnant fluid and the solid at constant temperature in the non-quenched zone. However, it can be seen on the velocity evolution that a flow is generated in the coil. Globally, the velocity increases in the quenched zone to slightly less than 2 m/s, and decreases in the non quenched-zone. The pressure of the helium increases in the quenched zone to around 5 bars, due to the power deposited by the heaters in a first step, and by the quench in a second step.

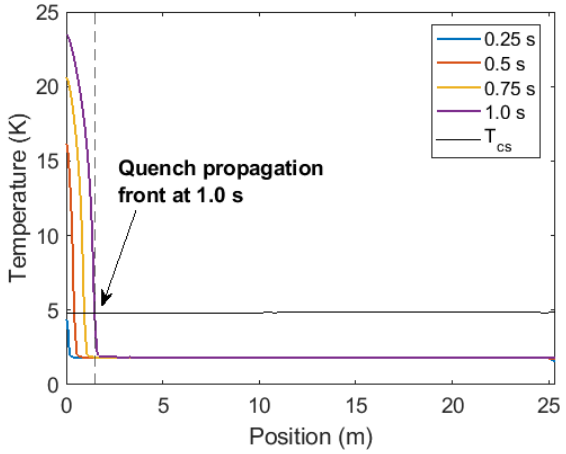

(a) Temperature profile.

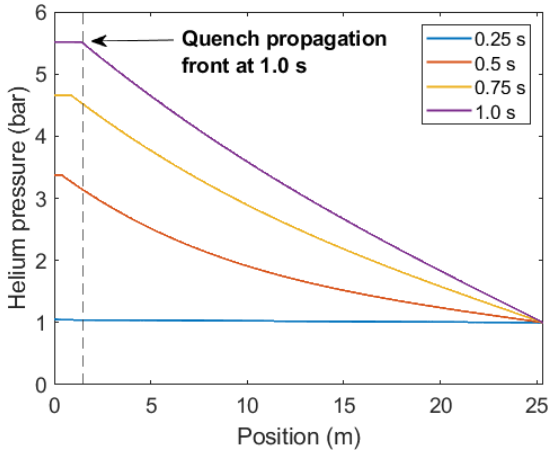

(b) Pressure profile.

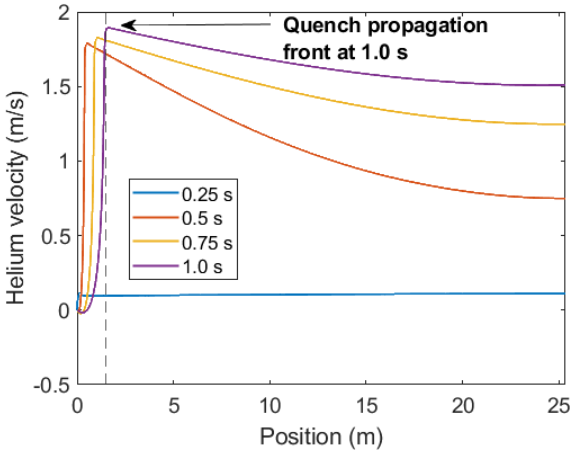

(c) Velocity profile.

Figure 5.5: Evolution of the temperature, pressure and velocity profiles during the *quasi-linear phase* along the length of the MACQU coil. In the quenched zone, the temperature increases and the pressure is constant. The velocity increases in the quenched zone while decreases in the non-quenched zone.

By focusing now at X = 0.5 m, it can be seen in figure 5.6 that the temperature of the helium and the conductor remain constant until 0.25 s, where the temperature increasing very slowly until 0.4 s, corresponding to the time where the quench starts propagating. Then, as the quench gets closer, both temperature increases. Moreover, the temperatures remain very close between the conductor and the helium, the maximum difference is reached at 0.48 s and is 0.05 K. The velocity remains constant, and after a plateau until 0.25 s, increases until 1.77 m/s. It is interesting to notice that the velocity increases much before the arrival of the quench.

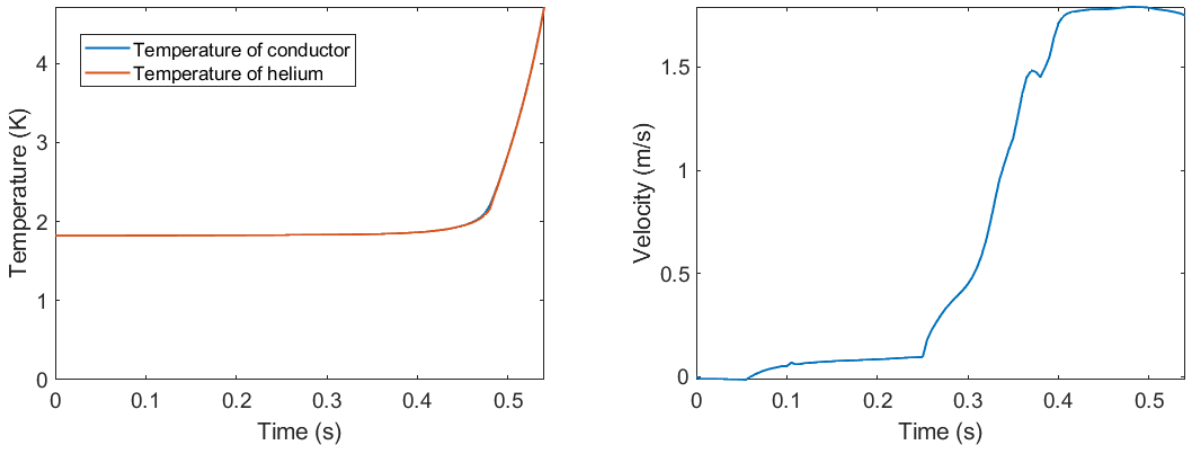

(a) Temperature evolution.

(b) Velocity evolution.

Figure 5.6: Time evolution of the temperature and velocity at X = 0.5 m. The temperature starts increasing at 0.4 s while the velocity, after a plateau until 0.25 s, increases strongly to a plateau around 1.8 m/s.

Therefore, in order to understand which phenomena is responsible for the time variation of the variables before the quench initiation, the following section presents the different terms of the fluid model and their time integrals.

5.2.2.2. Identification of the dominant phenomena during the *quasi-linear phase*

As identified earlier, the temperature and the velocity of the helium are increasing before the quench arrival. To identify which phenomenon is responsible of such increases, the different terms of the temperature of the fluid model and the sum of the temperature balance terms of the solid parts model have been computed in figure 5.7. The different terms are shown only until the quench, as the Joule effect term is largely dominant after. The terms of the velocity balance have not been plotted, as it is an equilibrium between the friction term and the pressure gradient term, showing that the pressure drop is generated by the friction forces.

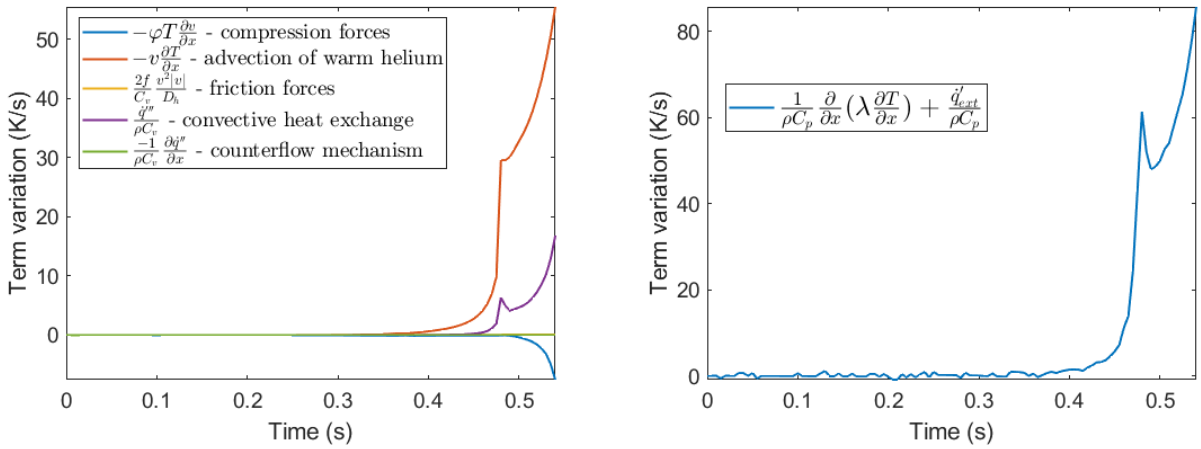

Figure 5.7: Time evolution of the terms from the fluid temperature equation and terms from the solid parts temperature equation at X = 0.5 m. The advection term is dominant in the fluid model while the conduction term is dominant for the solid parts.

The first evident result is that the convective heat exchange term is positive, meaning that

the helium extracts heat from the solid. The temperature of the helium increases then by convection with the solid part but also due to the advection of warm helium. An important result to highlight is that the Gorter-Mellink heat exchange mechanism of the helium does not contribute at all to the temperature change of the helium. Indeed, due to the too small helium cross-section, this heat transfer is totally negligible, contrarily to what could be expected.

Important peaks can be noticed for most of the terms around 0.45 s, corresponding to the λ transition of the helium. Due to the inversion of the sign of the Grüneisen parameter, the compression forces term becomes negative and contributes to slow down the temperature increase. At the opposite, the pressure increases as the friction term and the convective heat exchange term become positive.

Finally, the heating of the coil is done by heat conduction. Indeed, when the quench starts propagating after 0.25 s, a strong thermal gradient is established at the interface of the heaters region, and by conduction, the temperature of the coil starts increasing.

By plotting the time integral of the terms from the fluid temperature equation (figure 5.8), it is confirmed that the transport term is the dominant term in the temperature increase of the helium. About 2.5 K increase comes from the transport term. The convective term weights only for 0.4 K in comparison while the compression term contributes to decrease the temperature by 0.1 K. Without advection, the temperature of the helium would increase less, and this would slow down the quench, being comparable to the "infinite exchange" quench case. In our case, it is clear that the transport term also contributes to drive the quench propagation close to the quench propagation front and confirms that the "infinite exchange quench speed" formula 1.14 is not valid in our case.

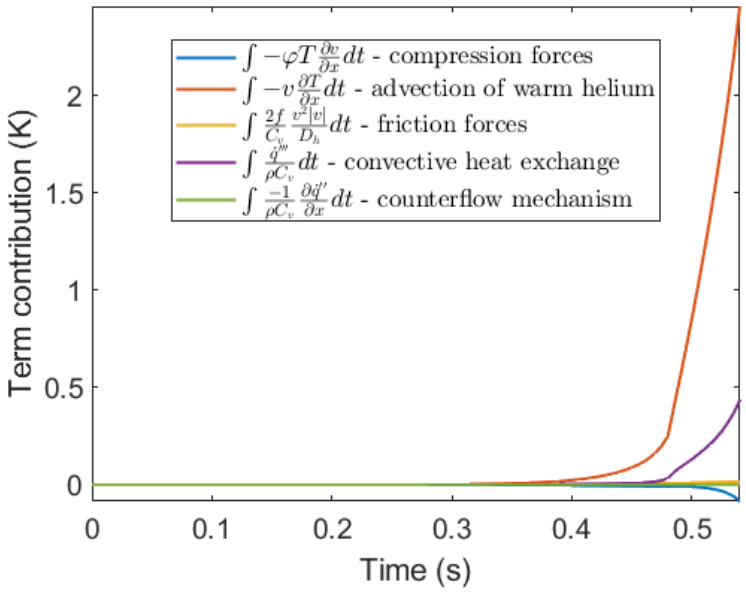

Figure 5.8: Time evolution of the integral of the terms from the fluid temperature equation at X = 0.5 m. The advection term contributes the highest to the temperature increase of the helium. The convective heat exchange term being positive, the solid part warms the helium during the quasi-linear phase.

To summarize, the superconducting cable remains at initial temperature until the quench initiation. Before the quench arrives at a defined position, several phenomena start: the superconducting cable starts to slowly warm due to heat conduction and the helium's temperature increase is mostly generated by advection and convection. The quench propagates at constant

speed during this phase. In these conditions, it is possible to estimate the different terms of the "helium flow quench velocity" by the formula 4.9 recalled below. The advection term can be estimated to 1.71 m/s and the heat source term, composed of the friction contribution and the Joule dissipation contribution, to 0.44 m/s. The quench propagation speed is thus 2.15 m/s.

$$v_q = \frac{\Delta\hat{h}_h}{\Delta\hat{h}_h + \Delta h_s} v_h + \frac{1}{\Delta\hat{h}_h + \Delta h_s} \sqrt{(\lambda_s \Delta T)[\frac{2 f \rho_h v_h^2 |v_h|}{D_h} \frac{S_h}{S_c} + \eta_{eq} J^2]} \tag{4.9}$$

The helium velocity is 1.77 m/s. The current is 15003 A and 1.97 T, for a RRR of 125. ΔT is 5.76 K.

The heat conduction in the solid plays an important role in the quench propagation and the warming until T_{cs}. However, based on equation 4.9, the heat source term, in which the conduction and the Joule dissipation are dominant, is much smaller than the advection term. Both drive the quench propagation but the advection is the main driver of the quench propagation speed. Therefore, if the quench propagation speed is constant, it is mainly due to the fact that the helium velocity is constant. The consideration of the advection in the quench propagation speed computation appears then as mandatory, and shows the limits of the "infinite exchange quench speed" formula 1.14.

The flow established in the coil thus contributes to the quench propagation. It is shown in the following section that the pre-heating of the coil starts also thanks to the flow downward in the coil and far away from the quench propagation front.

5.2.3. Analysis of the *acceleration phase*

After showing that the conditions for initiating the *acceleration phase* are reunited during the *quasi-linear phase*, this section is dedicated to the analysis of the *acceleration phase*. The goal is to identify the variation of the physical parameters describing the quench behavior but also to identify the causes of these variations. In a first step, a phenomenological analysis of the *acceleration phase* is done, to illustrate the variations of the physical parameters along the coil. In a second step, the different terms of the models, and their time integrals, are computed to identify and quantify the effect of the different phenomena driving the quench propagation. However, as the *acceleration phase* is the longest phase of the three phases, the study is done at two positions: X = 7.5 m and X = 15 m. It allows showing the evolution of the different phenomena even during the *acceleration phase*.

5.2.3.1. Phenomenological analysis of the normal length evolution during the *acceleration phase*

The *acceleration phase* starts when the normal length curve deviates from the initial quasi-linear regime, as it can be seen in figure 5.9. The acceleration is progressive, but by a simple linear regression at X = 15 m, it can be computed that the quench is already propagating at 3.45 m/s, comparing to the 2.10 m/s initial speed.

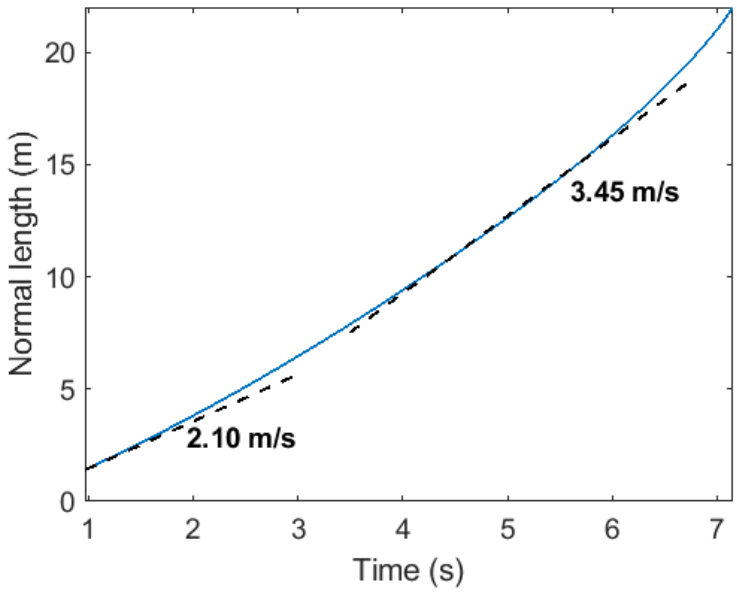

Figure 5.9: Time evolution of the normal length in the *acceleration phase* of the quench propagation, obtained with THEA®.

This acceleration was assumed to be due to the THQB phenomenon, generating a pre-heating of the coil due to the helium flow inside the conduit. It can be seen in figure 5.10 that the coil is effectively pre-heated. At the beginning of the *acceleration phase* the non-quenched zone is still at 1.8 K, but at 6.5 s at the end of the *acceleration phase*, the non-quenched zone is at 4.0 K and has increased continuously in between.

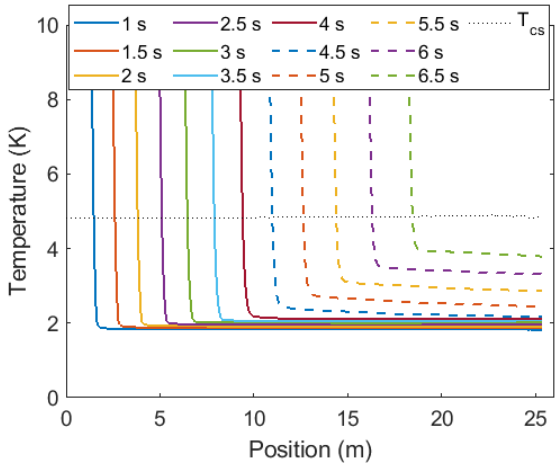

Figure 5.10: Evolution of the temperature profiles during the *acceleration phase*. The temperature increases in the non-quenched zone due to pre-heating.

In addition, unlike to the *quasi-linear phase*, after 4.5 s, the speed is higher in the non-quenched zone than in the normal zone (figure 5.11 (a)), and keeps increasing while the quench propagates. The pressure is at 8 bar inside the quenched zone and keeps increasing (figure 5.11 (b)), but remains at 1 bar at the extremity, meaning that the pressure gradient increases along the coil.

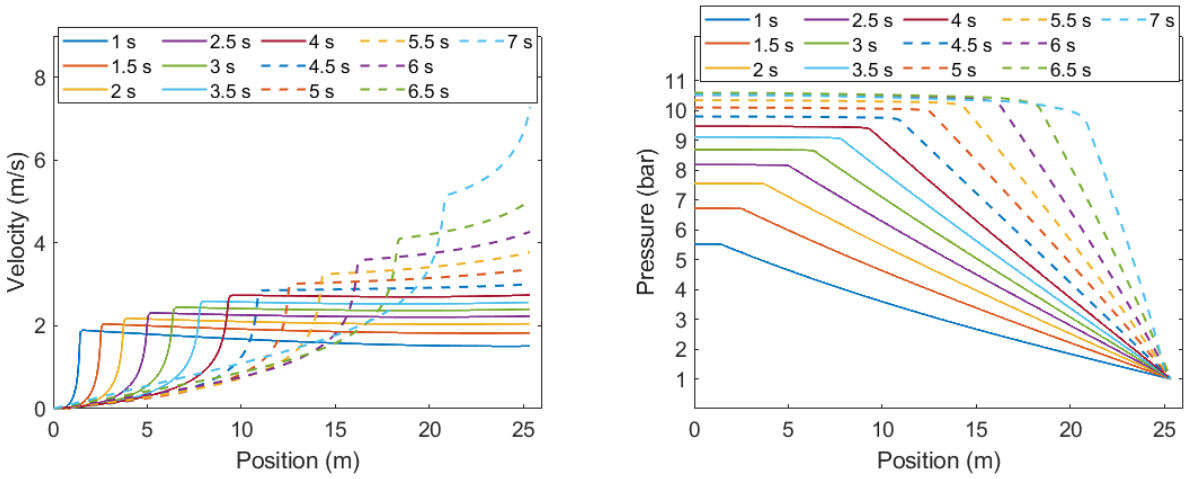

(a) Velocity profile.

(b) Pressure profile.

Figure 5.11: Evolution of the velocity and pressure profiles during the *acceleration phase*. The pressure increases in the quenched-zone, the pressure gradient increases thus in the non-quenched zone. The velocity is more important in the non-quenched zone than in the normal zone.

With the pressure increase, several parameters are modified. The most important one is the decrease of the temperature of the λ transition of the superfluid helium, that happens at a lower temperature 2.10 K at 8 bar, instead of 2.17 K at the saturation. The heat capacity of the superfluid helium decreases when transiting to normal liquid. As it can be seen in figure 5.12, at the location X = 7.5 m, the temperature exhibits an important increase after 3 s at 2.10 K because the pressure at this location is around 8 bars. Further in the coil, the pressure is lower and the temperature increases at 4 s and around 6 bars. The temperature of the conductor and the helium are well-superposed and no difference can be seen between them. The velocity increases continuously until the quench arrival, and keeps increasing with the quenched length increase. Therefore, in contrast to the transport contributing to quench propagation in the vicinity of the quench propagation front, preheating here also occurs at a distance from the quench propagation front.

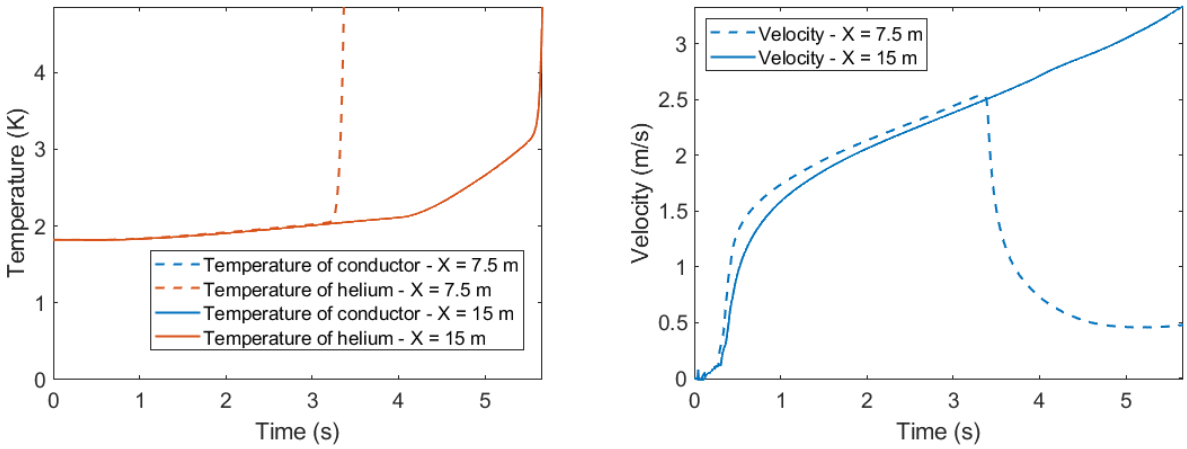

(a) Temperature evolution.

(b) Velocity evolution.

Figure 5.12: Time evolution of the temperature and velocity at X = 7.5 m and X = 15 m.

The velocity of the helium has then greatly increased, going from 1.77 m/s to 3.30 m/s at X = 15 m, and keeps increasing with the quenched length. All the terms composing the fluid model that are involved with the velocity and particularly the transport term and the friction forces term will increase strongly. The goal in the following section is to verify the evolution of these terms and corresponding phenomena, in order to identify which one is the most dominant during the *acceleration phase* and how it influences the quench propagation.

5.2.3.2. Identification of the dominating phenomena during the *acceleration phase*

This section is dedicated to verifying the effect of the velocity increase on the quench propagation. The evolution of the time integrals of the different terms of the fluid model have been computed in figure 5.13. Until 4 s, only the friction term contributes to increase the temperature of the helium, making the helium transit from superfluid to normal liquid. After 4 s, the advection term increases showing that heat is transported while the quench gets closer. In terms of temperature increase, both phenomena generate an equivalent temperature increase. However, the advection contributes to the temperature increase only when the quench propagation front is close the looked-at position, as in the *quasi-linear phase*. At the opposite, the friction forces strongly contribute since the beginning and even when the quench propagation front is far away from the position. The friction forces generate a slower temperature increase than the advection, but with enough propagation time their contribution to the temperature increase of the helium can be equivalent (or higher) to the advection one. Therefore, there is a clear competition between both phenomena, but at different spatial scales, close to the quench propagation front or far upfront the quench front. Finally, the convective term is still negative even above T_λ, meaning that the helium warms the solid.

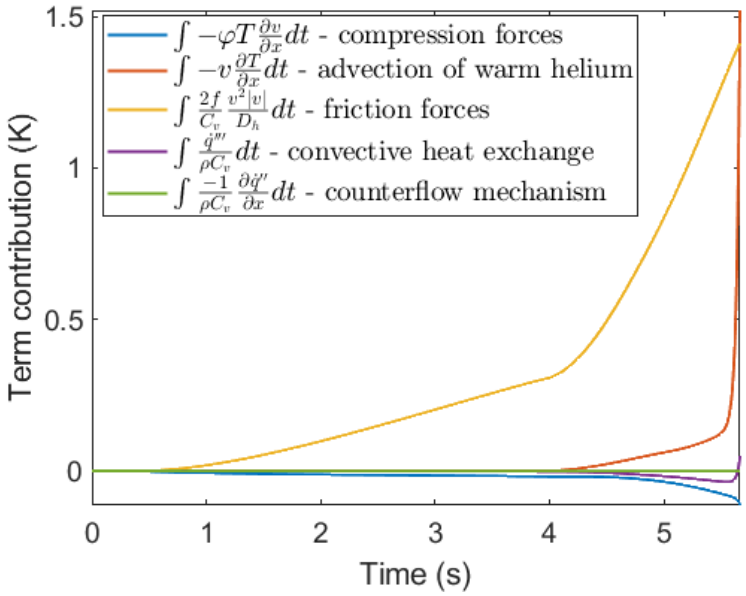

Figure 5.13: Time evolution of the integrals of the terms from the fluid temperature equation at X = 15 m.

Concerning the temperature increase of the solid, as it can be seen in figure 5.14, the convective heat exchange and the conduction have an equivalent contribution. Indeed, the exchanged convective heat flux is the same, but the term ρC_p is lower in the solid parts case, so the contribution to the temperature increase of the solid parts is more important. The friction

forces indirectly make the temperature of the coil increase. By heat conduction, T_{cs} is reached in the coil, as the conduction term increases greatly after 5.5 s. Therefore, it is clear that even if the quench propagates continuously by conduction, the contribution of the helium to the heating of the coil is higher along the coil.

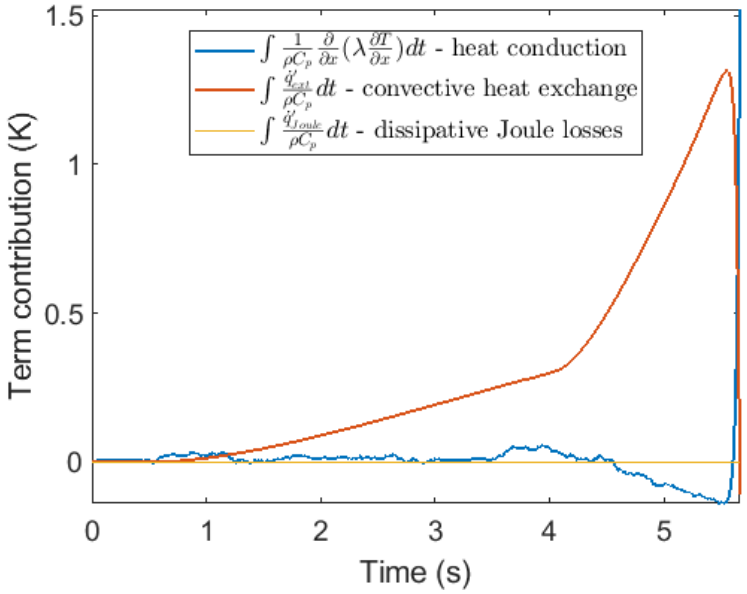

Figure 5.14: Time evolution of the integral of the terms from the solid parts temperature equation at X = 15 m.

To summarize the analysis of the *acceleration phase*, the helium warms the coil. The helium is warmed by both advection and friction at different spatial scales. Indeed, close to the quench propagation front, the transport of warm helium is predominant, and the velocity of helium that increases with the quenched length contributes to accelerate the quench. Further in the coil and far away from the quench propagation front, the friction forces make the temperature of the helium increase, making the quench propagation speed increase. In a first step, the helium transits from superfluid to normal liquid, but its temperature keeps increasing. There are then two phenomena contributing to accelerate the quench. These results seem to confirm again the relevance of the "helium flow quench velocity" formula 4.9, with the effect of the advection but also the pre-heating due to the friction forces. However, the last moment normal transition of the superconducting cable is still due to heat conduction, with the continuous arrival of the quench by heat conduction.

In the following section, the *breaking phase* is analyzed, in order to understand the physics behind the characteristic break observed during the quench of the MACQU coil, and highlight the role of the friction forces in it.

5.2.4. Analysis of the *breaking phase*

After showing that both the advection and the friction forces were responsible of the progressive acceleration of the quench, this section is dedicated to the analysis of the *breaking phase*. During this phase, after a clear break, the quench reached its highest quench propagation speed. It has been shown in the previous chapter that the current and the temperature margin were important parameters to trigger the *breaking phase*, as well as the time while the quench propagated and the distance from the quench initiation. The goal of this section is also to identify the links between these parameters and the *breaking phase*.

5.2.4.1. Phenomenological analysis of the *breaking phase*

A clear break of the normal length happens at 7.15 s, as it can be seen in figure 5.15. It indicates the transition between the *acceleration phase* and the *breaking phase* and is characterized by a discontinuity of the second derivative of the normal length curve. After the break, an important increase of the quench propagation speed can also be seen and the quench propagation speed is estimated to be 28.4 m/s. However, before the plateau indicating that the entire coil has quenched, at 7.3 s, an important decrease of the quench propagation speed can be seen.

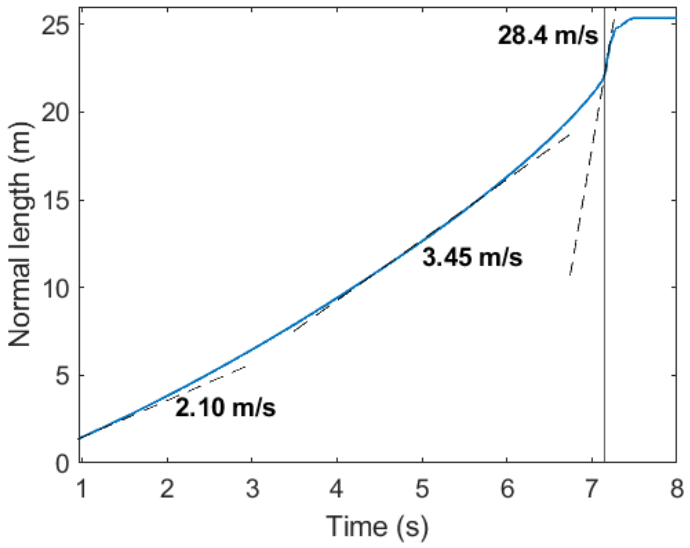

Figure 5.15: Time evolution of the normal length during the *breaking phase* of the quench propagation, obtained with THEA®.

Due to the pre-heating, the temperature at 7 s is between 4.6 K and 4.0 K outside the quenched zone, which is below the T_{cs} curve (figure 5.17). However, it is clear that the temperature is still increasing. At 7.15 s, when the temperature crosses the T_{cs} curve, there is a change of dynamics. Initially, inside and close to the quenched zone, the temperature rose when the quench arrived. Here, between 7.15 s and 7.2 s, the temperature of almost 1.5 m of the coil exceeds T_{cs}, but there is no big increase of the temperature yet. An inflection point can then be seen at the intersection between the T_{cs} curve and the temperature profile.

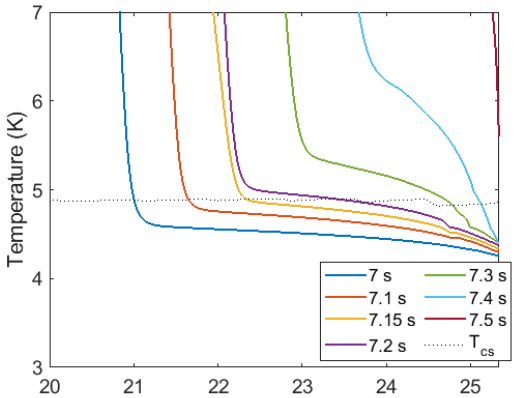

Figure 5.16: Evolution of the temperature profile during the *breaking phase*.

Moreover, while the quenched zone increases, the pressurized zone also increases (figure 5.16 (a)). However, it can be seen above 7.5 s, the pressure is decreasing in the coil, while the velocity of the helium increases strongly (figure 5.17 (b)). The increase of the velocity gradient leads to dominant compression forces, negative in our case, and then make decrease the pressure.

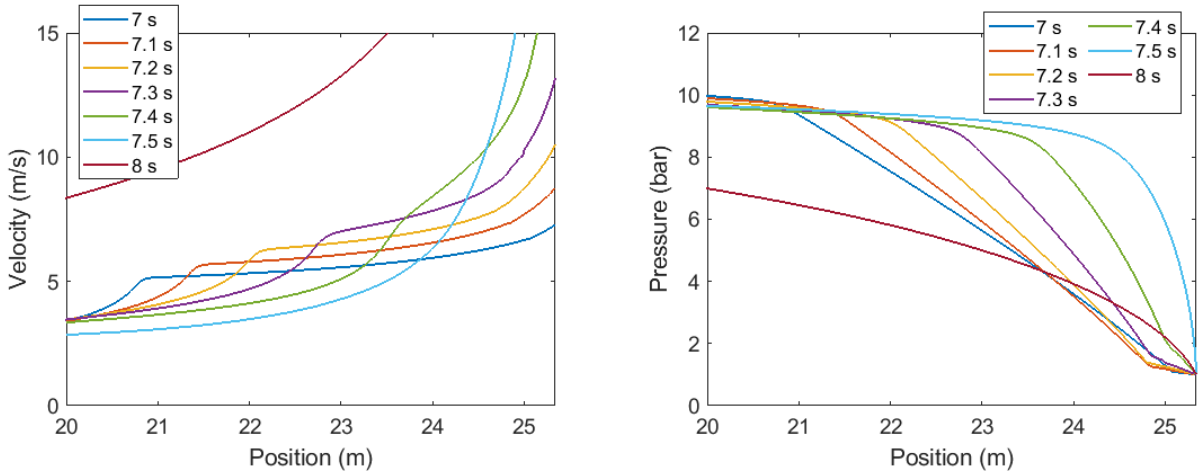

(a) Velocity profile.

(b) Pressure profile.

Figure 5.17: Evolution of velocity and pressure profiles during the *breaking phase*.

As it can be seen in figure 5.18, after an initial phase where the temperature remains constant, the temperature of the helium starts increasing. At 4.2 s, the helium loses its superfluid properties and goes into the liquid normal phase. Its heat capacity decreases thus strongly. The temperature of the helium increases then much faster. However, it can be noticed that the temperature increase is continuous until T_{cs}. The final temperature increase seen during the *acceleration phase* can not be seen here. In addition, the temperature increase is continuous until T_{cs}. The velocity increase is also continuous. The goal of the following section is then to identify the causes of the continuous acceleration, that will highlight the causes of the triggering of the *breaking phase*.

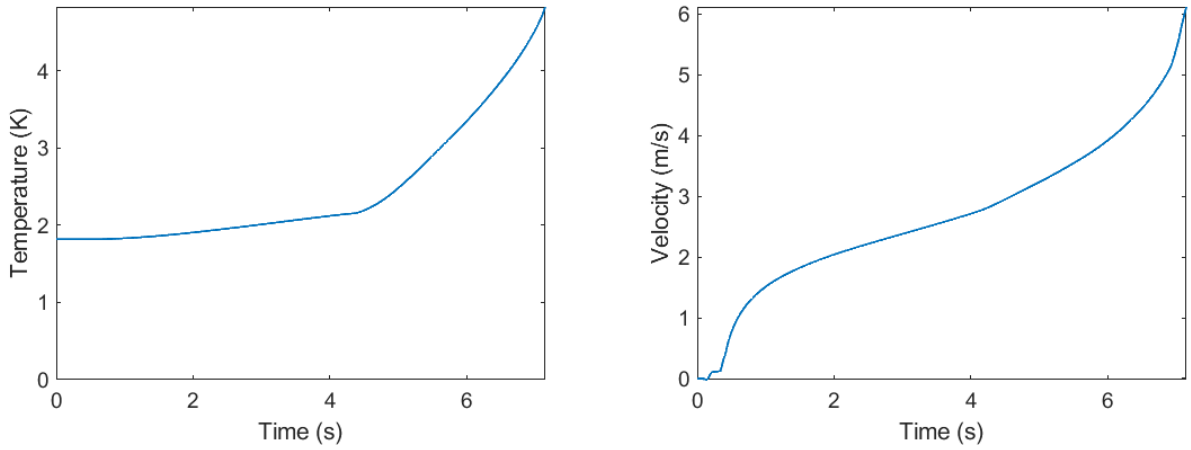

(a) Temperature evolution.

(b) Velocity evolution.

Figure 5.18: Time evolution of the temperature and velocity at X = 22.5 m.

5.2.4.2. Identification of the dominating phenomena during the *breaking phase*

During the *acceleration phase*, the temperature of the helium increases due to the friction forces downward from the quenched length. Close to the quench propagation front, the advection and conduction are dominant though. During the *breaking phase*, as it can be seen in figure 5.19, the contribution of the friction forces term is largely dominant compared to the advection term. Indeed, the friction forces term increases because while the temperature increases, the heat capacity of the liquid helium, smaller than the superfluid one, decreases. Therefore, due to the friction forces, the temperature of the helium reaches T_{cs} downward the quench propagation front. By convection, the helium warms the coil. The break represents then the temperature increase of the coil until T_{cs}, caused by the indirect pre-heating due to the friction forces. It corresponds therefore perfectly to the THQB theory.

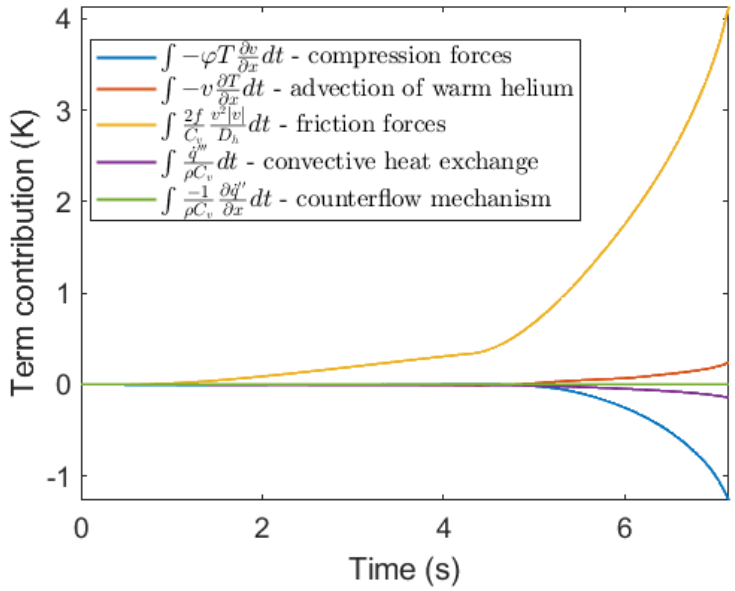

Figure 5.19: Time evolution of the integral of the terms from the fluid temperature equation at X = 22.5 m.

This idea is confirmed by the time evolution of the integral of the terms from the solid parts temperature equation, represented in figure 5.20. Indeed, the conduction term is largely negligible in front of the convection term. The earlier phases highlighted a large temperature increase due to the quench arrival by conduction. However, as the conduction term is negligible here, it indicates that the quench is initiated locally due to the convection, so indirectly by the heating of the helium caused by the friction forces. Therefore, the friction forces are the cause of the characteristic acceleration of the *breaking phase*.

The friction forces had to overcome the temperature margin "alone" to trigger the *breaking phase*. Therefore, it is clear that the triggering of the *breaking phase* is highly linked with the temperature margin: a higher temperature margin could not let the temperature of the helium reach T_{cs} before the entire quench of the coil. In this case, the heat conduction and the advection would be dominant and there would be no *breaking phase*. At the opposite, a lower temperature margin could allow reaching T_{cs} closer from the quench initiation point. Indeed, less energy would be needed to overcome the temperature margin.

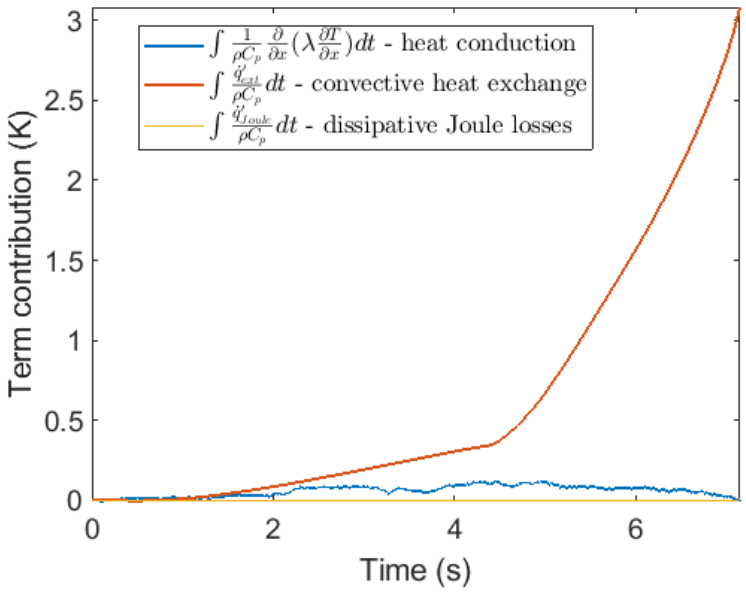

Figure 5.20: Time evolution of the integrals of the terms from the solid parts temperature equation at X = 22.5 m.

To summarize, due to the friction forces, the temperature of the helium is increased to T_{cs} downward the quenched length. The superconducting cable is then warmed up by convection. However, contrarily to earlier phases, the contribution of the heat transport (conduction or advection) is negligible in front of the friction term one. T_{cs} is reached only by the pre-heating of the friction forces. Therefore, far away from the quench propagation front, a "new" quench is initiated. This type of quench is represented by the *breaking phase*. With an important velocity of several m/s, the friction term adds its contribution in the "helium flow quench velocity", making the quench propagation speed strongly increase.

In the following section, the quench study is extended to a parametric study of the current. The goal is to qualitatively verify the quench behavior in function of the current, particularly in terms of acceleration and *breaking phase*, and to compare with the conclusions done in the previous chapter.

5.2.5. Parametric study of the current on the quench behavior

By keeping the same temperature conditions than the previous case, a parametric study of the current has been done on the quench behavior. The goal of this section is then to analyze the results of this study, to verify the computed results for a different current. The results of the parametric study can be seen in figure 5.21. The parametric study goes from 13 kA to 21 kA, with a step of 1000 A. The characteristic break of the *breaking phase* can be clearly seen above 15 kA, slightly at 14 kA and not below.

As it can be seen, the quench propagation speed clearly increases with the current. Moreover, the *breaking phase* happens earlier and closer to the initiation point with the current increase. The exact initiation point of the quench is unknown but is in the heaters zone, from the center at X = 0 m to X = 0.104 m. For simplification purpose it is considered at X = 0 m. It is then clear that qualitatively, an equivalent behavior is observed between the numerical computations and the experimental results.

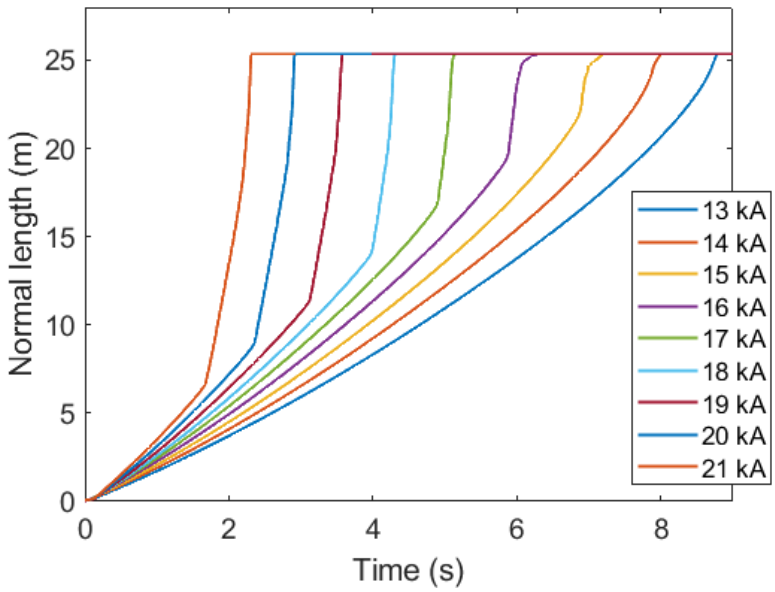

Figure 5.21: Parametric study of the normal length evolution, in fonction of the current. The *breaking phase* can be seen above 14 kA but not below.

To push further the analysis, by plotting the quenched-length and the propagation time before the *breaking phase*, it can also be seen in figure 5.22 that the quasi-linearity of both parameters in function of the current is conserved with respect to the previous chapter (section 4.3.1). A similar conclusion can be done: depending on the available conductor length and the propagation time, there is an offset to initiate the *breaking phase*.

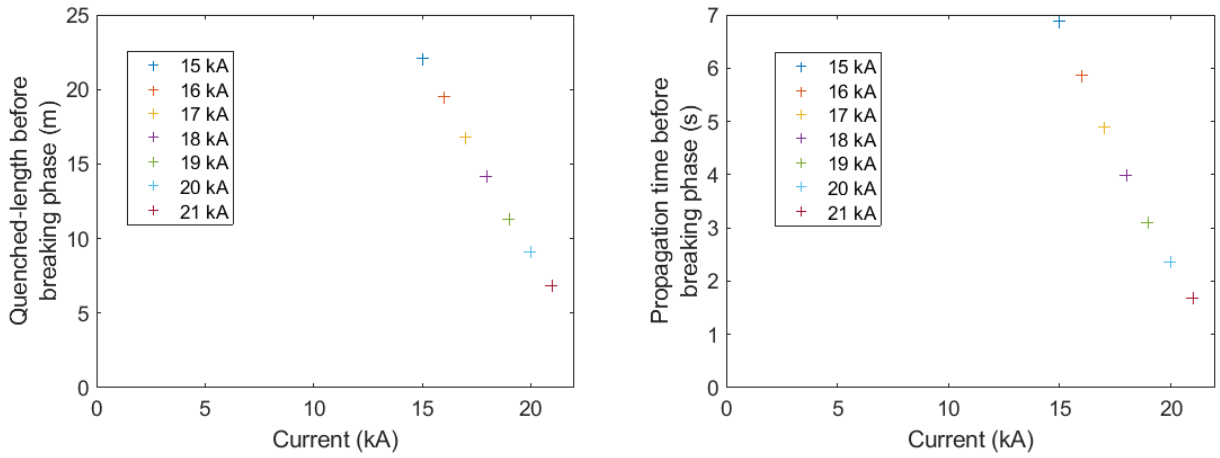

Figure 5.22: Quenched-length and progation time before the *breaking phase* in function of the current, obtained with THEA®.

In conclusion, the quench behavior predicted by THEA® is qualitatively similar to the one observed experimentally, with three phases quench propagation. During the *quasi-linear phase*, the quench propagates in the superconducting cable at a constant speed at a constant temperature. Due to the dissipative heat losses by Joule effect generated in the solid, the helium is warmed up by convection, and the helium is set in motion inside the CICC. This helium velocity has an important effect on the quench propagation. Close to the quench propagation

front, advection in the helium transports heat and contributes to accelerating the quench propagation, on the contrary to the "infinite exchange" theory where the quench only propagates by conduction with the stagnant fluid at a constant temperature. Moreover, the helium velocity increases with the normal length. Further in the coil, upfront the quenched length, the friction forces make the temperature of helium increase and the temperature of the coil. With this pre-heating, the quench propagation is also accelerated due to the decrease of the temperature margin. Therefore, there is competition between both phenomena, with the advection driving the quench propagation close to the front, while the friction forces drive the quench propagation far from the front. However, the temperature increase due to the friction forces can make the helium and the coil reach T_{cs} upfront the quenched length if the available length and time are enough. In these conditions, the quench is fully initiated by the indirect heating of the friction forces and not by conduction. This "new" quench is characterized by an important flow, where the friction forces add their contribution to the transport and the "infinite exchange" quench propagation speed, and make the quench propagation speed increase greatly.

Therefore, THEA® allowed us to further understand the phenomena, and also shown that the predicted behavior was qualitatively in coherence with the observed experimental behavior in function of the current. The quenched-length and the propagation time before the *breaking phase* seem to be quasi-linear with the current, as observed experimentally. The quench behavior appears then as qualitatively well predicted by THEA®. The goal of the next section will then be to reproduce the experimental cases and quantitatively compare the numerical results with the experimental ones.

5.3. Comparison between numerical and experimental quench behavior

After verifying the qualitative quench behavior predicted by THEA®, this section is dedicated to the comparison between the numerical and experimental results. In order to compare the experimental results with the THEA® computations, the initial conditions of the different cases studied during the MACQU experiment have been reproduced. In a first step, the two results obtained for the already studied case at 15 kA and 1.82 K have been superposed in figure 5.23. The slight difference in length comes from the modeling because the arms are not modeled, while the SQD measurement takes into account the arms. It does not affect the analysis as it is clear that the quench behavior is similar, with the quench propagation pattern in three phases. However, it can be seen that the numerical quench dynamics is much slower than the experimental one. The numerical initial quench propagation speed has been measured at 2.1 m/s while the experimental one was measured at 4.9 m/s. Moreover, the *acceleration phase* lasts longer and the *breaking phase* appears later. It seems that the friction forces last longer to initiate the breaking phase. The temperature margin and the material properties being the same, the $\frac{2f}{C_{v_h}}\frac{v_h^2|v_h|}{D_h}$ term can only be influenced by a slower velocity. This slower velocity explains the decrease of the effect of the friction forces but also the decrease of the quench propagation speed, based on the "helium flow quench velocity" formula 4.9.

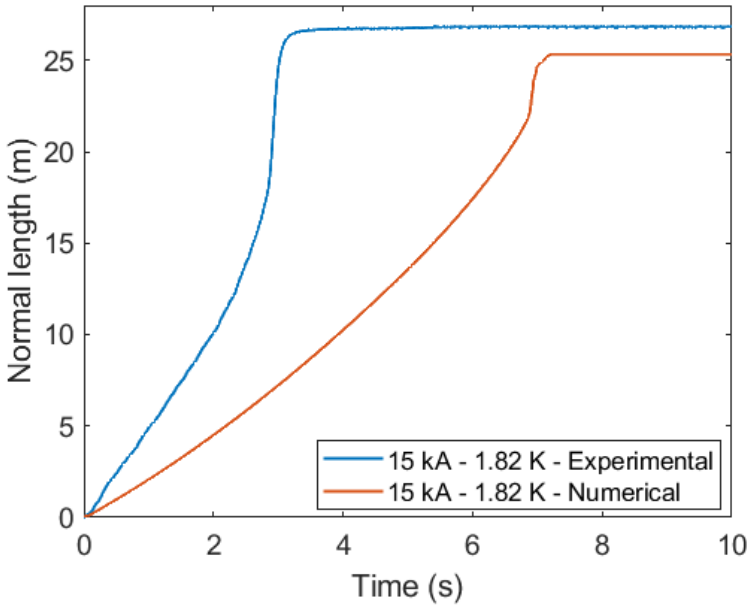

Figure 5.23: Comparison between the experimental and the numerical results obtained for the already studied case, at 15 kA and 1.82 K.

The same observation can be done for the other cases, as the results obtained with the THEA® code can be seen on the left in figure 5.24, while the experimental results can be seen on the right. Indeed, the global quench behavior is similar, with the quench propagation speed increasing with the current, and decreasing with the temperature margin. It was also observed that a minimal current of 14 kA was needed to trigger the *breaking phase*, and this behavior is captured here. However, it is obvious that the numerical quench dynamics appears two to five times slower than the experimental one.

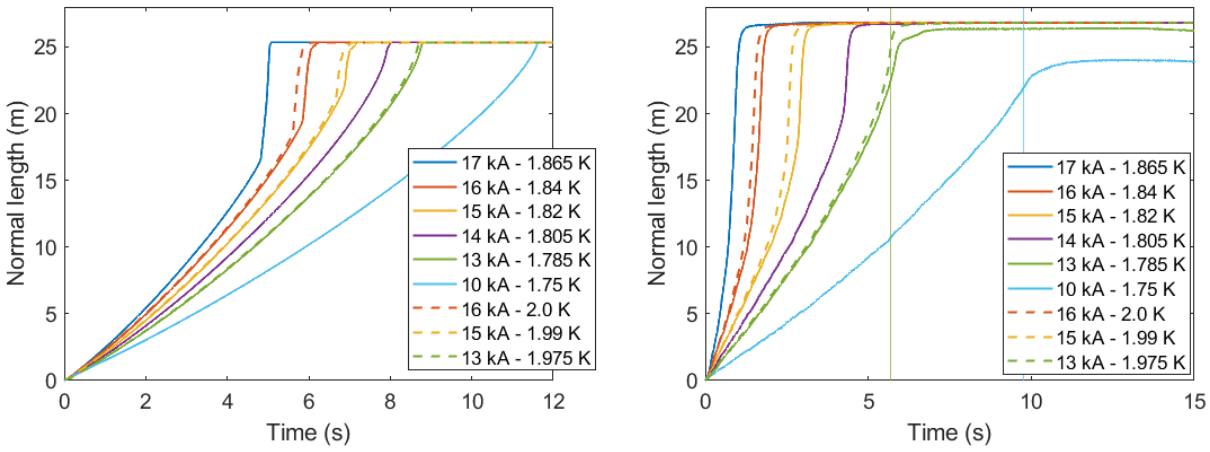

(a) Numerical results.

(b) Experimental results.

Figure 5.24: Comparison of the numerical (left) and experimental (right) results. The quench propagation divided in three phases appears in both cases.

By comparing more globally the initial quench propagation speeds, the same result is observed: the quench propagation speed computed by THEA® is between two and five times slower than the experimental one, except for the 10 kA case. As it can be observed in fig-

ure 5.25, the 10 kA case is the only case where the numerical quench propagation speed is higher than the experimental one. Moreover, it can also be seen that the "helium flow quench velocity" formula 4.9 gives comparable results than the results computed with THEA®. To obtain such results, the velocity of the helium has been considered at 0.5 s at the quench propagation front location. Therefore, with the "helium flow quench velocity" formula 4.9, the quench propagation speeds given by THEA® can be retrieved.

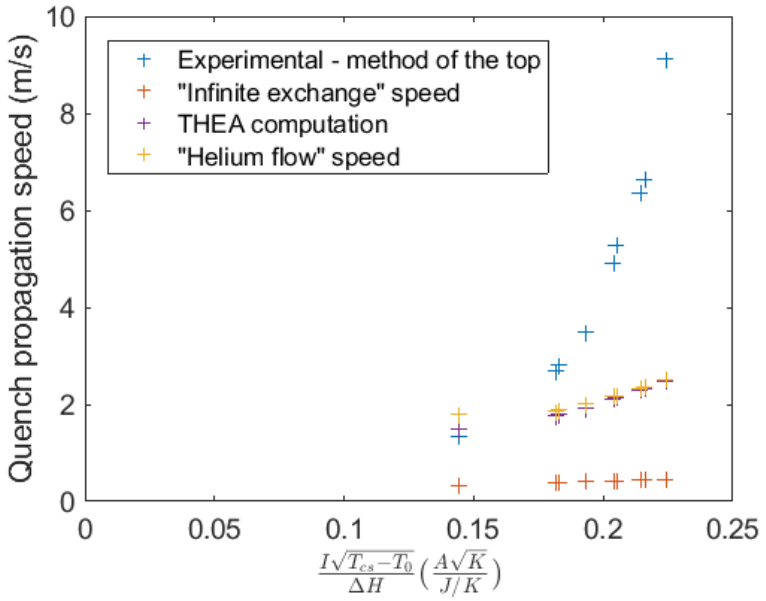

Figure 5.25: Comparison between the numerical and the experimental quench propagation speed.

However, it is not enough to find the experimental quench propagation speeds, and a phenomenon must be in cause to explain this important gap. The main hypothesis is the diffusion of the current inside the copper profile. This phenomena has been observed on the Atlas project [30]. Indeed, during the quench, the current is redistributed from the superconducting cable to the whole copper cross-section, and particularly the copper profile. However, this redistribution is not instantaneous and behaves like a diffusion phenomena that creates a competition between the redistribution of the current and the quench propagation. If the diffusion is faster, the current is fully redistributed in the profile while the quench propagates and the dissipative heat losses by Joule effect are evenly distributed inside the full copper cross-section. If the quench is faster, there is a time where the current is not flowing through the full copper section but only in a portion of it, so the dissipative heat losses by Joule effect defined by $\eta_{Cu} I/S_{Cu}^2$ are more important than they should be during the diffusion time. Obviously, with more important Joule losses, the quench propagation speed would be more important. In addition, more important Joule losses would arrive on the helium and its pressure and velocity would also increase. It is also a runaway phenomena because with a higher velocity, the effect of the advection and the friction forces is also more important. The quench propagation speed is thus increased and the *breaking phase* happens earlier.

Therefore, to verify this assumption, the timescale of the two phenomena must be compared. To do so, the characteristic time of the quench is compared with the magnetic diffusion characteristic time, both defined respectively in equation 5.13 and equation 5.14. The magnetic diffusion characteristic time is obtained from the commonly used magnetic diffusion equation.

Figure 5.26 compares the characteristic time of the quench with the characteristic time of current redistribution.

$$\tau_{quench} = \frac{\lambda_{Cu}}{\rho_{Cu} C_{p_{Cu}} v_q^2} \tag{5.13}$$

$$\tau_{magnetic} = \frac{L^2 \mu_0}{\eta_{Cu}} \tag{5.14}$$

with τ_{quench} being the characteristic time of the quench, λ_{Cu} the conductivity of the copper, ρ_{Cu} the density of the copper, $C_{p_{Cu}}$ the specific heat at constant pressure of the copper, v_q the quench propagation speed, $\tau_{magnetic}$ the magnetic diffusion characteristic time, L the characteristic length of diffusion considered here being 5 mm, corresponding to the thickness of the half profile, μ_0 the vacuum permeability and η_{Cu} the resistivity of the copper.

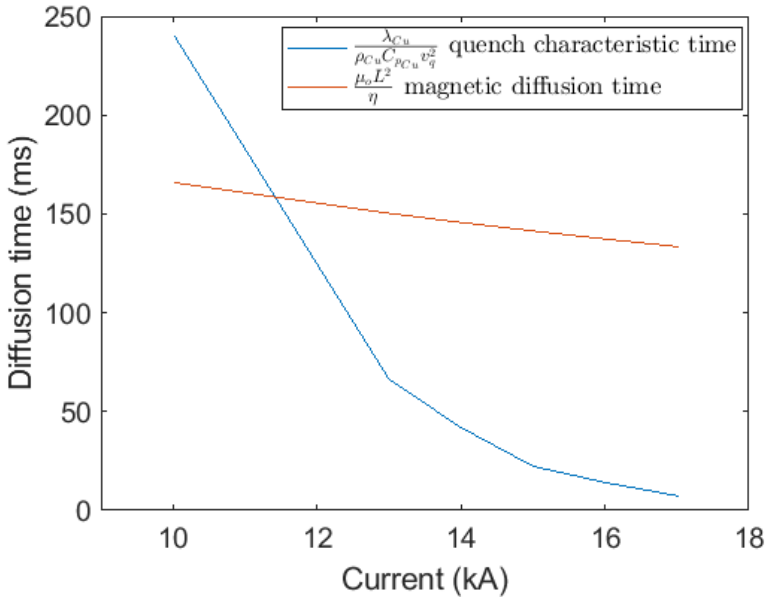

Figure 5.26: Comparison of the experimental quench characteristic time with the estimated current diffusion time.

The characteristic time of the quench is lower than the magnetic diffusion time, except for the 10 kA case. As is, it would mean that during a certain time depending on the current, the current would flow in a part of the copper cross-section at the quench propagation front. The dissipative Joule losses would then be, during the redistribution time, more important than estimated, generating an over estimated quench propagation speed. In these conditions, there is a clear competition between the current redistribution and the quench establishment, and could explain the big difference between the computation and the experimentation. Moreover, the only case where the obtained results are close is the 10 kA case, assumed to be the only case where there should not be any current diffusion issue. It seems then that without current diffusion issues, the quench propagation speed estimated by THEA® or by the "helium flow quench velocity" formula 4.9 is not far from the reality. Therefore, to obtain a more realistic result, a current diffusion model should be integrated to THEA®. However, due to lack of time, this model could not be implemented, and a future work should be done to integrate this assumption to the actual model.

After comparing experimental and numerical results, it appeared clearly that the numerical results predicted by THEA® are qualitatively representative of the quench behavior of the MACQU coil. The typical quench propagation in three phases appeared clearly and the global behavior was conserved: the quench propagation speed was increasing with the current and with the decrease of the temperature margin. It also appeared that the current offset for the *breaking phase* was around 14 kA. However, it was also shown that quantitatively, the numerical results were between two and five times slower than the experimental ones. This important gap seems to be due to a current redistribution issue in the copper cross-section during the quench. During the current diffusion time, the current flows in a part of the whole copper cross-section and it generates excess dissipative heat losses by Joule effect, accelerating strongly the quench. No current redistribution model has been done to correct the numerical results but should be done in future studies. However, the obtained results with the MACQU coil allowed to highlight the current redistribution issue but also to show that the results predicted by THEA® are conservative. The quench protection study of MADMAX could then be done with conservative values, allowing a more important margin.

Conclusions

This chapter has been dedicated to the analysis of the numerical results computed with the numerical tool THEA® to understand the physics of the quench and the observed phenomena both qualitatively and quantitatively. For that matter, a THEA® thermal and hydraulic model has been constructed and presented. The different assumptions, such as modeling only half of the solenoid, the field map, or the friction coefficient or the convective heat exchange coefficient correlations were detailed. Then, the code has been used to study a typical quench presented in chapter 4 (15 kA and an initial temperature of 1.82 K). The different quench phases were analyzed as well as the different phenomena governing the physics of the quench. It appeared that the *quasi-linear phase* is mostly driven by the helium advection in addition to heat conduction. The quench is propagating at a constant speed as the helium velocity is constant. However, with increasing energy deposited by the quench on the helium, the temperature and pressure increase, and higher helium velocity is generated along the CICC. The helium starts then moving in the whole CICC. With higher advection, warm helium is close to the quench propagation front. Upfront the quenched length, since the beginning of the *acceleration phase*, the friction forces start to pre-heat the helium and therefore the coil by convection. Indeed, due to this pre-heating, the coil is slightly warmed-up, decreasing the temperature margin, and the propagation of the quench progressively accelerates. The normal length is also larger and increases the helium velocity contributing to the increase of the speed of the quench. With higher pre-heating, if the length and the time are enough for the quench to propagate, the coil can reach T_{cs} in the non-quenched zone due mainly to friction and not conduction. At this moment, the *breaking phase* starts with its characteristic discontinuity in the normal length evolution. Indeed, it is the initiation of a "new" quench generated by friction forces far away from the quench propagation front. There are two phenomena driving the quench but at different spatial scales. The consideration of both phenomena in the "helium flow quench velocity" formula appears relevant and gives equivalent results to our code. However, even if the physics is qualitatively well predicted, it appears that quantitatively the numerical quench dynamics are slower than the experimental findings. Current diffusion is assumed to be the cause of this difference. When the conductor quenches, the current is temporarily flowing in a portion of the copper profile instead of the whole copper cross-section. The current needs a certain time to fill the full copper cross-section. It generates more Joule losses and increases the

quench propagation speed. No current redistribution model is integrated into THEA®. This physics should be added in the future to improve THEA®. Nonetheless, THEA® can be used for the MADMAX quench protection study since the quench behavior of such a CICC is well identified and understood using a conservative quench propagation speed and behavior.

General conclusion

This Ph.D. study focused on the study of the thermohydraulic phenomena taking place during the quench of a novel copper CICC superconducting magnet cooled with stagnant superfluid helium. It should be noted that the quench behavior of such a magnet has not been investigated in the past, because, for the MADMAX project, a novel type of CICC conductor has been developed. It is composed of a superconducting cable inserted in a rectangular copper profile playing the role of thermal stabilizer and filled with stagnant superfluid helium. This novel conductor configuration has never been used before and the risk of the novel conductor had to be mitigated by improved understanding. For this reason, it was decided to study the quench propagation in the MADMAX configuration to demonstrate that a large magnet like MADMAX can be safely operated with such a CICC. To do so, the first work done during this Ph.D. was to design a mock-up coil, called MACQU, to experimentally study a MADMAX-representative quench behavior and measure its quench propagation speed. Several guidelines have been considered for the design of the MACQU coil and the most important parameters that drove our design were the dissipative Joule effect heat losses for a similar load line margin (10 %) and an initial temperature of 1.8 K. The MACQU coil has been designed to reproduce 73 % of the linear heat dissipation of MADMAX, corresponding to a heat dissipation of 855 W/m, with a CICC cross-section two times smaller than the MADMAX one. After the design, the coil has then been manufactured and integrated, after some modifications, to the JT60-SA cryostat, where several quench tests were performed. The goal of these tests was to simulate a non-detected quench that could propagate at constant current, before having an instantaneous fast discharge.

Thanks to the performed tests, the experimental quench behavior of such CICC has been observed and the quench propagation speed was measured. It allowed us both to validate the safety of the MACQU detection system to be used on MADMAX in the future and to study the MACQU quench physical behavior. Three different quench dynamics phases have been identified for most of the quench tests: a *quasi-linear phase*, an *acceleration phase* and a *breaking phase*.

The *quasi-linear phase* is the first phase of the quench propagation following the quench initiation. During this phase, the dissipative heat losses by Joule effect generated by the quench contribute to increase the temperature and pressure of the helium and creating a helium flow in the CICC. Advection of heat by the helium in movement in the whole conduit and compression in the helium contributes to increasing the temperature of the helium close to the quench propagation front. During this phase, the quench propagates at nearly constant speed. This speed has been measured between 1.3 m/s and 9.1 m/s, for a current range going from 10 kA to 17 kA. A first important result here is that these speeds are high enough to ensure a fast detection of the quench on MADMAX without damaging it. This validates the first main objective of the project. In order to study the physics involved in this phase, we decided to have first an analytical approach to evaluate the quench speed. It appeared that the "infinite exchange quench speed" formula was estimating the quench speed much slower than in reality. Therefore, an "improved" equation for the computation of the quench propagation speed has been demonstrated, called the "helium flow quench velocity" formula, taking into account the advection of warm helium and the friction forces. This formula allowed us to show that the conduction is not the main contributor to the quench propagation but the helium velocity. In fact, in the *quasi-linear phase*, the conduction and frictions terms are clearly non predominant

such that the quench propagation speed is nearly equal to the helium flow velocity.

During the *acceleration phase*, the quench propagation speed starts increasing. The movement of the helium contributes to making its temperature increase by two means at different spatial locations: the advection of the warm helium is dominant close to the quench front, while the friction forces have an effect upfront the quenched length and far away from the front. This two phenomena both contribute to increasing progressively the quench velocity in the *acceleration phase* but by two different means. First, as said before, the advection of warm helium is a driving phenomena in our case making the quench speed nearly equal to the helium velocity in the first phase. Our analysis of the heat equations showed that the helium velocity is increasing with the overall Joule effect deposited in the coil. This means that when the quench propagates, the integrated Joule effect on the normal zone becomes higher and thus increases the helium velocity. The increase of the helium velocity increases then the quench speed and contributes to the *acceleration phase*. Secondly, the work of pressure and friction forces upfront of the quenched length warm helium even far from the propagation front. This induces a clear pre-heating of the non-quenched zone that reduces its temperature margin against T_{cs}. As the analytical formulas show, the lower the temperature margin, the higher the quench propagation speed. The pre-heating due to the friction forces then also contributes to explaining the acceleration of the quench in this phase.

When the *breaking phase* is triggered, a characteristic break of the normal length curve and a spectacular acceleration of the quench happens. The quench propagation speed can reach more than 100 m/s. The *breaking phase* is triggered when the superconducting cable reaches T_{cs} due to the pre-heating of the helium. With the helium temperature increase, created by the friction forces, the main heat source for the superconducting cable is the convective heat exchange and not the heat conduction inside the solid. Reaching T_{cs} is then only due to the contribution of the helium. In this phase, contrarily to the *acceleration phase*, the work of the friction forces becomes predominant upon the advection of warm helium. The pre-heating that it generates becomes high enough to make the helium reach T_{cs} upfront of the quench front when the advection and conduction terms are still far and negligible. A "new" quench is then initiated, upfront the quench propagation front, and is not correlated with the conduction in the solid. The quench dynamics are totally different as the helium becomes the driving parameter of the quench propagation. It is the cause of this characteristic acceleration observed above 13 kA on the MACQU coil.

Indeed, the smaller the temperature margin $\Delta T = T_{cs} - T_0$, the less the frictional forces have to contribute to the temperature increase, and the shorter the time needed for the quench to initiate the *breaking phase*. With the increase of the current or the increase of the initial temperature, both leading to a decrease in the temperature margin, the *breaking phase* happens sooner and closer to the quench initiation point. In addition, the dissipative heat losses by Joule effect increase with the current and so the heat dissipation in the helium. This increases the helium velocity and contribute to increasing the effect of both advection and friction forces to the acceleration of the quench. Moreover, it appeared both by an experimental and numerical approach that the time needed for the quench and the distance crossed by the quench before the triggering of the *breaking phase* is quasi-linear with the current. Therefore, the current, the temperature margin, the available CICC length and the time while the quench propagates appeared as key parameters driving the triggering of the *breaking phase*.

Finally, some directions on which the continuation of this doctoral work can be focused are given below. The numerical results obtained with the computation tool THEA® were qualitatively representative of the quench behavior of a copper conduit CICC cooled with su-

perfluid helium. However, it has been shown that numerically the quench dynamics is much slower than observed experimentally. In the current model, it is considered that the current redistribution between the superconducting cable and the copper cross-section during a quench is nearly instantaneous as it is driven only by the electrical power law of the Nb-Ti strands. Indeed, it is not the reality and it has been shown experimentally that the observed quench behavior is accelerated due to the current copper diffusion phenomenon. Therefore, to obtain representative results with THEA®, a current diffusion model is to be developed and integrated or coupled to THEA®. To get a more realistic quench behavior, the Joule effect at the propagation front should be increased simulating the fact that the current is in reality flowing in a smaller section than the full copper one during a certain magnetic diffusion time constant. This add-on could provide a reliable numerical tool for the quench propagation speed computation of such a CICC. Another issue that should be studied is the effect of the hydraulic diameter on the quench behavior and especially on the Thermal-Hydraulic-Quench-Back (THQB). This study could orient the future cable design of the MADMAX conductor. Indeed, for a cable design, several strands diameters could be chosen and several cabling patterns are possible to have the same magnetic performances. Nevertheless, from the hydraulic point of view, this different patterns have very different wet perimeters and hydraulic diameters. So, even if the magnetic performances are the same, the thermal hydraulic behavior of the quench could be very different. We have shown in this Ph.D. that the friction forces had a great effect on the quench dynamics by generating the *breaking phase* and the hydraulic diameter appears in the friction forces term. For this study, the hydraulic diameter is rather small which creates large friction forces. Future studies should include a hydraulic diameter parametric study to evaluate its effect on the thermal hydraulic of the quench. As the initial quench propagation speed is driven by the helium velocity, the choice of the hydraulic diameter at equivalent magnetic performances could facilitate the quench detection. Finally, unexpected quenches appeared in the terminals that couple hydraulic and electric circuits used on MACQU. These quenches are at the origin of under-performances because only 76 % of the load line has been reached on MACQU, compared to the 90 % target. It has been assumed that the quenches were generated by current diffusion issues in the terminals. The superconducting cable is destranded and split in triplets in the terminals but the current could be different from one bundle to an other. Even if their configuration will probably be different, terminals will also be used in the MADMAX magnet. To avoid under-performances that would limit the Figure of Merit generated by MADMAX, the issue of the terminals must be addressed and the hint of the current diffusion issue should be verified. The current transported by each superconducting strand should be evaluated and different distribution of the bundles could be tested. These tests could confirm or not the origin of the terminals dysfunctioning for MACQU and also orient the technical choices for the terminals of MADMAX.

A - Non-conservative form of conservation equations of the helium

The three conservation equations of the helium are the mass conservation equation A.1, the momentum conservation equation A.2 and the energy conservation equation A.3. The equations are written for a unique 1-D channel. The cross-section being constant, the cross-section term is already simplified.

$$\frac{\partial \rho}{\partial t} + \frac{\partial \rho v}{\partial x} = 0 \tag{A.1}$$

$$\frac{\partial \rho v}{\partial t} + \frac{\partial \rho v^2}{\partial x} + \frac{\partial P}{\partial x} = -F \tag{A.2}$$

$$\frac{\partial \rho e}{\partial t} + \frac{\partial \rho e v}{\partial x} + \frac{\partial P v}{\partial x} = \dot{q}_h''' + \dot{q}_{cf}''' \tag{A.3}$$

with ρ being the density, v the velocity, P the pressure, F the friction term defined as $F = 2\rho f \frac{v|v|}{D_h}$, e is the total specific energy defined as $e = u + v^2$ with u being the specific internal energy, $\dot{q}_h'''$ is the external and convective heat flux reunited for simplicity and $\dot{q}_{cf}'''$ is the heat flux exchanged during the counter-flow mechanism [44]. The x and t are the space and time coordinates.

The equation in the non-conservative form are written in terms of velocity v, temperature T and pressure P. To obtain such equations, the thermodynamic relations A.4 and A.5 must be used.

$$du = \left(\frac{P}{\rho} - \varphi C_v T \right) \frac{d\rho}{\rho} + C_v dT \tag{A.4}$$

$$\left(c^2 - \frac{P\varphi}{\rho} \right) d\rho = dP - \varphi \rho du \tag{A.5}$$

with φ being the Grüneisen parameter, C_v the specific heat at constant volume and c the sound speed.

The momentum equation in the non-conservative form, expressed in v, can be easily obtained by the operation $(A.2) - v \times (A.1)$:

$$\rho \frac{\partial v}{\partial t} + \rho v \frac{\partial v}{\partial x} + \frac{\partial P}{\partial x} = -F \tag{A.6}$$

To obtain the energy equation expressed in T, the operation $(A.3 - (u + \frac{v^2}{2}) \times (A.1)$ is done. After explicitating the total energy terms into $\frac{\partial \rho e}{\partial t} = \frac{\partial \rho u}{\partial t} + \frac{\partial \frac{1}{2} \rho v^2}{\partial t}$ and $\frac{\partial \rho e v}{\partial x} = \frac{\partial \rho u v}{\partial x} + \frac{\partial \frac{1}{2} \rho v^3}{\partial x}$, equation A.7 is obtained.

$$\rho \frac{\partial u}{\partial t} + \rho v \frac{\partial u}{\partial x} + P \frac{\partial v}{\partial x} + v \left[\rho \frac{\partial v}{\partial t} + \rho v \frac{\partial v}{\partial x} + \frac{\partial P}{\partial x} \right] = \dot{q}_h''' \tag{A.7}$$

The term inside the brackets corresponds to the left side of the non-conservative momentum equation A.6, and can be simplified as in equation A.8.

$$\rho\frac{\partial u}{\partial t} + \rho v\frac{\partial u}{\partial x} + P\frac{\partial v}{\partial x} = \dot{q}_h''' + vF \tag{A.8}$$

By using relation A.4 to adapt the du terms, and after replacing the terms in the equation, the equation A.9 is obtained.

$$\rho C_v\frac{\partial T}{\partial t} + \rho v C_v\frac{\partial T}{\partial x} + \frac{P}{\rho}\left[\frac{\partial \rho}{\partial t} + v\frac{\partial \rho}{\partial x} + \rho\frac{\partial v}{\partial x}\right] - \varphi C_v T\left[\frac{\partial \rho}{\partial t} + v\frac{\partial \rho}{\partial x}\right] = \dot{q}_h''' + vF \tag{A.9}$$

The terms in the first brackets correspond to the mass conservation equation, so the sum is null, and the terms in the second brackets can be assembled as $-\rho\dfrac{\partial v}{\partial x}$ thanks to the mass equation. Therefore, the non-conservative form of the energy equation is obtained in equation A.10.

$$\rho C_v\frac{\partial T}{\partial t} + \rho v C_v\frac{\partial T}{\partial x} + \rho\varphi C_v T\frac{\partial v}{\partial x} = \dot{q}_h''' + vF \tag{A.10}$$

To finish, the non-conservative form of the mass equation expressed in P is obtained by substituting the $d\rho$ terms of the equation A.1. After substitution, equation A.11 is obtained.

$$\frac{\partial P}{\partial t} + \rho c^2\frac{\partial v}{\partial x} + v\frac{\partial P}{\partial x} - \varphi\left[\frac{\partial u}{\partial t} + \rho v\frac{\partial u}{\partial x} + P\frac{\partial v}{\partial x}\right] = 0 \tag{A.11}$$

The brackets form the left part of equation A.8, and can be substituted into $\dot{q}_h''' + vF$. Finally, equation A.12 is obtained.

$$\frac{\partial P}{\partial t} + \rho c^2\frac{\partial v}{\partial x} + v\frac{\partial P}{\partial x} = \varphi\dot{q}_h''' + \varphi vF \tag{A.12}$$

B - Superfluid helium production and filling of a magnet

To produce superfluid helium and then fill our magnet, a "Claudet bath" is used [85]. The goal of such a bath is to use two other baths in order to reach the working temperature and pressure conditions in the main superfluid bath. For a superfluid bath at 1.8 K and 1 bar, the functioning is detailed below, based on figure B.2.

- The first bath is a first pressurized and saturated liquid helium bath at 4.2 K, connected to the main superfluid bath with a small leak through the insulating T_{lambda} plate. The small leak allows to maintain a pressure balance between both bathes.
- The second bath is a saturated superfluid bath at 16 mbar. This bath acts as a heat exchanger with the main bath and maintains the temperature of the main bath close to 1.8 K.
- The third bath is the main pressurized superfluid bath, at 1.8 K and 1 bar. The helium is extracted from this bath to fill the magnet.

The saturated bath, to act as a heat exchanger, must be pumped. Therefore, it also must be supplied with superfluid helium. It can be seen in figure B.1 that a Joule-Thompson valve depressurizes the liquid helium from 1 bar to 16 mbar to supply the saturated bath. The helium gas vapor, in a counter-flow heat exchanger, cool down the 4.2 K liquid helium before the valve, in order to increase the efficiency of the depressurization.

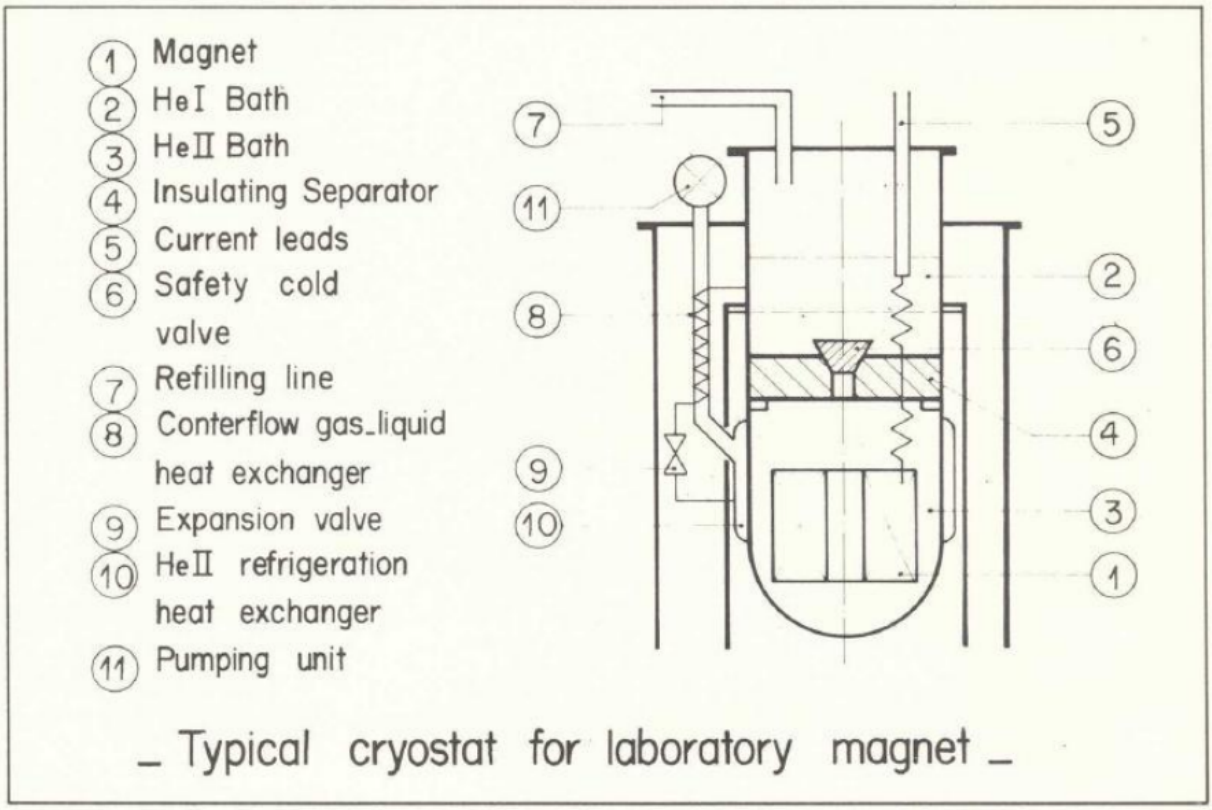

Figure B.1: Scheme of the functioning of a Claudet bath, with the liquid bath, saturated superfluid helium exchanger and pressurized superfluid bath [86].

The Claudet bath creates superfluid helium at 1.8 K and 1 bar and supplies the magnet in order to fill it according to the scheme represented in figure B.2. The cryogenic concept has been inspired from ISEULT and SETH cooling concepts [87]. In fact, after a pre-cooling phase, the caloduc linking the Claudet bath to the coil will start filling it with liquid helium. When superfluid helium is produced, thanks to its thermal extracting properties, the layers of gaseous helium will start condensing until the entire coil is filled with superfluid helium.

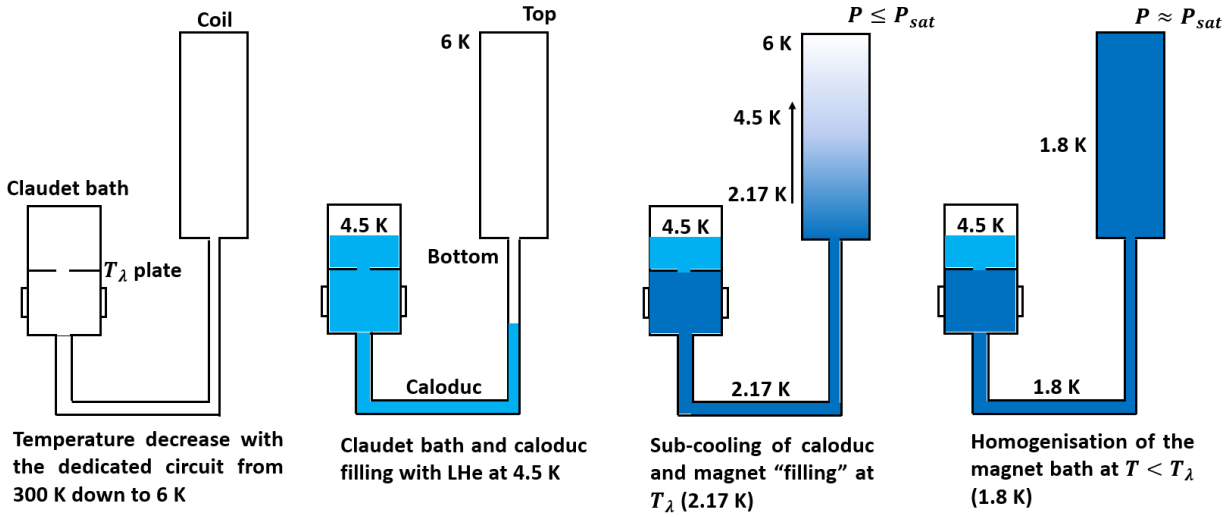

Figure B.2: Cooling down scheme of MACQU, inspired from SETH. The light blue is for liquid helium and dark blue is for superfluid helium.

C - Résumé en français

Depuis 2010, une nouvelle stratégie a émergé à l'Institut Max-Planck (MPI) concernant la recherche de la matière noire. Cette stratégie est basée sur la recherche de particules hypothétiques nommées "axions". L'intérêt de l'axion réside dans sa gamme de masse (40 - 400 µeV) qui n'a jamais été explorée auparavant. Pour explorer une telle gamme de masse, des "haloscopes diélectriques", composés de disques diélectriques placés dans un champ magnétique, sont utilisés. À l'interface des différents milieux diélectriques, l'axion est supposé se comporter comme un photon, générant ainsi un rayonnement électromagnétique dans un champ magnétique. Toutefois, avec les techniques actuelles, générer un facteur de mérite de 100 T^2m^2 (défini dans l'équation C.1) à l'intérieur du trou chaud dans lequel les milieux diélectriques sont insérés reste un objectif scientifique et technologique ambitieux.

$$FoM = \iint B_y^2 dS \tag{C.1}$$

avec FoM le facteur de mérite et B_y le champ magnétique dans la direction du trou chaud.

Dans le cadre d'un partenariat d'innovation lancé par le MPI en 2018, le rôle du CEA est de dimensionner, développer et construire un aimant dipôle possédant des caractéristiques exceptionnelles: un champ magnétique de 9 T, une large ouverture de 1.35 m sur une longueur de 1.3 m, et une gigantesque énergie magnétique stockée de 527 MJ.

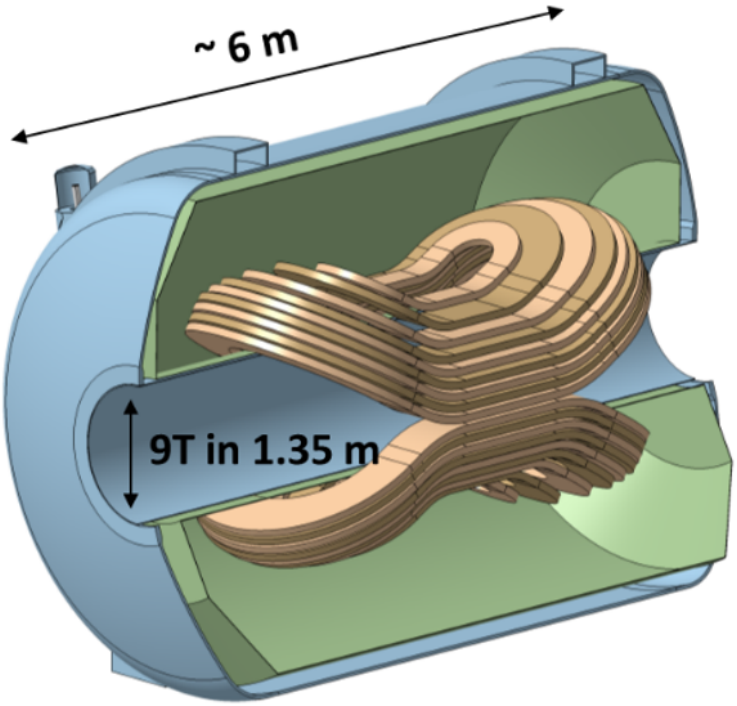

Figure C.1: Schéma de l'aimant MADMAX. Le champ magnétique est maximisé dans le trou chaud via le positionnement des bobines en forme de skateboard en position dipôle.

C'est la première fois qu'un dipôle combine toutes ces caractéristiques en comparaison de précédents dipôles. Pour générer de telles conditions, la meilleure option est d'utiliser des amants supraconducteurs. Ces aimants peuvent, via leur conducteur, transporter des courants

électriques importants sans perte grâce à leur résistance électrique nulle sous une certaine température. Toutefois, les aimants supraconducteurs peuvent subir des transitions, allant de leur état supraconducteur à un état résistif. Lors de cette transition, l'énergie magnétique stockée dans l'aimant se dissipe par effet Joule dans le conducteur et le fluide réfrigérant. Le fluide est chauffé et pressurisé pendant que la zone transitée se propage le long de l'aimant. Une augmentation excessive de la température ou de la pression du fluide peut mener à une détérioration locale des propriétés supraconductrices de l'aimant.

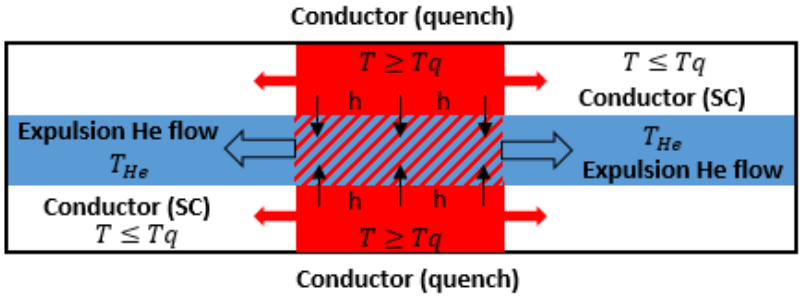

Figure C.2: Schéma du débit d'hélium à l'intérieur du CICC généré par le quench.

Toutefois, en détectant la transition et sa propagation suffisamment tôt, l'aimant peut être protégé de toute dégradation. Cette transition multi-physique s'appelle un "quench" et doit être analysée lors du dimensionnement d'un aimant supraconducteur. Le quench a été décrit par de nombreux modèles prédictifs analytiques et numériques. En se basant sur les équations de la chaleur du conducteur et du fluide, ces modèles décrivent la propagation du quench en considérant des phénomènes thermiques, hydrauliques et électriques. Néanmoins, même si le phénomène de quench a été fortement étudié dans la littérature, cela reste un risque important du dimensionnement d'un aimant, particulièrement lorsque l'aimant dissipe une importante énergie stockée et utilise un nouveau type de conducteur, comme dans le cas de MADMAX. En effet, pour le dimensionnement de l'aimant MADMAX, un concept innovant de conducteur a été développé. Le conducteur est basé sur la technologie de "Cable-In-Conduit" (CICC). Cette technologie a été bien maîtrisée lors de projets comme JT60-SA, W7X, ITER, DEMO etc. Aujourd'hui, cette technologie est industrialisée par de nombreuses entreprises dans le monde alors que d'autres concepts n'existent plus dans l'industrie.

Le conducteur MADMAX combine la technologie CICC avec le concept de refroidissement en bain avec de l'hélium superfluide. L'idée est de remplir le vide du CICC avec de l'hélium superfluide stagnant qui assure la stabilité thermique du conducteur contre des perturbations thermiques et l'initiation d'un quench.

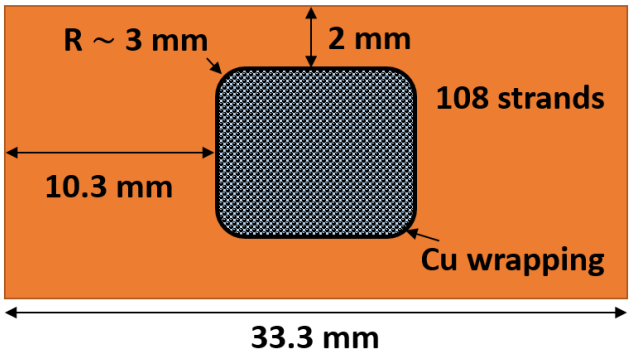

Figure C.3: Section du CICC utilisé pour MADMAX.

De plus, l'utilisation d'hélium superfluide sous les 2 K permet l'utilisation de courant électrique plus important en comparaison du traditionnel refroidissemen en convection forcée à 5 K utilisé pour les CICC. Toutefois, la combinaison inhabituelle d'hélium superfluide et d'un CICC a été rarement utilisée. A notre connaissance, le projet d'aimant hybride à 45 T du NHMFL est le seul autre projet utilisant de l'hélium superfluide pour refroidir un conducteur CICC classique. Il existe toutefois une différence importante entre l'aimant 45 T du NHMFL et l'aimant MADMAX. Dans le 45 T, le stabilisant en cuivre est composé des brins en cuivre tressé avec les brins supraconducteurs en Nb-Ti. Ce tressage assure un bon contact électrique entre les brins de Nb-Ti et les brins de cuivre ce qui permet également une protection efficace contre le quench. Dans MADMAX, le câble est entièrement composé de brins Nb-Ti et le stabilisant est un profilé extérieur en cuivre. Ce conducteur innovant est unique et aucune étude n'existe dans la littérature. De plus, même avec un concept de CICC classique, l'aimant 45 T du NHMFL fonctionne finalement à un courant réduit de 8 kA au lieu de 10 kA suite à un quench non protégé survenu sur l'aimant qui a endommagé les bobines. Cela démontre encore une fois la difficulté de protéger un aimant contre un quench et accentue l'importance de notre étude pour MADMAX, d'autant plus dans le cas où aucune étude antérieure n'existe.

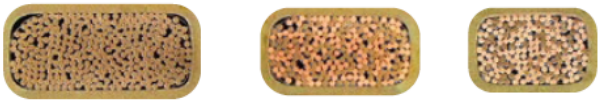

Figure C.4: Différents conducteurs utilisés sur l'aimant hybride 45 T du NHMFL, très différents du conducteur MADMAX.

La combinaison d'hélium superfluide dans un CICC tout en assurant la stabilité thermique avec un stabilisant externe en cuivre n'a jamais été fait. De ce fait, ces deux nouveautés combinées sont suffisantes pour justifier le fait que le comportement du quench est imprévisible et justifie donc notre intérêt à étudier et à modéliser les phénomènes thermo-hydrauliques résultant du quench d'un aimant supraconducteur refroidi en hélium superfluide.

Lorsqu'un quench se produit, le câble supraconducteur transite localement et génère une tension au sein de l'aimant. Le quench commence à se propager par conduction de la chaleur et augmente donc la tension générée. Cette tension doit être mesurée pour assurer la détection du quench afin de protéger l'aimant. Le paramètre moteur de la détection du quench est la vitesse de propagation de quench. Évidemment, si la vitesse de propagation du quench est suffisamment grande, la tension augmente rapidement et permet de détecter le quench efficacement. Si le quench est trop lent, le temps nécessaire à sa détection devient trop important et le quench risque de générer des dégâts sur l'aimant. Ainsi, pour étudier et comprendre le comportement du quench de MADMAX, il a été décidé de dimensionner, construire et tester une bobine prototype appelé MACQU (MAdmax Coil for Quench Understanding) reproduisant les conditions nominales de MADMAX. L'objectif de MACQU est de reproduire et d'étudier un comportement de quench représentatif de celui de MADMAX et de mesurer une vitesse de propagation de quench similaire à celle de MADMAX. Une non-détection du quench sur MACQU pourrait amener à une non-validation du concept de CICC développé pour MADMAX.

Pour valider les objectifs de notre étude, la première étape est de dimensionner et de construire une bobine prototype reproduisant le comportement de quench de MADMAX. Le chapitre 2 de ce manuscrit de thèse est justement dédié au dimensionnement de la bobine prototype supraconductrice MACQU. L'objectif de ce chapitre est de présenter les différentes lignes directrices

du dimensionnement ainsi que les différentes méthodes utilisées pour reproduire le comportement de quench de MADMAX. Les paramètres pilotant le dimensionnement sont évidemment le concept de conducteur (hélium superfluide stagnant à l'intérieur d'un CICC ayant un profilé extérieur en cuivre), les dissipations par effet Joule et la marge en température pour une même marge sur la droite de charge (10 %). MACQU a été dimensionné pour reproduire 73 % des dissipations par effet Joule de MADMAX. Lors de la construction de la bobine, certains changements (augmentation du RRR du profilé notamment, section de cuivre plus importante que celle dimensionnée...) ont menés à une diminution de cette dissipation (44 % de MADMAX en fonctionnement nominal).

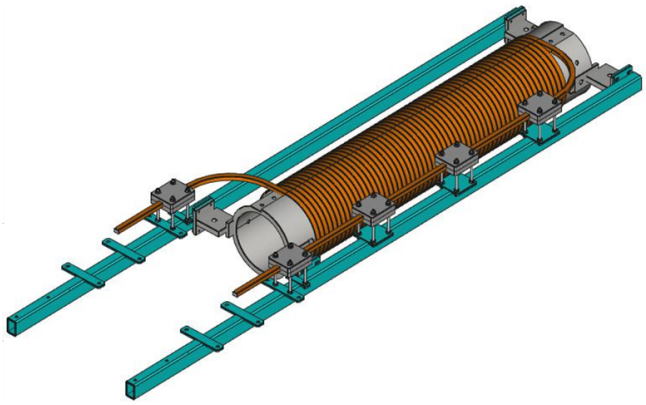

Figure C.5: Schéma de MACQU une fois la construction terminée. Des "bras" (parties rectilignes en sortie du solénoide) ont été ajoutés afin de faciliter l'intégration e la bobine au sein du cryostat JT60-SA disponible au CEA Saclay.

Le chapitre 3 est dédié à la construction et l'intégration de la bobine au sein de l'environnement expérimental. L'instrumentation utilisé sur MACQU est également détaillé. Les différentes méthodes de mesures comme les sondes de températures, les mesures de tensions ainsi que les Superconducting Quench Detectors (SQD) y sont détaillées.

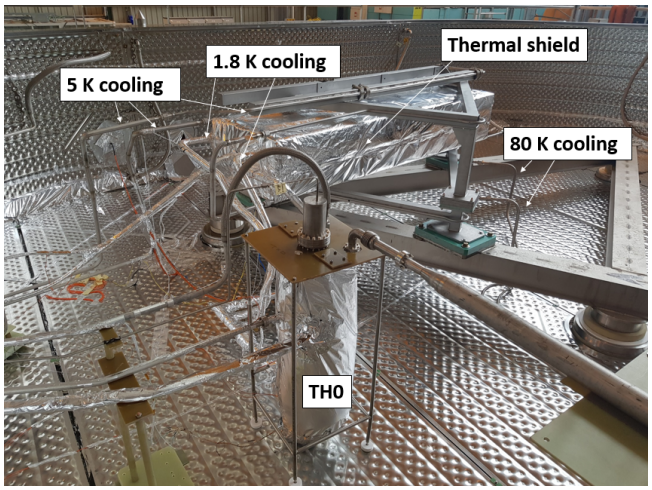

Figure C.6: Photo de MACQU dans la structure support et l'écran thermique, entouré d'isolation MLI.

Les résultats expérimentaux de quench réalisés sur MACQU sont présentés et analysés dans le chapitre 4. Ces résultats ont montrés que le quench était totalement détectable, validant

ainsi le concept de conducteur pour MADMAX. Ces tests ont également démontrés que la propagation du quench était divisée en 3 phases principales pour la plupart des quenchs: une phase quasi-linéaire, une phase d'accélération et une phase de cassure. Un exemple de quench à 15 kA est détaillé en figure C.7.

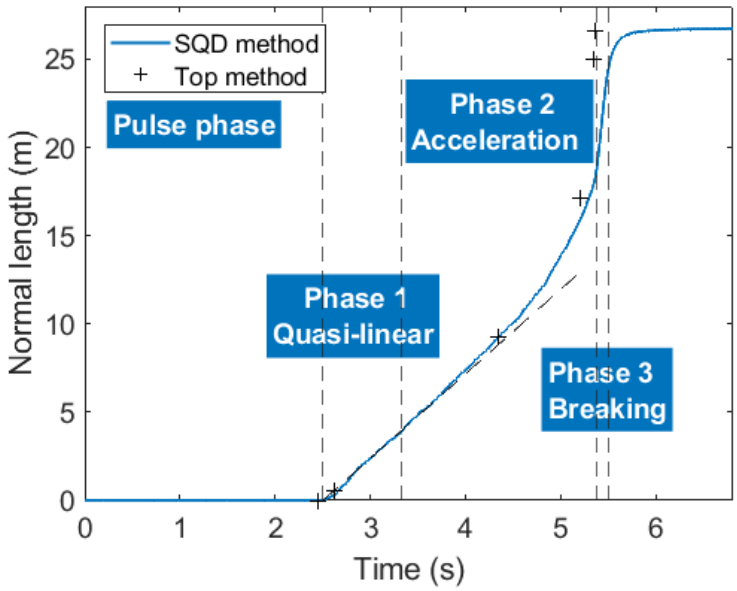

Figure C.7: Les différents régimes de propagation de quench: la *phase quasi-linéaire*, la *phase d'accélération* et la *phase de cassure*. Le cas étudié est à 15 kA et 1.82 K.

Finalement, le chapitre 5 est dédié à la simulation de propagation de quench sur MACQU. Les simulations sont effectués avec le logiciel THEA (Thermal, Hydraulic, Electric Analysis). L'objectif de ces simulations est de vérifier et de compléter les études expérimentales menées. Ainsi, en simulant les variation de pression, de vitesse d'hélium et de température dans le conducteur et dans le fluide, les résultats numériques permettent d'analyser plus en détail chaque terme de l'équation de la chaleur, équation de conservation de la masse et conservation du moment. Cette analyse permet d'identifier précisément les phénomènes physiques prépondérants qui pilotent chaque phase de propagation du quench.

$$\frac{\partial P_h}{\partial t} + \rho_h c_h^2 \frac{\partial v_h}{\partial x} + v_h \frac{\partial P_h}{\partial x} = 2f\rho_h \varphi \frac{v_h^2 |v_h|}{D_h} + \varphi \dot{q}'''_{conv} - \varphi \frac{\partial \dot{q}''_{cf}}{\partial x} \tag{C.2}$$

$$\frac{\partial v_h}{\partial t} + v_h \frac{\partial v_h}{\partial x} + \frac{1}{\rho_h}\frac{\partial P_h}{\partial x} = -2f \frac{v_h |v_h|}{D_h} \tag{C.3}$$

$$\frac{\partial T_h}{\partial t} + \varphi_h T_h \frac{\partial v_h}{\partial x} + v_h \frac{\partial T_h}{\partial x} = \frac{2f}{C_{v_h}} \frac{v_h^2 |v_h|}{D_h} + \frac{\dot{q}'''_{conv}}{\rho C_{v_h}} - \frac{1}{\rho C_{v_h}} \frac{\partial \dot{q}''_{cf}}{\partial x} \tag{C.4}$$

avec P la pression, ρ la densité, c la vitesse du son isentropique, v la vitesse d'hélium, f le coefficient de frottement, φ_h le paramètre de Grüneisen, D_h le diamètre hydraulique, T la temperature, C_v la chaleur spécifique à volume constant, l'indice h pour l'hélium et les coordonnées t et x pour le temps et l'espace. Les termes $\dot{q}'''_{conv}$ et $\dot{q}''_{cf}$ sont des termes sources convectifs et de Gorter-Mellink.

Cette analyse a permit de démontrer que la phase de cassure était du à un Quench-Back-Thermo-Hydraulique (QBTH). Le débit d'hélium généré par le quench engendre un préchauffage de la bobine jusqu'à la température de quench, ce qui engendre une accélération importante de la vitesse du quench, indépendamment de sa propagation par conduction dans le conducteur. Il s'agit de la toute première apparition dans la littérature d'un QBTH en hélium superfluide.

Grâce à THEA, il a également été possible de démontrer que la vitesse de propagation de quench mesurée était plus importante que celle estimée numériquement (2 à 4 fois). De plus, l'écart entre numérique et expérimental augmente avec le courant. La piste principale pour expliquer cet écart viendrait de la diffusion du courant au sein du stabilisant. En effet, lorsqu'un quench de produit, le courant va se redistribuer du câble supraconducteur au stabilisant en cuivre mais cette diffusion n'est pas instantanée. Pendant un court instant de l'ordre de 100 ms, le courant est reparti dans une plus petite section que l'entièreté du stabilisant en cuivre, ce qui génère des pertes par effet Joule plus importantes et donc un quench plus "virulent" et donc plus rapide. Cette étude est une des pistes en cours d'analyse pour reproduire les résultats expérimentaux avec un outil numérique.

Bibliography

[1] Jan Schütte-Engel. Simulation studies for the madmax axion direct detection experiment, 2018.

[2] P. Brun, , A. Caldwell, L. Chevalier, G. Dvali, P. Freire, E. Garutti, S. Heyminck, J. Jochum, S. Knirck, M. Kramer, C. Krieger, T. Lasserre, C. Lee, X. Li, A. Lindner, B. Majorovits, S. Martens, M. Matysek, A. Millar, G. Raffelt, J. Redondo, O. Reimann, A. Ringwald, K. Saikawa, J. Schaffran, A. Schmidt, J. Schütte-Engel, F. Steffen, C. Strandhagen, and G. Wieching. A new experimental approach to probe QCD axion dark matter in the mass range above 40 µev. *The European Physical Journal C*, 79(3), mar 2019.

[3] Allen Caldwell, Gia Dvali, Béla Majorovits, Alexander Millar, Georg Raffelt, Javier Redondo, Olaf Reimann, Frank Simon, and Frank Steffen. Dielectric haloscopes: A new way to detect axion dark matter. *Phys. Rev. Lett.*, 118:091801, Mar 2017.

[4] Joerg Jaeckel and Javier Redondo. Resonant to broadband searches for cold dark matter consisting of weakly interacting slim particles. *Physical Review D*, 88(11), dec 2013.

[5] S. Beurthey, N. Böhmer, P. Brun, A. Caldwell, L. Chevalier, C. Diaconu, G. Dvali, P. Freire, E. Garutti, C. Gooch, A. Hambarzumjan, S. Heyminck, F. Hubaut, J. Jochum, P. Karst, S. Khan, D. Kittlinger, S. Knirck, M. Kramer, C. Krieger, T. Lasserre, C. Lee, X. Li, A. Lindner, B. Majorovits, M. Matysek, S. Martens, E. Öz, P. Pataguppi, P. Pralavorio, G. Raffelt, J. Redondo, O. Reimann, A. Ringwald, N. Roch, K. Saikawa, J. Schaffran, A. Schmidt, J. Schütte-Engel, A. Sedlak, F. Steffen, L. Shtembari, C. Strandhagen, D. Strom, and G. Wieching. Madmax status report, 2020.

[6] Valerio Calvelli, Guillaume Dilasser, Walid Abdel Maksoud, Christophe Berriaud, Francois-Paul Juster, Jean-Pierre Lottin, Arnaud Madur, Francois Nunio, Jean-Michel Rifflet, and Loris Scola. 2D and 3D Conceptual Magnetic Design of the MADMAX Dipole. *IEEE Transactions on Applied Superconductivity*, 30(4):1–5, 2020.

[7] Christophe Berriaud, Walid Abdel Maksoud, Valerio Calvelli, Guillaume Dilasser, Francois-Paul Juster, Arnaud Madur, François Nunio, J. M. Rifflet, and Loris Scola. Conductor Design of the Madmax 9 T Large Dipole Magnet. *IEEE Transactions on Applied Superconductivity*, 30:1–5, 2020.

[8] F. Negrini and R. Penco. A 62 mj superconducting mhd dipole. *IEEE Transactions on Applied Superconductivity*, 5(2):461–464, 1995.

[9] A. Portone, W. Baker, E. Salpietro, A. Vostner, P. Bruzzone, F. Cau, A. della Corte, A. Di Zenobio, E. Theisen, A. Baldini, P. Testoni, J. Lucas, M. Pinilla, and G. Samuelli. Design and procurement of the european dipole (edipo) superconducting magnet. *IEEE Transactions on Applied Superconductivity*, 18(2):499–504, 2008.

[10] B. Gastineau, C. Mayri, B. Baudouy, C. Berriaud, G. Disset, A. Donati, J.-E. Ducret, D. Eppelle, P. Fazilleau, P. Graffin, J.-L. Jannin, D. Loiseau, J.-P. Lottin, M. Massinger, C. Pes, Y. Queinec, Z. Sun, P. Charon, P. Contrepois, and H. Neyrial. Progress in design and construction of the r^3b -glad large acceptance superconducting dipole spectrometer for gsi-fair. *IEEE Transactions on Applied Superconductivity*, 20(3):328–331, 2010.

[11] Paul Brindza, Steven Lassiter, Eric Sun, Mike Fowler, Frederick Forrest, Amaury Porheil, David Raumage, Pierre-Eric Mallard, Sylvain Antoine, and Vincent Sigalo. Final assembly and factory testing of the jefferson lab shms spectrometer quadrupole and dipole superconducting magnets. *IEEE Transactions on Applied Superconductivity*, 27(4):1–5, 2017.

[12] L. Dresner. Quench pressure, thermal expulsion, and normal zone propagation in internally cooled superconductors. *IEEE Transactions on Magnetics*, 25(2):1710–1712, 1989.

[13] L. Bottura and O.C. Zienkiewicz. Quench analysis of large superconducting magnets. part i: model description. *Cryogenics*, 32(7):659–667, 1992.

[14] A. Shajii and J. P. Freidberg. Quench in superconducting magnets. ii. analytic solution. *Journal of Applied Physics*, 76(5):3159–3171, 1994.

[15] A. Shajii and J. P. Freidberg. Quench in superconducting magnets. i. model and numerical implementation. *Journal of Applied Physics*, 76(5):3149–3158, 1994.

[16] L. Bottura. A Numerical Model for the Simulation of Quench in the ITER Magnets. *Journal of Computational Physics*, 125(1):26–41, 1996.

[17] R ZANINO, S DE PALO, and L BOTTURA. A two-fluid code for the thermohydraulic transient analysis of cicc superconducting magnets, 1995.

[18] M. Hoenig and D. Montgomery. Dense supercritical-helium cooled superconductors for large high field stabilized magnets. *IEEE Transactions on Magnetics*, 11(2):569–572, 1975.

[19] C. Portafaix, P. Barabaschi, Florent Gauthier, P. Hertout, B. Lacroix, J. Lesage, S. Nicollet, Louis Zani, and Rosaria Villari. Development of the pseudo 3d thermo hydraulic tool tacos: Application to jt-60sa tf coils design optimization. *Applied Superconductivity, IEEE Transactions on*, 20:1794 – 1797, 07 2010.

[20] H Viebke, D Gustke, T Rummel, C Sborchia, R Schroeder, D Williams, S Bates, B Leigh, and R Winter. Lessons learned from the manufacture of the w7-x planar coils. *Journal of Physics: Conference Series*, 43:748–752, jun 2006.

[21] Jinggang Qin, Y Wu, L.L. Warnet, and Arend Nijhuis. A novel numerical mechanical model for the stress–strain distribution in superconducting cable-in-conduit conductors. *Superconductor Science and Technology*, 24:065012, 04 2011.

[22] V. Corato, C. Vorpahl, K. Sedlak, V.A. Anvar, J. Bennet, M.E. Biancolini, F. Bonne, R. Bonifetto, D.P. Boso, A. Brighenti, P. Bruzzone, G. Celentano, A. della Corte, G. De Marzi, V. D'Auria, F. Demattè, A. Dembkowska, O. Dicuonzo, C. Fiamozzi Zignani, W.H. Fietz, C. Frittitta, L. Giannini, F. Giorgetti, R. Guarino, R. Heller, C. Hoa, M. Huguet, G. Jiolat, M. Kumar, B. Lacroix, M. Lewandowska, N. Misiara, L. Morici, L. Muzzi, D.S. Nickel, S. Nicollet, A. Nijhuis, F. Nunio, C. Portafaix, X. Sarasola, L. Savoldi, I. Tiseanu, G. Tomassetti, A. Torre, S. Turtù, D. Uglietti, R. Vallcorba, K.-P. Weiss, R. Wesche, M.J. Wolf, K. Yagotintsev, L. Zani, R. Zanino, and A. Zappatore. The demo magnet system – status and future challenges. *Fusion Engineering and Design*, 174:112971, 2022.

[23] S. W. Van Sciver, S. J. Welton, K. Bartholomew, M. Gorbunov, J. R. Miller, G. E. McIntosh, G. Bon Mardion, F. Viargues, D. Balcer, and K. Kreinbrink. *Design, Development and Testing of the Cryogenic System for the 45-T Hybrid*, pages 1273–1282. Springer US, 1996.

[24] J.R. Miller. The nhmfl 45-t hybrid magnet system: past, present, and future. *IEEE Transactions on Applied Superconductivity*, 13(2):1385–1390, 2003.

[25] U. Durañona, W. Abdel Maksoud, B. Baudouy, C. Berriaud, V. Calvelli, G. Dilasser, C. Lorin, J.-P. Lottin, T. Pontarollo, and F. Stacchi. Design of a magnet to study quench propagation in a cable-in-conduit-conductor filled with stagnant superfluid helium. *Cryogenics*, 125:103499, 2022.

[26] L Muzzi, G De Marzi, A Di Zenobio, and A della Corte. Cable-in-conduit conductors: lessons from the recent past for future developments with low and high temperature superconductors. *Superconductor Science and Technology*, 28(5):053001, mar 2015.

[27] A. Portone, B. Baker, P. Bauer, E. Salpietro, A. Vostner, P. Bruzzone, Francesca Cau, A. della.Corte, E. Theisen, Pietro Testoni, J. Lucas, and G. Samuelli. Design and procurement of the edipo superconducting magnet. 01 2007.

[28] C. Portafaix, P. Barabaschi, Florent Gauthier, P. Hertout, B. Lacroix, J. Lesage, S. Nicollet, Louis Zani, and Rosaria Villari. Development of the pseudo 3d thermo hydraulic tool tacos: Application to jt-60sa tf coils design optimization. *Applied Superconductivity, IEEE Transactions on*, 20:1794 – 1797, 07 2010.

[29] P. Pugnat, R. Barbier, C. Berriaud, R. Berthier, G. Caplanne, F. Debray, P. Fazilleau, P. Hanoux, B. Hervieu, P. Manil, F. Molinié, C. Pes, R. Pfister, Y. Queinec, M. Pissard, L. Ronayette, C. Trophime, and B. Vincent. Status of the 43-t hybrid magnet of lncmi-grenoble. *IEEE Transactions on Applied Superconductivity*, 26(4):1–5, 2016.

[30] E.W. Boxman, M. Pellegatta, Alexey Dudarev, and Herman Kate. Current diffusion and normal zone propagation inside the aluminum stabilized superconductor of atlas model coil. *Applied Superconductivity, IEEE Transactions on*, 13:1684 – 1687, 07 2003.

[31] L Bottura, P. Bruzzone, and Claudio Marinucci. Analysis of current redistribution in a cicc under transient heat pulses. 711, 06 2004.

[32] Walid Abdel Maksoud. *Modélisation des phénomèmes thermohydrauliques résultant du quench d'un aimant supraconducteur refroidi à l'hélium superfluide.* PhD thesis, 2010. http://www.theses.fr/2010PA112254.

[33] J R Miller, L Dresner, J W Lue, S S Shen, and H T Yeh. Pressure rise during the quench of a superconducting magnet using internally cooled conductors. 1 1980.

[34] C. Meuris, S. Nicollet, and W. Abdel Maksoud. Using the vincenta code to analyse pressure increases in helium during the quench of a superconducting magnet. *Cryogenics*, 50(3):177–186, 2010. CHATS on Applied Superconductivity Workshop 2008.

[35] L. Bottura. A practical fit for the critical surface of nbti. *IEEE Transactions on Applied Superconductivity*, 10(1):1054–1057, 2000.

[36] Martin S. Lubell. Empirical scaling formulas for critical current and critical field for commercial nbti. *IEEE Transactions on Magnetics*, 19:754–757, 1983.

[37] CHARLES P. BEAN. Magnetization of high-field superconductors. *Rev. Mod. Phys.*, 36:31–39, Jan 1964.

[38] Martin N. Wilson. *Superconducting magnets*. Clarendon Press ; Oxford University Press Oxford : New York, 1983.

[39] G. Pasztor and C. Schmidt. Dynamic stress effects in technical superconductors and the "training" problem of superconducting magnets. *Journal of Applied Physics*, 49(2):886–899, 1978.

[40] W.H. Cherry and J.I. Gittleman. Thermal and electrodynamic aspects of the superconductive transition process. *Solid-State Electronics*, 1(4):287–305, 1960.

[41] R.G. Mints, T. Ogitsu, and A. Devred. Quench propagation velocity for highly stabilized conductors. *Cryogenics*, 33(4):449–453, 1993.

[42] Ciazynski D. *A contribution to the study of superconducting magnets.* PhD thesis, 1983.

[43] A. Shajii, J.P. Freidberg, and E.A. Chaniotakis. Universal scaling laws for quench and thermal hydraulic quenchback in Cable in Conduit coils. *IEEE Transactions on Applied Superconductivity*, 5(2):477–482, 1995.

[44] C.J. Gorter and J.H. Mellink. On the irreversible processes in liquid helium II. *Physica*, 15(3):285–304, 1949.

[45] Cryosoft. Thea® v2.4, January 2021.

[46] Horizon Technologies. Hepak v3.4, October 2002.

[47] Eckels Engineering Inc. Cryocomp v3.06, October 2002.

[48] Steven Van Sciver. *Helium Cryogenics*. International Cryogenics Monograph Series., 2012.

[49] F.C. Schwerer, J.W. Conroy, and Sigurds Arajs. Matthiessen's rule and the electrical resistivity of iron-silicon solid solutions. *Journal of Physics and Chemistry of Solids*, 30(6):1513–1525, 1969.

[50] G. K. White and S. B. Woods. Low temperature resistivity of transition elements: Vanadium, niobium, and hafnium. *Canadian Journal of Physics*, 35(8):892–900, 1957.

[51] V D Arp. Stability and thermal quenches in force-cooled superconducting cables. final report. 5 1979.

[52] Piotr Leonidovich Kapitza. The study of heat transfer in helium II. 1971.

[53] A. Kashani and S.W. Van Sciver. High heat flux kapitza conductance of technical copper with several different surface preparations. *Cryogenics*, 25(5):238–242, 1985.

[54] P. Vedrine, G. Aubert, F. Beaudet, J. Belorgey, C. Berriaud, P. Bredy, A. Donati, O. Dubois, G. Gilgrass, F. P. Juster, C. Meuris, F. Molinie, F. Nunio, A. Payn, T. Schild, L. Scola, and A. Sinanna. Iseult/inumac whole body 11.7 t mri magnet status. *IEEE Transactions on Applied Superconductivity*, 20(3):696–701, 2010.

[55] Renard, Bertrand and Genini, Laurent and Duchateau, Jean-Luc. JT-60SA TF Coil Testing Cooling Prevision. *IEEE Transactions on Applied Superconductivity*, 20(3):1835–1839, 2010.

[56] J. Lue, J. Miller, and J. Lottin. Pressure drop measurement on forced flow cable conductors. *IEEE Transactions on Magnetics*, 15(1):53–55, 1979.

[57] Aurubis. M3HE0014. http://aurubis.com.

[58] WST. https://wstitanium.com.

[59] C. Lesmond. Formulaire d'éléctromagnétisme, October 2000.

[60] Dassault Systemes Simulia. Opera 18r2, 2021.

[61] Théophile Pontarollo, Walid Abdel Maksoud, Christophe Berriaud, Ricardo Correia-Machado, Thomas Donga, Yannick Drouen, Unai Durañona, Pascal Godon, Romain Godon, Stéphane Jurie, Clément Lorin, Loris Scola, Léo Segrestan, Nicolas Solenne, and Francesco Stacchi. Cryogenic design of a new cable-in-conduit conductor filled with static superfluid helium. *To be published.*

[62] Francesco Stacchi, Walid Abdel Maksoud, Christophe Berriaud, Valerio Calvelli, Loic Denarie, Guillaume Dilasser, Unai Durañona, Clément Lorin, J-P Lottin, François Nunio, and Théophile Pontarollo. Conductor qualification and fabrication for the macqu solenoid. *To be published.*

[63] Chang Tong Inc, 2021.

[64] Wu, Yu and Qin, Jing-Gang and Liu, Bo and Liu, Fang and Liu, Hua-Jun and Long, Feng and Jin, Huan and Jin, Jing and Yang, Ze-Yuan and Pang, Yu-Chun and Wei, Zhou-Rong and Xue, Tian-Jun and Su, Cheng and Wang, Kun and Liu, Sheng and Li, Hong-Wei and Niu, Er-Wu. Status of the ITER Conductors in China. *IEEE Transactions on Applied Superconductivity*, 26(4):1–5, 2016.

[65] Noell Bilfinger, 2021.

[66] A. Portone, B. Baker, P. Bauer, E. Salpietro, A. Vostner, P. Bruzzone, Francesca Cau, A. della.Corte, E. Theisen, Pietro Testoni, J. Lucas, and G. Samuelli. Design and procurement of the edipo superconducting magnet. 01 2007.

[67] K. Rißе and Th. Rummel and S. Freundt and A. Dudek and S. Renard and V. Bykov and M. Köppen and S. Langish and G.H. Neilson and Th. Brown and J. Chrzanowski and M. Mardenfeld and F. Malinowski and A. Khodak and X. Zhao and G. Eksaa. Design and manufacturing status of trim coils for the wendelstein 7-x stellarator experiment. *Fusion Engineering and Design*, 88(9):1518–1522, 2013. Proceedings of the 27th Symposium On Fusion Technology (SOFT-27); Liège, Belgium, September 24-28, 2012.

[68] Minco. https://catalog.minco.com/.

[69] Loctite Black Stycast. https://www.henkel-adhesives.com.

[70] Clément Lorin, Walid Abdel Maksoud, Jérome Allard, Christophe Berriaud, Valerio Calvelli, Loic Denarie, Dilasser Guillaume, Thomas Donga, Yannick Drouen, Unai Durañona, Pascal Godon, Romain Godon, Stéphane Guihard, Quentin Jurie, Jean-Pierre Lottin, Jean-François Millot, Frédéric Molinié, François Nunio, Théophile Pontarollo, Correia-Machado Ricardo, Loris Scola, Léo Segrestan, Nicolas Solenne, Francesco Stacchi, Bela Majorovits, Dagmar Kerikemeyer, Alan Caldwell, Jörn Schaffran, Achim Hobl,

Michael Gehring, J Amend, J Steinmann, H Wu, and H Zoeller. MADMAX quench analysis: Development, integration and test of the MACQU demo-coil. *To be published.*

[71] Alexey Dudarev, Andrew Gavrilin, Herman Kate, E. Sbrissa, Akira Yamamoto, David E Baynham, M.J.D. Courthold, and C. Lesmond. Quench propagation and detection in the superconducting bus-bars of the ATLAS magnets. *Applied Superconductivity, IEEE Transactions on*, 10:381 – 384, 04 2000.

[72] Fazilleau, Philippe and Berriaud, Christophe and Juster, François-Paul and Gastineau, Bernard. The R3B-GLAD Quench Protection System. *IEEE Transactions on Applied Superconductivity*, 20(3):2074–2077, 2010.

[73] Lakeshore. CX-1050-SD-HT-1.4L temperature sensor. https://www.lakeshore.com/products/categories/specification/temperature-products/cryogenic-temperature-sensors/cernox.

[74] Yawei Huang. *Study and modelling of the thermohydraulic phenomena taking place during the quench of a superconducting magnet cooled with supercritical helium.* PhD thesis, 2018.

[75] Lionel Quettier, Guy Aubert, Jean Belorgey, Christophe Berriaud, Philippe Bredy, Guillaume Dilasser, Olivier Dubois, Graham Gilgrass, Quentin Guihard, Vincent Jannot, Francois-Paul Juster, Herve Lannou, Frederic Molinié, Francois Nunio, Arnaud Roger, Thierry Schild, Loris Scola, Armand Sinanna, Vadim Stepanov, and Pierre Vedrine. Commissioning completion of the iseult whole body 11.7 t mri system. *IEEE Transactions on Applied Superconductivity*, 30(4):1–5, 2020.

[76] T. Schild, J. Germain, J.B. Berton, B. Dupont, and A. Forgeas. Current distribution in a reusable junction for w7-x coil tests. *IEEE Transactions on Applied Superconductivity*, 12(1):1313–1318, 2002.

[77] M. Chantant, L. Genini, P. Bayetti, F. Millet, M. Wanner, V. Massaut, A. Della Corte, F. Ardelier-Desage, V. Catherine-Dumont, A. Dael, P. Decool, A. Donati, J.L. Duchateau, P. Garibaldi, S. Girard, J.C. Hatchressian, P. Fejoz, P. Jamotton, L. Jourdheuil, F.P. Juster, O. Kuster, P. Lebourg, F. Leroux, F. Molinie, B. Renard, P. Reynaud, T. Schild, P. Spuig, S. Turtu, L. Vieillard, and C. Walter. A coil test facility for the cryogenic tests of the jt-60sa tf coils. *Fusion Engineering and Design*, 86(6):561–564, 2011. Proceedings of the 26th Symposium of Fusion Technology (SOFT-26).

[78] J.W. Lue, L. Dresner, S.W. Schwenterly, C.T. Wilson, and M.S. Lubell. Investigating thermal hydraulic quenchback in a cable-in-conduit superconductor. *IEEE Transactions on Applied Superconductivity*, 3(1), 1993.

[79] Ali Shajii. Theory and modelling of quench in cable-in-conduit superconducting magnets. pages 338–341, 1994.

[80] L. Dresner. Theory of thermal hydraulic quenchback in cable-in-conduit superconductors. *Cryogenics*, 31(7):557–561, 1991. Symposium on Superconductor Stability.

[81] Toshinari Ando, Masataka Nishi, Takashi Kato, Jun Yoshida, Noboru Itoh, and Susumu Shimamoto. Measurement of quench back behavior on the normal zone propagation velocity in a CICC. *Cryogenics*, 34:599–602, 1994. Fifteenth International Cryogenic Engineering Conference.

[82] L. Bottura and C. Rosso. Finite element simulation of steady state and transient forced convection in superfluid helium. *International Journal for Numerical Methods in Fluids*, 30(8):1091–1108, 1999.

[83] Luca Bottura. Friction Factor correlations. *CRYO/98/009*, February 1999.

[84] Luca Bottura. Heat Transfer correlations. *CRYO/98/010*, February 1999.

[85] G. Bon Mardion, G. Claudet, P. Seyfert, and J. Verdier. *Helium II in Low-Temperature and Superconductive Magnet Engineering*, pages 358–362. Springer US, Boston, MA, 1978.

[86] G. Claudet. *Bath cryostats for superfluid helium cooling*, pages Part D9, pp. 795—800. IOP Publishing, Bristol, 1998.

[87] P. Bredy, J. Belorgey, P. Chesny, B. Hervieu, H. Lannou, F. P. Juster, W. Abdel-Maksoud, C. Mayri, F. Molinie, and A. Payn. Cryogenics around the 11.7 t mri iseult magnet. *IEEE Transactions on Applied Superconductivity*, 20(3):2066–2069, 2010.

université PARIS-SACLAY

ÉCOLE DOCTORALE
Particules, hadrons, énergie et noyau : instrumentation, imagerie, cosmos et simulation (PHENIICS)

Titre: Etude et modélisation de phénomènes thermohydrauliques résultant du quench d'un aimant supraconducteur refroidi en hélium superfluide

Mots clés: thermohydraulique, quench, aimant supraconducteur, hélium superfluide

Résumé: Une des problématiques majeures autour de la conception d'aimant supraconducteur est d'être capable de protéger l'aimant en cas de quench accidentel. Le quench est la transition de l'état supraconducteur vers l'état résistif d'un aimant supraconducteur, ce qui engendre une grande quantité d'énergie par effet Joule. Ce quench ainsi que sa propagation par conduction vont mener à une forte montée de température, pouvant dégrader voire endommager irrémédiablement l'aimant. Il est donc nécessaire de détecter un quench lorsqu'il se produit afin d'éviter tout risques de dégradation. Dans le cadre du projet MADMAX, projet européen autour de la recherche de la matière noire, un type de conducteur inédit a été développé, la protection demande donc une attention toute particulière. En effet, avec un conducteur de type Cable-In-Conduit-Conductor (CICC) avec un profilé en cuivre, refroidi avec de l'hélium superfluide stagnant à l'intérieur du conduit, et sans bain d'hélium superfluide autour des bobines afin de les refroidir, le comportement du quench est imprévisible. Ainsi, afin de mieux appréhender le comportement du quench, une maquette d'aimant supraconducteur (MACQU), reprenant en grande partie les caractéristiques de MADMAX, a été conçue puis testée au CEA Saclay, au sein de la station d'essais JT60-SA. Une large plage de température a été testée, allant de 1.75 K à 2.01 K, ainsi qu'une large plage de courant allant de 10 kA à 17 kA. Elle a permis de démontrer la sécurité du système de détection, tout en permettant d'étudier un phénomène de propagation de quench particulier: le Quench Back Thermo Hydraulique. Ce phénomène physique a été aussi observé via THEA®, outil de simulation numérique. Il est apparu que la propagation du quench se faisait en 3 phases principales. La première phase est la phase quasi-linéaire où le quench se propage à vitesse constante. La vitesse de propagation de quench est pilotée par la vitesse d'expansion de l'hélium qui, suite au dépot d'énergie du quench, s'écoule dans le conduit. La conduction thermique dans la goulotte en cuivre n'est donc pas le phénomène dominant de la propagation du quench. La deuxième phase est la phase d'accélération, où le quench accélère progressivement. La vitesse de l'hélium augmentant avec la longueur transitée, la vitesse de l'helium pilote toujours celle du quench et contribue à l'accélérer. Dans le même temps, les forces de friction préchauffent l'aimant loin du front de propagation et la temperature de l'aimant augmente dans la zone supraconductrice. La troisième phase démarre lorsque sous l'effet des forces de friction, une grande partie de la zone supraconductrice restante transite instantanément et génère un second quench beaucoup plus rapide que le précédent. Cette phase est appelée la phase de cassure, caractérisée par une importante cassure de la longueur transitée, correspondant à cette caractéristique accélération.

Title: Study and modelling of the thermohydraulic phenomena taking place during the quench of a superconducting magnet cooled with superfluid helium

Keywords: thermohydraulic, quench, superconducting magnet, superfluid helium

Abstract: One of the biggest issues in the design of a superconducting magnet is to be able to protect the magnet during an accidental quench. The quench is the transition between the superconducting state and the resistive state of a superconducting magnet, generating an important amount of energy due to Joule effect. This quench and its propagation by heat conduction will lead to an important temperature increase. It can totally burn the magnet and degrade irreversibly its properties. It is then mandatory to detect a quench if it occurs to avoid any degradation risk. In the framework of the MADMAX project, a European project around dark matter research, the protection asks for a particular attention. In fact, with a conductor of Cable-In-Conduit-Conductor (CICC) with a copper profile, cooled with stagnant superfluid helium, and without a superfluid helium bath around the coils to cool down the coils, the quench behavior appears as unpredictable. Then, in order to study the quench behavior, a mock-up coil (MACQU), that has the same MADMAX's features, has been designed and tested at CEA Saclay, in the JT60-SA testing facility. A large testing temperature range (from 1.75 K to 2.01 K), with a large testing current (from 10 kA to 17 kA) were tested. It allowed to demonstrate the safety of the detection system, and to study a particular quench propagation behavior: the Thermal Hydraulic Quench Back. This physical phenomenon has been also observed with THEA®, a numerical simulation tool. It appeared that the quench propagation was divided in three main phases. The first phase is the *quasi-linear phase*, where the quench propagates at constant speed. The quench propagation speed is driven by the velocity of the helium that, due to the Joule energy deposition of the quench, flows in the conduit. The thermal conduction in the copper stabilizer is not the main phenomena of the quench propagation. The second phase is the *acceleration phase*, where the quench accelerates progressively. The velocity of the helium increasing with the normal length, the velocity of the helium still drives the quench propagation speed and contributes to accelerate it. At the same time, the friction forces pre-heat the coil upfront the quench propagation front and the temperature of the non-quenched zone increases. The third phase starts when, due to the friction forces, an important part of the non-quenched zone instantaneously transits and generates a second quench, much faster than the first one. This phase is called the *breaking phase*, characterized by the important break of the normal length, corresponding to this characteristic acceleration.